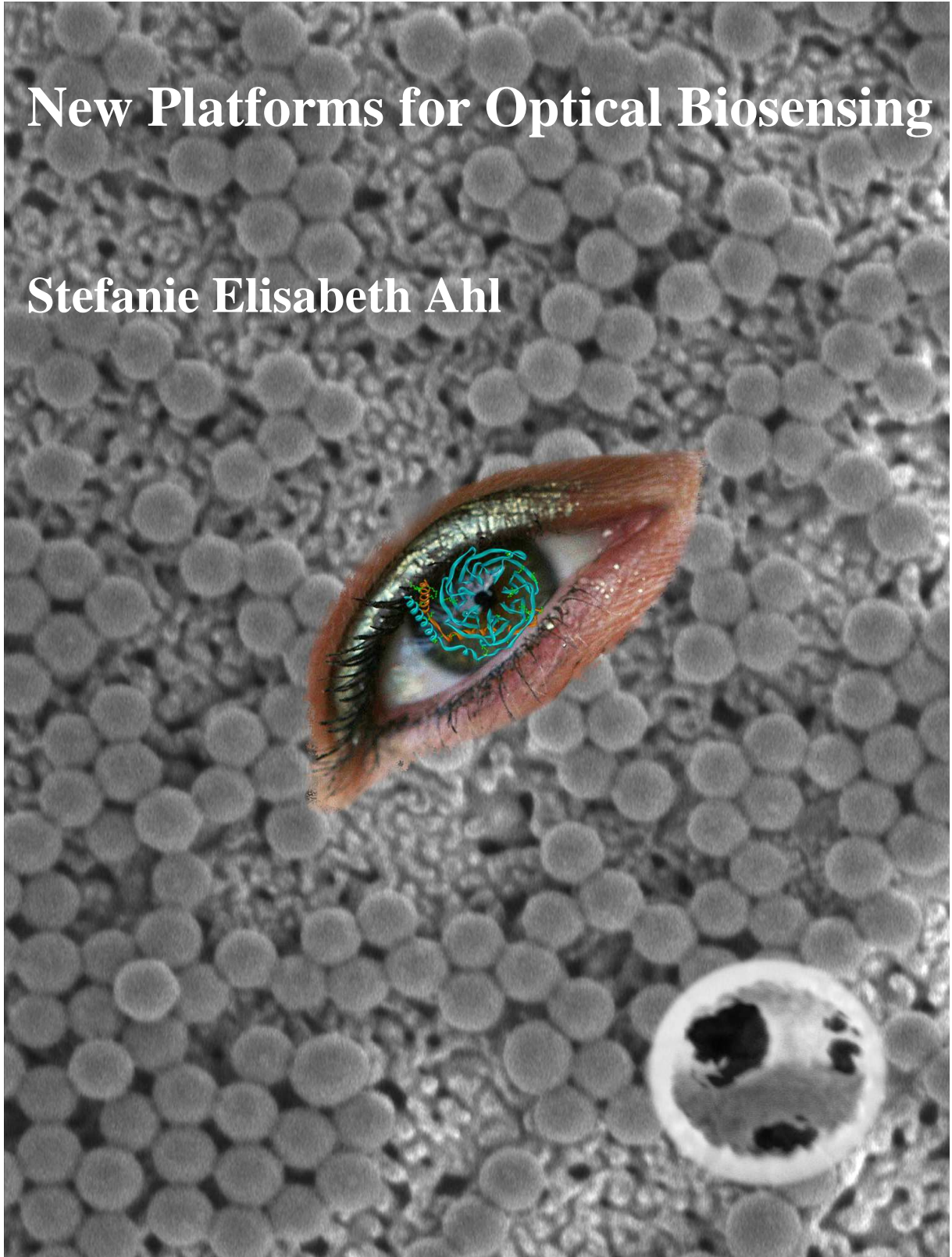


# New Platforms for Optical Biosensing

Stefanie Elisabeth Ahl



# **„New Platforms for Optical Biosensing“**

Dissertation

zur Erlangung des Grades

Doktor der Naturwissenschaften

Am Fachbereich Biologie

Der Johannes Gutenberg-Universität Mainz

Stefanie Elisabeth Ahl

Geb. am 07.Januar 1980 in Ludwigshafen am Rhein

Mainz, Juli 2007

Dekan: Prof. Dr. H. Paulsen  
1. Berichterstatter: Prof. Dr. W. Knoll  
2. Berichterstatter: Prof. Dr. U. Wolfrum  
Tag der mündlichen Prüfung: 24. Juli 2007

Die vorliegende Arbeit wurde unter Betreuung von Herrn Prof. Dr. W. Knoll im Zeitraum zwischen Dezember 2004 bis Juli 2007 am Max Planck Institut für Polymerforschung, Mainz, Deutschland angefertigt.

Alle Weisheit kommt vom Herrn und ist bei ihm auf ewig.  
< Die Bibel, Sir 1,1 >

# Contents

<b>1. Introduction .....</b>	<b>1</b>
1.1 Biosensors .....	1
1.2 Aim of the study .....	2
1.3 References .....	4
<b>2. Methods for surface characterization .....</b>	<b>5</b>
2.1 Theoretical Background – Surface Plasmon Resonance (SPR) Spectroscopy.....	5
2.1.1 Excitation of Propagating Surface Plasmons (p-SPR) .....	5
2.1.1.1. Optical properties of materials .....	5
2.1.1.2. Prism coupling .....	7
2.1.1.3. SPR signal .....	8
2.1.1.4. Influence of the excitation wavelength to the SPR signal .....	8
2.1.1.5 Changes in the dielectric due to adsorbates leading to changes in the plasmon resonance minimum .....	9
2.1.2 Excitation of Localized Surface Plasmons (l-SPR) .....	10
2.2 Basics of Cyclic Voltammetry (CV) .....	11
2.3 Introduction to Electrochemical Impedance Spectroscopy (EIS) theory .....	15
2.4 Scanning Electron Microscopy (SEM) .....	19
2.5 Autocorrelation.....	20
2.6 References .....	21
<b>3. Experimental Section .....</b>	<b>22</b>
3.1 Instrumental - SPR setup.....	22
3.2 Modifications of the SPR setup: Halogen lamp plus monochromator.....	25
3.3 Instrumental – CV/EIS- setup .....	26
3.4 Further instruments .....	27
3.4.1 Plasma cleaner .....	27
3.4.2 Surface profiler .....	27
3.4.3 UV/VIS/NIR Spectrometer.....	28
3.5 Preparation of Evaporated Gold (EG) films.....	29
3.6 Preparation of Template Stripped Gold (TSG) films .....	29
3.7 Preparation of silane monolayers .....	29
3.8 Materials.....	31
3.9 References .....	33
<b>4. Nanoporous gold (NPG) membrane .....</b>	<b>34</b>
4.1 Advantage of Porous Gold - new plasmonic material and the aim of the study .....	34
4.2 Fabrication of Random Nanoporous Gold Substrates .....	37
4.2.1 Cleaning of the glass slides.....	37
4.2.2 Silanization of the glass slides .....	37
4.2.3 Wet-chemical acid etching of the decorative gold leaves .....	37
4.2.3.1 Execution of dealloying .....	38
4.2.4 Electrochemical dealloying.....	40
4.3 Scanning Electron Microscopy as a tool to visualize the NPG morphology .....	41
4.4 Two Dimensional Autocorrelation to determine the typical structure size of the NPG for different etching times .....	43

4.5 Cyclic voltammetry and electrical impedance spectroscopy as methods to determine the surface area of NPG substrates.....	47
4.6 Simultaneous Excitation of Propagating and Localized Surface Plasmon Resonance in Nanoporous Gold Membranes (p-SPR and l-SPR).....	54
4.6.1 Multilayer architecture built on NPG and flat gold substrates.....	61
4.6.2 Environmental refractive index changes to NPG (glyceroltest) .....	68
4.6.3 Layer by layer (LbL) deposition of charged dendrimers .....	72
4.6.4 Layer by layer (LbL) deposition of avidin and antiavidin .....	77
4.7 Application of NPG	
The Protein-Tethered Lipid Bilayer established on the Nanoporous Gold Substrate .....	85
4.7.1 Characterization of the layer formation by SPR and EIS .....	88
4.7.2 Activation of the Cytochrome C Oxidase .....	91
4.8 Conclusion.....	93
4.9 References .....	96
<b>5. Gold/Silica Composite Inverse Opals .....</b>	<b>101</b>
5.1 Advantage of gold/silica composite inverse opals - new plasmonic material and the aim of the study .....	101
5.2 Fabrication of gold/silica composite inverse opals .....	102
5.3 Surface plasmon resonance features of gold/silica composite inverse opals .....	106
5.4 Conclusion and Outlook.....	107
5.5 References .....	109
<b>6. Epitope mapping to identify the centrin sequence interacting to transducin.....</b>	<b>111</b>
6.1 Processes of optical signaling .....	111
6.1.1. The vertebrate visual signal transduction cascade .....	112
6.1.2. Light and dark adaptation .....	114
6.1.3. Barrier hypothesis .....	116
6.2 Characteristics of Transducin.....	119
6.3 Centrins in vertebrate cells .....	121
6.4 Motivation .....	125
6.5 Development of the sensor architecture .....	127
6.5.1. Commercial CM5 sensor chip (Biacore) .....	127
6.5.2. Peptide P19 matrix.....	131
6.5.3. Combined mPEG thiol matrix .....	134
6.6 Regeneration of the sensor surface.....	136
6.7 Further experimental optimization .....	137
6.8 SPR results of centrin-transducin interactions .....	137
6.8.1. Centrin 1 (Cen1p) constructs .....	138
6.8.2. Centrin 3 (Cen3p) isoform.....	141
6.9 Conclusion and Outlook.....	142
6.10 References .....	145
<b>7. Summary .....</b>	<b>151</b>
<b>8. Appendix .....</b>	<b>153</b>
8.1 Summary of advantages and disadvantages of NPG at a glance.....	153
8.2 Supporting material for chapter 6.....	154

8.3 Table of standard amino acid abbreviations.....	155
8.4 List of Abbreviations.....	156
8.5 List of Figures .....	159
8.6 List of Tables.....	162
<b>Acknowledgements.....</b>	<b>164</b>
<b>Curriculum vitae .....</b>	<b>166</b>

# 1. Introduction

## 1.1 Biosensors

The combination of optical, electrochemical, piezoelectric, thermal and other physicochemical instrumental techniques with the specificity of a biological recognition system has resulted in a variety of new analytical devices known as biosensors. Biosensors are under intensive development worldwide because they have many potential applications, e.g. in the fields of clinical diagnostics<sup>1</sup>, food analysis<sup>2</sup>, environmental monitoring<sup>3</sup> and process control of industrial processes<sup>4</sup>.

Biosensors are devices that transform biochemical information into an analytically useful signal. Three structural parts are essential, a recognition system, a detector element and a transducer that associates the two other components (Figure 1.1.1). The recognition site is usually a biological material, e.g. tissue, cell receptor, enzyme, antibody, protein or nucleic acid. The main function of the recognition system is to be highly *selective* for the analyte to be measured. The detector element measures physicochemical properties, such as small optical, piezoelectric electrochemical, thermometric, or magnetic changes. In contrast to the recognition system, the main purpose of the detector element is to offer a high *sensitivity*.

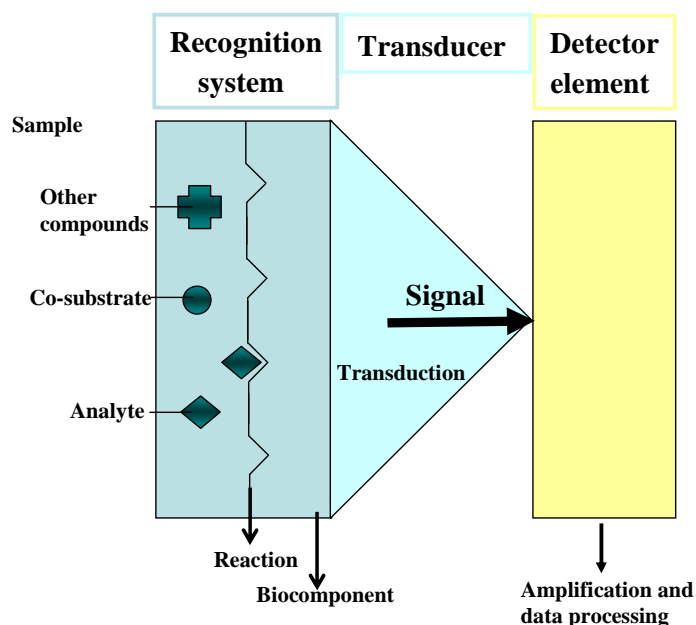


Figure 1.1.1: Principle of a biosensor.

Surface plasmon resonance (SPR) spectroscopy has become a routine technique in optical biosensor applications, where interactions between an analyte in solution and a biomolecular recognition element immobilized on the surface are probed<sup>5, 6</sup>. In 1990, the company Biacore introduced the first commercial SPR biosensing instrument where surface plasmon resonances are excited in a dense gold film and used to probe small changes in refractive index at the gold surface<sup>7</sup>.

Much effort is spent on the development of more sensitive sensor platforms. One strategy for amplifying the sensitivity is to increase the amount of analyte binding sites. This can be realized by an enhancement of the sensor surface area. Subsequently, Biacore modified the flat gold film by attaching a three dimensional dextran hydrogel matrix, that allows high loading of analytes<sup>8</sup>.

Other approaches try to influence the evanescent field of the plasmon wave to gain further sensitivity. The so-called long range surface plasmon, excited at the two sides of a metal layer in contact with two identical dielectric media<sup>9</sup>, promises high resolution, as the field intensity at the interface is higher than in case of conventional SPR and the decay length of the evanescent field can be in the extended range of 400 - 800 nm<sup>10</sup>. Another approach to enhance the sensitivity is the use of localized surface plasmon phenomena<sup>11, 12</sup> for the detection of small molecules<sup>13</sup>. Novel fabrication methods for plasmonic materials are developed<sup>14, 15</sup>.

### **1.2 Aim of the study**

This study is divided into three parts. In the first part, nanoporous gold, as a new plasmonic material, is investigated in detail (chapter 4). In the second part, plasmonic features of gold/silica composite inverse opals are studied (chapter 5). While parts one and two mainly focus on fundamental research by looking into the properties of novel substrate materials in order to provide a basis for new optical biosensors, part three addresses an application of biosensing (chapter 6).

Generally, nanoporous gold, as a rough, but continuous gold membrane, shows features of both planar metal films that exhibit propagating-SPR (p-SPR) and nanostructured metal materials that exhibit localized-SPR (l-SPR), two kinds of optical excitations used in state-of-the-art optical sensing technologies. Therefore, nanoporous gold is an interesting substrate that can be incorporated into the recognition system of improved biosensors. Detailed analyses of the nanoporous gold are described in chapter 4.

In chapter 5, silica inverse opals are used as a substrate to host gold nanoparticles in order to investigate the optical features that may be created as a combinatory result of both the ordered macropores and the L-SPR from the nano metallic particles.

The fundamental question addressed in chapter 6 is the development of a binding assay to probe the protein/protein interaction of the calcium binding protein centrin with the heterotrimeric G-protein transducin. Therefore, a commonly evaporated, flat/dense gold film was used to support a propagating surface plasmon mode.

### 1.3 References

1. Connolly, P., Clinical Diagnostics Opportunities for Biosensors and Bioelectronics. *Biosensors & Bioelectronics* **1995**, 10, (1-2), 1-6.
2. Lukacheva, L. V.; Zakemovskaya, A. A.; Karyakina, E. E.; Zorov, I. N.; Sinitsyn, A. P.; Sukhacheva, M. V.; Netrusov, A. I.; Karyakin, A. A., Determination of glucose and lactose in food products with the use of biosensors based on Berlin blue. *Journal of Analytical Chemistry* **2007**, 62, (4), 388-393.
3. Rickerby, D. G.; Morrison, M., Nanotechnology and the environment: A European perspective. *Science and Technology of Advanced Materials* **2007**, 8, (1-2), 19-24.
4. Patel, P. D., Overview of affinity biosensors in food analysis. *Journal of Aoac International* **2006**, 89, (3), 805-818.
5. Homola, J., Present and future of surface plasmon resonance biosensors. *Analytical and Bioanalytical Chemistry* **2003**, 377, (3), 528-539.
6. Shankaran, D. R.; Gobi, K. V. A.; Miura, N., Recent advancements in surface plasmon resonance immunosensors for detection of small molecules of biomedical, food and environmental interest. *Sensors and Actuators B-Chemical* **2007**, 121, (1), 158-177.
7. Jönsson, U.; Fägerstam, L.; Ivarsson, B.; Johnsson, B.; Karlsson, R.; Lundh, K.; Löfås, S.; Persson, B.; Roos, H.; Ronnberg, I.; Sjolander, S.; Stenberg, E.; Stahlberg, R.; Urbaniczky, C.; Ostlin, H.; Malmqvist, M., Real-Time Biospecific Interaction Analysis Using Surface-Plasmon Resonance and a Sensor Chip Technology. *Biotechniques* **1991**, 11, (5), 620-&.
8. Löfås, S.; Johnsson, B., A Novel Hydrogel Matrix on Gold Surfaces in Surface-Plasmon Resonance Sensors for Fast and Efficient Covalent Immobilization of Ligands. *Journal of the Chemical Society-Chemical Communications* **1990**, (21), 1526-1528.
9. Kasry, A.; Knoll, W., Long range surface plasmon fluorescence spectroscopy. *Applied Physics Letters* **2006**, 89, (10).
10. Kasry, A., Optical Biosensors; New Aspects in Surface Plasmon Fluorescence Spectroscopy. *PhD Thesis* **2006**, University of Mainz
11. Haes, A. J.; Van Duyne, R. P., A nanoscale optical biosensor: Sensitivity and selectivity of an approach based on the localized surface plasmon resonance spectroscopy of triangular silver nanoparticles. *Journal Of The American Chemical Society* **2002**, 124, (35), 10596-10604.
12. Yonzon, C. R.; Zhang, X.; Zhao, J.; Van Duyne, R. P., Surface-enhanced nanosensors. *Spectroscopy* **2007**, 22, (1), 42-+.
13. Haes, A. J.; Zou, S. L.; Schatz, G. C.; Van Duyne, R. P., Nanoscale optical biosensor: Short range distance dependence of the localized surface plasmon resonance of noble metal nanoparticles. *Journal of Physical Chemistry B* **2004**, 108, (22), 6961-6968.
14. Wiley, B.; Sun, Y. G.; Chen, J. Y.; Cang, H.; Li, Z. Y.; Li, X. D.; Xia, Y. N., Shape-controlled synthesis of silver and gold nanostructures. *Mrs Bulletin* **2005**, 30, (5), 356-361.
15. Mieszawska, A. J.; Jalilian, R.; Sumanasekera, G. U.; Zamborini, F. P., Synthesis of gold nanorod/single-wall carbon nanotube heterojunctions directly on surfaces. *Journal of the American Chemical Society* **2005**, 127, (31), 10822-10823.

## 2. Methods for surface characterization

### 2.1 Theoretical Background – Surface Plasmon Resonance (SPR) Spectroscopy

During the last 15 years surface plasmon resonance (SPR) spectroscopy has become a popular technique for optical immunosensor applications<sup>1</sup>. In general, it is a method for measuring the refractive index of very thin (order of nm)<sup>2</sup> layers of material adsorbed on metals. A change in the refractive index can be detected close to the metal, typically within a distance of 200 - 300 nm to the sensor surface<sup>3</sup>. Material adsorption can be converted into mass and thickness with knowledge of the respective refractive indices. The following chapter outlines the principles of SPR.

#### 2.1.1 Excitation of Propagating Surface Plasmons (p-SPR)

##### 2.1.1.1 Optical properties of materials

Plasmons are collective oscillations (non-radiative) of free electron gas at optical frequencies. Surface plasmons are confined to surfaces and occur at the interface of a material with a positive dielectric constant ( $\epsilon_{\text{dielectric}}$ ) and a material of a negative dielectric constant ( $\epsilon_{\text{metal}}$ ). Surface plasmons can be excited on metallic surfaces under certain conditions (depending on material, incident angle, polarization and wavelength of the incident light). The conditions depend on the dielectric constants ( $\cong$  refractive indices) of the metal, dielectric and dielectric adsorbate layers, and are consequently reliant on the excitation wavelength. Equations 2.1 and 2.2 describe the relationship between the dielectric constant and refractive index.

$$\epsilon' = n^2 - k^2 \quad \text{--- 2.1}$$

$$\epsilon'' = 2nk \quad \text{--- 2.2}$$

Optical properties of materials can be described by the refractive index,  $n$  which describes the real part and the absorption coefficient,  $k$  which describes the imaginary part. Alternatively the dielectric constants  $\epsilon'$  (real part) and  $\epsilon''$  (imaginary part) are used.

The electromagnetic field of the surface plasmon decays exponentially into both the dielectric and the metal, with the highest intensity at the interface. The plasmonic dispersion relation (between angular frequency  $\omega$  and wave vector  $k$ ) reveals that the longer the

excitation wavelength  $\lambda$  nm (smaller  $\omega_L$ , since  $\omega = 2\pi(c/\lambda)$ ), the smaller the  $k$  vector needed to match the plasmon excitation condition (cf. Figure 2.1.1).

The  $k_{ph}$  of the incident light (also called momentum) can be tuned/magnified using either prism or grating coupling, so that photons are not coupled directly to the metal/dielectric interface, but via high-index prism (with  $\epsilon_{prism} > \epsilon_{dielectric}$ )<sup>3</sup>. The wavevector  $k_{SP}$  is described by  $k_{SP} = (2\pi/\lambda) \cdot n_{prism} \cdot \sin\theta_{PSP}$ .

$$K_{SP} = \frac{\omega}{c} \sqrt{\frac{\epsilon_m \epsilon_d}{\epsilon_m + \epsilon_d}} \geq K_{Ph} = \frac{\omega}{c} \sqrt{\epsilon_d} \quad \text{--- 2.3}$$

Plasmonic dispersion relation: At any angle  $\theta$   $|k_{sp}|$  ( $k$  surface plasmon) is larger than  $|k_{ph}|$  ( $k$  photon, air).

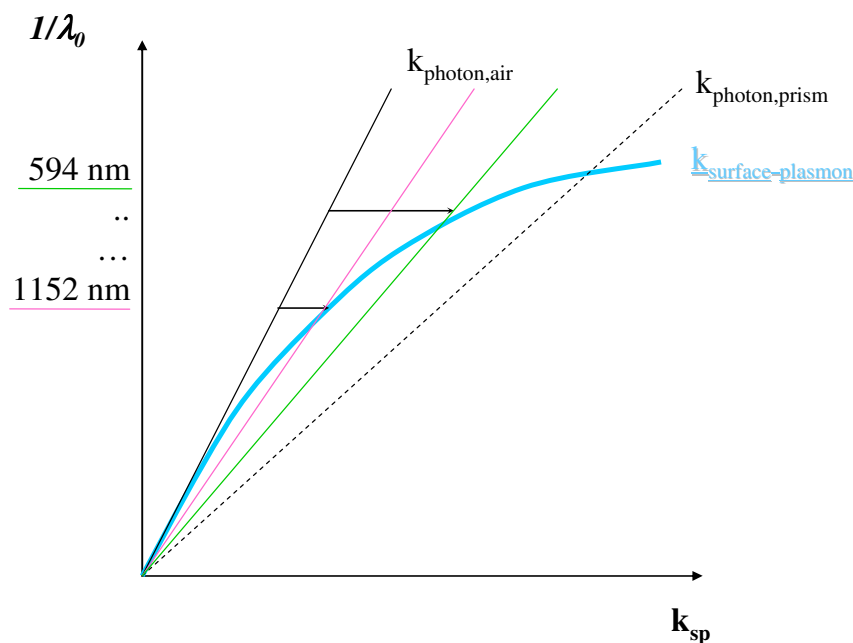


**Figure 2.1.1: Dispersion relation demonstrates the enhancement of  $k$  using a high index prism, e.g. LaSFN9. There is no intersection for  $k_{photon,air}$  and  $k_{surface-plasmon}$ , while  $k_{photon,prism}$  intersects  $k_{surface-plasmon}$ . It also becomes apparent that the light coupling needs smaller  $k$  for longer excitation wavelength.**

When the energy and the momentum of the photon are just right, it interacts with the free electrons of the metal. The incident p-light (transversal magnetic, TM- or p-polarized) photons are absorbed and converted into surface plasmons.

### 2.1.1.2 Prism coupling

Different configurations of SPR devices are capable of generating and measuring propagating surface plasmons: devices that use prism coupling<sup>4, 5</sup> or grating coupling<sup>6</sup>. Prism based SPR was firstly described in 1959 by Turbadar<sup>7, 8</sup>. One decade later, prism coupling was further developed and split in two coupling variations, known as the Otto<sup>5</sup> and the Kretschmann/Raether configurations<sup>4</sup>. In this thesis, only prism coupling in the Kretschmann/Raether configuration was used, in this arrangement the photons travel through a high index prism and couple through a gold film, that is in contact with the dielectric medium (Figure 2.1.2).

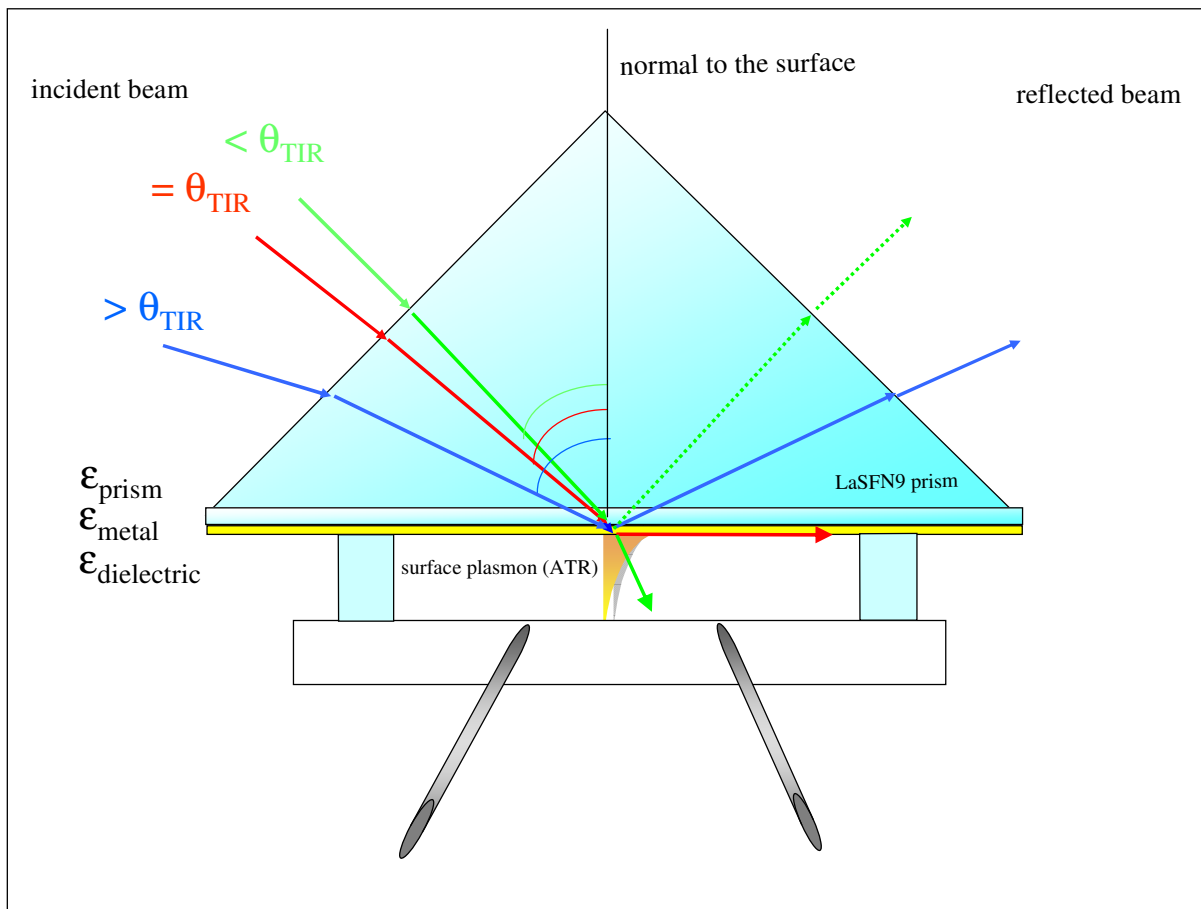


**Figure 2.1.2: Prism coupling in the Kretschmann/Raether configuration was used in this thesis to excite propagating surface plasmon resonances. Both the angle of incidence and the angle of reflection are defined as the angle between the corresponding light beam and the normal to the surface, so the reflected beam is detected at  $2\theta$ .**

The incident laser beam passes into the prism and is reflected, partially transmitted or absorbed at the base of the prism (Figure 2.1.2). Below  $\theta_{TIR}$  (angle of the total internal reflection) most of the light is transmitted (green line). At  $\theta_{TIR}$  the transmitted light propagates parallel to the surface (red line). If the angle of incidence is greater than  $\theta_{TIR}$ , no light is transmitted. The surface plasmon occurs at higher angle  $\theta$  dependent on the properties of the materials (gold film: thickness,  $\epsilon'$ ,  $\epsilon''$ , ...).

### 2.1.1.3 SPR signal

The SPR signal can be derived by monitoring the intensity of the reflected light as a function of the incident angle<sup>7, 8</sup>:

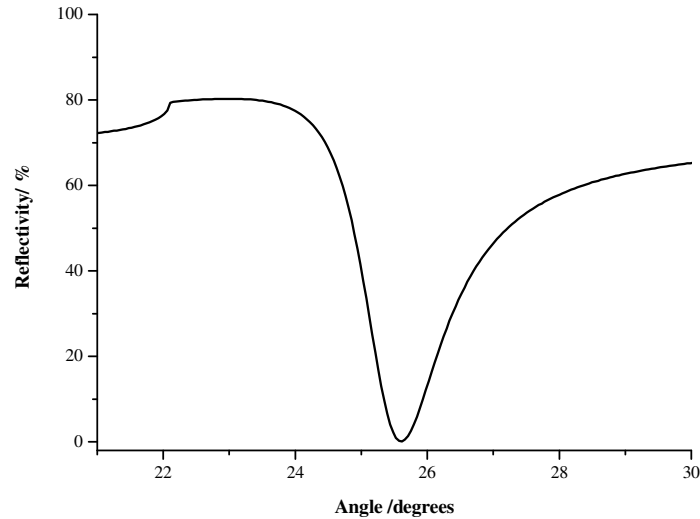


**Figure 2.1.3: Simulated surface plasmon resonance signal (Winspall, version 2.20): triangular prism, 50 nm Au film, air; 632.8 nm excitation in p-polarization.**

Due to absorption, the plasmon phenomenon is also called the *attenuated* total internal reflection (minimum of reflectivity). The thickness of the gold film, as well as the excitation wavelength influences the coupling angle and the coupling efficiency.

### 2.1.1.4 Influence of the excitation wavelength to the SPR signal

The SPR signal is strongly influenced by the excitation wavelength. With larger wavelengths the resonances become narrower and the angle of total internal reflection increases:

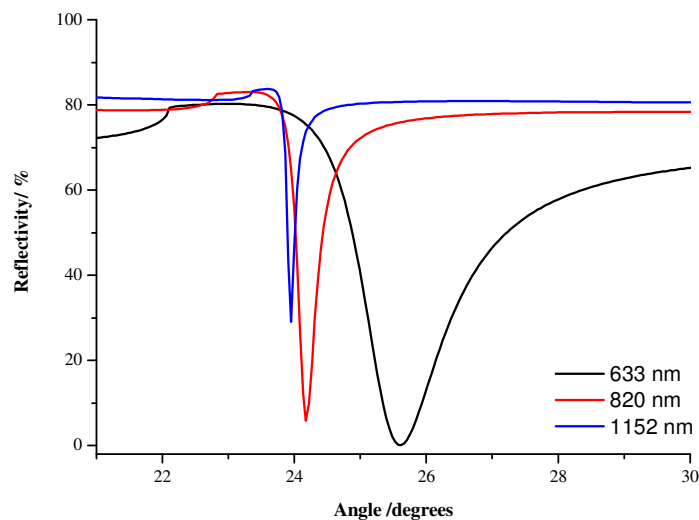


**Figure 2.1.4: Simulated surface plasmon resonance signals (Winspall, version 2.20) demonstrate the influence of the excitation wavelength for three different wavelengths. All other parameter stayed the same as in Figure 2.1.3.**

### 2.1.1.5. Changes in the dielectric due to adsorbates leading to changes in the plasmon resonance minimum

The SPR signal is highly sensitive to physical or chemical adsorption of molecules in the order of nm. During adsorption processes, the total internal reflection stays the same, while the surface plasmon minimum shifts to higher angles (Figure 2.1.5 C).

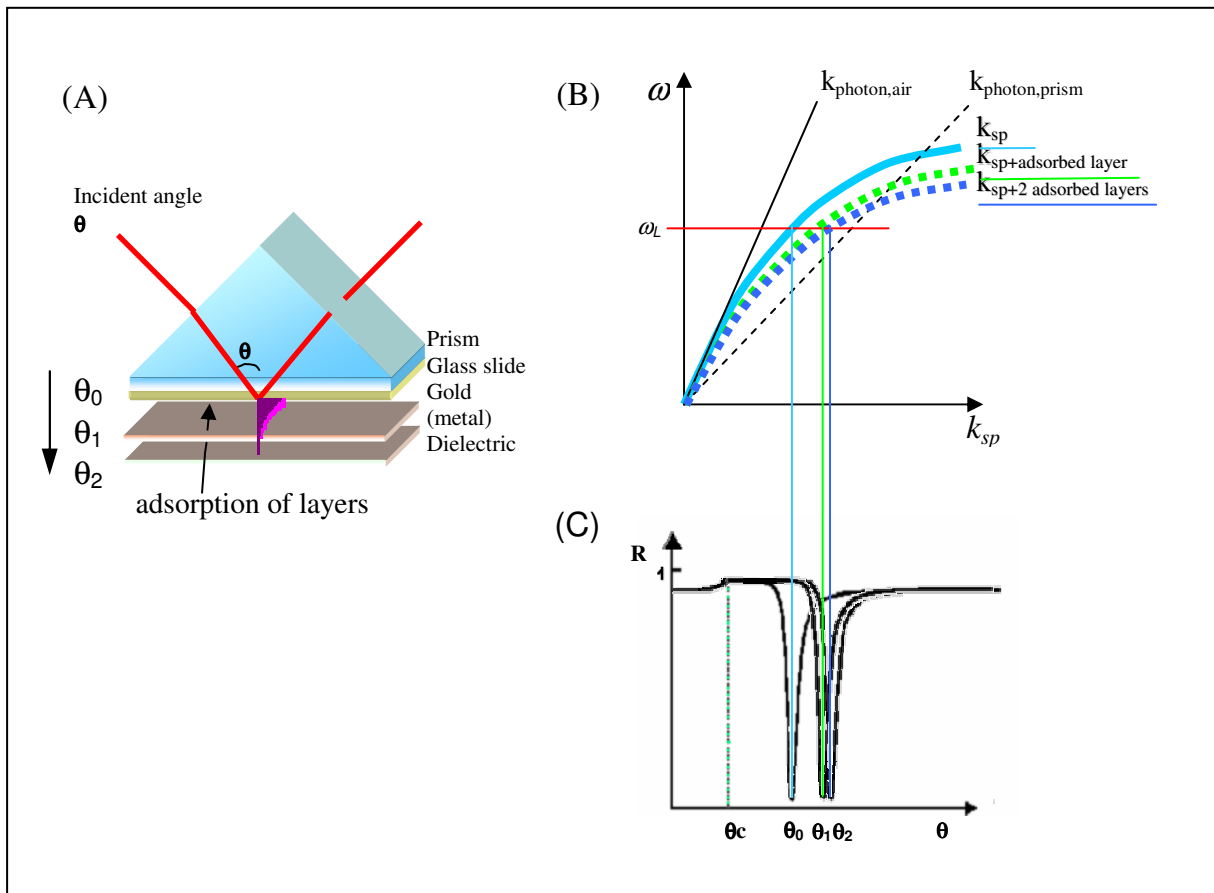


**Figure 2.1.5: Prism coupling in Kretschmann/Raether configuration to probe adsorption of layers (A). Dispersion relation (cf. Fig. 2.1.1), here  $\omega$  versus  $k_{SP}$ , shows that for a given  $\omega_L$  the momentum of surface plasmons increases, when the dielectric constant  $\epsilon_d$  increases e.g. due to adsorption of layers (B). The angular reflectivity curve (C) reveals a shift of the coupling angle  $\theta_0$  to  $\theta_1$  to  $\theta_2$ , if layers are adsorbed.**

A change in the refractive index can be only detected near the metal. At a distance of 200 - 300 nm to the sensor surface, the signal loses sensitivity.

Surface plasmon resonance curves, in opposition to optical waveguide systems, do not allow the separation of the refractive index ( $n$ ) and thickness ( $d$ ) of the layers. With known values for either  $n$  or  $d$ , the other parameter can be calculated assuming the formation of a dense homogeneous monolayer via the Fresnel equations based on Maxwell's theory.

### 2.1.2 Excitation of Localized Surface Plasmons (l-SPR)

Both propagating and localized surface plasmon resonance (p-/l-SPR) are collective electron oscillations<sup>9</sup>. But the p-SPR is a travelling wave, propagating along the interface shared with a dielectric as described above; whereas the l-SPR is a localized field confined to metallic nanoparticles and other nanostructures, e.g. voids with high curvature metal/dielectric interfaces. Raether defines the localized plasmon phenomenon as a resonance of a small sphere<sup>6</sup>. In general, the term localized plasmon is frequently used in the literature to describe a range of different phenomena.

The phenomenon of localized plasmons has found application in the field of biosensing<sup>10</sup>, because the l-SPR is medium dependent just like the p-SPR. An absorption in the visible or UV parts of the spectrum originates from the collective oscillation of the conduction electrons. The peak position shifts if the refractive index of the surrounding medium is changed. To exemplify, an absorbance spectrum before and after deposition of immunoglobulin onto a gold-nanoparticle-coated three-dimensionally ordered macroporous film is shown:

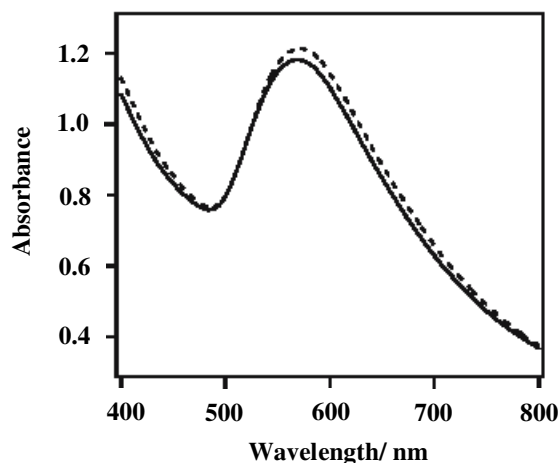


**Figure 2.1.6:** Absorption spectra of the gold-nanoparticle-coated three-dimensionally ordered macroporous film before (solid line) and after (dashed line) the immobilization of hIgG<sup>10</sup>.

The main advantage of the localized plasmon is its independence from the incident angle of the excitation light and sample orientation<sup>9</sup>. Thus angle-resolved spectroscopy allows l-SPR and p-SPR modes to be distinguished from each other. A setup was built to simultaneously monitor the angular dependent reflectivity and the absorbance from two different sides of the substrate [Chapter 3]. A second advantage of the l-SPR is the much shorter decay length of the evanescent field ( $\sim 20$  nm) compared to the p-SPR ( $\sim 200$  nm), so that only changes within this short distances are detectable, thus the crude bulk solution does not influence the signal.

The l-SPR is dependent on the material, particle shape and excitation wavelength, but independent of incident angle and polarization.

## 2.2 Basics of Cyclic voltammetry (CV)

Cyclic voltammetry as a three-electrode method (reference, working and counter electrode) has become a popular analytical technique for electrochemical studies. The choice of solvent, background electrolyte and specific working electrode material determines the potential window of the electrochemical measurement. The background electrolyte is a salt added both to increase the solution conductivity and to suppress charge transport by migration. A potential difference is measured between the reference and the working electrode while any current flowing is measured between the working and the counter electrode. The electrodes are connected to a potentiostat which is used to adjust the voltage to maintain a potential difference of choice between the reference and working electrodes.

In cyclic voltammetry the potential ( $E$ ) is continuously changed as a function of time ( $t$ ), the direction of the potential is reversed at the end of the first scan ( $E_2$ ) and scanned back to the original value,  $E_1$  (Figure 2.2.1). The different scans directions are also sometimes termed anodic and cathodic scans, respectively. The rate of change of potential with time is referred as the scan rate. A current response ( $i$ ) is obtained when an electro active species is oxidized or reduced at the electrode. A typical one-electron ( $e^-$ ) transfer reactions is<sup>11</sup>:



The ferricyanide  $\text{Fe(CN)}_6^{3-}$  (**hexacyanoferrate(III) ion**)/ferrocyanide  $\text{Fe(CN)}_6^{4-}$  (**hexacyanoferrate(II) ion**) redox couple is reversible and the electron transfer does not involve making or breaking of Fe-C bonds.

During the anodic scan the current increases as the potential reaches the oxidation potential of the analyte, but then drops as the concentration of the analyte is depleted close to the electrode surface. During the cathodic scan, the electrode is returned to a potential that will reoxidize the analyte and generate a current of reverse polarity from the forward scan. In the case of a simple reversible redox couple, such as the  $\text{Fe}^{2+}/\text{Fe}^{3+}$  couple, the oxidation and reduction peaks will have a similar shapes and the same amount of charge will be passed in the forward scan as in the reverse scan (Figure 2.2.1).

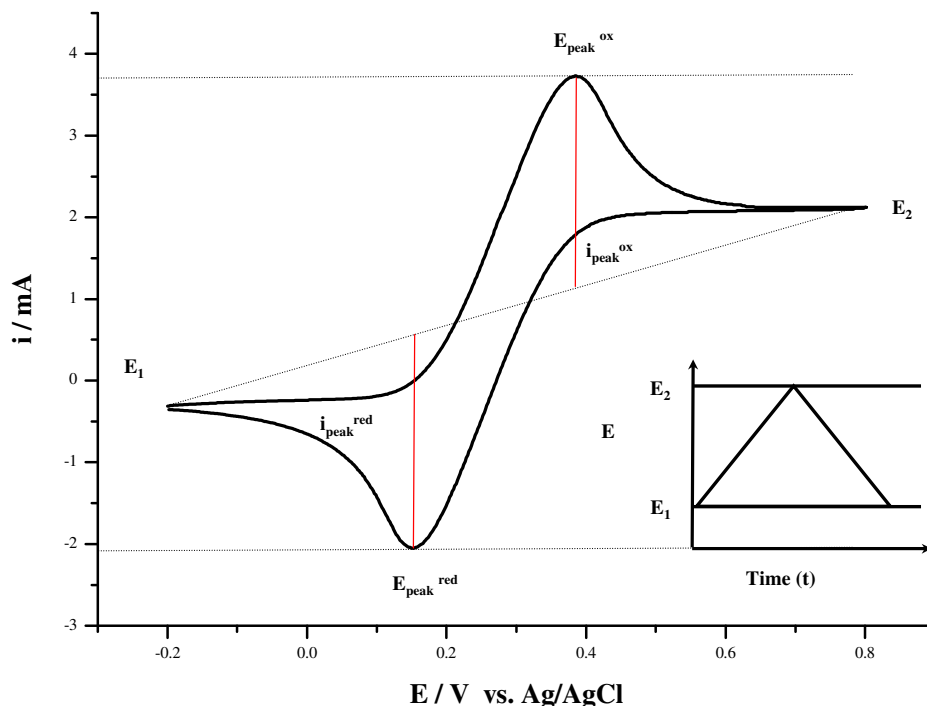


**Figure 2.2.1:** Representative cyclic voltammogram for a reversible electron transfer reaction: ferricyanide-ferrocyanide conversion measured on a large (0.5 cm<sup>2</sup>) flat evaporated gold electrode vs. Ag/AgCl reference electrode. Because of the non-optimal conditions, it is not an ideal cyclic voltammogram, e.g. the peak separation is too large. The inset shows the variation (waveform) of the applied potential (E) as a function of time (t) in a cyclic voltammetry experiment.

The potential of the electrode for a reversible half-reaction is given by the Nernst equation<sup>11</sup>:

$$E = E^0 + \frac{RT}{nF} \ln \frac{c[OX]}{c[RED]} \quad \text{--- 2.5}$$

where

- Electrode potential (E)
- Standard electrode potential (E<sup>0</sup>)
- Universal gas constant (R), equal to 8.314510 J K<sup>-1</sup> mol<sup>-1</sup>
- Temperature (T) in Kelvin (Kelvins = 273.15 + °C.)
- Faraday constant (F) (the charge per a mole of electrons), equal to 9.6485309·10<sup>4</sup> C mol<sup>-1</sup>
- Number of electrons (n) transferred in the half-reaction
- c[OX]/c[RED] are the concentrations of the oxidized and reduced species, respectively.

In my studies only reversible electron transfer reactions will be addressed.

Basics of Electrode processesFaradaic and Non-Faradaic processes

Both Faradaic and Non-Faradaic processes can occur at electrodes, when a potential difference is applied. If electron transfer causes oxidation or reduction (e.g.  $\text{Fe}^{2+}/\text{Fe}^{3+}$ ), the resulting current is termed Faradaic. In cyclic voltammetry the peak current ( $i_p$ ) is given by the Randles-Sevcik equation<sup>11</sup>:

$$i_p = (2.69 \times 10^5) n^{3/2} A C D^{1/2} v^{1/2} \quad \text{--- 2.6}$$

where A is the electrode area (in  $\text{cm}^2$ ), C the concentration (in  $\text{mol}/\text{cm}^3$ ), D the diffusion coefficient (in  $\text{cm}^2/\text{s}$ ), and v the scan rate (in  $\text{V}/\text{s}$ ).

The Non Faradic current is the charging current caused by the movement of ions in the solution when a potential is applied to the working electrode. When considering electrochemical data the Non-Faradaic processes always have to be taken into account.

Brief Explanation of the Electrical Double Layer

The whole array of charged species and oriented dipoles at the electrode - solution interface is termed the electrical double layer (Figure 2.2.2 B). So far several models have been developed to describe the nature of the electrical double layer. The earliest model is attributed to Helmholtz (~ 1853). He considered the double layer as a simple capacitor consisting of a single layer of ions close to the electrode surface (Figure 2.2.2 A). But the “double” layer at the solution side is thought to be made up of quite a few layers. In the beginning of the 19<sup>th</sup> century, Gouy and Chapman introduced a diffuse model, in which the potential at the electrode surface decreases exponentially due to a diffuse layer of charge compensating ions at the electrode-solution interface. Stern combined the two models.

The Bockris – Devanathan - Müller model (water-dipole model) is used as a current model (Figure 2.2.2 B). The zone of the specifically adsorbed ions at distance  $x_1$  is called the inner Helmholtz plane (IHP). The solvated ions can approach the electrode only to a distance  $x_2$  termed outer Helmholtz plane (OHP). The so called diffuse layer formed of charge compensating ions extends from the OHP into the bulk solution. The thickness of this diffuse

layer is dependent on the total concentration of ions in the solution. In low concentrated solution the charging current can be even larger than the Faradaic current, because of the double layer capacitance.

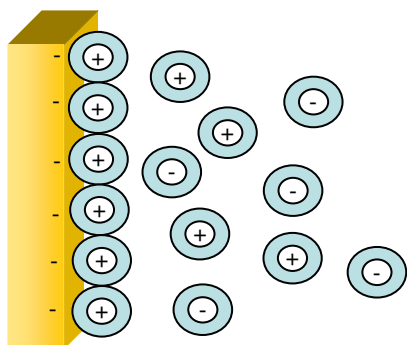


Figure 2.2.2 (A): The attracted positive ions are forming a layer balancing the negative electrode charge. The distance of approach is limited to the radius of the ion and salvation shell. The overall result is the double layer (two layers of charge) situation, which is analogue to a capacitor. Helmholtz (1853).

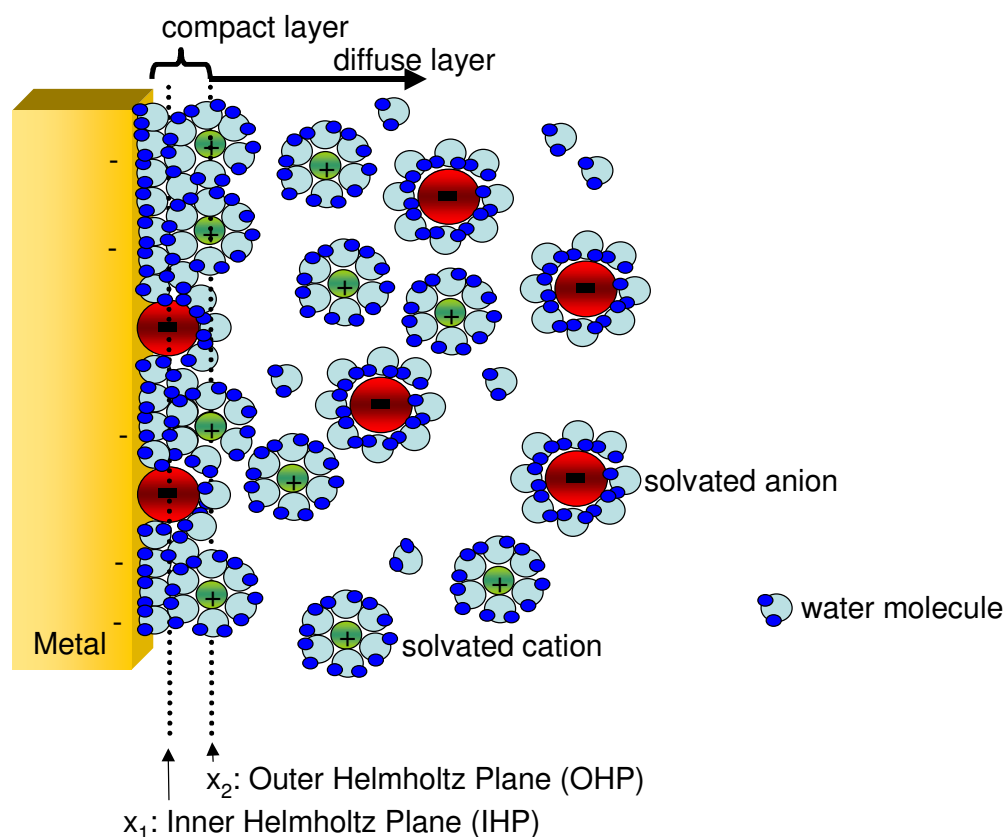


Figure 2.2.2 (B): The most modern model of the electrical double layer of Bockris, Devanathan, Müller, which also shows the presence and orientation of solvent dipoles. The sketch illustrates the double layer region, and also takes into account anions specifically adsorbed at the electrode surface.

### **2.3 Introduction to Electrochemical Impedance Spectroscopy (EIS) theory**

Electrochemical Impedance spectroscopy (EIS) is a powerful tool for the investigation of electrochemical systems. In recent years, EIS has found various applications and is routinely used in the characterization of batteries<sup>12</sup>, semiconductors<sup>13</sup>, fuel cells<sup>14</sup>, and corrosion phenomena<sup>15</sup>.

The advantage of EIS over CV (described above) is that EIS uses very small excitation amplitudes such as 5 - 10 mV causing only minimal perturbation of the tested system. CV is used to investigate the response of the system when a direct current (DC) voltage ramp is applied; EIS is measured by applying a small amplitude alternating current (AC) wave around a fixed DC potential. In the first characterization step of the substrate, the potential range of electrochemical phenomena can be found by running a cyclic voltammogram. In the following EIS measurements this range can be further examined by probing frequency dependent processes at a fixed DC potential. A broad range of frequencies can be investigated by EIS (typically between MHz and mHz). EIS measurements can be executed in low conductivity solutions such as physiological buffer systems. EIS provides data of electrode double layer capacitance and can give information about charge-transfer kinetics [Chapter 4.7; NPG capacitance; cytochrome c oxidase reaction].

#### The concept of complex impedance

In impedance spectroscopy a sinusoidally modulated voltage is applied to an electrochemical system. The modulation amplitude is chosen to be small so that the system responds linearly to the perturbation and the output is also a sine wave. In the case of EIS the input sine wave is a voltage and the measured output is a sinusoidally varying current at the same frequency. Depending on the nature of the electrochemical system the sinusoidal current response (Figure 2.3.1) can be phase shifted and display changes in amplitude relative to the incident voltage sine wave. Ohm's law known as  $E = I \cdot R$  for the resistance in DC (direct current, continuous current), can be expressed in  $E = I \cdot Z$  for the impedance in AC case.

$$Z = \frac{E}{I} \quad \text{--- 2.7}$$

Potential (E) values are measured in volts (V), current (I) in amperes or amps (A), and in this case impedance (Z) as well as resistance (R) in ohms ( $\Omega$ ). In AC circuits resistors, capacitors

and inductors impede the flow of electrons so that impedance can be expressed as a complex number with the resistance as the real component and the combined capacitance and inductance as the imaginary component, so called reactance. In the special case of measuring the pure resistance, no shift ( $\theta$ ) in the two waveforms is observed. They would be accurately in phase and different only in amplitude.

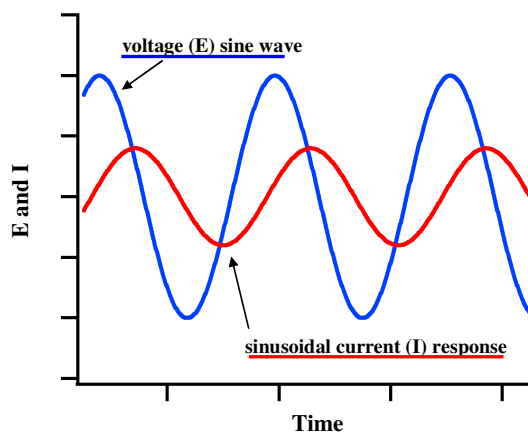


**Figure 2.3.1:** Drawing of sinusoidally varying AC voltage over and the resulting current which shows a different phase and amplitude to the incident signal.

### Equivalent circuit models

In EIS studies the response of the system to the voltage sine wave is modelled as the response of circuit elements, for example resistors and capacitors. The simplest equivalent (RC) circuit (resistor-capacitor circuit) that could be used to model the electrochemical cell described in this work is depicted in Figure 2.3.2.  $R_{\text{solution}}$  is the ohmic resistance of the solution between working (e.g. nanoporous gold) and reference electrode (e.g. silver/silver chloride).  $R_{\text{solution}}$  can be extracted directly from the Bode plot (Figure 2.3.4), when the frequency equals Zero.  $R_{\text{membrane}}$  is the resistance at the electrode/solution interface, e.g. where the lipid bilayer membrane is built [cf. Chapter 4.7].  $C_{\text{dl}}$  (capacitance of the double layer) or  $C_{\text{membrane}}$  is the capacitance at this interface. From this double layer capacitance measurements information on ad- and desorption processes can be derived.

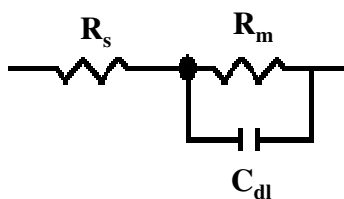


**Figure 2.3.2:** Equivalent circuit for a single electrochemical cell.

This simplified equivalent circuit was extended by a constant phase element (CPE) to model the complexity of the submembrane space of the tethered lipid bilayer established on the

nanoporous gold substrates [Chapter 4.7]. Several factors can cause the need of a CPE. One explanation for CPE behaviour is electrode roughness<sup>16</sup>, e.g. the fractal structure of the nanoporous gold substrates. Variations in thickness and composition of a coating can be second reason<sup>17</sup>. Further reasons can be inhomogeneous reaction rates on a surface<sup>18</sup> and non-uniform current distribution<sup>19</sup>.

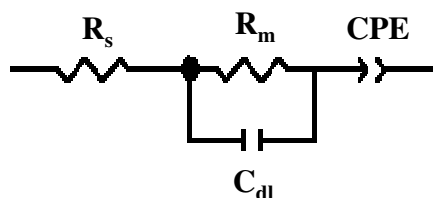


Figure 2.3.3: Equivalent circuit for a complex system.

### Impedance plots

The most prominent plot is the so called Bode plot. The Bode plot format shows directly the magnitude of the impedance  $|Z|$  and the phase shift ( $\theta$ ), both as a function of frequency (Figure 2.3.4). It is a log-log plot, so that a wide range of frequencies and corresponding values of impedance can be viewed.

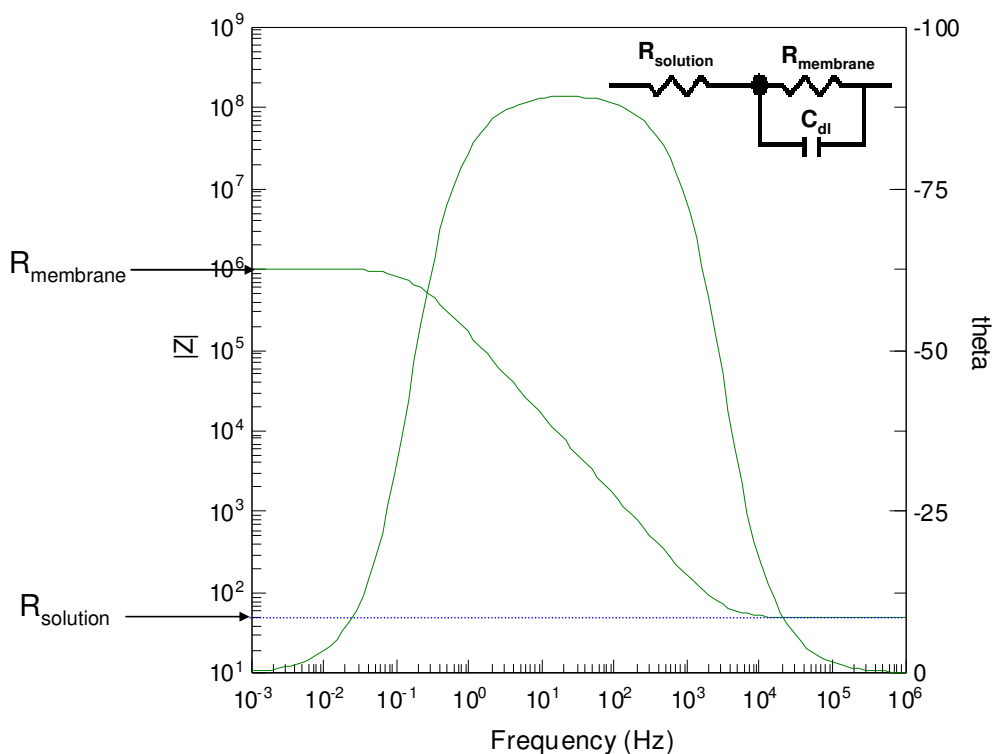
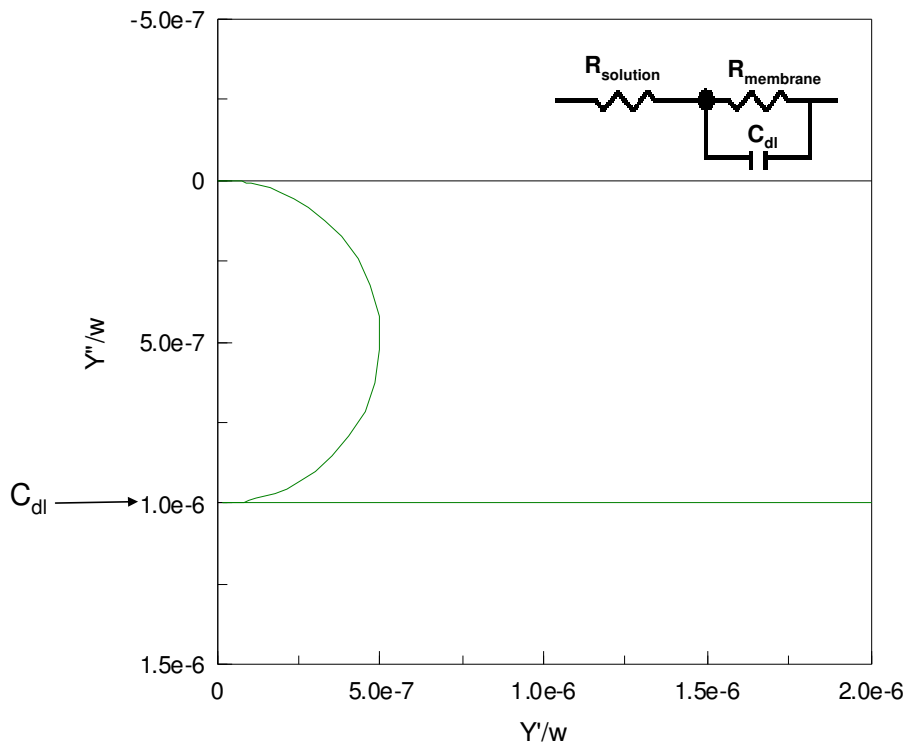


Figure 2.3.4.: Simulated Bode plot for a simple equivalent circuit model with  $R_{\text{solution}}$  ( $50\Omega$ ),  $R_{\text{membrane}}$  ( $1M\Omega$ ) and  $C_{\text{dl}}$  ( $1\mu\text{F}$ ).

The admittance, denoted  $Y$ , is simply the inverse of the impedance:  $Y = 1/Z$ . An admittance plot, also called capacitance plot, contains the same information as the other plot formats (e.g. Bode plot, Nyquist plot) but sometimes allows the system response to be viewed more clearly. The semicircle shape is due to the interaction between the resistance and the capacitance. The value of the capacitance can be directly extracted from the graph either from the extrapolation of the semicircle to the y-axis or from the  $Y'/w$  value on the horizontal line section of this plot (Figure 2.3.5).



**Figure 2.3.5.:** Simulated admittance plot (capacitance plot) for a simple equivalent circuit model with  $R_{solution}$  ( $50\Omega$ ),  $R_{membrane}$  ( $1M\Omega$ ) and  $C_{dl}$  ( $1\mu F$ ).

## **2.4 Scanning Electron Microscopy (SEM)**

The incident electron beam was emitted via a field emission gun (FEG). The interaction between the incident electron beam and the electrons of the sample (NPG as an electrically highly conductive material) resulted in the emission of low-energy electrons (<50 V) from near the sample's surface, so-called secondary electrons (SE). An in-lens SE detector (Zeiss) collected the secondary electrons with high efficiency on the same specimen site as the incoming e-beam. The resulting signal was rendered into a two-dimensional intensity distribution that was viewed and saved as a digital image. The resolution was about 2.5 nm at 1 kV (~ 1.0 nm at 20 kV and ~ 5 nm at 0.2 kV). This resolution is two orders of magnitude larger than optical light microscopy, which has its limitations due to the wavelength of visible light. The wavelength of an electron with a certain energy is around 3 - 6 nm<sup>20</sup> compared to 400 - 700 nm for the visible light.

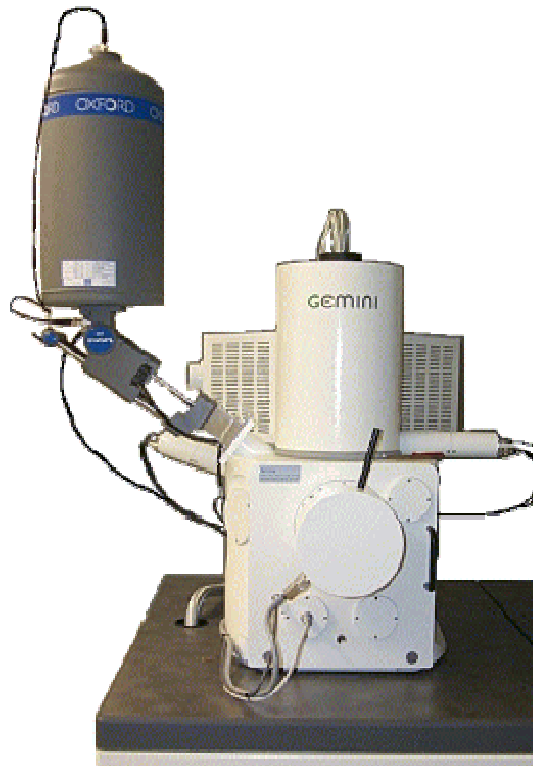


**Figure 2.4.1: LEO (Zeiss) 1530 Gemini**

## 2.5 Autocorrelation

The one dimensional (1D) autocorrelation function (ACF) can be expressed as a function of a single variable  $x$ :

$$ACF(\Delta x) = \frac{\sum_{i=1}^N F(i) \cdot F(i + \Delta x)}{\left[ \sum_{i=1}^N F(i) \right]^2} \quad \text{--- 2.8}$$

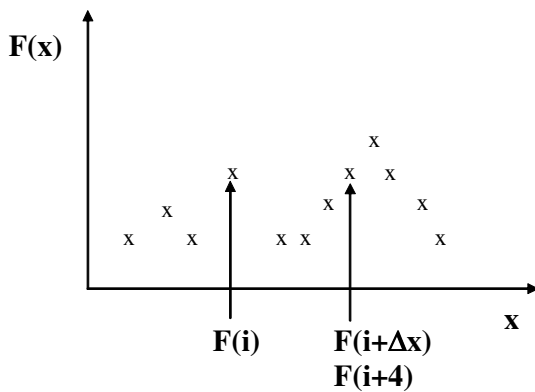


**Figure 2.5.1: Exploitation of the 1D correlation function. Exemplarily for one data point a shift of  $\Delta x = 4$  is shown.**

A sequence of discrete values is determined for the function  $F(i)$ , where  $i = 1, 2, \dots, N$  refers to the set of all natural numbers.  $\Delta x$  is the displacement in the  $x$  direction.

By adding a second variable  $y$  the two dimensional (2D) autocorrelation function (ACF) is formulated as follows:

$$ACF(\Delta x, \Delta y) = \frac{\sum_{i,k=1}^N F(i, k) \cdot F(i + \Delta x, k + \Delta y)}{\left[ \sum_{i,k=1}^N F(i, k) \right]^2} \quad \text{--- 2.9}$$

An illustration of the 2D correlation function is shown in Figure 4.4.2 [Chapter 4].

As in the case of the 1D autocorrelation function a sequence of discrete values is determined for the function  $F(i, k)$ , where  $i, k = 1, 2, \dots, N$  and  $\Delta y$  is the displacement in the  $y$ -direction. The software Igor Pro (version 5.02) was used to resolve the 2D autocorrelation function. The original SEM images were imported and the parameters such as dimensions in  $x$ - and  $y$ -direction, the autocorrelation dimensions and the step size were selected. The number of nanometers per pixel was defined by the SEM image, and was usually 1.00 nm/pixel. The larger the chosen area ( $x$ - and  $y$ -direction) and the smaller the step size, the more precise the values that could be calculated, but the longer the correlation process lasted.

## 2.6 References

1. Lippa, P. B.; Sokoll, L. J.; Chan, D. W., Immunosensors - principles and applications to clinical chemistry. *Clinica Chimica Acta* **2001**, 314, (1-2), 1-26.
2. Gordon, J. G.; Swalen, J. D., Effect Of Thin Organic Films On Surface Plasma Resonance On Gold. *Optics Communications* **1977**, 22, (3), 374-376.
3. Knoll, W., Interfaces and thin films as seen by bound electromagnetic waves. *Annual Review of Physical Chemistry* **1998**, 49, 569-638.
4. Kretschmann, E.; Raether, H., Radiative decay of nonradiative surface plasmons excited by light. *Z. Naturforsch. A* **1968**, 23, 2135-2136
5. Otto, A., Excitation of Nonradiative Surface Plasma Waves in Silver by Method of Frustrated Total Reflection. *Zeitschrift Fur Physik* **1968**, 216, (4), 398-&.
6. Raether, H., Surface-Plasmons on Smooth and Rough Surfaces and on Gratings. *Springer Tracts in Modern Physics* **1988**, 111, 1-133.
7. Turbadar, T., Complete absorption of Light by Thin Metal Films. *Proc. Phys. Soc.* **1959**, 73, 40
8. Turbadar, T., Complete absorption of plane polarized light by thin metallic films. *Optica Acta* **1964**, 11, 207
9. Kelf, T. A.; Sugawara, Y.; Cole, R. M.; Baumberg, J. J.; Abdelsalam, M. E.; Cintra, S.; Mahajan, S.; Russell, A. E.; Bartlett, P. N., Localized and delocalized plasmons in metallic nanovoids. *Physical Review B* **2006**, 74, (24).
10. Chen, H. H.; Suzuki, H.; Sato, O.; Gu, Z. Z., Biosensing capability of gold-nanoparticle-immobilized three-dimensionally ordered macroporous film. *Applied Physics a-Materials Science & Processing* **2005**, 81, (6), 1127-1130.
11. Bard, A. J.; Faulkner, L. R., *Electrochemical Methods, Fundamentals and Applications*, second edition. **2001**.
12. Thele, M.; Karden, E.; Surewaard, E.; Sauer, D. U., Impedance-based overcharging and gassing model for VRLA/AGM batteries. *Journal of Power Sources* **2006**, 158, (2), 953-963.
13. Gupta, R. K.; Singh, R. A., AC impedance studies on the molecular semiconductors based on aromatic diamines-iodine charge-transfer complexes. *Indian Journal of Engineering and Materials Sciences* **2004**, 11, (6), 505-510.
14. Schulze, M.; Wagner, N.; Kaz, T.; Friedrich, K. A., Combined electrochemical and surface analysis investigation of degradation processes in polymer electrolyte membrane fuel cells. *Electrochimica Acta* **2007**, 52, (6), 2328-2336.
15. Benchekroun, K.; Dalard, F.; Rameau, J. J.; El Ghazali, A., Inhibition of iron corrosion in 1 M HCl. Part II. Study of the protective properties of 2-aminothiophenol and 2-aminophenyl disulfide by impedance spectroscopy. *New Journal of Chemistry* **2002**, 26, (7), 946-952.
16. Mulder, W. H.; Sluyters, J. H.; Pajkossy, T.; Nyikos, L., Tafel Current at Fractal Electrodes - Connection with Admittance Spectra. *Journal of Electroanalytical Chemistry* **1990**, 285, (1-2), 103-115.
17. Schiller, C. A.; Strunz, W., The evaluation of experimental dielectric data of barrier coatings by means of different models. *Electrochimica Acta* **2001**, 46, (24-25), 3619-3625.
18. Kim, C.-H.; Pyun, S.-I.; Kim, J.-H., An investigation of the capacitance dispersion on the fractal carbon electrode with edge and basal orientations. *Electrochimica Acta* **2003**, 48, (23), 3455-3463.
19. Jorcin, J.-B.; Orazem, M. E.; Pebere, N.; Tribollet, B., CPE analysis by local electrochemical impedance spectroscopy. *Electrochimica Acta* **2006**, 51, (8-9), 1473-1479.
20. Flegler, S. L.; Heckman, J. W.; Klomparens, K. L., *Elektronenmikroskopie. Spektrum Akademischer Verlag GmbH Heidelberg, Berlin, Oxford* **1995**, 4.

### 3 Experimental Section

#### 3.1 Instrumental - SPR setup

A home-built surface plasmon resonance (SPR) instrument in the Kretschmann configuration<sup>1</sup> was used for optical p-SPR studies. The components of the setup are easily transposable or extendable for additional applications such as electrochemical<sup>2</sup> (Chapter 4.5/4.7) measurements or detection of surface enhanced fluorescence<sup>3</sup>. The setup was also modified to monitor localized SPR<sup>4</sup> and propagating SPR simultaneously utilizing a fiber-optic spectrometer, so that the localized plasmon response was recorded from the backside of the sample, while the propagating plasmon excited by a laser source was detected by measuring the reflected light from the prism with a photodiode detector. A schematic drawing of the setup is depicted in Figure 3.1.1. A photograph of this setup is then shown in Figure 3.1.2.

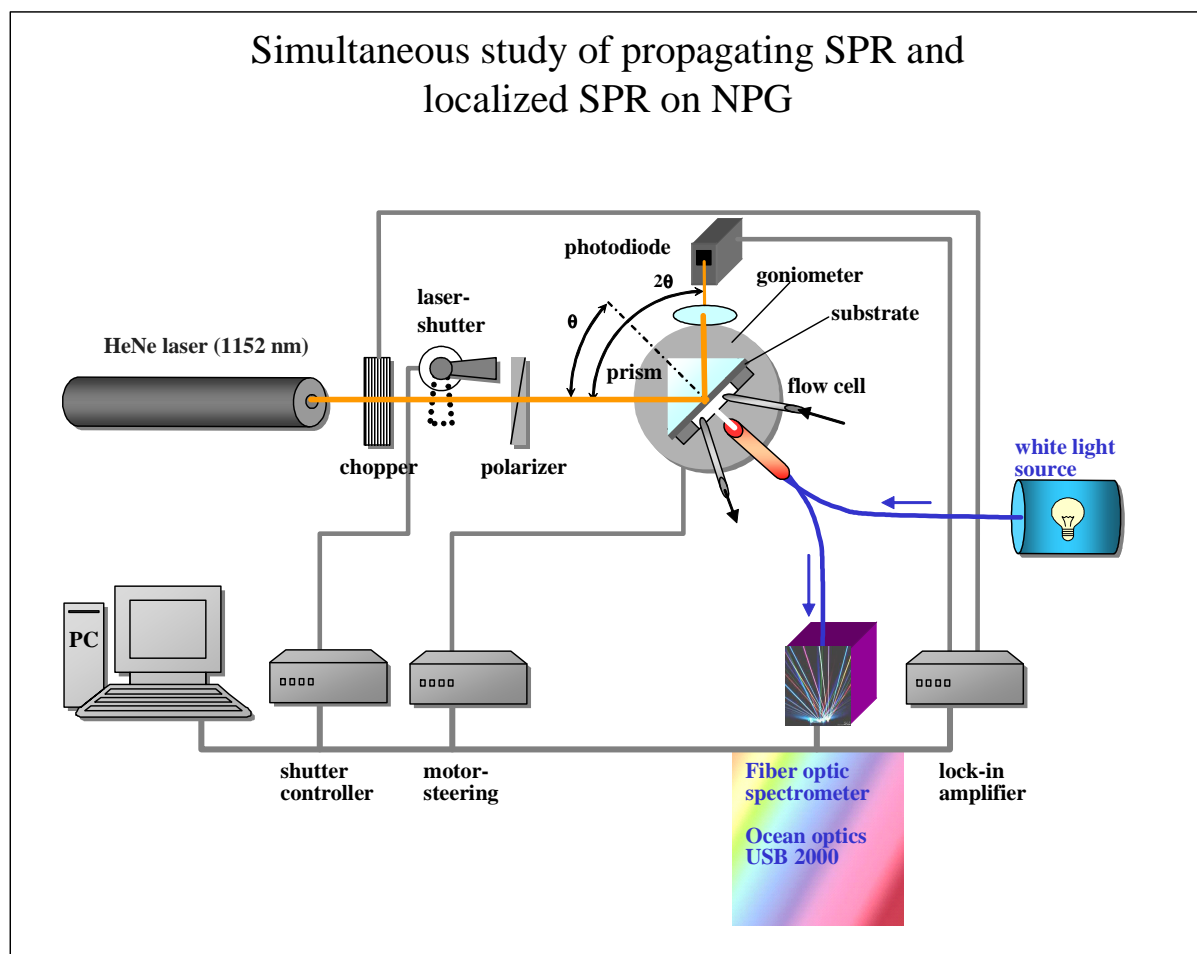


**Figure 3.1.1: Simultaneous propagating and localized surface plasmon resonance setup based on a Kretschmann configuration. In order to conduct the l-SPR study, a fiber optic spectrometer (Ocean optics) with a reflection probe was used. The reflection probe was used for both the illumination and the collection of reflected light from the NPG surface.**

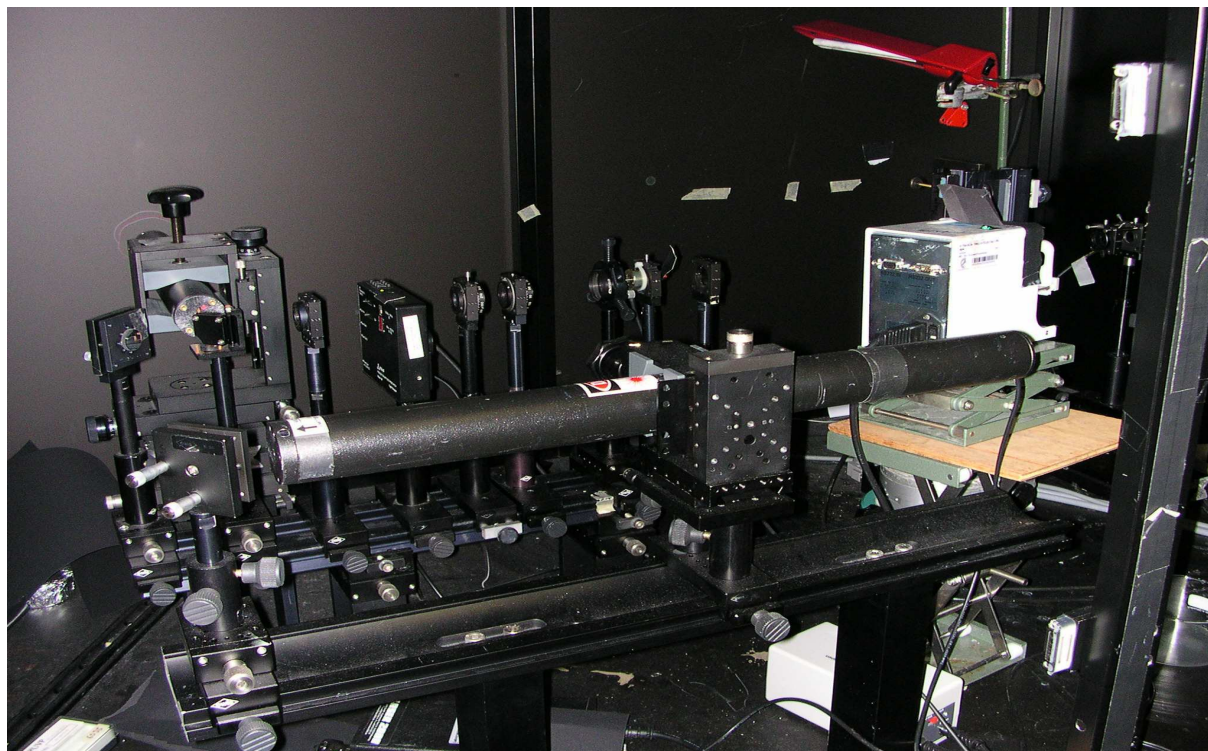


**Figure 3.1.2: Photograph of the setup.**

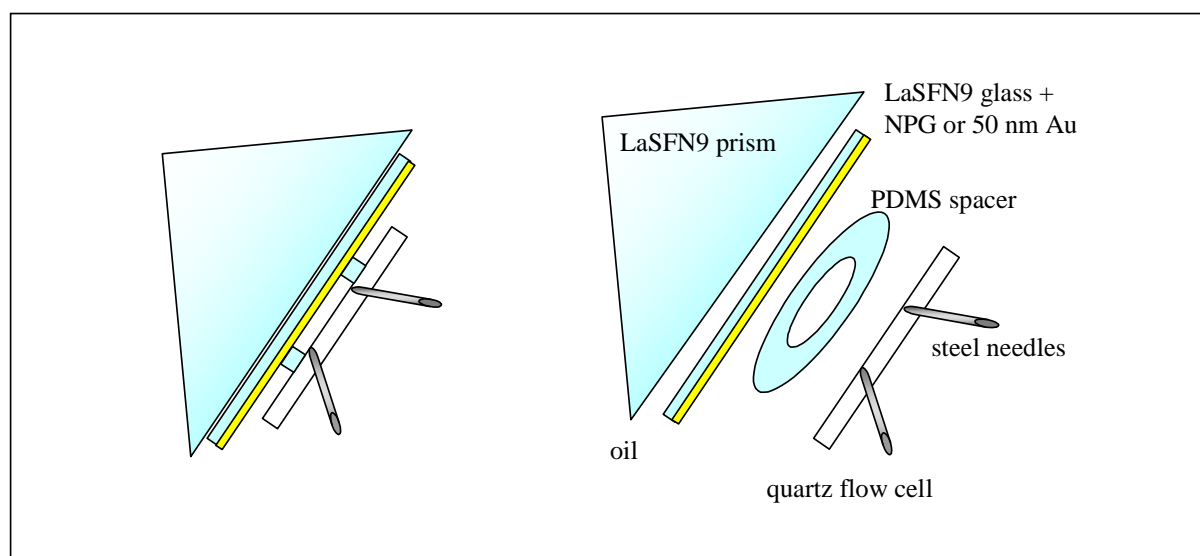
Briefly, linearly polarized frequency-modulated laser light was used to illuminate the sample through a right-angle glass prism. The reflected laser intensity was focused by a lens ( $f = 50$  mm, Owis) onto a photodiode detector. The frequency modulator, a chopper (frequency = 1331 Hz), and the detection unit (silicon pin photodiode; Infineon Technologies Corporation, BPW 34 B) were connected to a lock-in amplifier (EG&G) as a reference to filter the noise coming from other light sources with different frequencies.

For momentum matching on NPG substrate with high coupling efficiency at small incident angle an IR laser (HeNe, Laser 2000, 10 mW,  $\lambda = 1152$  nm) was used. The IR laser beam was invisible to the human eye light, so that the assistance of a parallel red laser (HeNe, Uniphase, 5 mW,  $\lambda = 632.8$  nm) was obligatory in order to properly align the beam. The red laser was also used to excite surface plasmons on evaporated, flat Au (50 nm) in the second project (epitope mapping). A flipping mirror (Owis) was utilized to select between these two lasers. Before starting experiments an infrared sensor card (0.75 - 1.35  $\mu\text{m}$ ; Newport, Model F-IRC1) was always used to ensure that the two laser beams remained parallel.

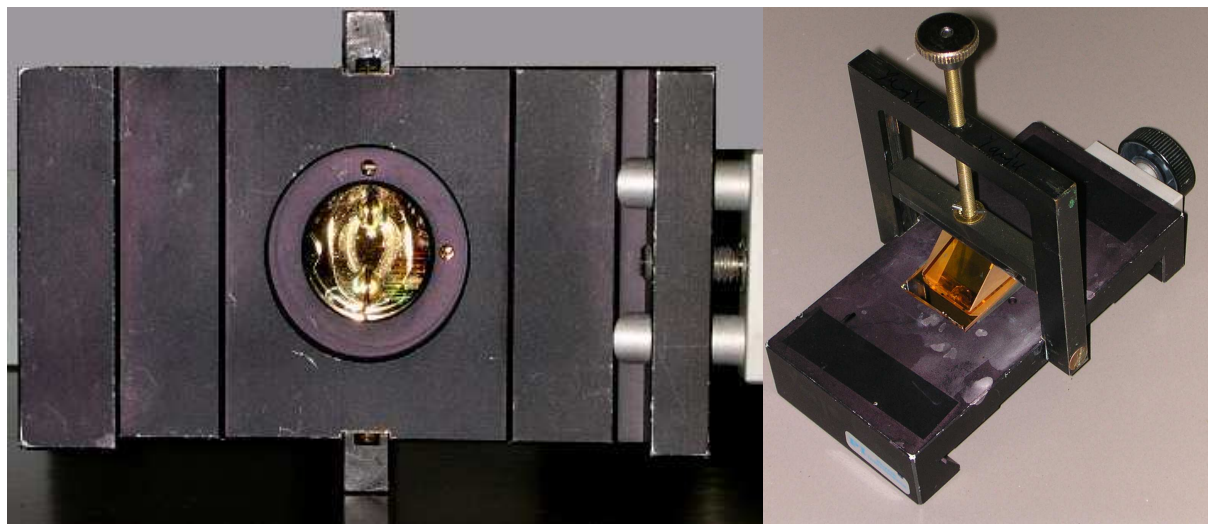
For characterization of the NPG membranes by SPR, various other excitation wavelengths (594, 780, 820 nm, respectively) were also selected. If other wavelengths were required the SPR measurements were performed on similar set-ups to the one shown in

Figure 3.1.2 which contained lasers with wavelengths other than the standard  $\lambda = 632.8$  nm red HeNe laser.

The chopped laser light was passed through a polarizer (Glan-Thompson) to adjust the polarization (TE, TM). In the case of high intensity lasers, e.g. 632.8 nm, a second polarizer (Glan-Thompson) was used to adjust their intensity. A shutter was installed to block the laser beam during any alterations of the setup or to protect fluorescent dyes from photo bleaching. The sample (prism, gold slide, and quartz flow cell) and the detector were mounted on two coaxial goniometers, enabling precise tuning of the incident angle of the laser ( $\theta$ ) and the detection angle ( $2\theta$ ). The sample configuration can be seen in Figures 3.1.3 and 3.1.4. The high refractive index prism (LaSFN9, Schott Glass Inc., refractive index  $n = 1.85$  at  $\lambda = 632.8$  nm) was connected via immersion oil ( $n = 1.7$  at  $\lambda = 632.8$  nm) to a LaSFN9 glass slide which was coated with gold (NPG, evaporated, or template stripped Au). A thin polydimethyl siloxane (PDMS) spacer (300  $\mu\text{m}$ , with an elliptical hole 5 mm  $\times$  7 mm) was used to seal the substrate to a quartz slide (Herasil glass). Two holes in the quartz glass slide provided an inlet and outlet. Two steel needles were carefully inserted and glued into the two holes to enable the connection to Tygon® tubing (inner diameter 0.76 mm). A peristaltic pump (Ismatec, Switzerland) was used to pump liquid from a small container (e.g. Eppendorf tube or other buffer container systems - manually exchanged) through the cell in a closed circulation loop<sup>5</sup>. The loop volume was  $\sim 300$   $\mu\text{L}$ , a minimum sample volume of  $\sim 400 - 600$   $\mu\text{L}$  was injected to guarantee a proper analyte working concentration<sup>6</sup>.



**Figure 3.1.3: Details of the sample configuration.**



**Figure 3.1.4: Photograph of the sample holder clamping the flow cell, the PDMS Spacer, the substrate and the prism. The left side shows the back of the sample (l-SPR) and the right side a top view (p-SPR) of the sample holder.**

L-SPR on NPG was measured using a spectrometer (USB2000, Ocean Optics Inc.) equipped with a reflection probe (R400-7, Ocean Optics Inc.) and a light source (HL-2000, Ocean Optics Inc.). The l-SPR experiments measured the reflection spectrum of the NPG sample through the quartz window of the flow-cell. The absorbance spectra were measured by taking the ratio between the raw detector spectrum of the measurement sample and the raw detector spectrum of the reference sample, followed by taking the logarithm of base 10 of this ratio ( $\log(\text{reference/sample})$ ). In all raw spectra, the dark spectrum was subtracted automatically by the Ocean Optics data acquisition software. The reference sample was either the bare NPG substrate or modified by soaking in pure Milli Q water or buffer. The particular reference used will be indicated in the text describing the different absorbance spectra.

### **3.2. Modifications of the SPR setup: Halogen lamp plus monochromator**

In order to excite surface plasmons on NPG with different pore sizes various laser wavelength (594, 632.8, 780, 820 and 1152 nm) were used. These lasers were located in different setups, so the cell mounted with the NPG samples had to be moved. It was never possible to illuminate exactly the same spot at the gold surface twice. Due to inhomogeneities of the gold film thickness the coupling efficiencies therefore altered slightly from measurement to measurement. In order to measure the same spot for all wavelengths the laser was replaced by a halogen lamp. The light of the halogen lamp was passed through a monochromator and was tuned to single wavelengths between 450 nm and 850 nm. Every 10 nm a SPR scan was recorded.

### 3.3 Instrumental – CV/EIS- setup

Electrochemical studies were carried out using an Autolab PGSTAT 30 (Ecochemie) with internal frequency response analyzer (FRA). The working electrode was a gold film (nanoporous or evaporated) supported on a glass slide. The electrochemical teflon cell was tightly clamped to the gold slide with an o-ring, which defined an active surface area of  $0.77 \text{ cm}^2$ . A platinum coil counter electrode and a silver/silver chloride reference electrode (World Precision Instruments, DriRef-2) completed the cell (Figure 3.3.1). Impedance spectra were fit using the modeling program contained within the Ecochemie FRA software. The equivalent circuit was  $R_S(R_F C_{dl})$ , where  $R_S$  was the series resistance,  $R_F$  the Faradaic resistance and  $C_{dl}$  the double layer capacitance.

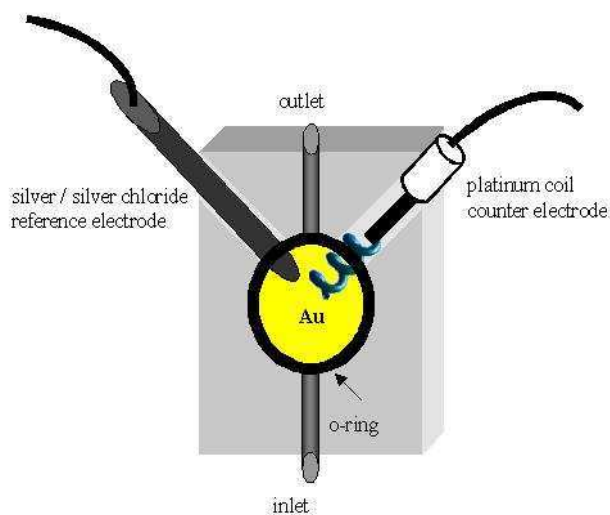


**Figure 3.3.1:** Sketch of the electrochemical flow cell, which can serve as a SPR flow cell as well.

### **3.4 Further instruments**

#### **3.4.1 Plasma cleaner**

LaSFN9 (“**L**anthan**S**chwer**f**lint“ Schott) or BK7 (“**B**ork**k**ron“ Fisher Scientific) glass slides for the preparation of nanoporous gold substrates were cleaned by using an Harrick Scientific Plasma Cleaner (Figure 3.4.1). The oxygen plasma reacted with organic impurities (hydrocarbons  $\text{CH}_x$ ) on the surface producing gaseous products (carbon dioxide and carbon monoxide) which were easily removed by the connected vacuum system.



**Figure 3.4.1: Harrick Scientific Plasma Cleaner (expanded model)**

#### **3.4.2 Surface profiler**

For thickness measurements a computerized surface profiler (KLA-Tencor P-10) was used. The P-10 is a stylus profilometer, that makes use of a sharp stylus ( $\sim 2 \mu\text{m}$  tip radius) to measure the surface topography precisely. The stylus is held at a fixed position, while the sample is scanned. The film thicknesses were measured across a step (2D line scan), where the nanoporous gold film was scratched away to the glass support by a plastic device.



**Figure 3.4.2: Computerized Surface Profiler: KLA-Tencor P-10**

### 3.4.3 UV/VIS/NIR Spectrometer

For transmission measurements of nanoporous gold substrates a Perkin Elmer Lambda 900 UV/VIS/NIR spectrometer was used. Tungsten-halogen and deuterium lamps serve as sources. Although "Lambda 900" is a double-beam and double-monochromator UV/VIS/NIR spectrophotometer, only one beam was exploited to measure first a BK7 glass slide as the reference and then the nanoporous gold membranes all samples in the transmission mode. The "Lambda 900" system enables spectral recording from 186 up to 3300 nm. In these studies, a range of 350 – 800 nm was scanned in an interval of 3 nm.



**Figure 3.4.3: Perkin Elmer Lambda 900 UV/VIS/NIR spectrometer**

### **3.5 Preparation of Evaporated Gold (EG) films**

New LaSFN9 (“Lanthanschwerflint“ Schott) or BK7 (“Borkron“ Fisher Scientific) glass slides were cleaned in 2 % Hellmanex® solution in an ultrasonic bath for 15 minutes. Then, the slides were rinsed with Milli Q water and ethanol. Afterwards, the slides were dried with nitrogen or argon. ~ 50 nm gold films were deposited by electrothermal evaporation ( $0.1 - 0.2 \text{ nms}^{-1}$ ,  $2 \times 10^{-6} \text{ mbar}$ ). The gold films were stored under argon atmosphere.

### **3.6 Preparation of Template Stripped Gold (TSG) films<sup>7</sup>**

Silicon wafer (roughness according to AFM was  $< 0.5 \text{ nm}$ ) were cleaned with a solution consistent of 32 % ammonia (1 part), 35 % hydrogen peroxide (1 part), and Milli Q water (5 parts) at  $75^\circ \text{ C}$  for 1 hour. Then, the slides were rinsed with Milli Q water and ethanol. Afterwards the slides were dried with nitrogen or argon. ~ 50 nm gold films were deposited by electrothermal evaporation ( $0.1 - 0.2 \text{ nms}^{-1}$ ,  $2 \times 10^{-6} \text{ mbar}$ ) on the cleaned silicon wafers. The gold films on the silicon wafers were then glued with EPO-TEK 353ND-4, ( $n = 1.5922$ ) to cleaned LaSFN9 or BK7 glass slides and heated at  $150^\circ \text{ C}$  for 1 hour. The silicon wafer was split off the gold film just before use.

### **3.7 Preparation of silane monolayers**

In the 1990s, the self-organisation and interfacial properties of long-chain alkyl-trichlorosilanes and alkyltrimethoxysilanes were investigated. Their properties such as SAM thickness, degree of surface coverage and surface orientation were studied by X-ray photoelectron spectroscopy (XPS)<sup>8</sup>, atomic force microscopy (AFM), ellipsometry<sup>9</sup> and contact angle measurements<sup>10</sup>.

One nice application for 3-MPT layers for micro patterning through reverse self-assembly was reported by Bandyopadhyay et.al, using the selective self-assembly attributes of the thio group binding to gold and the methoxy group binding to  $\text{SiO}_2$  substrates<sup>11</sup>.

It is known that silane SAMs form disordered heterogeneous domains. 3-MPT layers on  $\text{SiO}_2$  have been shown to consist of dispersed domains 20 - 200 nm in diameter, a continuous and flat monolayer is not formed<sup>12</sup>. The concentration of 3-MPT, the amount of water present, the solvent properties, deposition temperature<sup>10</sup> and incubation time are the controlling parameters in preparation of well-ordered 3-MPT SAMs.

For instance good self-assembly results from  $5 \times 10^{-3}$  M 3-MPT dissolved in benzene, but not above this concentration<sup>12</sup>. An increase of 3-MPT molecules on SiO<sub>2</sub> reveals disordered orientation and irregularities. The influence of the 3-MPT concentration on the morphology of 3-MPT layers might be due to the competition between condensation (self-polymerization), physisorption and chemisorption process (surface dehydration reaction) (Figure 3.7.1).

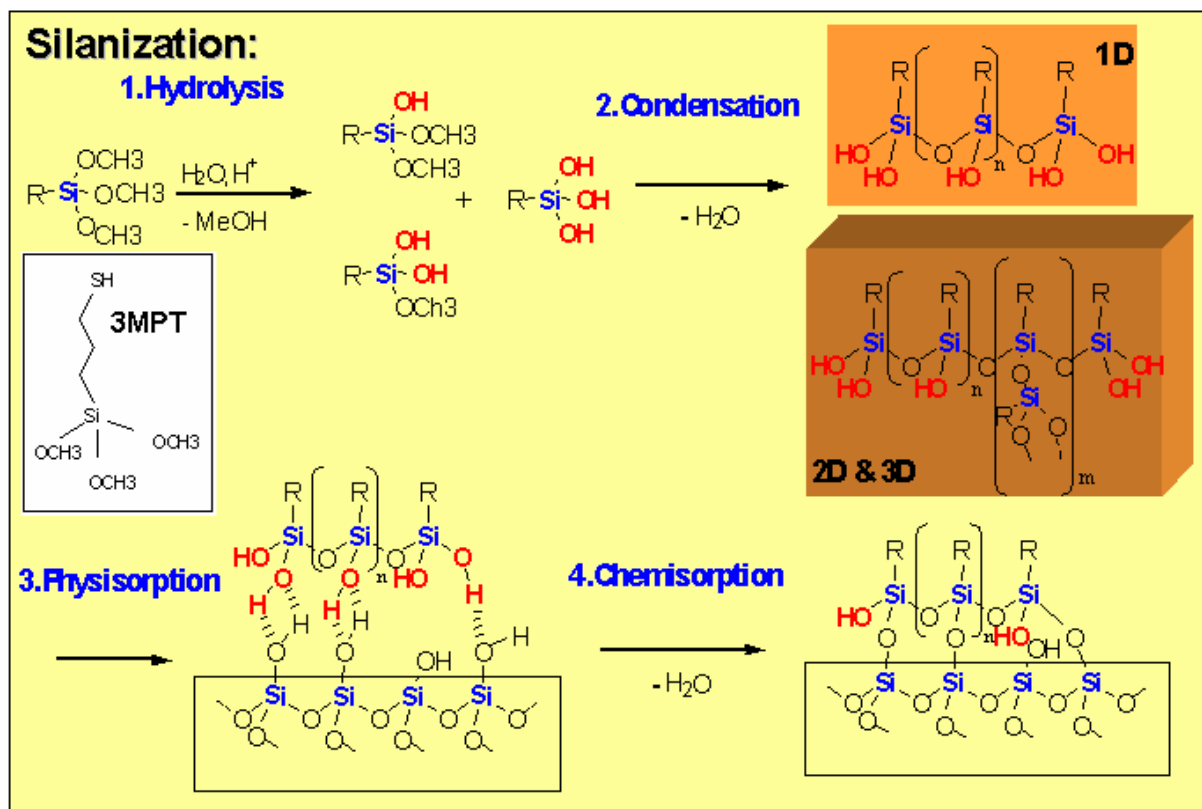


Figure 3.7.1: Schematic representation of the silanization reaction mechanism<sup>13</sup>

In the first step of a silanization process, hydrolysis, a trace amount of H<sub>2</sub>O or catalyzer H<sup>+</sup>, OH<sup>-</sup> is needed. In the second step, called condensation or self-polymerization, water is released. The second step is the critical step in the formation of 1D or 2D & 3D structures (oligomers). The physisorption of the 3-MPT molecules is followed again by water elimination termed chemisorption to link covalently to the glass substrate. The silanization solution together with the glass substrates was heated up to 80° C for two hours. After cooling down the samples back to RT and rinsing with Milli Q they were immediately used to attach the nanoporous gold, a delay could cause the mercapto group to oxidize.

### **3.8 Materials**

#### Materials used for investigations on nanoporous gold NPG [Chapter 4.6]:

Biotin thiol- and oligo-ethylene-glycol thiol- (spacer thiol-) derivatives and streptavidin were kindly provided by Roche Diagnostics and were used as received. 11-Mercaptoundecan-1-ol as a spacer thiol and 11-mercapto-(8-biotinamido-4,7 dioxaoctyl-)-undecanoylamide carrying a biotin function were used to form a mixed monolayer. The thiols (0.5 mM in absolute ethanol 99 %) <sup>14</sup> were mixed as follows: one part of biotinylated thiol to nine parts of spacer thiol in order to reduce the steric hindrance of the following streptavidin binding <sup>15</sup>.

Biotinylated rabbit anti-goat antibody (biotinylated IgG, with 5.2 biotins per IgG) was purchased from Molecular Probes. HBS-EP buffer (degassed 10 mM HEPES buffer saline, pH 7.4, 150 mM NaCl, 3 mM EDTA, 0.05 % (v/v) surfactant P-20, Biacore, Uppsala, Sweden) was used for the preparation of the protein solutions. The working concentration for both streptavidin and biotinylated IgG were 500 nM.

1 % (w/v) streptavidin modified polystyrene latex beads (from Roche Diagnostics; SA-LX;  $r = 56$  nm;  $n = 1.56$  at  $\lambda = 1152$  nm) were diluted in phosphate buffer (PBS) to a 0.01 % working solution. These beads were used for building up the multilayer architecture on NPG and flat gold substrates.

#### Materials used for applications on nanoporous gold NPG [Chapter 4.7]:

Nanoporous gold films were exposed to a solution of 1.2 mg/mL dithiobis (*N*-succinimidyl propionate) (DTSP, Fluka) and 0.42 mg/mL dithiodipropionic acid (DTP, Fluka) in DMSO for ~ 3 hours. After monolayer formation the samples were rinsed several times with pure DMSO and dried in a nitrogen stream. These samples were immersed in 0.5 M  $K_2CO_3$  buffer (pH 9.8) containing 150 mM amino-nitrilotriacetic acid (ANTA, Fluka) for several hours (~ 18 hours). This time the samples were rinsed with Milli Q water. In the next step, the NTA terminated surface is incubated with 50 mM  $NiCl_2$  (Sigma) solution (pH 5.5) for 20 minutes. The samples were rinsed again with Milli Q water. Then the sample was mounted on the SPR/EIS setup and the flow cell was floated with PBS buffer.

2  $\mu$ M cytochrome c oxidase (CcO) dissolved in 0.1 % *n*-Dodecyl- $\beta$ -D-maltoside (DDM; Merck) and 50 mM phosphate buffer was added to the Ni-NTA-modified gold surface. Excess CcO was removed by rinsing with phosphate buffer containing 0.1 % DDM.

Detergent- solubilization ensures the full functional integrity of CcO. Then, the lipid solution (0.01 mg/ml DiPhyPC/DDM buffer; 1,2-diphytanoyl-*sn*-glycero-3-phosphocholine (DiPhyPC), Avanti Polar Lipids; Alabaster AL) was added. Macroporous Bio-Beads (BioRad) were inserted carefully into the flow cell to remove the DDM.

Finally, cytochrome c (Cyt c; from bovine heart; Sigma) was injected to prove the functionality of the CcO.

### Materials used in the centrin project [Chapter 5]:

Gabi buffer (buffer for the transducin):

- 20 mM BTP (1,3-Bis[tris-(hydroxymethyl)methylamino]propan),
- 130 mM NaCl
- 1 mM MgCl<sub>2</sub>
- 2 mM DTT (Dithiothreitol)

Buffer F (buffer for the centrin):

- 20 mM Hepes (pH 8.0)
- 100 mM NaCl
- 2 mM EDTA
- 11 mM CHAPS
- 1 mM DTT in dd H<sub>2</sub>O
- Addition of 10 mM CaCl<sub>2</sub> or 6 mM EGTA

### 3.9 References

1. Kretschmann, E.; Raether, H., Radiative decay of nonradiative surface plasmons excited by light. *Z. Naturforsch. A* **1968**, 23, 2135-2136
2. Giess, F.; Friedrich, M. G.; Heberle, J.; Naumann, R. L.; Knoll, W., The protein-tethered lipid bilayer: A novel mimic of the biological membrane. *Biophysical Journal* **2004**, 87, (5), 3213-3220.
3. Liebermann, T.; Knoll, W., Surface-plasmon field-enhanced fluorescence spectroscopy. *Colloids And Surfaces A-Physicochemical And Engineering Aspects* **2000**, 171, (1-3), 115-130.
4. Yu, F.; Ahl, S.; Caminade, A. M.; Majoral, J. P.; Knoll, W.; Erlebacher, J., Simultaneous excitation of propagating and localized surface plasmon resonance in nanoporous gold membranes. *Analytical Chemistry* **2006**, 78, (20), 7346-7350.
5. Knoll, W.; Park, H.; Sinner, E. K.; Yao, D. F.; Yu, F., Supramolecular interfacial architectures for optical biosensing with surface plasmons. *Surface Science* **2004**, 570, (1-2), 30-42.
6. Yu, F.; Yao, D. F.; Knoll, W., Surface plasmon field-enhanced fluorescence spectroscopy studies of the interaction between an antibody and its surface-coupled antigen. *Analytical Chemistry* **2003**, 75, (11), 2610-2617.
7. Naumann, R.; Schiller, S. M.; Giess, F.; Grohe, B.; Hartman, K. B.; Karcher, I.; Koper, I.; Lubben, J.; Vasilev, K.; Knoll, W., Tethered lipid Bilayers on ultraflat gold surfaces. *Langmuir* **2003**, 19, (13), 5435-5443.
8. Evans, S. D.; Goppertberarducci, K. E.; Urankar, E.; Gerenser, L. J.; Ulman, A., Monolayers Having Large Inplane Dipole-Moments - Characterization Of Sulfone-Containing Self-Assembled Monolayers Of Alkanethiols On Gold By Fourier-Transform Infrared-Spectroscopy, X-Ray Photoelectron-Spectroscopy, And Wetting. *Langmuir* **1991**, 7, (11), 2700-2709.
9. Wu, K.; Bailey, T. C.; Willson, C. G.; Ekerdt, J. G., Surface hydration and its effect on fluorinated SAM formation on SiO<sub>2</sub> surfaces. *Langmuir* **2005**, 21, (25), 11795-11801.
10. Silberzan, P.; Leger, L.; Ausserre, D.; Benattar, J. J., Silanation Of Silica Surfaces - A New Method Of Constructing Pure Or Mixed Monolayers. *Langmuir* **1991**, 7, (8), 1647-1651.
11. Bandyopadhyay, A.; Ray, A. K.; Sharma, A., Micropatterning through reverse self-assembly using photolithographically produced templates. *Nanotechnology* **2004**, 15, (11), 1603-1608.
12. Hu, M. H.; Noda, S.; Okubo, T.; Yamaguchi, Y.; Komiyama, H., Structure and morphology of self-assembled 3-mercaptopropyltrimethoxysilane layers on silicon oxide. *Applied Surface Science* **2001**, 181, (3-4), 307-316.
13. Jonas, U.; Krüger, C., The Effect of Polar, Nonpolar, and Electrostatic Interactions and Wetting Behavior on the Particle Assembly at Patterned Surfaces. *Journal of Supramolecular Chemistry* **2002**, 2(1-3), 255-270.
14. Knoll, W.; Zizlsperger, M.; Liebermann, T.; Arnold, S.; Badia, A.; Liley, M.; Piscevic, D.; Schmitt, F. J.; Spinke, J., Streptavidin arrays as supramolecular architectures in surface-plasmon optical sensor formats. *Colloids And Surfaces A-Physicochemical And Engineering Aspects* **2000**, 161, (1), 115-137.
15. Spinke, J.; Liley, M.; Schmitt, F. J.; Guder, H. J.; Angermaier, L.; Knoll, W., Molecular Recognition At Self-Assembled Monolayers - Optimization Of Surface Functionalization. *Journal Of Chemical Physics* **1993**, 99, (9), 7012-7019.

## 4. Nanoporous gold (NPG) membrane

### **4.1 Advantage of Porous Gold - new plasmonic material and the aim of the study**

Nanoporous metal materials composed of two- and three-dimensional porous structures are becoming increasingly important in analytical and materials chemistry. The development of many new synthesis methodologies have resulted in a variety of novel materials that can exhibit extraordinary properties<sup>1, 2, 3, 4, 5</sup>.

Numerous possibilities are described to create porous structures such as: nano particle lithography<sup>6</sup>, templated growth<sup>7, 8</sup>, E-beam etching<sup>9</sup>, chemical etching<sup>10-13</sup>, electrochemical etching<sup>14</sup>, etc. All of these methods can be used to create structures with different pore sizes.

**Table 4.1.1: According to IUPAC nomenclature<sup>15, 16</sup>, microporous materials possess pore diameters of less than 2 nm and macroporous materials have pore diameters of greater than 50 nm; the mesoporous category belongs to the middle.**

<b>Porous materials</b>	<b>Pore diameter</b>	<b>IUPAC notation</b>
Carbon, nitroprussides	less than 2 nm	microporous
NPG, silica, aluminum; oxides of titanium, tin, zirconium	2 - 50 nm	mesoporous
Glass, polymeric	greater than 50 nm	macroporous

The types of pores are defined by IUPAC<sup>15, 16</sup> (Table 4.1.1). Materials with pore sizes less than 50 nm are termed mesoporous<sup>17</sup>. The term “nanoporous” refers to pore diameters between 1 and 100 nm.

Recently Erlebacher *et al*<sup>12</sup> reported a novel way to fabricate freestanding nanoporous gold (NPG) membranes using a wet-chemical dealloying method [Chapter 4.2 fabrication]. Dealloying is the dissolution of less noble components from a metallic solid. This phenomenon has an ancient history starting with the Incans dealloying copper from Cu/Au alloys known as depletion gilding. Other synonyms of dealloying are demetalification, etching, selective corrosion, selective leaching, roughening transition or parting.

In a binary  $A_xB_{(1-x)}$  alloy a porous structured metal A can be achieved by solving out the less noble component B<sup>18</sup>. There are many examples for this phenomenon: Au-Zn<sup>19</sup>, Au-Ag<sup>10,12</sup>, Au-Cu<sup>11</sup>, Cu-Al (selective dissolution of Al due to a leaching reaction in 2 - 8 M NaOH<sup>20</sup>).

Porous materials can be manufactured by different methods such as annealing of an alloy<sup>21</sup>, immersing an alloy in a corrosive bath<sup>10,12</sup>, radiation-assisted selective dealloying<sup>11</sup>, or some combination of these treatments<sup>17</sup>.

Nitric acid as a highly corrosive solution has been used in different concentrations for etching Ag/Au alloy in Europe since the twelfth or thirteenth century<sup>10</sup>.

Here, a commercially available, mechanically thinned 12 carat white-gold leaf is etched in nitric acid. This simple method produces a three-dimensional bicontinuous mesoporous metal with a tuneable ligament size on the order of  $\sim 10 - 50$  nm. The NPG leaves exhibit an enhanced surface area relative to flat gold, of the order of  $10 \text{ m}^2 \text{ g}^{-1}$  depending on the etching times. The ultra-thin ( $\sim 100$  nm thick) NPG sheets have a geometric surface area of  $\sim 100 \text{ cm}^2$ , whereas the accessible surface area of such samples is of the order of  $1000 \text{ cm}^2$ , and the material thus lends itself naturally to catalysis<sup>22</sup> and sensing.

There are many other benefits to using NPG substrates. For the fabrication of NPG one can utilize the ability of the thin gold leaf to float on the surface of aqueous solutions. The fabrication of the NPG substrates is described in detail in Chapter 4.2. The decorative gold leaf is also inexpensive, costing less than 1 cent per  $\text{cm}^2$ , as the gold sheets are widely sold for non-scientific purposes, such as the designing of reliefs in churches. The gold leaf is produced by a highly parallelized cold working process which allows thousands of sheets to be formed simultaneously with very few defects appearing in the hammered leaves.

The aim of this study was to further extend the application of NPG leaf into the (bio-) sensing field by investigating its intriguing ability to support both propagating and localized surface plasmon resonances (SPR) simultaneously [Chapter 4.6]. Generally, NPG can be considered as a rough, high curvature, yet continuous gold membrane. As a result, it shows features of both planar metal films that exhibit propagating-SPR (p-SPR) and nanostructured metal materials that exhibit localized-SPR (l-SPR), two kinds of optical excitations used in state-of-the-art optical sensing technologies. Within the context of the sensing application, one can notice that these NPG membranes are not only translucent, but also appear to be copper hued instead of being gold colored. In addition, color changes are discernable to the naked eye upon adsorption of thiolated monolayers. Figure 4.1.1 shows a photo of a nanoporous gold membrane with a thiol (3-mercaptopropionic acid) modification in the center position. The simple adsorption of such small molecules is enough to modify the absorbance spectrum to the naked eye, so that the modified material looks somewhat bluer. This effect motivated a study of the optical response of nanoporous gold leaf.

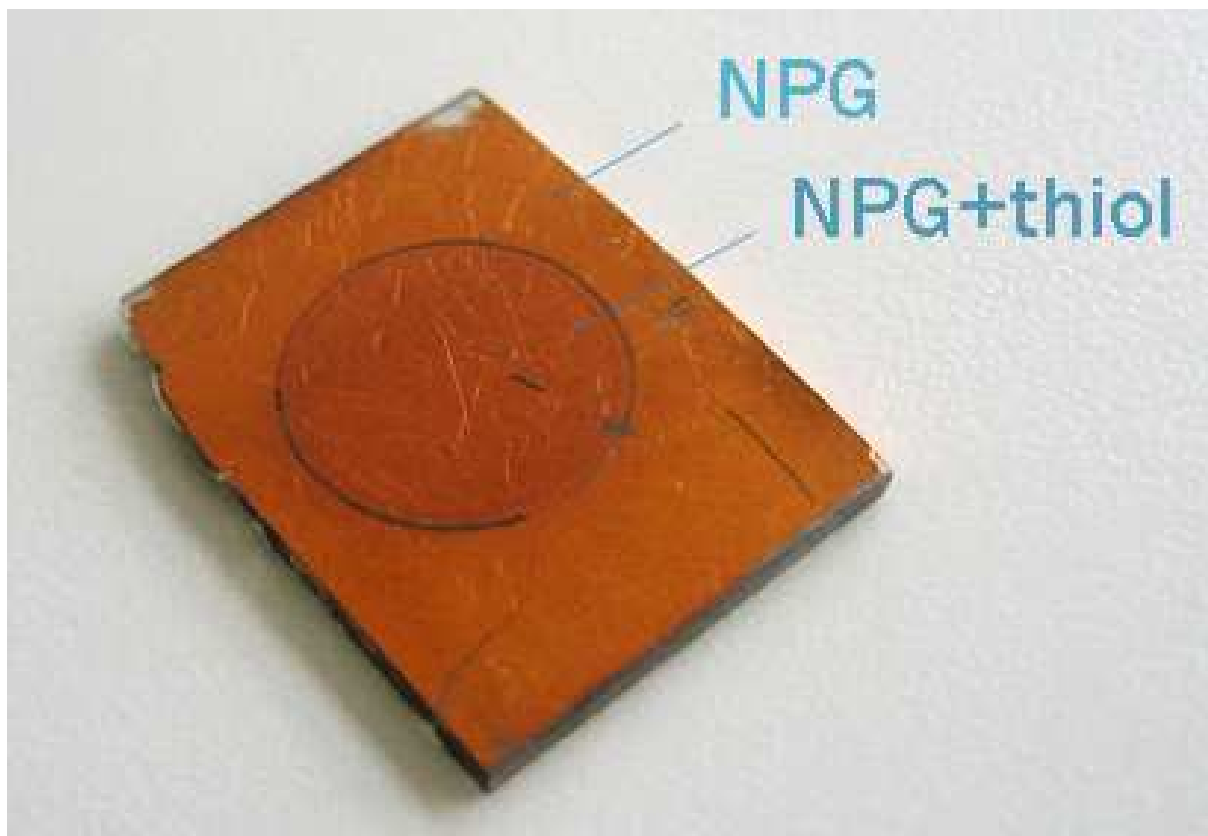


**Figure 4.1.1:** A photograph of a nanoporous gold membrane attached to a LaSFN9 glass slide with a thiol (3-mercaptopropionic acid) modification in the center position.

Another advantage of NPG compared to a planar, dense substrate is the possibility to transport ions through the porous network. As a result the substrates were investigated as supports for lipid membranes, where the pore could act as ionic reservoirs underneath the bi-layer [Chapter 4.7]. A summary of advantages and disadvantages of NPG can be found in the appendix [Chapter 8.1].

## **4.2. Fabrication of Random Nanoporous Gold Substrates**

### **4.2.1 Cleaning of the glass slides**

New LaSFN9 (“Lanthanschwerflint“ Schott) or BK7 (“Borkron“ Fisher Scientific) glass slides were rinsed by Milli Q water, dried with nitrogen or argon and treated with oxygen plasma (Harrick Plasma); RF level: “High” for 15 min.

Conventional cleaning methods cannot completely remove contaminations from glass surfaces, which are mainly from solvents after cleaning. The glass substrates were plasma cleaned to remove even non-visible contaminations of hydrocarbons. An additional advantage is that plasma treatment activates the surface for increased bonding strength. Finally, plasma cleaning is much safer than cleaning and activating the glass slides with piranha solution (3:1 mixture of sulfuric acid and 30 % hydrogen peroxide).

### **4.2.2 Silanization of the glass slides**

The plasma activated glass slides were directly immersed into the silanization solution; a mixture of absolute ethanol, Milli Q water and 0.1 molar (3-mercaptopropyl) trimethoxy-silane. [400 g EtOH/10 g water/10 g 3-MPT equivalent to 506 ml EtOH/10 ml water/9.46 ml 3-MPT converted by the specific gravities; (3-MPT: molecular weight 196.3; C<sub>6</sub>H<sub>16</sub>O<sub>3</sub>SSi)].

The 3-MPT silane molecules formed self assembly monolayers (SAMs) on the substrates and acted like a glue providing adhesion between the silica surface and the (nanoporous) gold<sup>23</sup>. The principle of this strong adhesion is covalent bonding<sup>24</sup>. If 3-MPT is not used, the porous gold is poorly adherent to the glass substrate and is easily removed in water.

### **4.2.3 Wet-chemical acid etching of the decorative gold leaves**

Commercially available decorative, genuine 12 carat white gold leaves containing Ag/Au alloy (1:1 ratio by weight; Monarch brand) were purchased from Sepp Leaf Products. Inc (New York). The chemical etching process, also called dealloying, was used to fabricate NPG.

During the etching process of the decorative gold leaves the silver is dissolved while the gold atoms tend to cluster and form larger structures of gold-rich islands (Figure 4.2.1),

rather than to distribute themselves homogeneously over the whole surface, which would stop further etching<sup>12</sup>.

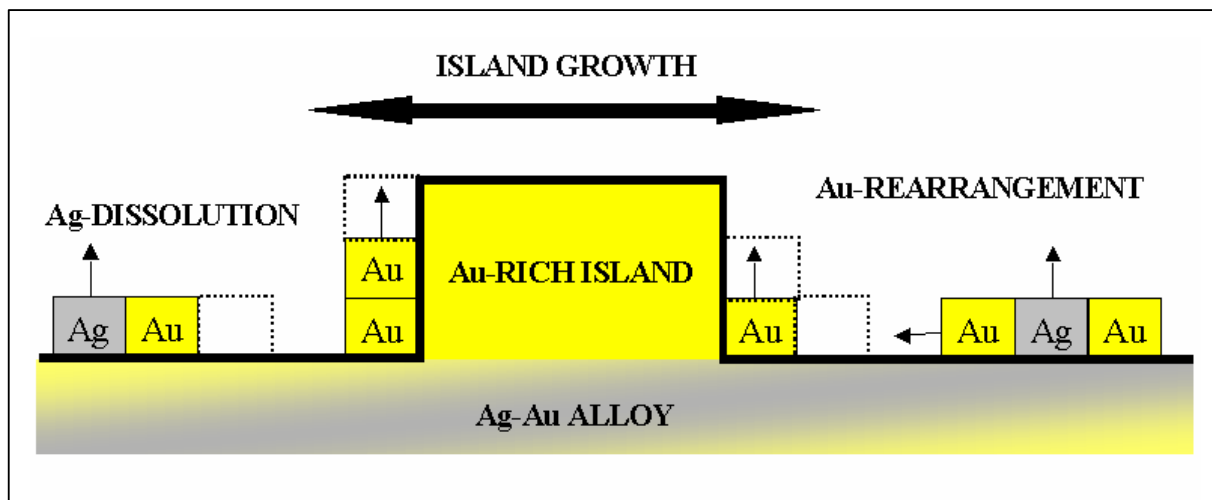
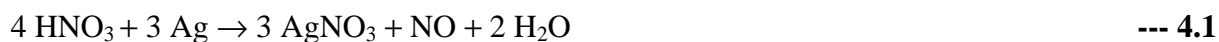


Figure 4.2.1: Gold island nucleation and growth due to high concentration of gold adatoms by the surface dis- and reordering mechanism<sup>10</sup>.

#### 4.2.3.1 Execution of dealloying (experimental part):

With the help of a moistened graphite roller the approx. 100 nm thick decorative gold leaf was taken out of the booklet (500 gold leaves) and spread on Milli Q water in order to be flattened (Figure 4.2.2.1). In the next step this leaf was transferred via the graphite roller to a concentrated (70 %) nitric acid (Fisher) bath, where the silver was dissolved within minutes at room temperature. During the etching of the gold leaf irregularly shaped structures were formed (“spongy” gold, Figure 4.2.2.2). Degradation of the light- and oxygen sensitive nitric acid was avoided by always using a fresh nitric acid solution and a teflon trough with teflon lid/cover. This teflon trough was designed in such a way that there was almost no air above the nitric acid level. The chemically etching procedure is described as follows:



For safety reasons the corrosive etching procedure was carried out in a fume hood. After 5 minutes immersion most of the silver was selectively dissolved as easily soluble silver nitrate. Leaving the gold leaf for longer time periods in the concentrated nitric acid caused the pore size to become larger due to the rearrangement of the gold atoms. The gold atoms are able to move  $\sim 1 \text{ nm}$  during  $1 \text{ sec}$ <sup>25</sup>. This fast surface diffusion occurs only in electrolyte and

can be easily stopped by taking the leaf out of the nitric acid and transferring it to Milli Q water (Figure 4.2.2.3). It has been shown that the morphology achieved during the etching process remains stable in water for at least six month<sup>12</sup>.

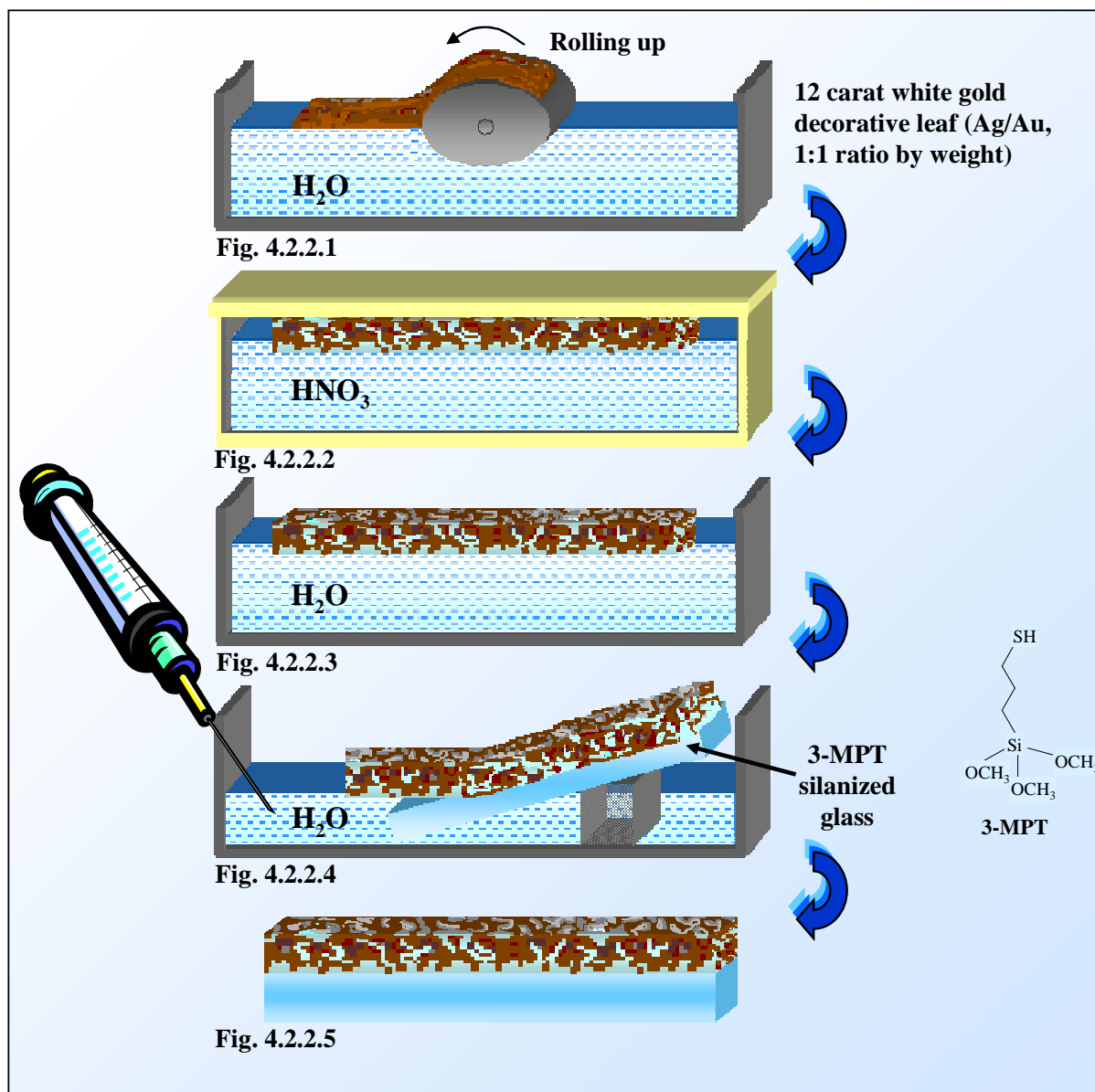


Figure 4.2.2: Fabrication of the NPG substrates

After etching, the nitric acid solution was removed from the teflon trough and the NPG was washed several times by pumping in Milli Q water with a syringe. A silanized glass substrate [Chapter 4.2.2] was adjusted at an angle that allowed the thin nanoporous gold membrane to be attached onto it by further lowering of the water level (Figure 4.2.2.4).

After air-drying of the samples the nanoporous gold membrane were permanently bound to the glass slide via the thiolate layer and remained stable<sup>12</sup>. Only a very small amount of gold remains (per area of the NPG, the gold content is only  $0.12 \text{ mg cm}^{-2}$ )<sup>22</sup>.

#### 4.2.4 Electrochemical dealloying

For some special applications of NPG it was thought to be useful to fabricate smaller pores than those resulting from 5 min chemical etching process, which is the minimum time needed to chemically dissolve the silver. Upon applying a potential difference during the dealloying process, the resulting silver nitrate is dissolved within seconds, so that the resultant pores were much smaller than the pores achieved by only chemical etching.

The slightly varied experimental set-up is depicted in Figure 4.2.3. Crocodile clamps were fixed on the metal screws of two graphite rollers placed in the concentrated (70 %) nitric acid bath, so that an electric current can be passed between them.

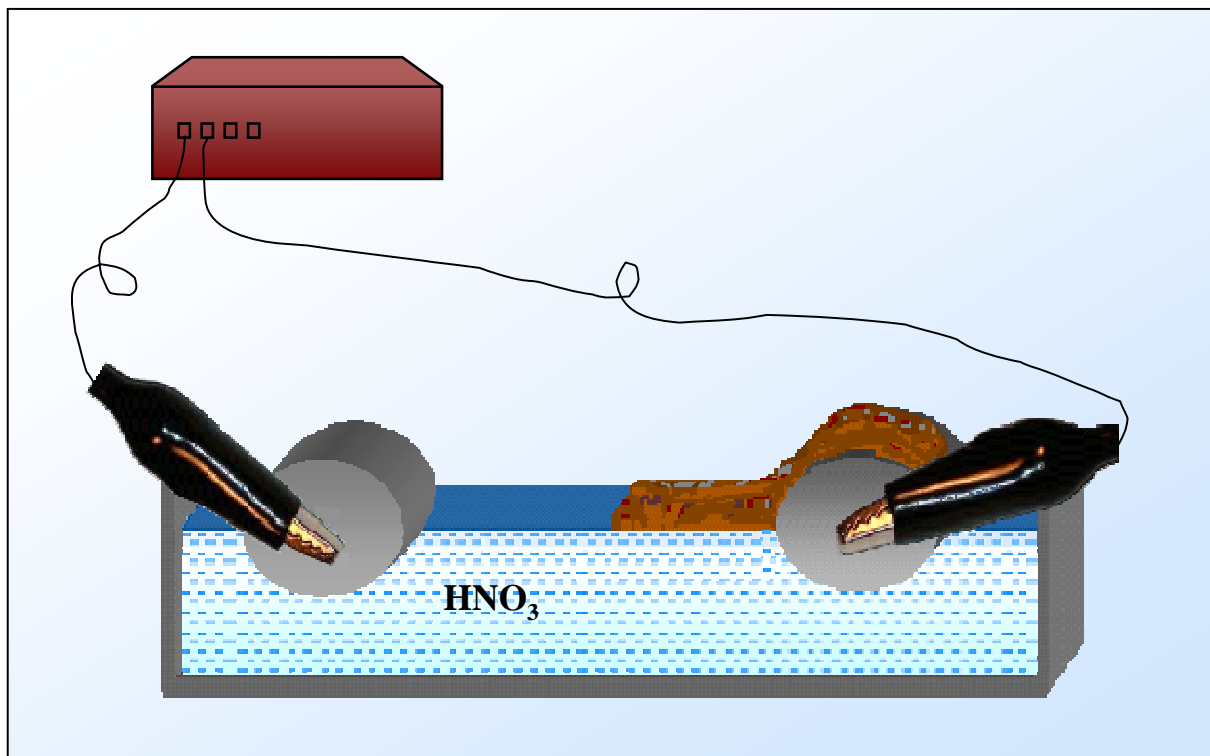


**Figure 4.2.3: Experimental setup for electrochemical dealloying method.**

In this case the gold leaf is not completely rolled off the graphite roller as it is done for the chemical etching process. If a potential is applied the corrosion of the decorative white gold leaf is so fast, that no teflon coverage is needed during the acid treatment. The color change due to the dealloying can be easily followed by the naked eye; the smaller the resulting pores the blacker the substrates appeared.

### **4.3 Scanning electron microscopy as a tool to visualize the NPG morphology**

Scanning electron microscopy (SEM) is capable of producing high resolution images of the nanoporous gold surface. All images were acquired using a LEO 1530 Gemini SEM operated at an acceleration voltage of 3 kV (low voltage SEM) (Figure 2.4.1)<sup>26</sup>

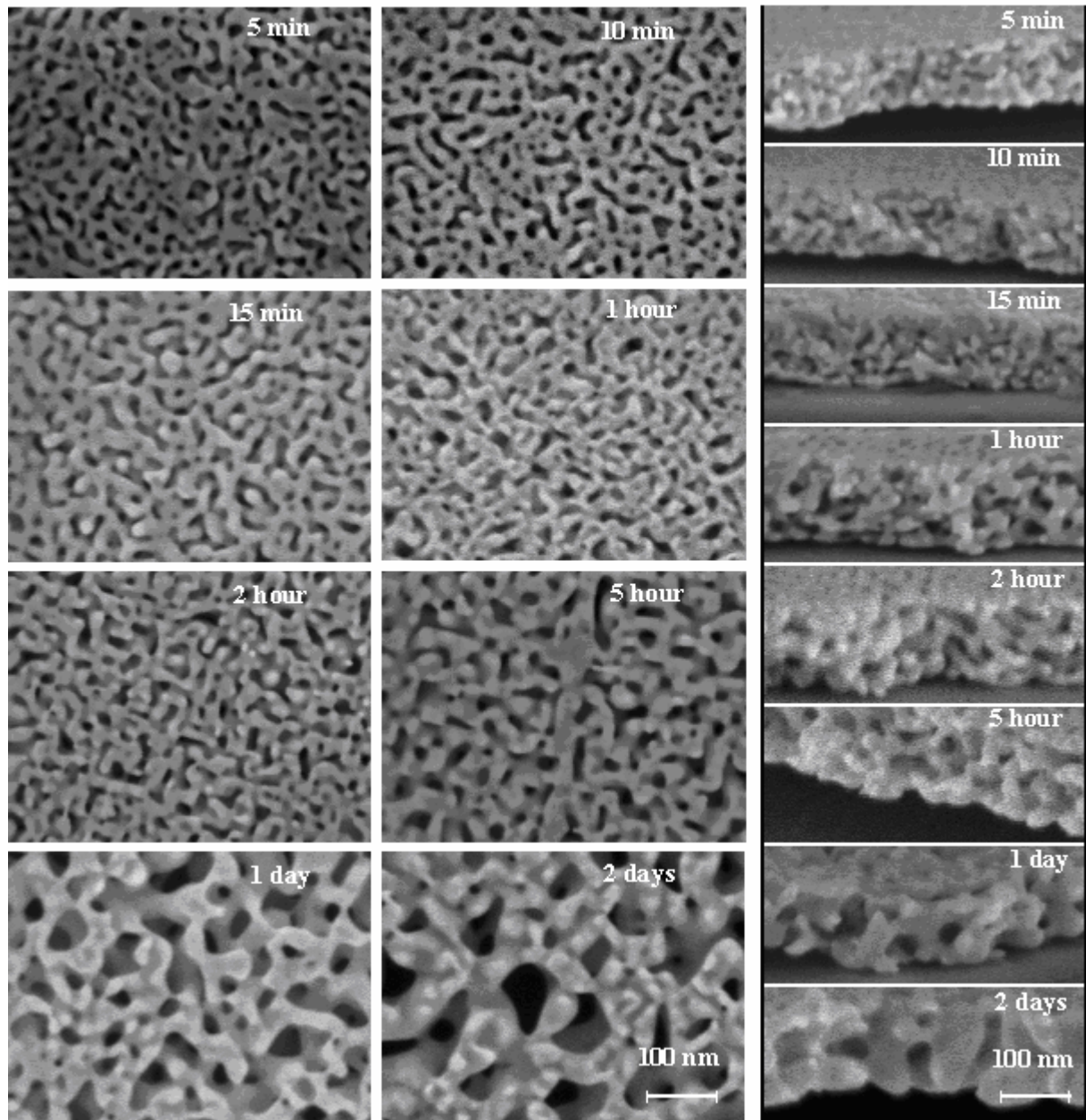


**Figure 4.3.1: Scanning electron micrographs of the NPG substrates for different etching times (chemical etching method). The shortest dealloying time was 5 minutes, the longest was 2 days. On the left side the up views (top views) are depicted; and on the right side the lateral views are shown.**

The SEM technique was employed in order to monitor the porous structure evolution of the NPG substrates for different etching times. Figure 4.3.1 presents a series of SEM

images starting from five minute etched NPG, and ending with the 2 days etched NPG. The longer the decorative white-gold leaf remained in the nitric acid bath [Chapter 4.2, fabrication] the larger were the resulting pores<sup>12</sup>. For the five minute etched NPG a small pore size was found. Continued immersion in the nitric acid bath resulted in bigger pore sizes. The biggest pore sizes were obtained in the 2 days dealloyed sample.

The scanning electron microscope images revealed also that NPG slides possessed large crack-free areas that were important for further investigations of the substrates.

The two volt electrochemically dealloyed NPG possessed the smallest pores, followed by the 1.2 volt electrochemically etched NPG (Figure 4.3.2).

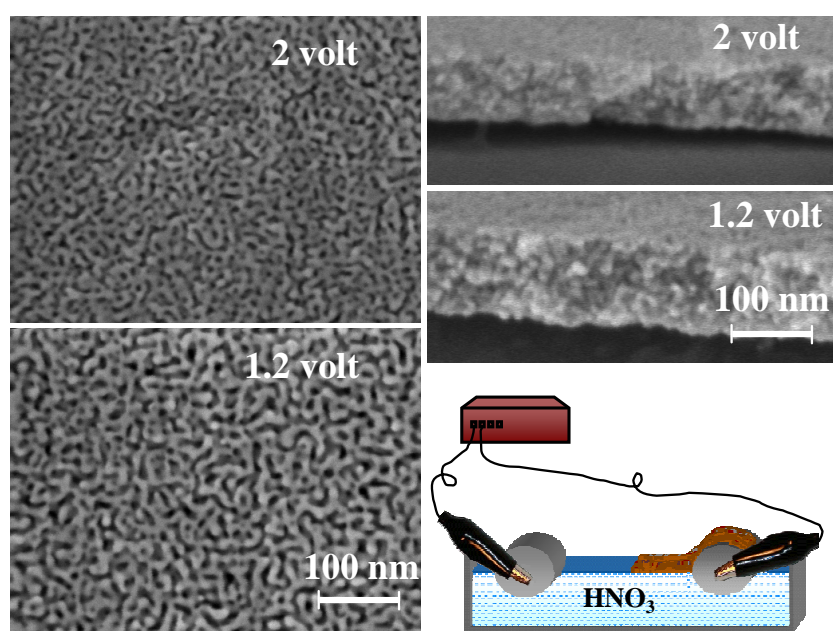


**Figure 4.3.2:** SEM images of the electrochemically dealloyed NPG substrates applying a potential of 2 volt and 1.2 volt, respectively, are shown. On the left side one can see the up views (top views); and on the right side the lateral views and the electrochemical setup are depicted.

As the average pore size was determined by SEM images (plan view), the thickness of the NPG was extracted directly from the lateral view SEM (cross section). The thicknesses were around 100 nm. A surface profiler (Figure 3.4.2) confirmed thicknesses of ~ 100 nm – 150 nm for the NPG substrates.

The side views also showed that bigger structures were formed during the gold adatom rearrangement and thus with longer etching times the original three dimensional nanoporous structure became a two dimensional structure.

#### **4.4 Two dimensional autocorrelation to determine the typical structure size of the NPG for different etching times**

Autocorrelation as a mathematical tool is frequently used in signal processing for analysing functions or series of values. An autocorrelation function can be applied to find typical length scales in specimen<sup>27-29</sup>. Scanning electron micrographs consist of picture elements (abbr.: pixels) and contain information about the typical length scale of nanoporous gold substrates expressed in gray scales. The pixels are the smallest addressable imaging elements (discrete values). In the x-and y- variation of the gray scales the microstructure of NPG is represented. The gray scales correspond to numbers, the high numbers represent bright area (rough gold “knobs”) and the lower numbers dark areas (void/pore fraction).

The pore size difference shown in the SEM images of the samples of different etching times is obvious even to the naked eye and could be estimated. But the two dimensional autocorrelation is a well defined algorithm that was used to obtain a more accurate number for the typical length scale of each NPG sample.

The 2D autocorrelation procedure is illustrated in detail for the 2 volt etched NPG sample below. The gray scale of the SEM image reflects the morphology of the porous substrate, even if the numbers associated with the intensity do not necessarily refer to the absolute height of the gold and depth of the pores respectively. Some inhomogeneities, like the grain boundaries, crinkles or cracks in the gold membrane can be averaged out choosing a large enough area.

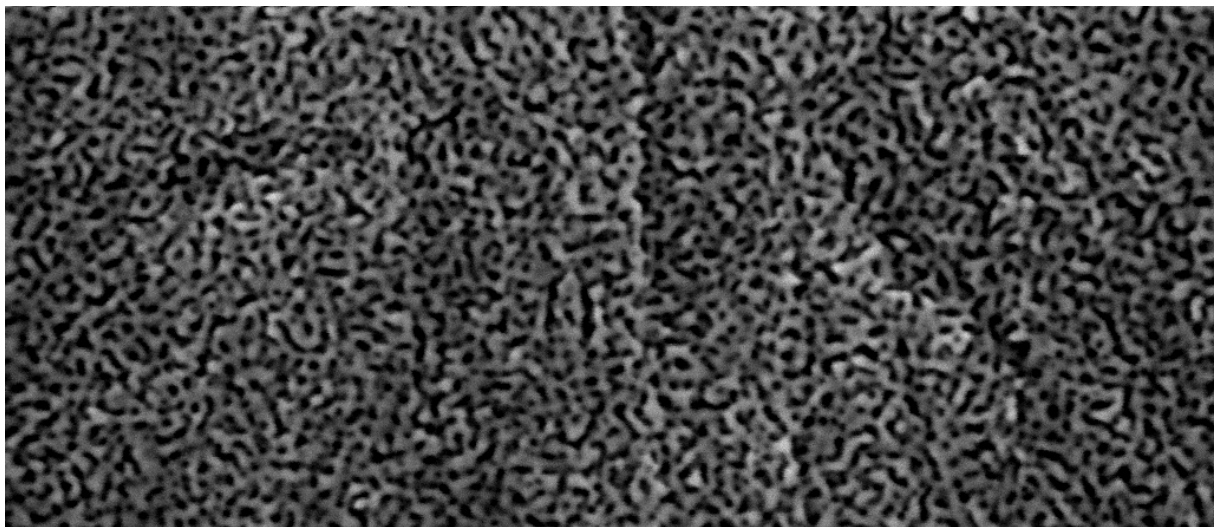


**Figure 4.4.1: Scanning electron microscope image of the two volt electrochemically dealloyed nanoporous gold substrate, loaded in Igor Pro.**

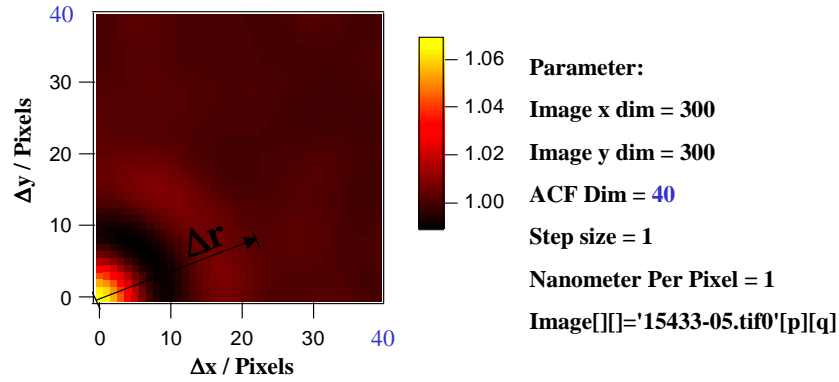


**Figure 4.4.2:** This three D image plot represents the autocorrelation function ACF ( $\Delta x$ ,  $\Delta y$ ). The parameters described on the right hand side are selected for this autocorrelation process. The colors give information about the surface of the 2 volt etched sample.

Running a 2D autocorrelation procedure generated a 3D image plot (Figure 4.4.2), which could be converted into a 2D diagram, where the correlated data points are plotted versus  $\Delta r$  (Figure 4.4.3 + 4.4.4). In order to obtain the value for the typical length scale, it was first necessary to average over all of the data points. The straight line displays the arithmetic mean of all the data points in one x interval corresponding to the step size.

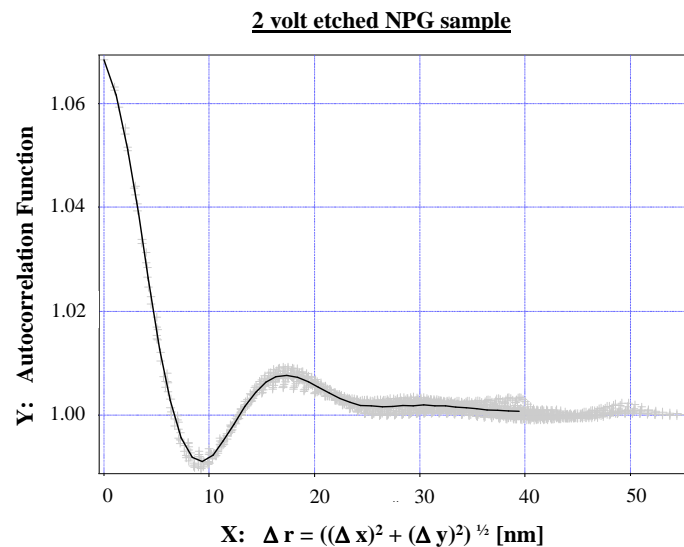


**Figure 4.4.3:** The 2D diagram shows the data points resulting from the ACF, which are plotted versus  $\Delta r$ . The solid line is the arithmetic mean derived from one x interval. (2 volt etched NPG sample for instance).

Reading off the maximum and minimum y - value of the mean curve leads to the  $y_{\text{middle}}$  value ( $y_{\text{max}} - y_{\text{min}} = y_{\text{middle}}$ ). In this study it was defined that the corresponding x - value to this  $y_{\text{middle}}$  value identifies the number for the half typical length scale; and the full width at half maximum equals the typical length scale.

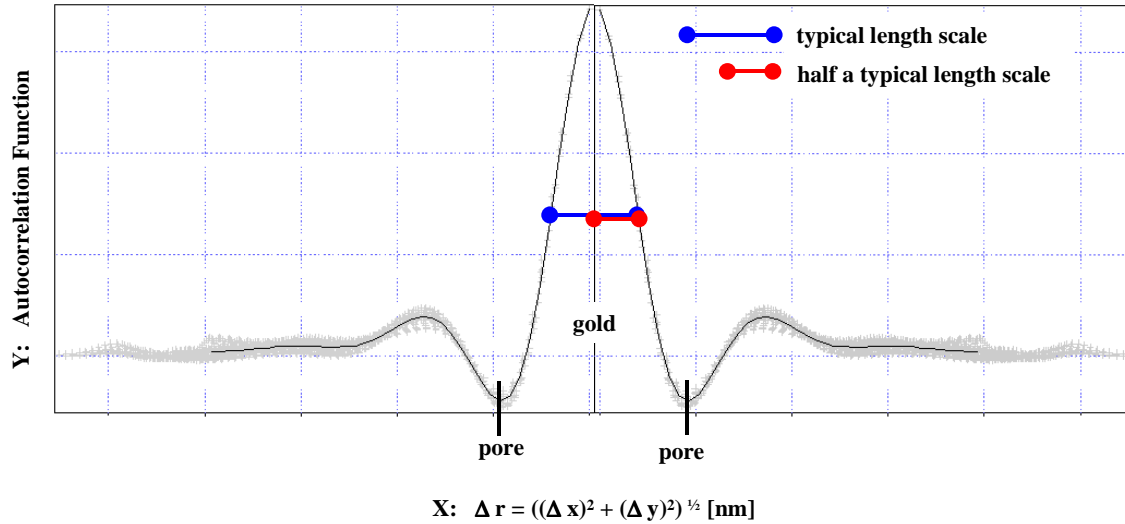


Figure 4.4.4: Schematic presentation to find typical length scales with ACF method.

The two dimensional autocorrelation procedure described above has been carried out for all the different NPG samples created by electrochemical and chemical dealloying. Scanning electron micrographs were recorded for each NPG sample at several different spots on the surface.

Due to the irregularities of the NPG substrates a distribution of values for the typical length scale was derived. The error was calculated by the standard deviation  $\sigma$ :

$$\sigma = \sqrt{\frac{1}{N} \sum_{i=1}^N (X_i - \bar{X})^2} \quad \text{--- 4.3}$$

The resulting error is shown as error bars together with the values of the typical length scale derived from the autocorrelation method (cf. Figure 4.4.5).

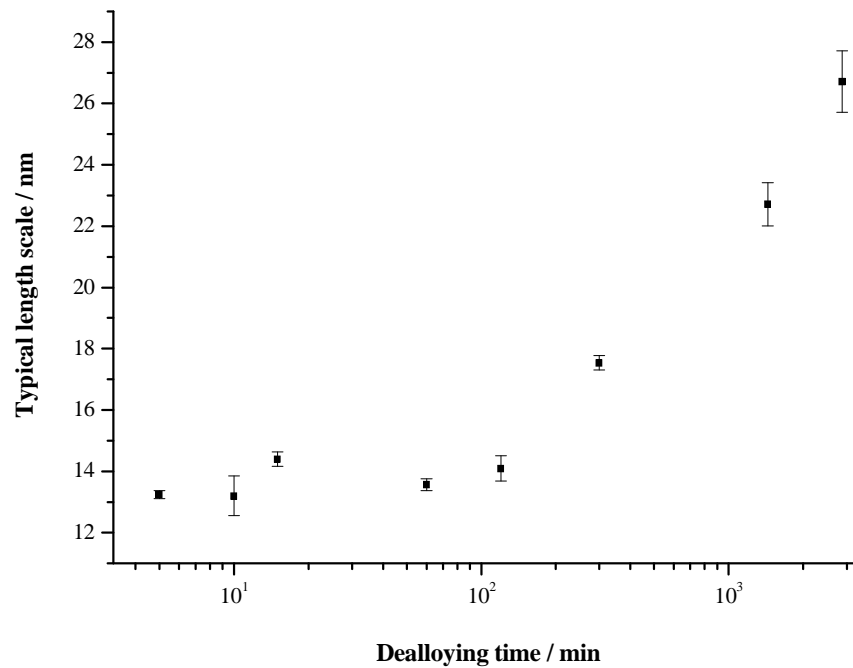


**Figure 4.4.5:** The values of the typical length scale resulting from the 2D correlation of the NPG samples created by a chemically etching procedure are plotted versus the dealloying time. The error bars indicate the standard deviation.

The correlation procedure confirmed the increase in pore size that could be seen from the SEM images by the naked eye. The electrochemically etched NPG substrates had the smallest structures, such as length scales between 6.72 – 7.9 nm for the 2 volt sample and 9.2 – 9.4 nm for the 1.2 volt sample (not shown in Figure 4.4.5). It was not possible to produce length scales less than ~ 12 nm by the chemical dealloying method; this was due to the fact that at least a five minute residence time in the nitric acid was needed to dissolve the silver, which leads to a morphology with typical length scales around 12 to 14 nm.

There is nearly no discrimination in structure development between the 5 min etched sample and the 2 hour etched sample. However by leaving the decorative gold leaf in the acidic bath for 5 hours, 24 hours or 48 hours it was possible to monitor the structure development up to 28 nm as a typical value to describe the structure elements.

It can be concluded that analysing the SEM pictures with the 2D autocorrelation tool is useful for finding typical length scales of the NPG substrates created with different etching times. It should be remembered that these numbers are not absolute values that can completely characterize the pore sizes, because the SEM images did not accurately reflect the fractal morphology (randomly distributed pores) of the NPG and the NPG also exhibited a lot of inhomogeneities (structural irregularities).

#### **4.5 Cyclic voltammetry and electrical impedance spectroscopy as methods to determine the surface area of NPG substrates**

The surface area of the NPG was characterized by cyclic voltammetry (CV) and electrochemical impedance spectroscopy (EIS)<sup>30</sup>. In cyclic voltammetry an oxide layer ( $\text{Au}_2\text{O}_3$ ;  $\text{Au}_x\text{O}_y$ ) was formed at potentials positive of 1 V during anodic scans in 1 M sulfuric acid ( $\text{H}_2\text{SO}_4$ ). As the applied potential was reversed, the oxide layer was stripped and a sharp peak was seen in the cathodic scan of the voltammogram<sup>5</sup>. The area under the reduction peak is proportional to the charge needed to reduce the gold oxide monolayer and is related to the surface area of the gold film<sup>31</sup>. In order to obtain the enhancement (roughness) factor, the area under the cathodic peak of the different porous samples was compared to the area obtained for evaporated flat gold films. As an example for the oxidative and reductive scans, the complete cyclic voltammogram of a 15 minutes etched NPG sample is shown in Figure 4.5.1. The current in amperes is plotted versus the potential in volts with respect to the silver/silver chloride reference electrode. The area under the reduction curve for integration is marked in orange.

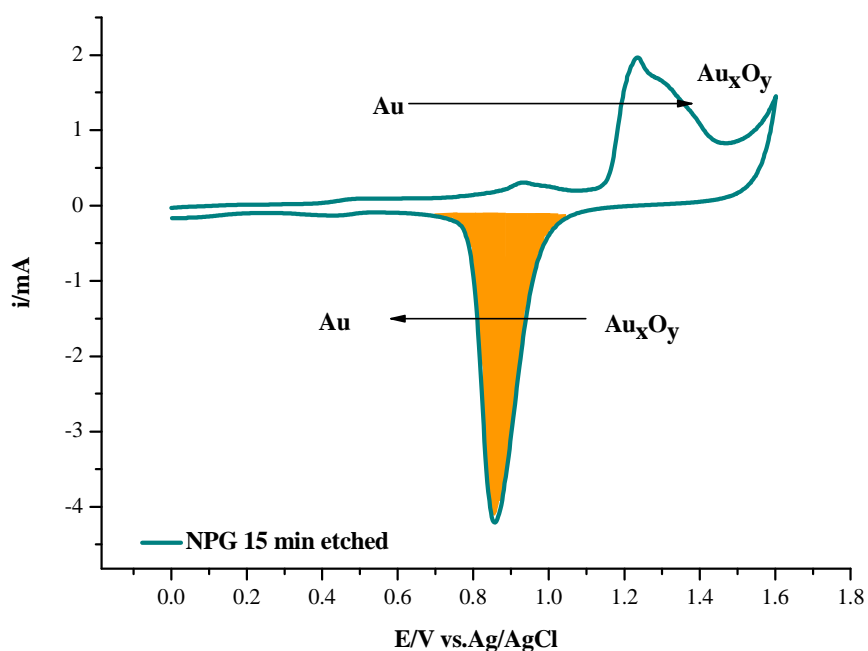


**Figure 4.5.1:** The cyclic voltammogram for a 15 minutes etched NPG sample. Gold oxides were formed at positive potentials and reduced at less positive potentials. The sweep rate in 1M  $\text{H}_2\text{SO}_4$  amounted  $100 \text{ mVs}^{-1}$ .

In Figure 4.5.2 the cyclic voltammograms of NPG substrates (chemically etched for 5 minutes, 15 minutes, and 1 hour) and evaporated dense gold films are depicted to demonstrate the large surface enhancement of the porous substrates. The reduction peaks were integrated by using the software Origin (version 7.5).

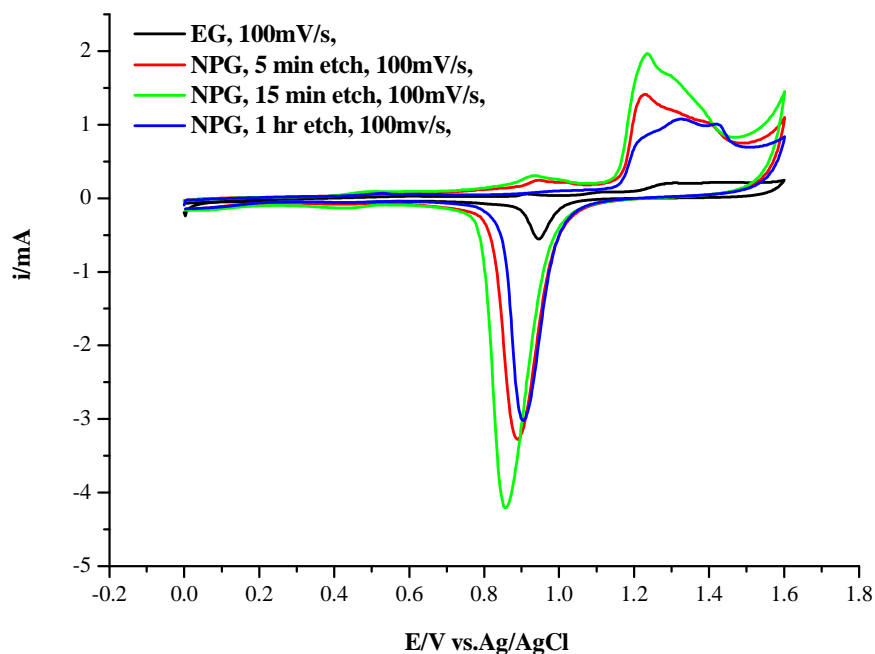


**Figure 4.5.2:** The cyclic voltammograms of the 5 minutes, 15 minutes, 1 hour dealloyed NPG (colored lines) and the EG film (black line). A sweep rate of 100 mV/sec was applied.

As a second method electrochemical impedance spectroscopy was used to obtain values for the double layer capacitance of the NPG films<sup>32</sup> [Chapter 2.3]. Provided that the distance of closest approach of the counter ions is sufficiently small, the double layer capacitance will be proportional to the surface area of the gold films. The impedance spectra reported were taken at 0.3 V versus silver/silver chloride in 1 M sulfuric acid; at this potential no Faradaic peaks were seen in the cyclic voltammetry.

Figure 4.5.3 shows then the variation in the surface area of the different NPG substrates with respect to chemical dealloying time, measured by both CV and EIS, whereas Figure 4.5.4 shows that area enhancement after electrochemical dealloying. In all cases it is assumed that the EG films had a relative surface area of 1 and the numbers shown refer to the surface increase relative to these films. All NPG films show enhanced surface areas relative to EG.

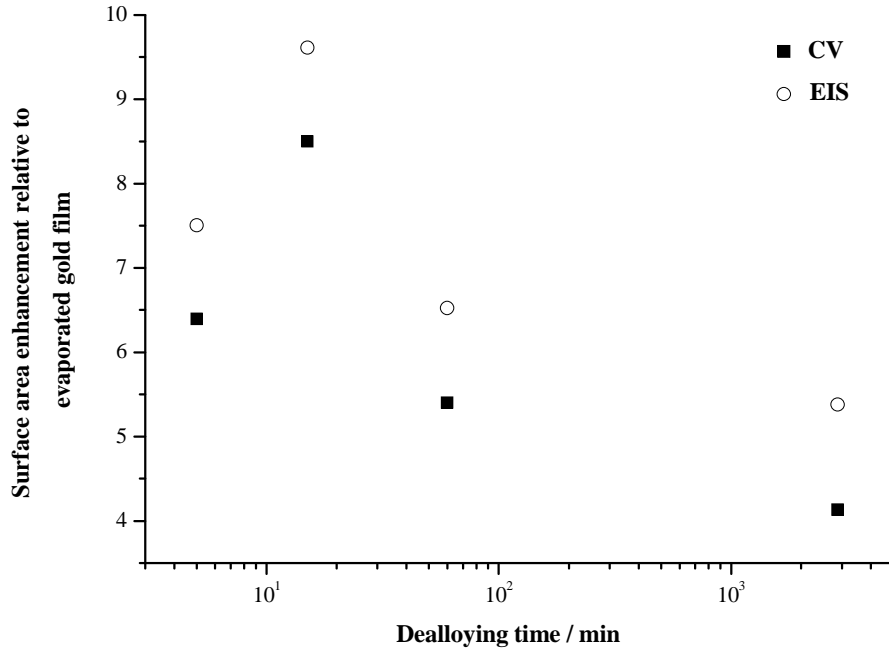


Figure 4.5.3: CV and EIS measurements for the chemically dealloyed NPG samples compared to EG. The NPG samples etched for 5 min, 15 min, 60 min and 2 days are shown.

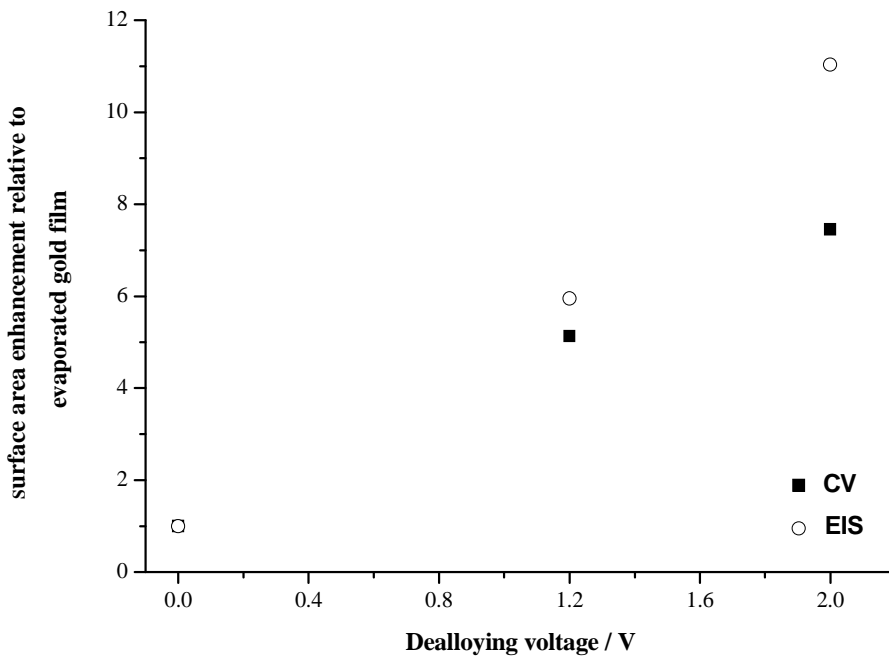


Figure 4.5.4: CV and EIS results of electrochemically etched NPG (1.2 volt and 2 volt) in comparison to EG. The first data point displays an evaporated gold film with a dealloying time of zero.

The 2 volt etched NPG samples exhibit the smallest pores (SEM) and show an 11 fold increase in the double layer capacitance relative to EG. The 1.2 volt electrochemically etched

NPG substrates show 5 - 7 times larger surface areas than the EG substrate. The 5 min chemically etched NPG films have surface areas 6 times larger than the EG. The largest surface enhancement (~ 10 fold increase; 9.6 (EIS) and 8.5 (CV)) was seen for the 15 minute chemically etched sample. Chemical dealloying times longer than 15 minutes led to a decrease in the surface area enhancement. This decrease was thought to correlate to the formation of bigger structures during the gold adatom rearrangement (Figure 4.5.6). Large structures possess a much smaller surface to volume ratio than little structures. The development of large structures was seen in the lateral view of the SEM images [Chapter 4.3].

The surface enhancement measured by CV agrees roughly with that measured by EIS; in addition the same trends are seen by both methods with respect to increasing chemical dealloying time. The EIS revealed slightly higher values for the surface enhancement in comparison to the values measured by CV. A reason could be that gold oxides were not formed all over the NPG surface.

Since mechanically thinned 12 carat white-gold leaf was the starting material for the fabrication of nanoporous gold membranes, a few inhomogeneities in the thickness of the NPG substrates are expected. By using a surface profiler [Chapter 3.4.2] the thicknesses were pre-estimated. Here, a more precise method was needed to calculate the thicknesses and possibly correct the factors of surface enhancement obtained by cyclic voltammetry and electrical impedance spectroscopy, respectively.

For that reason, an UV/VIS/NIR spectrometer [Chapter 3.4.3] was used as a second method to determine the thickness of the nanoporous gold membranes by measuring the absorbance in transmission mode. The UV/VIS spectra of the differently etched NPG substrates are shown in Figure 4.5.5. Three to four different positions per substrate were measured to get an average of the respective sample. As in the UV region no plasmonic features were seen, the absorbance was read off at  $\lambda = 400$  nm in all cases. These values were used to correct the electrochemical data.

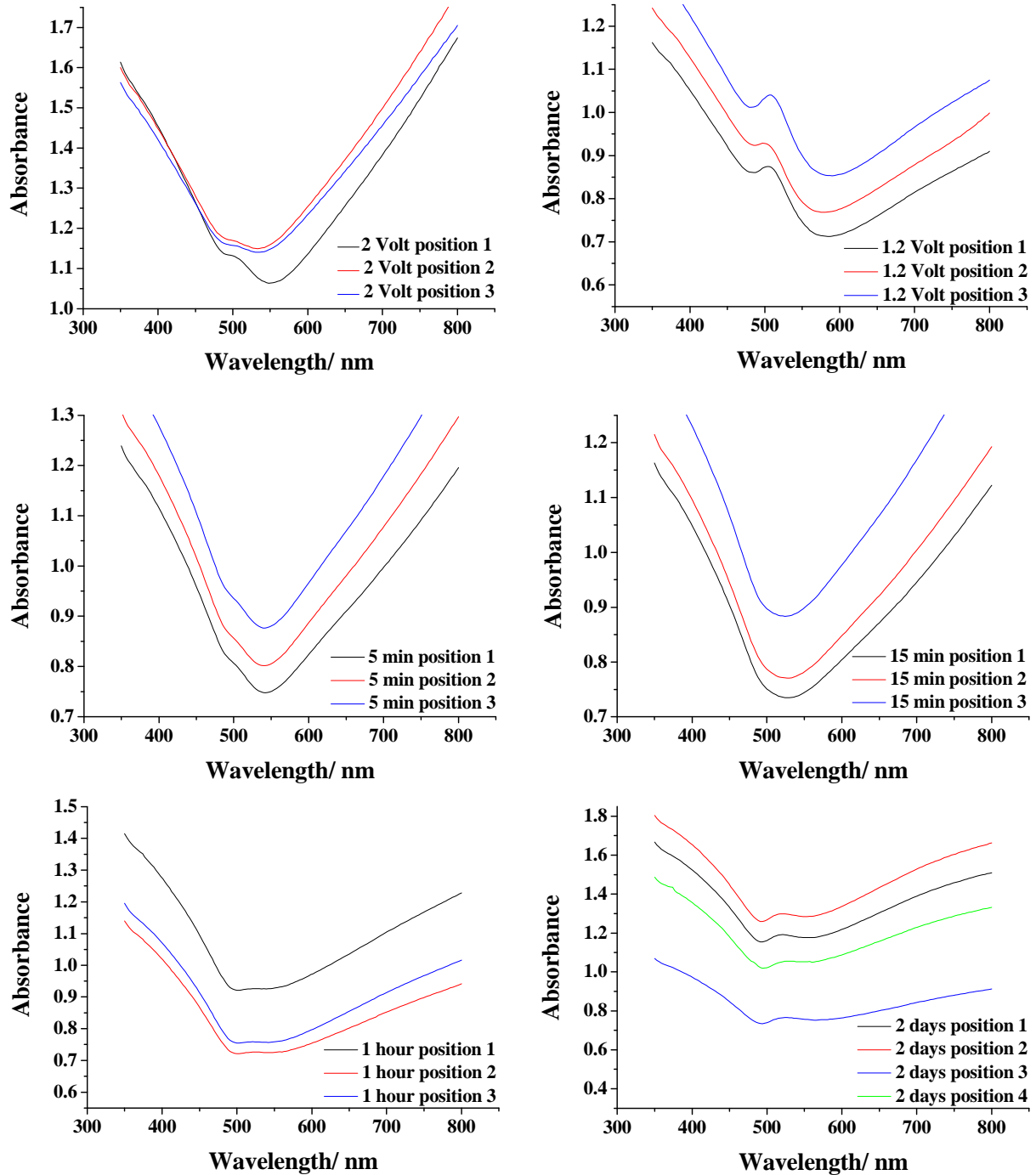
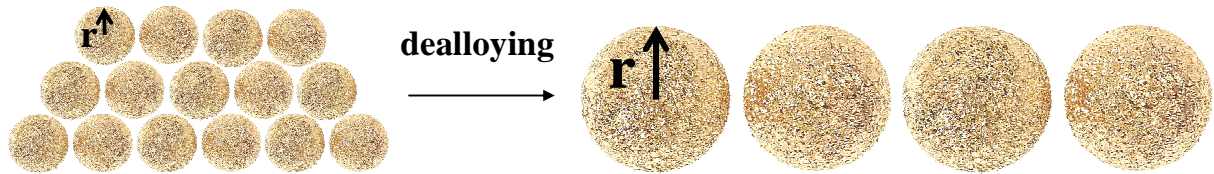


Figure 4.5.5: UV/VIS spectra of the differently etched NPG substrates: 2 volt and 1.2 volt electrochemically etched; 5 min, 15 min, 60 min and 2 days chemically etched. BK7 glass was the reference.

The UV/VIS spectra indeed revealed inhomogeneities of the samples, not only between the differently dealloyed samples, but also within the sample. Especially, the 2 days chemically etched sample was measured at four different positions and showed huge differences in the absorbance.

In the following paragraph, the mathematic correlation between surface area (determined by CV and EIS) and volume (thickness measured by UV/VIS) is described briefly. A spherical model of NPG is chosen for simplification. Here, a sketch of gold spheres illustrates the structural changes caused by the dealloying procedure (Figure 4.5.6).



**Figure 4.5.6: The formation of bigger gold structures during the dealloying procedure leads to larger radii and smaller surface areas, but constant volumes.**

The surface area (A) of a sphere of radius (r) is

$$A = 4 \cdot \pi \cdot r^2 \quad \text{--- 4.4}$$

and the volume (V) of this sphere is

$$V = \frac{4}{3} \cdot \pi \cdot r^3 \quad \text{--- 4.5}$$

Subsequently, the ratio of the surface area and the volume is

$$\frac{A}{V} = \frac{3}{r} \quad \text{--- 4.6}$$

Therefore, the decrease in surface area during the dealloying procedure was thought to correlate to the formation of bigger structures due to the gold adatom rearrangement (Figures 4.5.6 and 4.2.1).

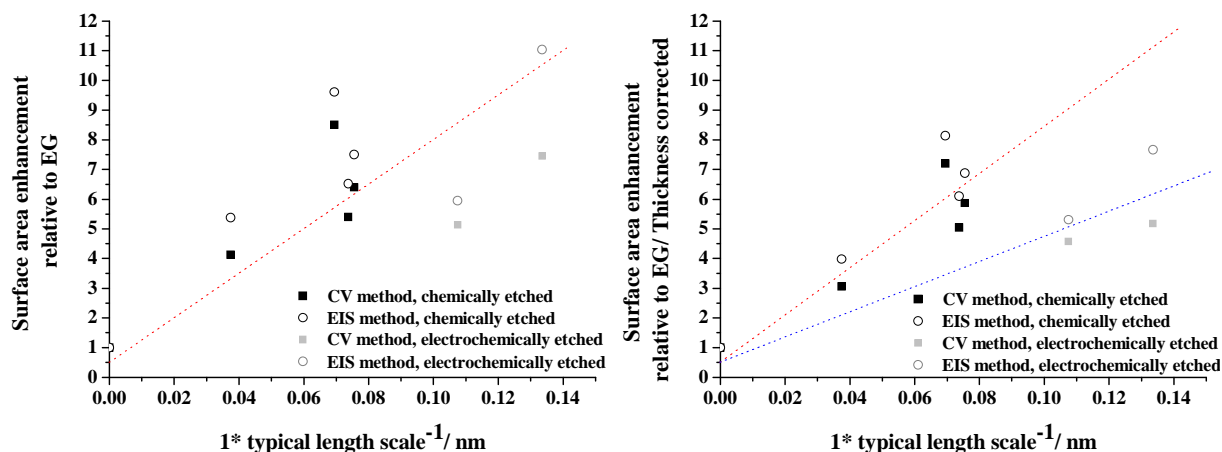


**Figure 4.5.7: Coherency between surface area enhancement measured and 1/typical length scale. Results of CV (unfilled circles) and EIS (filled squares) are plotted. The chemically etched NPG samples are shown in black and the electrochemically etched ones in gray. The dashed lines are a guide for the eye of the beholder. Left: uncorrected CV and EIS data. Right: thickness corrected data sets.**

In Figure 4.5.7 the experimental data obtained by CV and EIS were summarized. The data of chemically and electrochemically etched NPG substrates were plotted against the inverse typical length scales that were determined by autocorrelation function. The data point at  $x = 0/ y = 1$  represents the evaporated dense gold film.

Generally, the surface area ( $A$ ) of a sphere is inversely proportional to its radius ( $r$ ), ( $A \propto r^{-1}$ ). Therefore, the gold-rich islands of the NPG simplified as spheres were expected to show a similar correlation of the surface area to the determined typical length scales. The dotted lines through 0.5 guide the eye of the beholder to follow the trend of surface enhancement compared to the flat case. Since NPG originally was a white gold leaf, composed of 1:1 silver and gold, the non etched surface is thought to possess half of the surface area of an evaporated pure gold film.

The graph on the left side shows the uncorrected CV and EIS data, while the graph on the right side contains the thickness corrected data sets. The right plot identifies a different behavior of the chemically and the electrochemically etched samples (two dotted lines). The chemically etched NPG substrates came closer to the predicted model, while the electrochemically etched NPG membranes further diverged. Several reasons can be considered why the electrochemically dealloyed samples behaved differently to the other samples. One reason could be an error in the UV/VIS absorbance. For example, loss of light due to more scattering compared to the chemically etched samples leads experimentally to an overestimation of the absorbance, thus falsify the thickness measurement enormously.

#### **4.6 Simultaneous Excitation of Propagating and Localized Surface Plasmon Resonance in Nanoporous Gold Membranes (p-SPR and l-SPR)<sup>1</sup>**

The use of nanoporous materials for the optical sensing of adsorbates has obvious advantages – in addition to the potential for greater sensitivity, the different length scales associated with a variety of optical phenomena allow for a greater variety of adsorption characteristics to be examined. Here, it is shown that ultra-thin (~ 100 nm) nanoporous gold (NPG) membranes possess features of both planar metal films that exhibit propagating SPR (p-SPR) excitations and nanostructured metals that exhibit localized SPR (l-SPR) excitations. This is the first report of such multifunctionality in a plasmonic material. Illustrative examples of using this material to probe bio-recognition reactions and to probe the structure evolution of different layer-by-layer deposition systems are given. The results are consistent with the very different lengths of the tail of the evanescent field decays associated with each of these plasmon excitation modes (Figure 4.6.1).

Generally, surface plasmon resonance refers to the generation and propagation of plasmons at metal/dielectric interfaces [Chapter 2.1]. The propagating and localized plasmon resonances that were studied here were both excited through interaction with a stimulating radiation, but the geometries of the excitations were different. In p-SPR, plasmon waves were generated at metal/dielectric interfaces in the tested multilayer systems (See Fig. 4.6.5 and 4.6.6; 4.6.13 and 4.6.15) under conditions of total internal reflection of the probe light source<sup>33</sup>. When examining such a multilayer (for instance, in the geometry of a thin film), at just the right incident angle/probe radiation wavelength, there was resonant absorption. The evanescent tails of p-SPR waves are long, in the range of 200 – 300 nm, much longer than the thickness of the applied multilayer films, and thus represented a long-range average response of the multilayer. Analytically, p-SPR scans of reflectivity versus angle are analyzed in a straightforward way using the Fresnel equations. The typical experiment employs the so-called Kretschmann configuration<sup>34</sup> where a probe laser reflects off the backside of the multilayer through a high index glass prism (LaSFN9). In contrast, localized SPR excitations occur around high (nanoscale) radii of curvature metal/dielectric features; consequently, the evanescent tail of l-SPR excitations are typically of a similar length scale as the nano-feature. The theoretical underpinning of l-SPR, developed by Mie et al, can be used to model the l-SPR response of nanoparticles with spherical symmetry<sup>35</sup> and more recently, a

---

<sup>1</sup> Chapter 4.6 is based on the following publication: Yu, F.; Ahl, S.; Caminade, A. M.; Majoral, J. P.; Knoll, W.; Erlebacher, J., Simultaneous excitation of propagating and localized surface plasmon resonance in nanoporous gold membranes. *Analytical Chemistry* **2006**, 78, (20), 7346-7350.

computational methodology to calculate the response of arbitrary-shaped metal/dielectric interfaces has become available<sup>36</sup>. Experimentally, localized SPR has been examined in two and three-dimensionally roughened gold films made by a variety of methods<sup>37, 38</sup>, but not in nanoporous gold. The primary mode of examination of l-SPR excitations is to look at an absorption or reflection spectrum as a function of wavelength at a fixed angle of incidence. Anomalous absorption peaks, usually in the visible range, that can be correlated to size effects within the target material are ascribed to localized surface plasmons.

The trick to make a material exhibiting good l-SPR is to make it microscopically extremely rough in order that the statistical number of field magnification points is large enough to generate a macroscopic response. Usually, then, l-SPR excitations are events within the bulk of a porous metal/dielectric composite, occurring at sharp curvatures and small structures, where the geometry is just right. For these conditions, there is a huge resonance leading to greatly enhanced absorption, usually in the optical spectrum<sup>39-42</sup>. In random porous media with a statistically relevant number of these points exhibiting l-SPR excitations, the overall material response will be a characteristic optical absorption spectrum. If there is a chemical adsorption event that changes the dielectric constant within the porous media, then the absorption spectrum will also change.

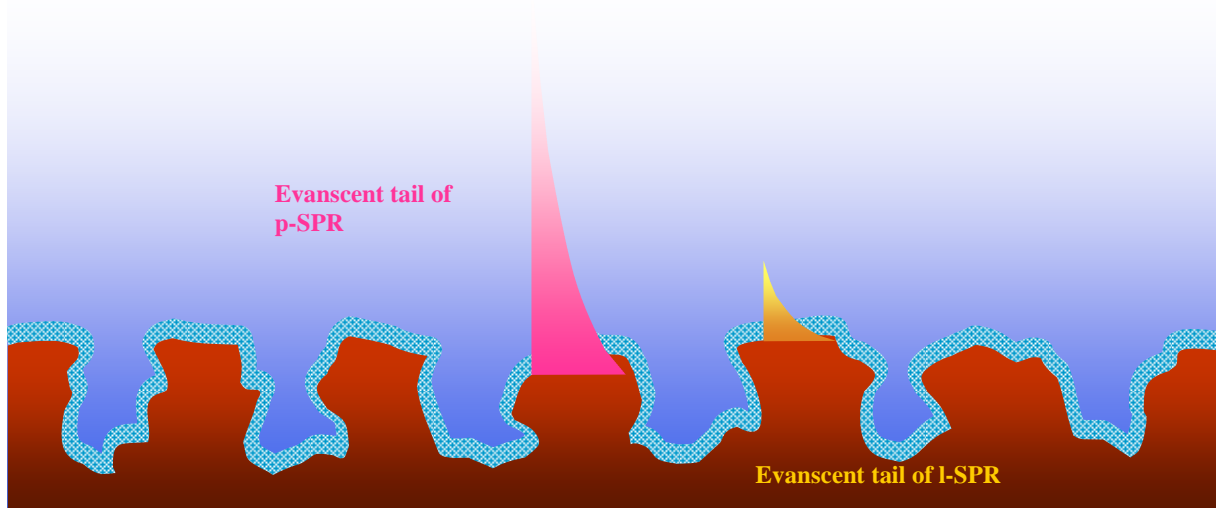


**Figure 4.6.1:** A sketch of NPG substrate coated with a dielectric demonstrates the different evanescent decay length of l-SPR and p-SPR field.

The SPR setup in the Kretschmann configuration [Chapter 3.1] was used to characterize the p-SPR response by monitoring the reflectivity of the nanoporous gold as a function of incident angle with irradiation at different wavelengths (594 nm, 632.8 nm, 780 nm, 820 nm and 1152 nm, respectively). A series of angularly resolved reflectivity scans

for NPG samples (Fig. 4.6.2(A)) clearly shows a strong wavelength dependence of the p-SPR signal. The longer the laser wavelength, the sharper is the SPR dip and the smaller the dip angle. For example, using the  $\lambda = 632.8$  nm laser, the p-SPR response was heavily damped by the rough NPG and showed a broad minimum with a FWHM of  $\sim 23$  degrees in the reflectivity curve, in contrast to a much sharper SPR dip obtained from an evaporated gold sample using the same laser wavelength (FWHM  $\sim 2$  degrees) (data not shown). With the  $\lambda = 1152$  nm laser, however, the FWHM of SPR dip was improved to  $\sim 1.1$  degrees; this may be ascribed to a more efficient SPR propagation at the metal-dielectric interface, which to some extent compensates for the inevitable impingement/scattering loss of light due to roughness at the NPG/glass interphase. Referring to Raether's theory<sup>33</sup>, the dispersion-relation (between angular frequency  $\omega$  and wave vector  $k$ ) [Chapter 2.1.1] curve at the metal/dielectric interface approaches asymptotically to that of the free photon in air. At a longer laser wavelength, these two dispersion curves become closer and smaller  $k$ -vector amplification factor by the high-refractive-index prism is needed to fulfill the SPR excitation condition. Therefore, for longer laser wavelengths, the resonance coupling happens at a smaller incident angle where the in-plane component of the  $k$ -vector is smaller.

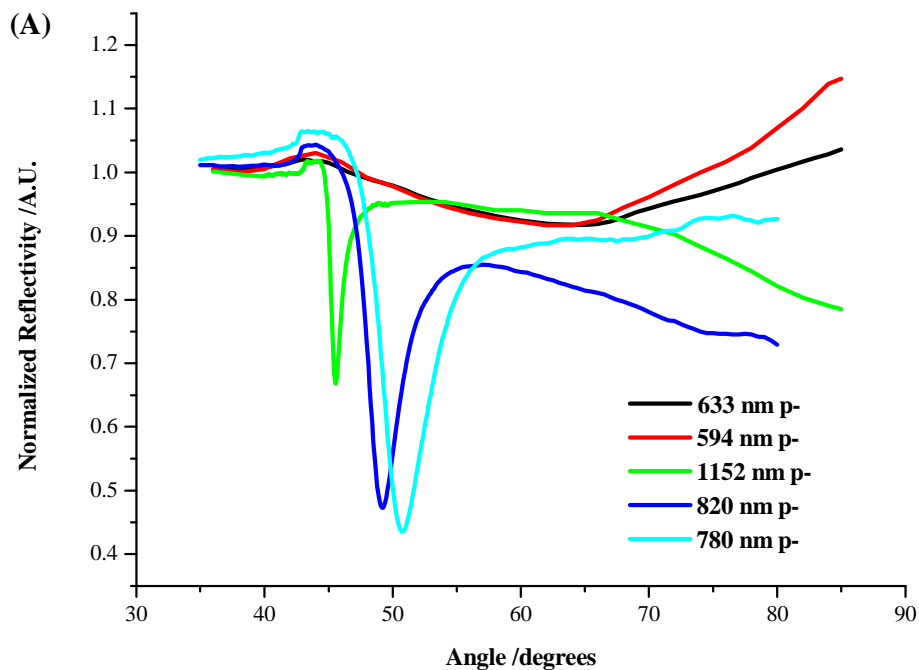


**Figure 4.6.2:** (A) The excitation of p-SPR on 100 nm thick NPG using lasers of different wavelengths. The measurements were performed in air using a right-angle BK7 glass prism.

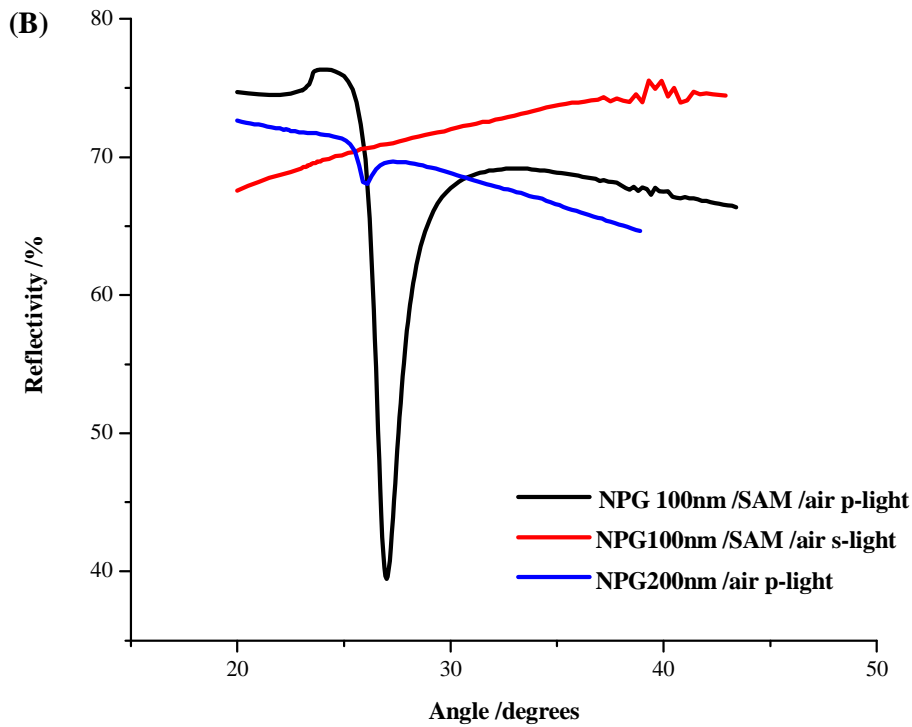


**Figure 4.6.2: (B) p-SPR curves of (1) 100 nm NPG, p-polarized laser,  $\lambda=1152$  nm; (2) 100 nm NPG, s-polarized laser,  $\lambda=1152$  nm; (3) 200 nm NPG, p-polarized laser,  $\lambda=1152$  nm. The measurements were performed in air using a right-angle LaSFN9 (Schott glass) glass prism.**

The argument that p-SPR excitation is obtained with NPG was supported by the reflectivity results in Figure 4.6.2 B, which show that the SPR minimum was absent if the sample was irradiated with an s-polarized  $\lambda = 1152$  nm laser. Additionally, a 200 nm NPG layer only exhibited very limited SPR coupling efficiency using a p-polarized  $\lambda = 1152$  nm laser.

One may expect that the porous network and microscopic roughness of a nanoporous gold membrane will have a significant effect on its p-SPR behavior. A few studies<sup>33, 43</sup> have examined p-SPR on rough metal films, and these studies may be considered being the foundations of the work reported here. Generally, the effect of roughness is to strongly perturb the reflectivity band by damping propagating surface plasmon modes (SPs). Such perturbations may be analytically described by considering the forward scattering and directional backward scattering of non-radiative SPs due to roughness. The general result is that resonant absorption peaks in the angular reflectivity scan tends to be broadened in comparison to volume-equivalent films with sharp interfaces.

Dense, non-porous, gold films thicker than 47 nm exhibit very limited plasmon coupling efficiency as evidenced by the Winspall simulations depicted in Figure 4.6.3. A 100 nm dense gold substrate, for instance, reveals a similar degree of surface plasmon coupling to a 200 nm thick NPG substrate (see Figure 4.6.2 (B) above).

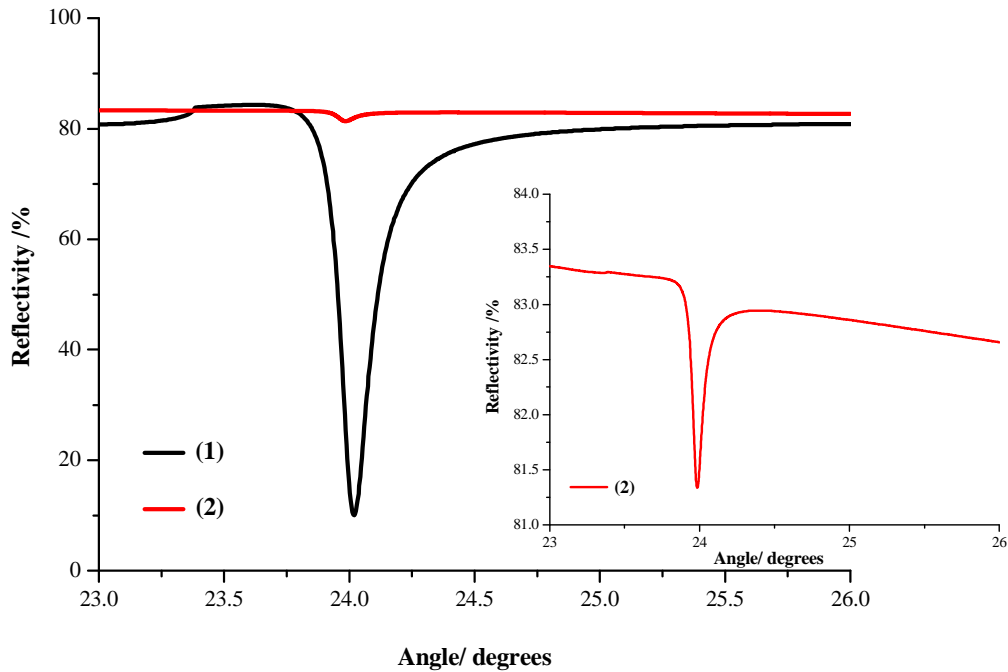


Figure 4.6.3: Winspall (version 2.20) simulations are shown for surface plasmon excitation of 47 nm (1) and 100 nm (2) evaporated flat gold films, respectively. The excitation source was an infrared laser with wavelength of 1152 nm. The measurements are simulated in air. The inset is an enlargement of the reflectivity curve of the 100 nm thick film. The parameters used for the Winspall simulations can be found in Table 4.6.1.

Table 4.6.1: Parameters used in Winspall (version 2.20) simulations to model the surface plasmon events on pure, dense gold surface. The resulting reflectivity curves are depicted in an angular dependency in Figure 3. P- polarized light and a right-angle LaSFN 9 prism were presumed.

Layer	Thickness/[Å]	$\epsilon'$	$\epsilon''$	Thickness/[Å]	$\epsilon'$	$\epsilon''$
1 LaSFN9	0	3.31487	0	0	3.31487	0
2 gold	470	-61.2413	4.0716	1000	-61.2413	4.0716
3 air	0	1.00053	0	0	1.00053	0

A systematic study of the appearance of p-SPR on NPG substrates was completed using a white source (halogen) with a monochromator to select wavelengths at  $\Delta\lambda = 10$  nm intervals in the range of 450 nm to 850 nm. The plasmon matching condition was reached at certain excitation wavelengths and incident angles (Figure 4.6.4). The longer the wavelength, the sharper the surface plasmon resonance response and the smaller the resonance angle as described above. Measuring the same spot on the NPG substrate showed that the coupling efficiency also increased with increasing excitation wavelength. The different coupling efficiencies seen in Figure 4.6.2 A were thought to be due to NPG sample inhomogeneities, such as diverse thicknesses or differences in the local gold morphology.

With increasing pore size it becomes harder to match the plasmon coupling condition. The 2 days dealloyed NPG has a 2D porous gold layer, where the pores reach through the entire film. At the same time the 2 day etched sample absorbs  $\sim 2$  times more light than the 2 volt etched NPG membrane.

In a series of experiments the influence of different sized Au colloids on the surface plasmon resonance response of a colloidal Au modified Au film was studied by L.A. Lyon *et al.*<sup>44</sup>. Plasmon angle, minimum reflectance and curve breadth were manipulated by the deposition of 30 – 59 nm diameter colloidal Au on the surface of a 47 nm thick Au layer. With larger particle size the p-SPR curve became shallower and broader due to damping (imaginary component of colloid Au) and localized coupling. A similar effect was observed using NPG substrates that were etched for longer times and contained larger gold islands.

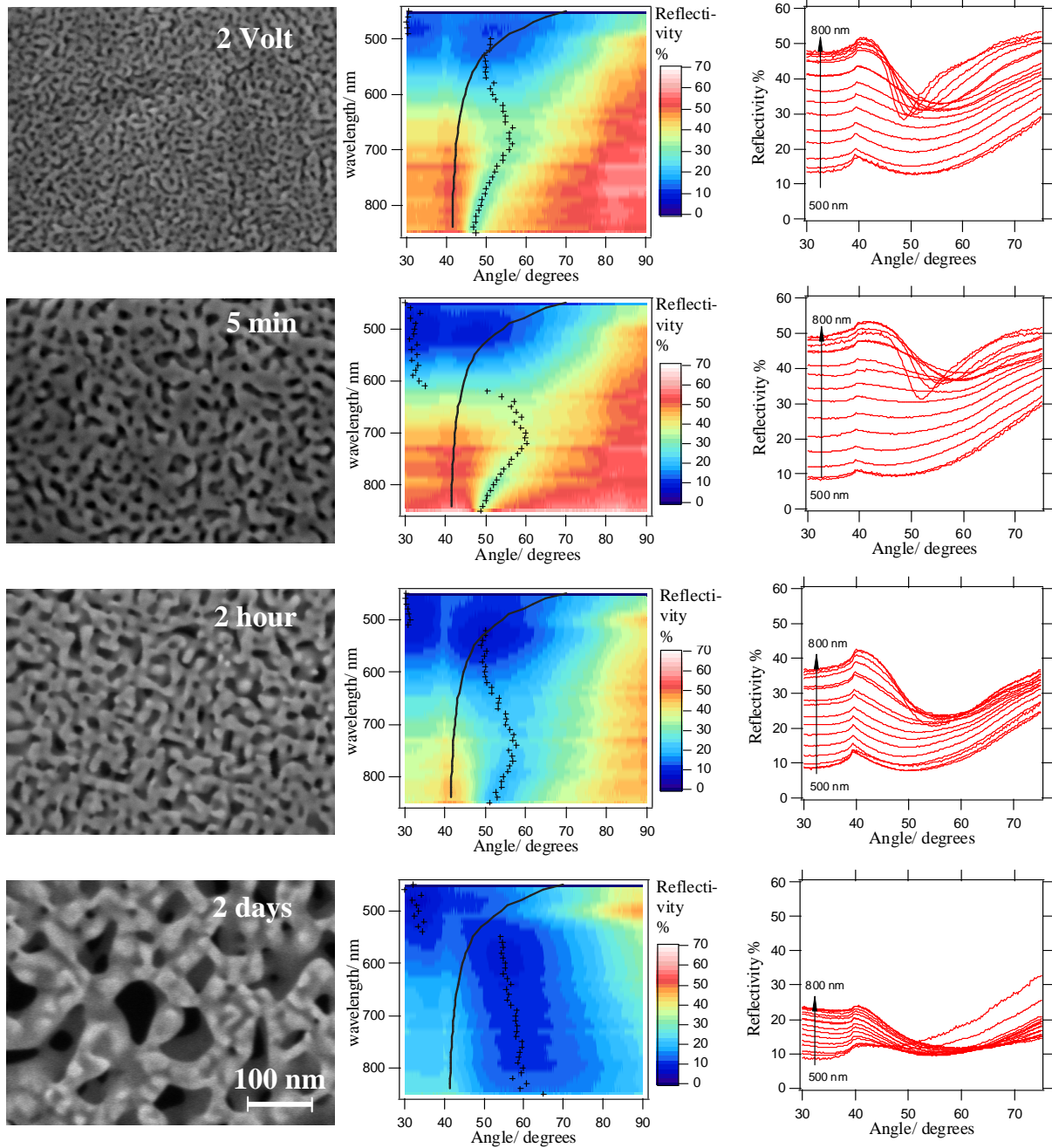


**Figure 4.6.4: SPR excitation on 100 nm thick NPG substrates of different pore sizes; left column: SEM images of the NPG substrates under investigation; middle column: 2D plot of the different excitation wavelengths vs. incident angle. The colors indicate the intensity of the reflected light, while the crosses mark the intensity minima. Additionally the dispersion relation for a flat/dense gold film is shown plotted as a solid line. The measurements were performed in air using a right-angle BK7 glass prism; right column: view of the data in a plot of reflectivity vs. angle of incidence.**

The relation between the energy of a system and its corresponding momentum, here  $1/\lambda$  vs. Theta, is known as the dispersion relation. The crosses in Figure 4.6.4 mark the measured intensity minima for the NPG. Instead of following the dispersion relation of evaporated gold, the NPG show an “S shaped” feature. For larger pore sizes it becomes more and more linear. These minima are thought to be due to localized plasmon resonances, which occur at a fixed excitation wavelength.

### 4.6.1 Multilayer architecture built on NPG and flat gold substrates

Firstly, some simple experiments that typify the p- and l-SPR responses of NPG (15 minute etched) will be described. The NPG with a relatively short dealloying time and consequently small pores was chosen in order to have optimal conditions for p-SPR. Even though the electrochemically etched NPG substrates provide smaller pores and a better coupling, they are more brittle and less easy to work with. The applicability of using p-SPR in NPG for detecting bio-recognition events is demonstrated in Figure 4.6.5 (I) by the extensively-studied interfacial biotin-streptavidin binding system. NPG was first functionalized by a biotinylated self-assembled monolayer (SAM) containing about 10 % biotin functional groups<sup>45</sup>. Then, a streptavidin monolayer was formed via the strong biotin-streptavidin interactions (strongest non covalent interaction known:  $K_a \sim 10^{15} \text{ M}^{-1}$ )<sup>46</sup>. Finally, a biotinylated antibody (IgG) was bound to the streptavidin layer.

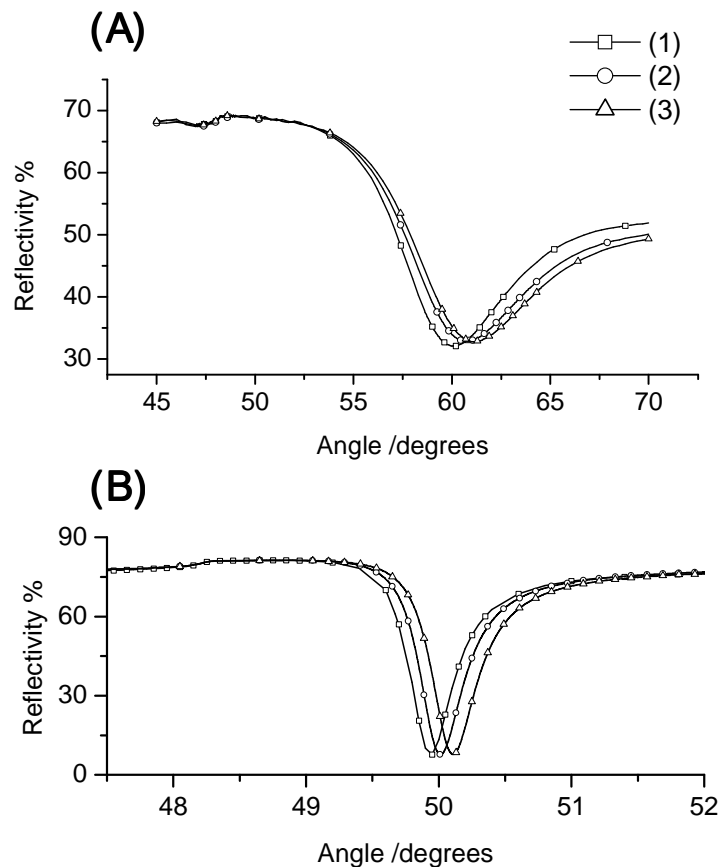
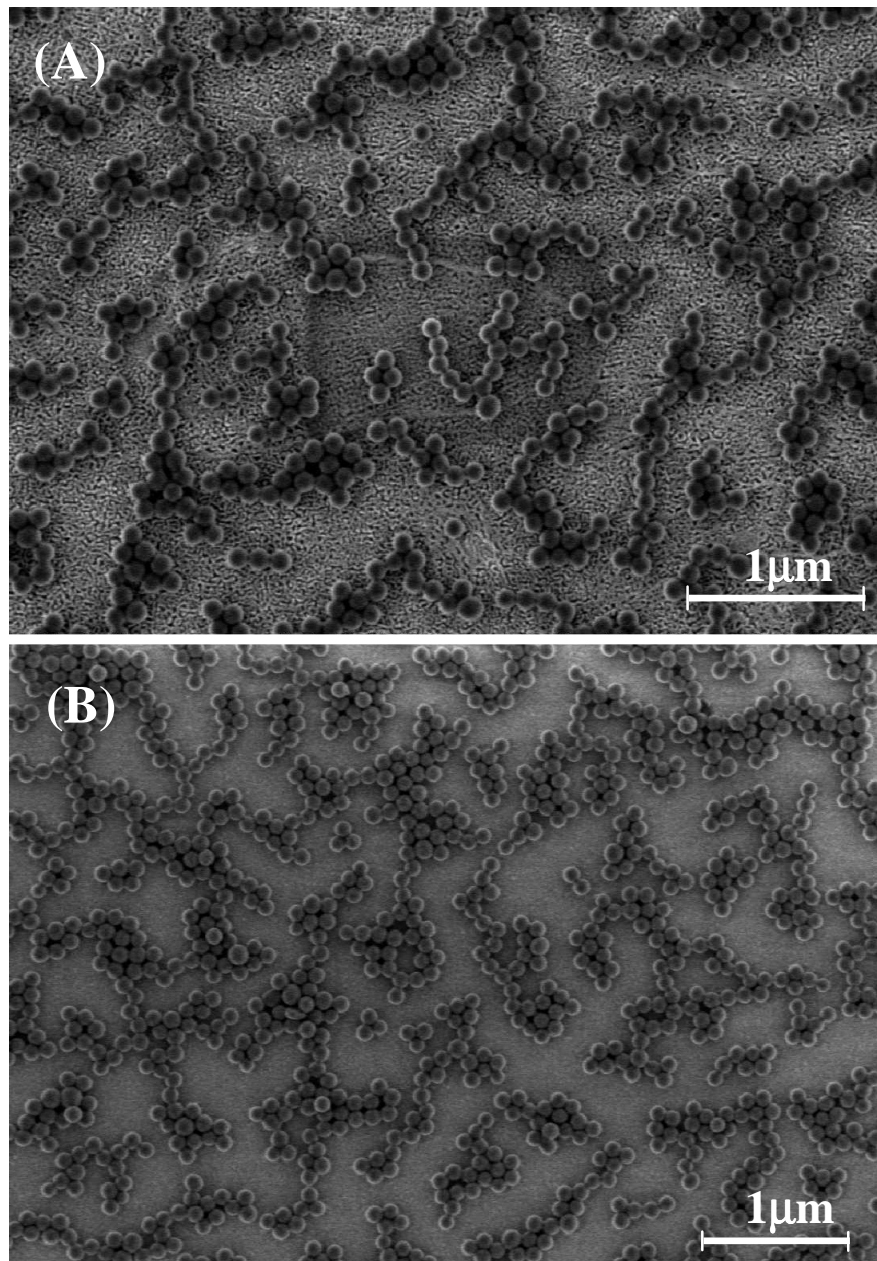
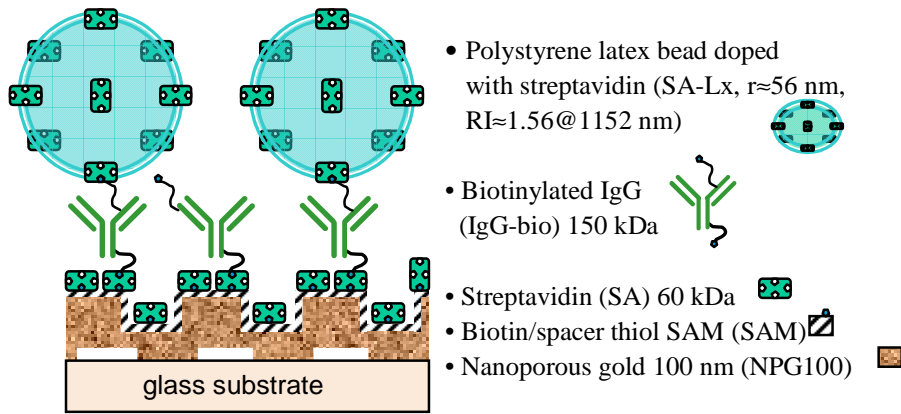


Figure 4.6.5: (I) p-SPR ( $\lambda=1152 \text{ nm}$ ) measurements of streptavidin/biotinylated IgG bindings on biotin SAM modified (A) 100 nm thick NPG membrane and (B) 50 nm evaporated gold film surface, respectively. For both figures, curve (1) is for SAM modified sample, curve (2) for after streptavidin binding, and curve (3) for after biotinylated IgG binding (published<sup>47</sup>, Yu et al. 2006).

In the resulting SPR reflectivity curves, significant shifts of the resonance angle were monitored upon the formation of each biological layer. The same experiment was performed on an evaporated gold film (~ 50 nm in thickness) for comparison. The average pore size of the 15 min etched NPG sample (as determined by top view and cross section SEM) and the molecular sizes of streptavidin and IgG are comparable (~ 15 nm compared to ~ 5 nm and ~ 12 nm, respectively); in fact, the sizes are such that only a limited amount of streptavidin (60 kDa; streptavidin dimension<sup>48</sup> ~  $4.5 \times 4.5 \times 5.2 \text{ nm}^3$ ) should penetrate into the NPG, and it is unlikely that any IgG (150 kDa) penetrates into the pores at all, instead binding should occur only on the top surface of the NPG sample.

The optical fits confirm this hypothesis: assuming that to first approximation the NPG (with and without adsorbates) can be modeled as a smooth metal/dielectric film, Fresnel fits were applied in order to correlate the SPR angular shifts to the optical thickness of the biological layers (refractive indices are all assumed to be 1.45). On the NPG samples (cf. Fig. 4.6.5 (I)(A)), the thickness of the streptavidin and IgG layers were found to be  $70 \pm 4.1 \text{ \AA}$  and  $40 \pm 1.4 \text{ \AA}$ , whereas on flat gold samples (cf. Fig. 4.6.5 (I)(B)) (Table 4.6.2 and 4.6.3), the thickness of streptavidin and IgG became  $34.5 \pm 0.7 \text{ \AA}$  and  $41 \pm 1.7 \text{ \AA}$ . The apparent thicker streptavidin layer on NPG compared to the flat sample suggests some binding *into* the nanopores of the NPG whereas the similar IgG layer thicknesses in the two cases suggest binding *onto* the NPG surface exterior to the pores only. It remains questionable whether the Fresnel equation is perfectly suitable to model the streptavidin binding if this binding might happen inside the NPG layer; i.e., there might be an interpenetration between the virtual “streptavidin layer” and the “NPG layer”. In order to answer this question, rigorous calibration experiments need to be performed using independent instruments, such as FT-IR or QCM.

In order to visualize the surface coverage with scanning electron microscopy an additional layer of polystyrene latex beads doped with streptavidin (SA-LX) [Chapter 3.8, Materials] was deposited on top of the architecture (cf. Figure 4.6.5 (II)). First NPG and flat gold samples were investigated by SPR in air; then buffer was introduced into the flow cell and SPR scans were taken after each layer was deposited (Figure 4.6.6).



**Figure 4.6.5: (II) Multi-layer formation on NPG – a model system:** A schematic representation on which the measurements are based is shown above. One scanning electron micrograph (A) shows the porous structure covered by the latex beads from the perpendicular view. The second SEM image (B) views the polystyrene latex bead coverage for the evaporated gold film.

In buffer a huge minimum shift was observed following the polystyrene latex bead binding. Subsequent to drying the samples, attenuated total reflection scans were recorded once more; and finally, SEM images of the samples were made. So measurements in air were only done for the bare gold surface, the thiolated surface and after the polystyrene latex bead (SA-LX) binding at the end of the experiment (Figure 4.6.7).

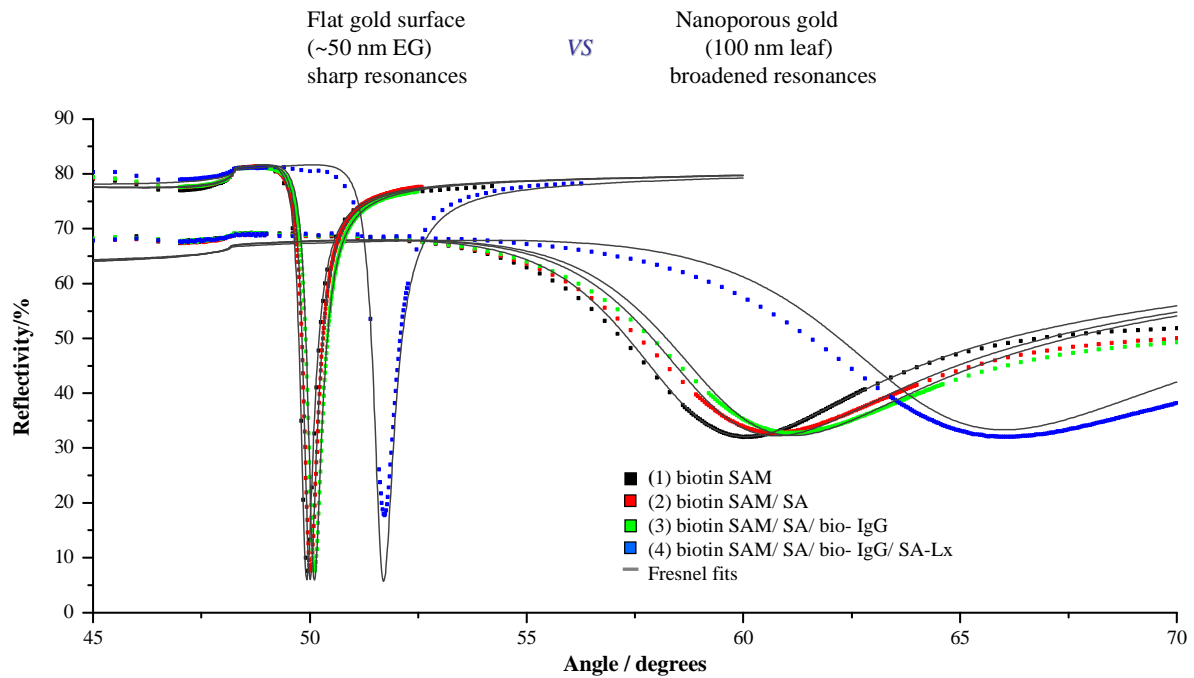


**Figure 4.6.6:** p-SPR ( $\lambda=1152$  nm) measurements in buffer condition monitoring of streptavidin/biotinylated IgG bindings on biotin SAM modified 100 nm thick NPG membrane and 50 nm evaporated gold film surface, respectively [= Figure 4]. Additionally polystyrene latex bead were deposited on top of the supramolecular architecture. For both substrates, curve (1) is for SAM modified sample, curve (2) for after streptavidin binding, curve (3) for after biotinylated IgG binding; and finally curve (4) represents the latex bead binding.

Due to the partial coverage of the latex beads and the large latex particle size -112 nm in diameter - a heterogeneous film was created. For the partially polystyrene latex bead (SA-LX) uncovered area the attenuated total reflection minimum in air appeared at an angle of  $27,9^\circ$ ; for the SA-LX dense covered area at an angle of  $32,8^\circ$ . The value for the combined thickness increase after streptavidin and biotinylated IgG binding (10.2 nm sample 1; 11.6 nm sample 2, Table 4.6.3) resulted from the Fresnel fit of the first minimum after the latex bead binding was measured in air (Figure 4.6.7).

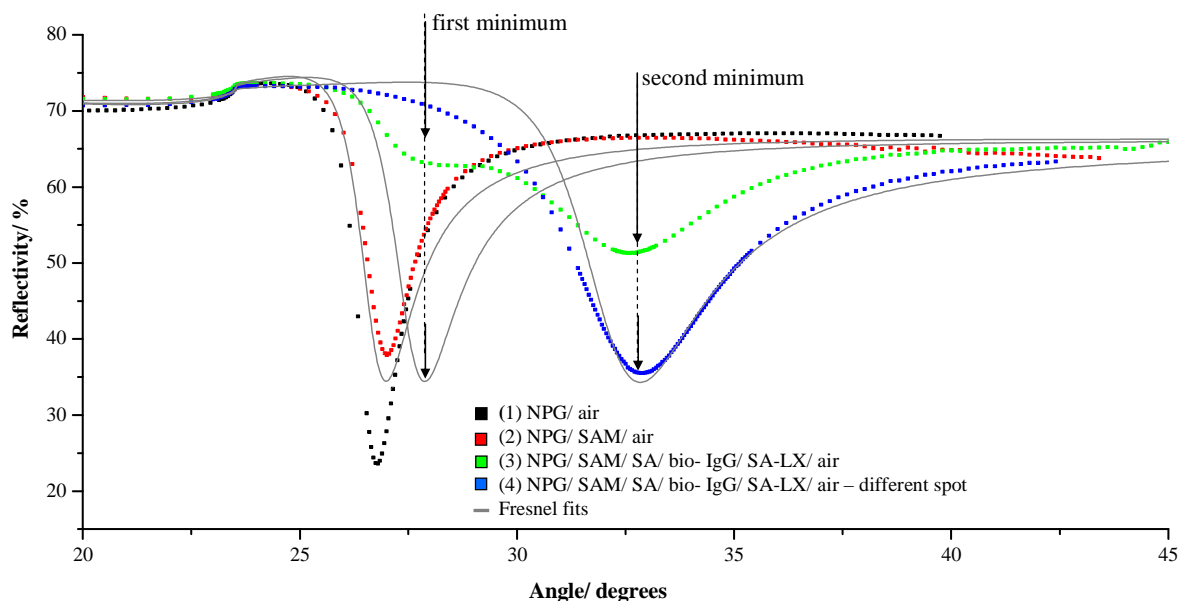


**Figure 4.6.7:** p-SPR ( $\lambda=1152$  nm) measurements on NPG sample in air. Scan curve (1) resulted for the bare gold surface, curve (2) the thiolated surface and after the polystyrene latex bead binding curve (3) is derived. The solid lines stem from the Fresnel simulation. Remarkably after latex bead binding, the curve featured two minima in the attenuated total reflection scan. The first minimum was characteristic for the streptavidin/biotinylated IgG binding, while the second minimum was indicating the optical thickness of the polystyrene latex beads. The two minima were fitted separately by applying Fresnel equation. Curve (4) recorded another spot of the NPG with densely packed SA-LX area.

*Fresnel curve fitting.* For each SPR scan a simulation was run with the software Winspall (version 2.20) based on the Fresnel equations to calculate the optical thickness of each layer deposited. The refractive indices of the materials are summarized in Table 4.6.2.

**Table 4.6.2:** Refractive indices at wavelength of 1152 nm IR laser and a temperature of 25,00°C.

material	n	$\kappa$	$\epsilon'$	$\epsilon''$
LaSFN 9 prism <sup>49</sup>	1.82068	0	3.31487566	0
gold <sup>50</sup>	0.26	7.83	-61.2413	4.0716
nano porous gold	0.3186	3.5	-12.42	2.23
mixed thiol	1.5	0	2.25	0
streptavidin	1.45	0	2.1025	0
IgG	1.45	0	2.1025	0
latex beads	1.56	0	2.4336	0
air <sup>51</sup>	1.000263	0	1.000526	0
water/buffer <sup>52</sup>	1.32359	0	1.75189	0

In order to obtain the SA-LX volume ratio values based on the SPR scans and the Fresnel calculations, the polystyrene latex bead thickness was fixed at 112.0 nm for each sample and the refractive index was the variable parameter ( $n_{\text{average}}$ ). Thus, the volume fraction of polystyrene beads ( $x$ ) was calculated with the following equation, where  $n$  was the refractive index:

$$n_{\text{average}} = n_{\text{water}} \cdot (1-x) + n_{\text{ps}} \cdot x \quad \text{--- 4.7}$$

In order to obtain the volume ratio values based on the SEM images, the total volume of the polystyrene latex beads doped with streptavidin (SA-LX) was calculated by equation 4.8, where  $N$  was the number of the counted beads. The total film thickness was given by equation 4.9, where  $A$  was the area of the SEM image times pixel properties. The radius of the beads was about 56 nm. Finally, the volume ratio  $x$  was obtained by equation 4.10.

$$V_{\text{total spheres}} = (4/3)\pi r^3 \cdot N \quad \text{--- 4.8}$$

$$V_{\text{total film}} = A \cdot 2r \quad \text{--- 4.9}$$

$$V_{\text{spheres fraction}} = V_{\text{total spheres}} / V_{\text{total film}} \quad \text{--- 4.10}$$

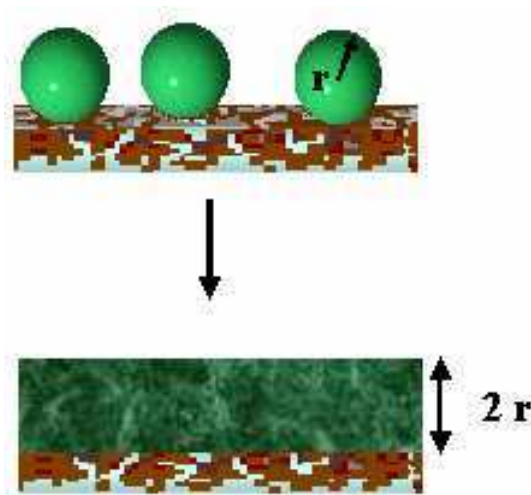


**Figure 4.6.8 (A): Sketch of the polystyrene latex beads deposited on the NPG substrate to calculate the total volume of the spheres and the total volume of a homogeneous film.**

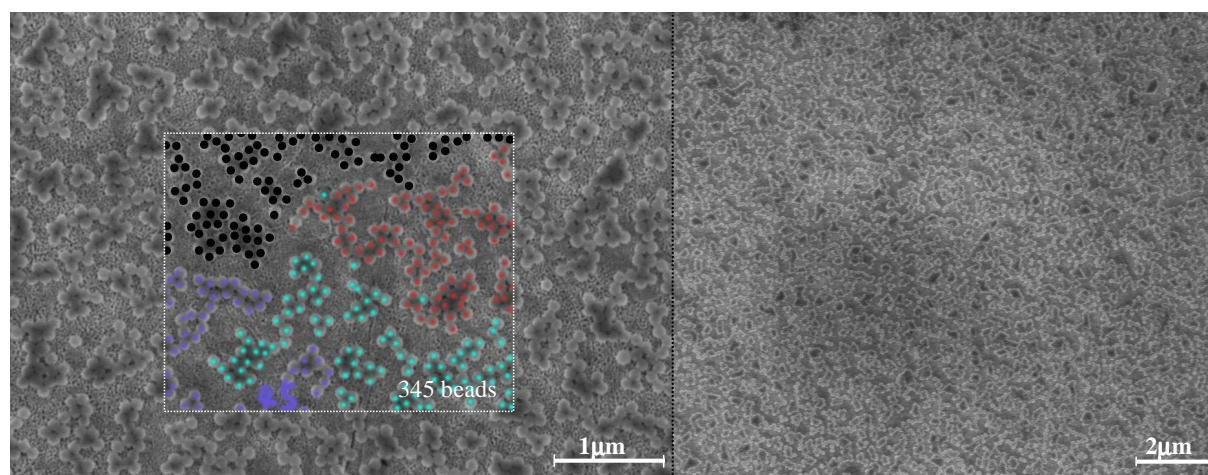


**Figure 4.6.8 (B):** Two authentic scanning electron micrographs at different magnifications show the surface coverage of the latex beads on 15 min etched NPG. On the left side it is demonstrated how the beads were counted to calculate the total volume ( $V_{total}$ ) of the beads. Inside the white frame 345 beads were counted, labelled with randomly chosen colors to avoid counting them twice.

The polystyrene latex beads coverage was found to be  $27 \pm 1\%$  for the NPG and the evaporated gold film (50 nm) calculated using SPR and SEM. Table 4.6.3 summarizes the thicknesses of all the different layers in the multilayer system for two NPG substrates compared to a flat/dense gold sample.

**Table 4.6.3:** p-SPR on NPG (2 substrates shown) and flat gold was demonstrated by a multilayer assembling system involving 112 nm streptavidin doped latex beads. The p-SPR signals were converted via Fresnel fits into the corresponding thicknesses [nm]. The optical thickness found for the latex beads correlated well with the bead density calculated from scanning electron microscope (SEM) images.

	NPG1 in air	NPG1 in solution	SEM (NPG1)	NPG2 in air	NPG2 in solution	SEM (NPG2)	Flat Au in solution	SEM (flat)
SAM (Å)	17.4	-	-	17	-	-	13	-
SA (Å)		73	-		67	-	34	-
IgG-bio (Å)	102	41	-	116	39	-	40	-
SA-LX volume ratio (%)	27	28	29	20	18	21	26.8	26.9

The sequential build-up of this functional supramolecular architecture showed that the diffusion of molecules to the NPG interior was hindered if the pore size was comparable to the molecular dimensions; this “molecular sieve” effect was used to for realizing of size-selective adsorption.

#### 4.6.2 Environmental refractive index changes to NPG (glycerol test)

In order to examine the sensitivity of I-SPR on NPG to environmental refractive index changes, the refractive index (RI) of the dielectric volume was adjusted within the pores of the NPG by filling them with aqueous solutions of glycerol, and then examine the I-SPR response via changes in the visible light absorption spectrum. Representative reflection absorption spectra are shown in Figure 4.6.9, collected using the fiber-optic spectrometer. It is seen that, even with 5 % glycerol, corresponding only to an  $\sim 0.5$  % change in RI, an absorbance peak centered at  $\lambda = 590 - 600$  nm was detected. As the glycerol concentration/medium RI was increased, this peak became more pronounced. Overall, a linear increase in the peak absorbance value and a slight red-shift of the peak wavelength was seen (Figure 4.6.10). This observation agrees with those of Dahlin<sup>42</sup> et al., who examined I-SPR in gold films decorated with nanometric holes made by colloidal lithography.

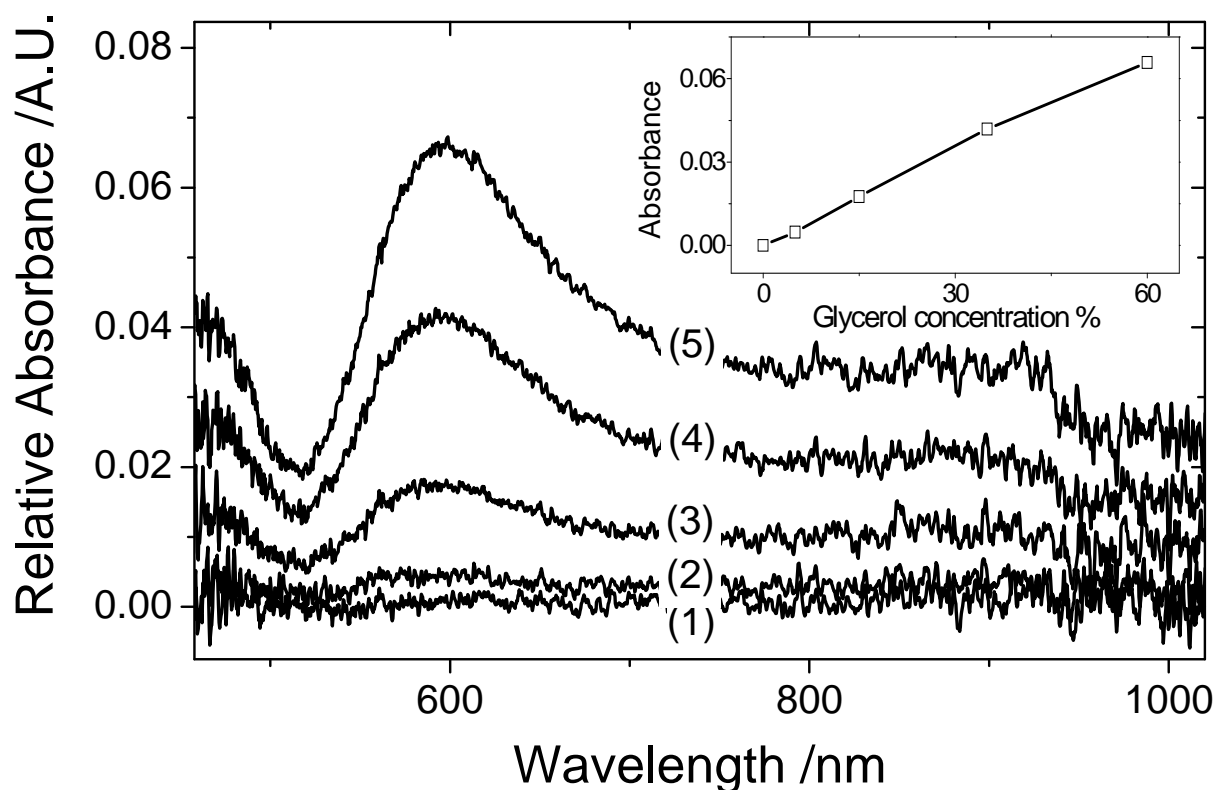
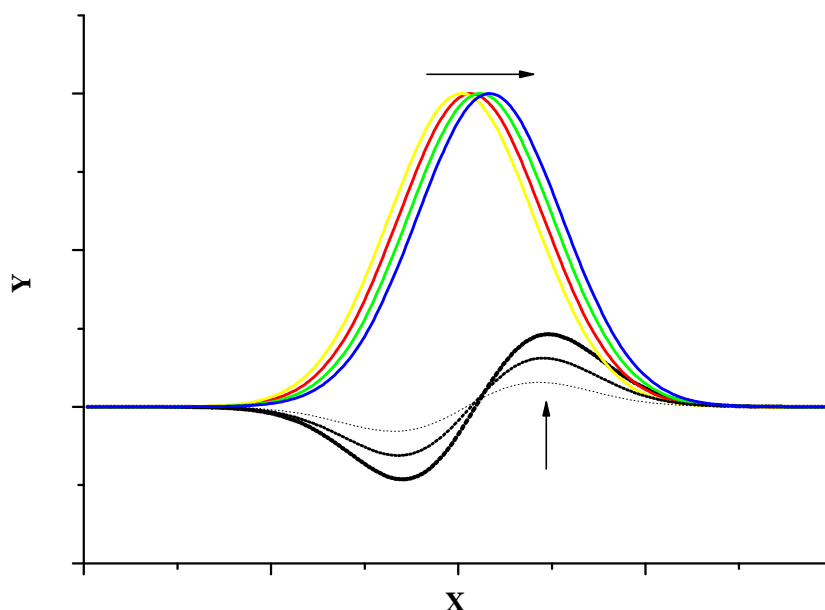


Figure 4.6.9: Evolution of the relative reflection absorbance spectrum of a 100 nm thick, 15 min etched NPG membrane (the reference sample is: NPG in pure water) immersed in solutions of increasing glycerol concentration: (1) pure water, RI=1.333, (2) 5 % RI=1.339, (3) 15 % RI=1.352, (4) 35 % RI=1.378, (5) 60 % RI=1.413; the RI of the glycerol solutions are calculated by the mass fraction of glycerol in water. The inset shows a linear relationship between the glycerol concentration and the intensity of absorbance peak at  $\lambda = 600$  nm (published<sup>47</sup>, Yu et al. 2006).



**Figure 4.6.10:** Explanation of the absorbance results. The four solid lines represent Gaussian curves that were simply shifted to higher x-values. The three dotted lines resulted if the Gaussian curves were subtracted from the first Gaussian curve, respectively.

The increase in intensity with only a slight red shift for all the absorbance curves measured in reflection mode can be explained mathematically. Therefore, a plot was generated by the software Igor Pro (version 5.02) that represents Gaussian curves (Figure 4.6.10). These curves were simply shifted to higher x-values. Then, the curves were subtracted from the first Gaussian curve, respectively. The dotted lines resultant of the subtraction, simulate the measured absorbance spectra. But the left parts of the dotted lines were not seen in the measured absorbance spectra due to the noise of the lamp spectrum. The NPG samples soaked in water/aqueous buffer solution served as reference and comply with the yellow solid line.

Further refractive index studies on different samples were carried out using the same optical setup. The refractive index change was experimentally compared for a series of the NPG substrates possessing different pore sizes to an evaporated flat gold film. After injecting various glycerol concentrations the flat/dense gold showed only a limited absorbance at small excitation wavelength ( $\sim 400 - 550$  nm) near the noise range of the white lamp serving as the excitation source (Figure 4.6.11 (A)). This absorbance was also seen even more pronounced in all the other samples of the experimental series (Figure 4.6.11 (B - D)), which still lack a satisfying explanation. Additionally, for all the NPG samples flushed with a 5 % glycerol solution that permeates into the pores an effective change in the absorbance spectrum ( $\sim 530 - 800$  nm) was derived. Exposure to higher glycerol concentrations caused an obvious increase in the peak intensity and a slight red shift of the peak position ( $\lambda_{\text{peak}}$  shift), which is additional evidence for the excitation of l-SPR.

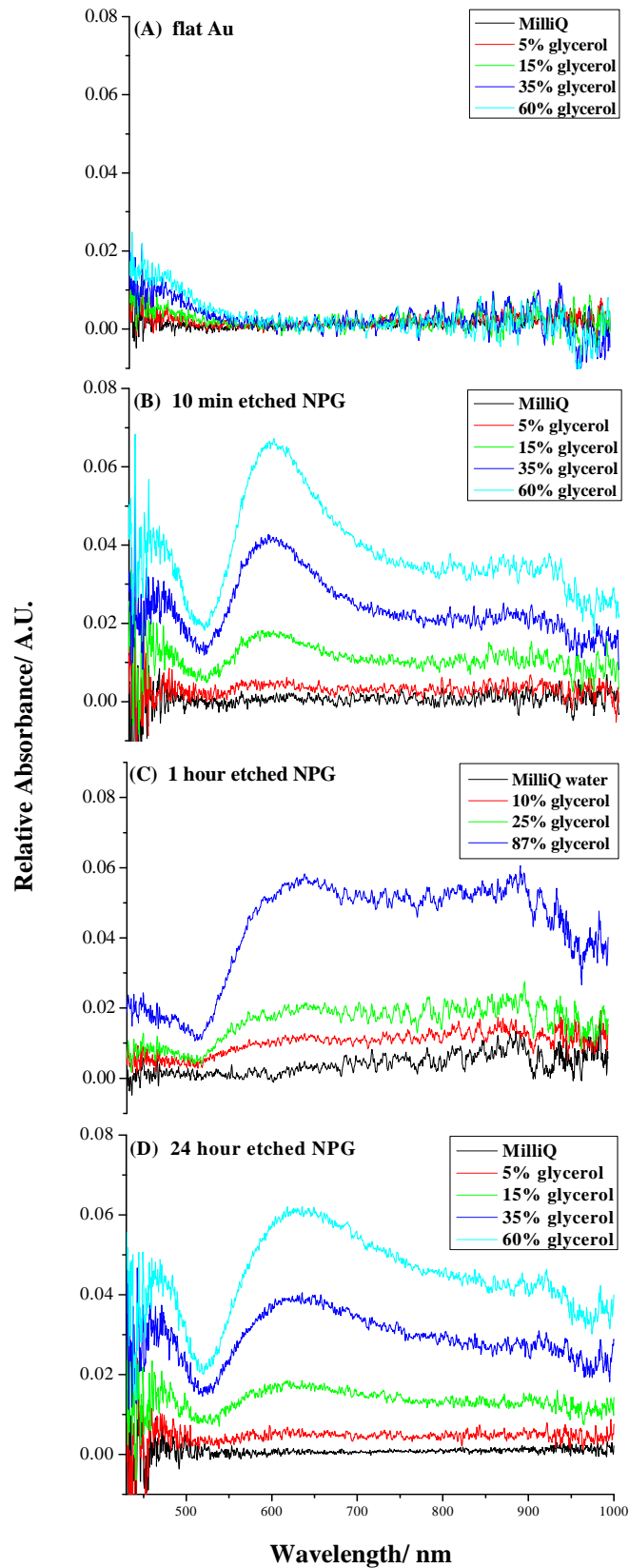
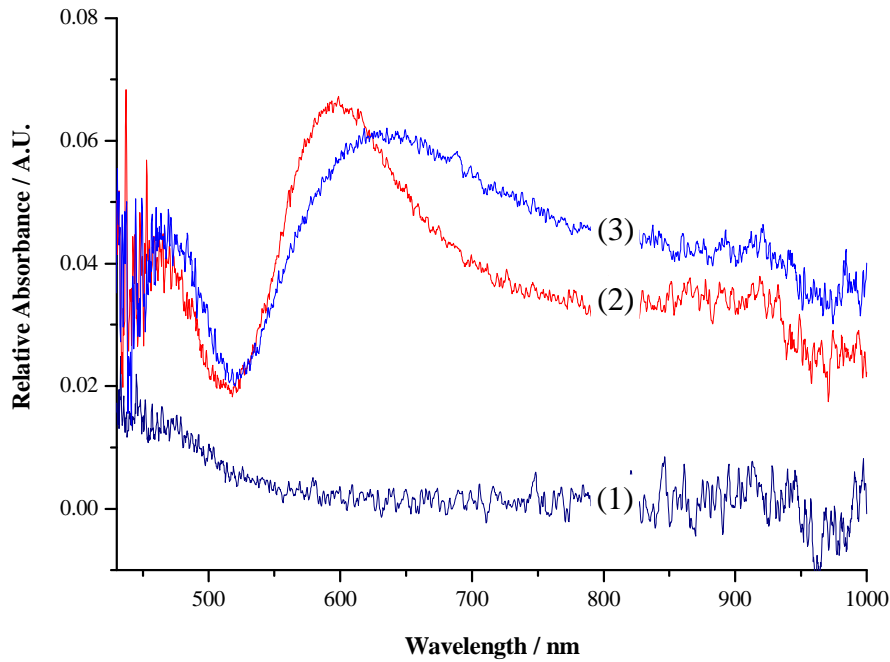


Figure 4.6.11: Exposure of different gold substrates to increasing glycerol concentrations: The response of a flat evaporated gold film (A), a 10 minutes dealloyed NPG (B), an one hour dealloyed NPG (C) and a 24 hours dealloyed NPG membrane (D), respectively was monitored by the optical fiber spectrometer.

The peak wavelength was slightly higher for NPG 24h ( $\lambda = 630$  nm) than for NPG 10 min ( $\lambda = 597$  nm) due to the larger nano-sized features in NPG 24 h. With pore size increase of the NPG membranes a general red shift of the peak position ( $\lambda_{\text{peak}}$  shift) (Figure 4.6.12) in the absorbance spectra for all the glycerol concentrations was observed.



**Figure 4.6.12: Evolution of the relative reflection absorbance spectrum of different samples exposed to a 60 % glycerol concentration: (1) flat/dense gold film, (2) 10 min and (3) 24 hours dealloyed NPG membrane soaked in 60 % glycerol solution.**

### 4.6.3 Layer by layer (LbL) deposition of charged dendrimers

Simultaneous p-SPR and I-SPR was used to monitor the stepwise variation of the dielectric environment within the pores of NPG (15 min etched) created by using a layer-by-layer (LbL) system based on charged dendrimers (cationic  $[G_4(NH^+Et_2Cl)_{96}]$  and anionic  $[G_4(CH-COO^-Na^+)_{96}]$ )<sup>53</sup> (see Figure 4.6.13 and 4.6.14). This LbL system was particularly interesting for the NPG experiments because it has been shown<sup>54</sup> that the layer build-up is highly uniform and regular with excellent penetration leading to good coverage even of the inner walls of deep nanopores. Here, NPG leafs bonded to LaSFN9 slides were first functionalized by 3-mercaptopropionic acid (MPA thiol) to generate a negatively charged surface on which the first cationic layer adsorbs. The consecutive repetition of anionic/cationic dendrimer deposition should lead to the stepwise formation of a multilayer coating inside the pores of NPG until the pores get clogged; at this point, the multilayer should continue growing only outside the NPG membrane extending the overall thickness of the film.

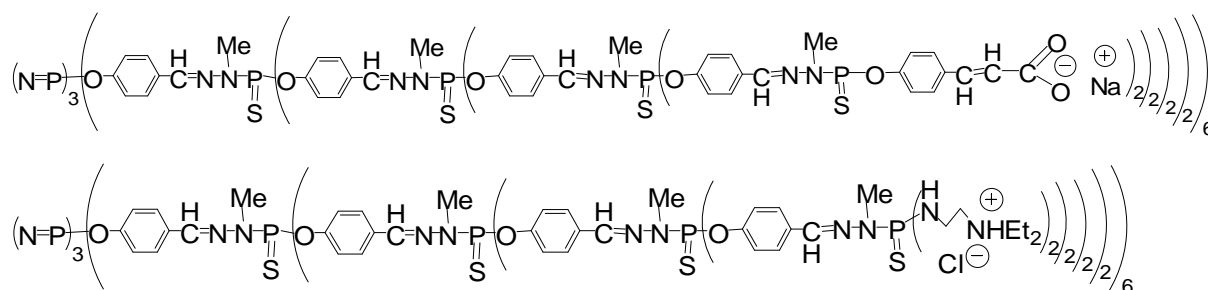


**Figure 4.6.13: Molecular structures of the charged dendrimers used in this study: (Up)  $G_4(CH-COO^-Na^+)_{96}$ ; (Down)  $G_4(NH^+Et_2Cl)_{96}$ . These N,N disubstituted hydrazine phosphorus - containing dendrimers of the 4th generation comprise 96 functional groups at the surface<sup>53, 55, 56</sup>. The molecular masses are  $M=33.702g\cdot mol^{-1}$  for  $G_4^+$  and  $M=34.819g\cdot mol^{-1}$  for  $G_4^-$ .**

Optically, the multilayer dendrimer evolution was accompanied by a very regular shift of the resonance angle of the p-SPR excitation, as shown in Figure 4.6.15 (A). Fresnel's equations were again used to fit the p-SPR curves. After establishing the first p-SPR fit, the geometrical thickness of dendrimer layers was determined from the shift of the resonance angle by assuming a refractive index of 1.5 for the dendrimer. The thickness increment per deposited double layer was calculated to be 2.2 nm, which is unexpectedly identical to the value of  $2.2 \pm 0.3$  nm obtained by a previous study of the same dendrimer multilayer system deposited on flat, dense, gold samples<sup>54</sup>. Taking into account the enhanced surface area of NPG (shown by the streptavidin binding result), this result indicates a slightly smaller dendrimer coverage per layer on the NPG surface, which may suggest that electrostatically driven binding can be biased inside nanopores.

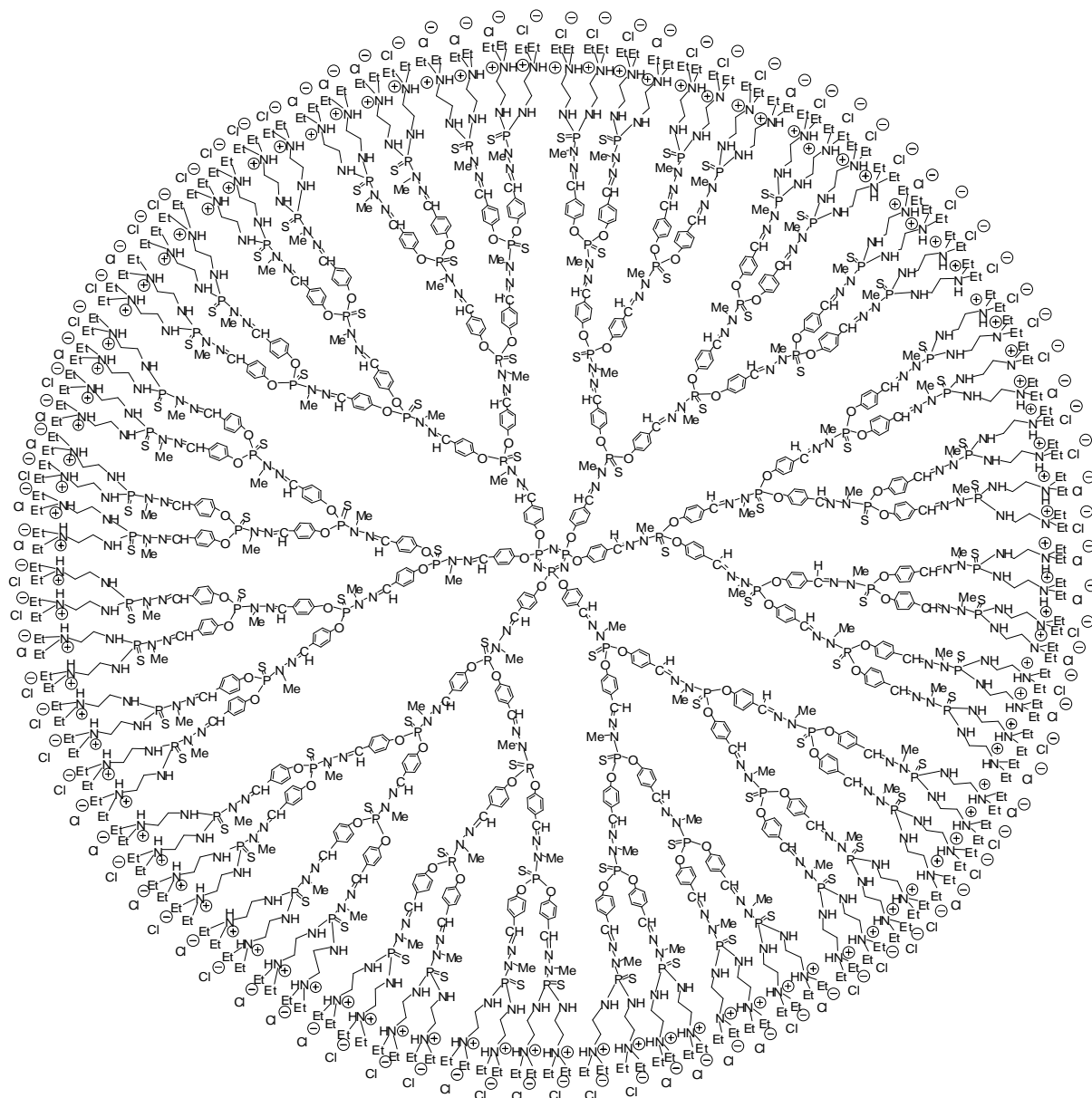


**Figure 4.6.14:** Picture of the dendrimer molecule  $G_4(\text{NH}^+\text{Et}_2\text{Cl})_{96}$  showing all the 96 functional groups.

On the other hand, it was observed that the SPR minimum reflectivity for NPG slightly increased (Figure 4.6.15 (A)) as the multilayer grew in thickness whereas it remained constant for flat/dense gold. This observation suggests the penetration of the initial dendrimer layers into the NPG in such a way that the effective dielectric constants of the NPG/dendrimer membrane was altered, becoming lossier to the incident light. As mentioned before, this might cause a deviation in the Fresnel modeling and needs further consideration.

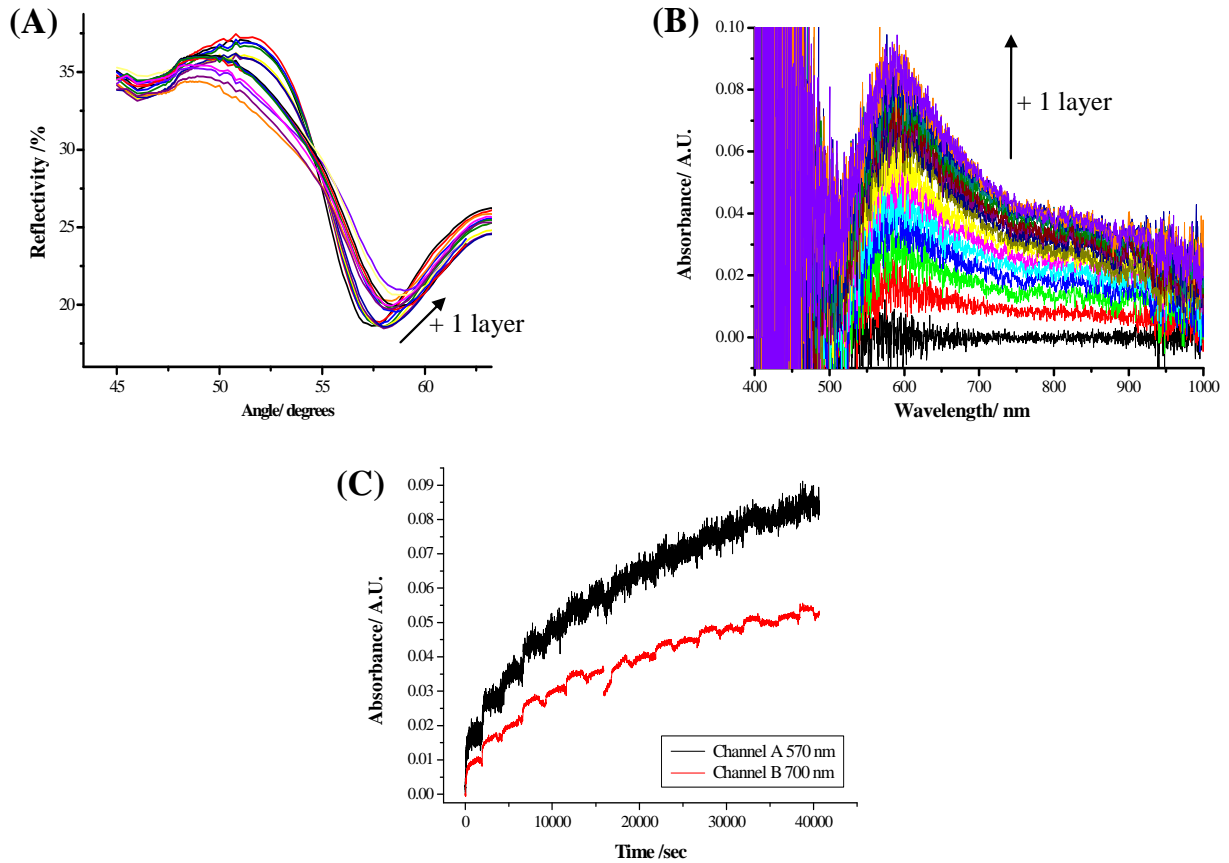


Figure 4.6.15: Simultaneous monitoring of p-SPR and I-SPR on NPG (15 min dealloyed) during the formation of dendrimer multilayers: (A) SPR raw data; (B) original absorbance spectra taken at the same time as the SPR scans. (C) Kinetic measurement recorded at  $\lambda = 570$  nm and  $\lambda = 700$  nm. The SPR minimum reflectivity increased during the dendrimer deposition and constantly shifted to higher angles, while the absorbance spectra showed a peak intensity increase at  $\lambda = 600$  nm.

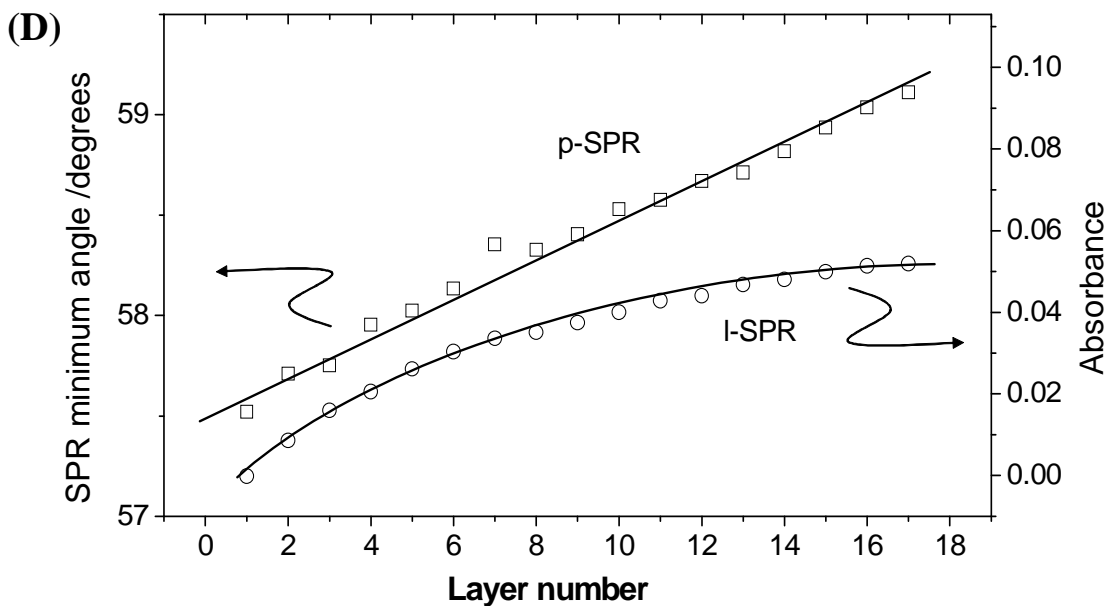
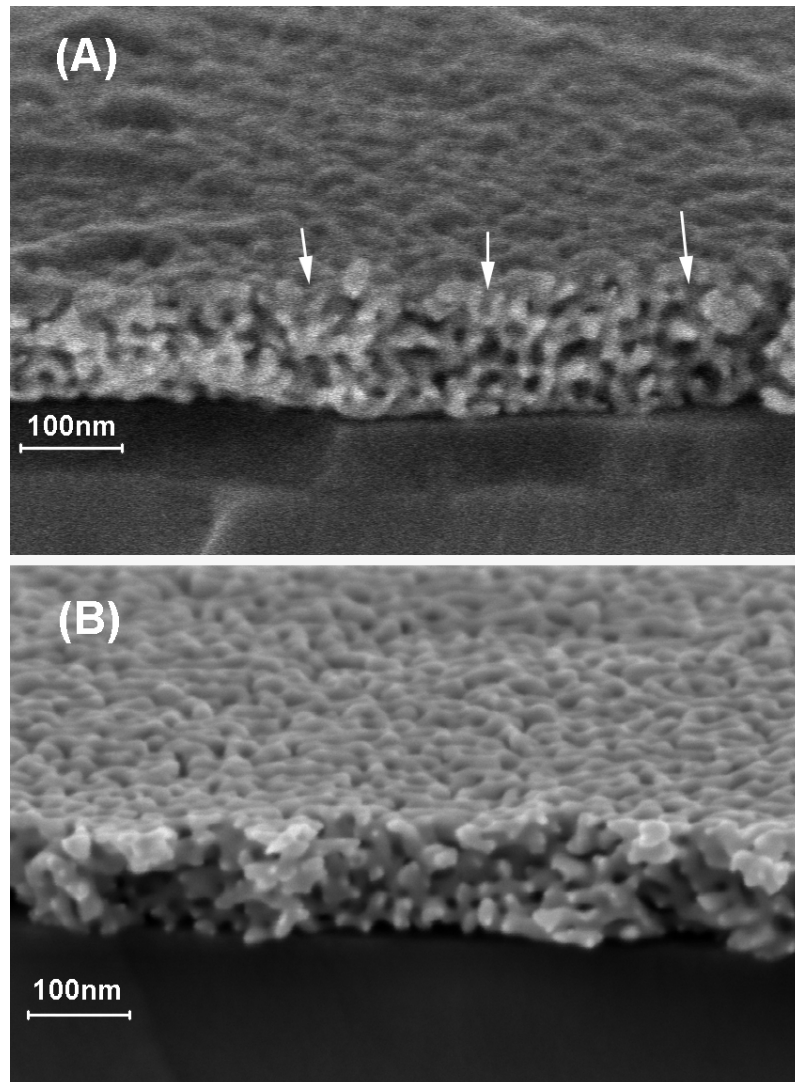


Figure 4.6.15 (D): Simultaneous monitoring of p-SPR and I-SPR on NPG (15 min dealloyed) during the formation of dendrimer multilayers. The solid lines represent the trend of the signal as the layers grow. The first layer is a self-assembled monolayer (see text for details). The reference sample for I-SPR measurement is the SAM modified NPG in pure water (published<sup>47</sup>, Yu et al. 2006).

The SEM micrographs (Figure 4.6.16) of dendrimer – deposited NPG support the p-SPR results by showing that the dendrimer layers grow by simply following the profile of the NPG surface. Even after the deposition of 16 dendrimer layers (nominally filling the pores), the nanosized features of NPG are still pronounced. In this case, the thickness variation between dendrimer layers was expected to be regular, if not constant, with the result that if the pores do clog, the p-SPR signal will not change in any dramatic way.



**Figure 4.6.16:** SEM images of a nanoporous gold membrane - 15 min etched (A) after (and (B) before LbL deposition of 8 double layers of dendrimers. White arrows in (A) indicate pores on the geometric exterior surface that were obviously clogged by dendrimer (published<sup>47</sup>, Yu et al. 2006).

Although the p-SPR minimum shifted linearly with the increasing number of dendrimer layers, the I-SPR signal weakened and eventually saturated after ~ 8 double layers. By this number of layers, dendrimers are no longer depositing *in* the pores, but are clogging them so that further layers are only deposited *on* top of the geometric surface of the NPG

membrane. This is consistent with the scanning electron microscope (SEM) observations shown in Figure 4.6.16 where one sees that at  $\sim 8$  double layers deposited, the pores directly opening to the interface are filled with dendrimers whereas those indirectly connected pores appear empty. Saturation at  $\sim 8$  double layers ( $\sim 17$  nm) is in excellent agreement with the geometric constraint associated with a  $\sim 15$  nm pore size.

The smooth saturation of the l-SPR excitation is understandable by noting that the evanescent electric field of the l-SPR mode decays quickly moving away from the metal-dielectric interface and an l-SPR response (here, the increasing of absorbance peak intensity at  $\lambda = 600$  nm (Figure 15B)) should be only observed when dendrimer layers are being deposited within this field. Thus, if the pores are clogged and the surface multilayer is thicker than evanescent electric field, the l-SPR response should remain unchanged, as observed.

A similar distance dependency has been reported by Van Duyne's group<sup>40, 41</sup>, who monitored the l-SPR spectrum evolution while depositing multiple self-assembled monolayers or  $\text{Al}_2\text{O}_3$  monolayers on triangular silver nanoparticles (NPs). By solving Maxwell's equations for light interacting with an arbitrary shape/composition NP using a finite element calculation, they showed that the  $1/e$  decay length  $l_d$  of the electrical field near the NP is around 5 – 15 nm (1 – 3 % of the light's wavelength, depending on NP's shape, size and composition). This contrasts dramatically with the 200 – 300 nm decay length (20 – 25 % of the light's wavelength) of the evanescent field of a p-SPR excitation, and indicates a much sharper distance-dependence of l-SPR sensors. Due to the lack of a 'regular' nanostructure in NPG, we can not perform a similar calculation and can only provide qualitative descriptions. An exponential fit of the l-SPR curve yields a decay length  $l_d = 12.3$  nm, which falls into the theoretical range. But the l-SPR field distribution is extremely heterogeneous and usually is the strongest at sharp turns or corners. Therefore, clogging of the nanopores may reduce the sensitivity of l-SPR to the dendrimer layer, hastening the saturation of the l-SPR signal, and leading to an underestimation of the value of  $l_d$ .

#### **4.6.4 Layer by layer (LbL) deposition of avidin and antiavidin**

A different LbL assembly system<sup>57</sup> was employed here to alter the interfacial refractive index in a fast pace. The use of biotinylated anti-avidin IgG and avidin (Figure 4.6.17; Chapter 3.8) formed a mutual recognition system and greatly enhanced the thickness of each double layer (~ 9.3 nm with the assumed refractive index of 1.45). This fast-growing LbL system has been studied extensively in our group by Liu<sup>58</sup> and Christensen<sup>59</sup>.

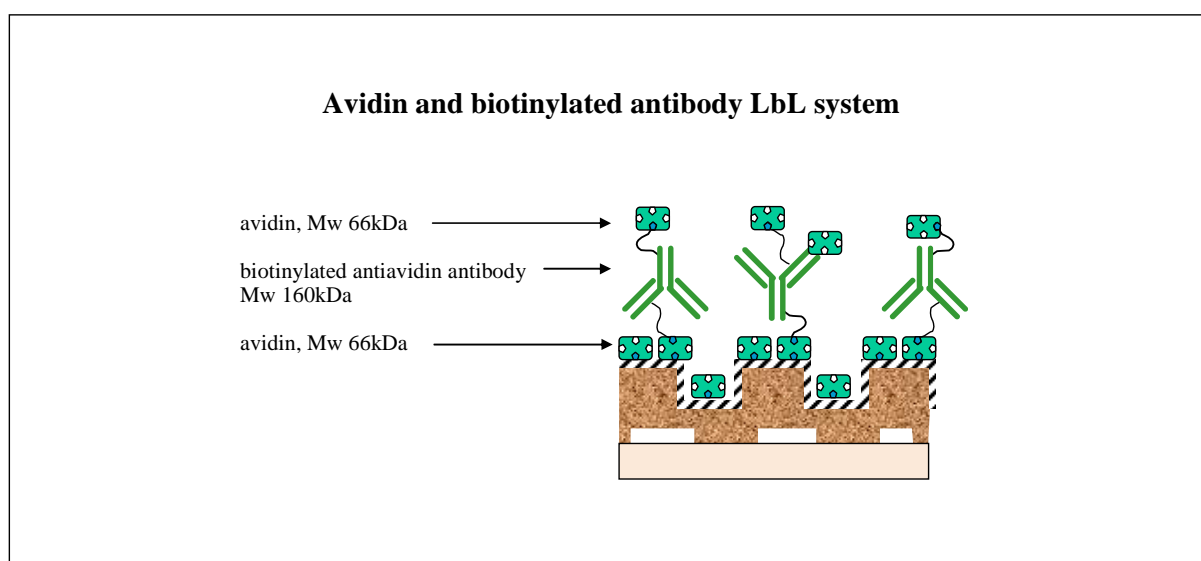


**Figure 4.6.17:** A schematic representation of the layer-by-layer assembly of multilayer films composed of avidin and biotinylated antiavidin antibody on NPG substrate.

A gold (nanoporous or evaporated) film was first functionalized by a biotinylated SAM containing ~ 10 % functional biotin groups. Then avidin/ biotinylated anti-avidin IgG solution (both 1  $\mu\text{M}$  in PBS buffer with 0.01 % (w/t) Tween-20<sup>R</sup>) were alternated in the flow cell, leading to the stepwise formation of an avidin/ anti-avidin multilayer. The use of biotinylated anti-avidin IgG significantly enhances the recognition probability to avidin and accelerates the layer thickness increase.

Phosphate buffered saline (PBS) with 0.01 % (w/t) Tween-20<sup>R</sup> was used as solvent for all the sample solutions. For each layer-forming step the binding was monitored kinetically and terminated by a PBS buffer rinse when equilibrium was reached.

In comparison to the LBL system, which involved oppositely charged dendrimers with molecular weight of ~ 35 kDa, the current system had a molecular size that can cause dramatically different binding pattern on NPG substrates with different pore sizes. As shown in the SEM pictures (cf. Figure 4.6.18), the protein layers on NPG 5 min had a distinctive

divide line to the NPG film, meaning the proteins were mostly binding *onto* the NPG. Whereas in the NPG 24 h image, it was hard to tell where the protein layer started which clearly indicated a “binding-into” mechanism.

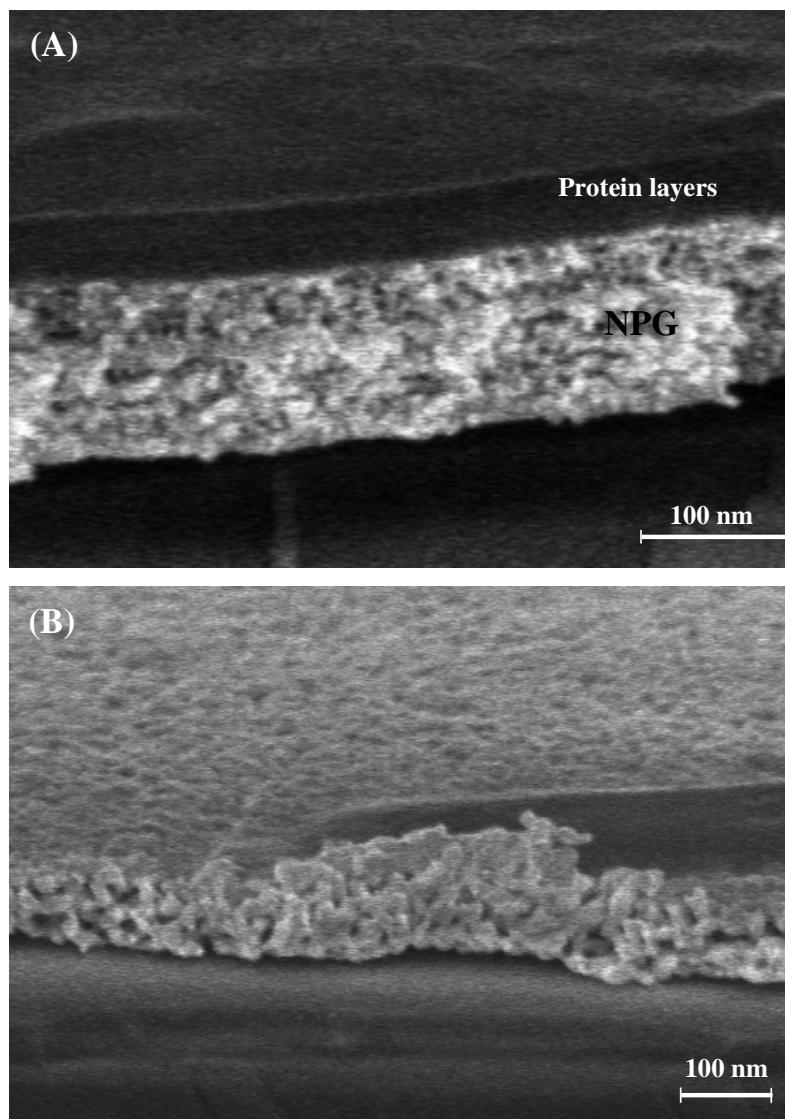


**Figure 4.6.18:** SEM images of a nanoporous gold membrane - 5 min etched NPG (A) after LbL deposition of 18 double layers of avidin/biotinylated anti-avidin. The proteins were binding mostly *onto* the NPG. 24 h etched NPG (B) after deposition of 11 double layers of avidin/biotinylated anti-avidin, which were binding *into* the NPG pores.

The SEM observation was confirmed by the I-SPR results. For clarity, only the deposition of up to 3.5 double layers is shown (cf. Figure 4.6.19). On the EG surface, there was a growing peak between 430 – 600 nm. This turned out to be a typical reflection interference phenomenon caused by the deposited dielectric layer, as manifested by the later periodical oscillation in reflectivity as the protein layer grew. Similar interference patterns were observed on NPG 5 min (Figure 4.6.20). The seemingly larger modulation in the NPG

curves was simply due to the fact that the reflectivity  $I_{ref}$  for bare NPG was smaller than for bare EG. In NPG 24 h curves, not only the similar interference pattern was seen, but also a distinctive peak at 625 nm, exactly matching its peak induced by glycerol irrigation (4.6.11 D). In contrast, the curves of NPG 5 min sample were free of any peak at the characteristic wavelength – 590 nm. This observation was in agreement with the SEM image that only proteins binding *into* the nano-pores could modify the dielectric environment and thus altered the I-SPR signal. The fast saturation of the I-SPR signal was also in agreement with the fact that the I-SPR had very short evanescent decay ( $\sim 10 - 20$  nm).

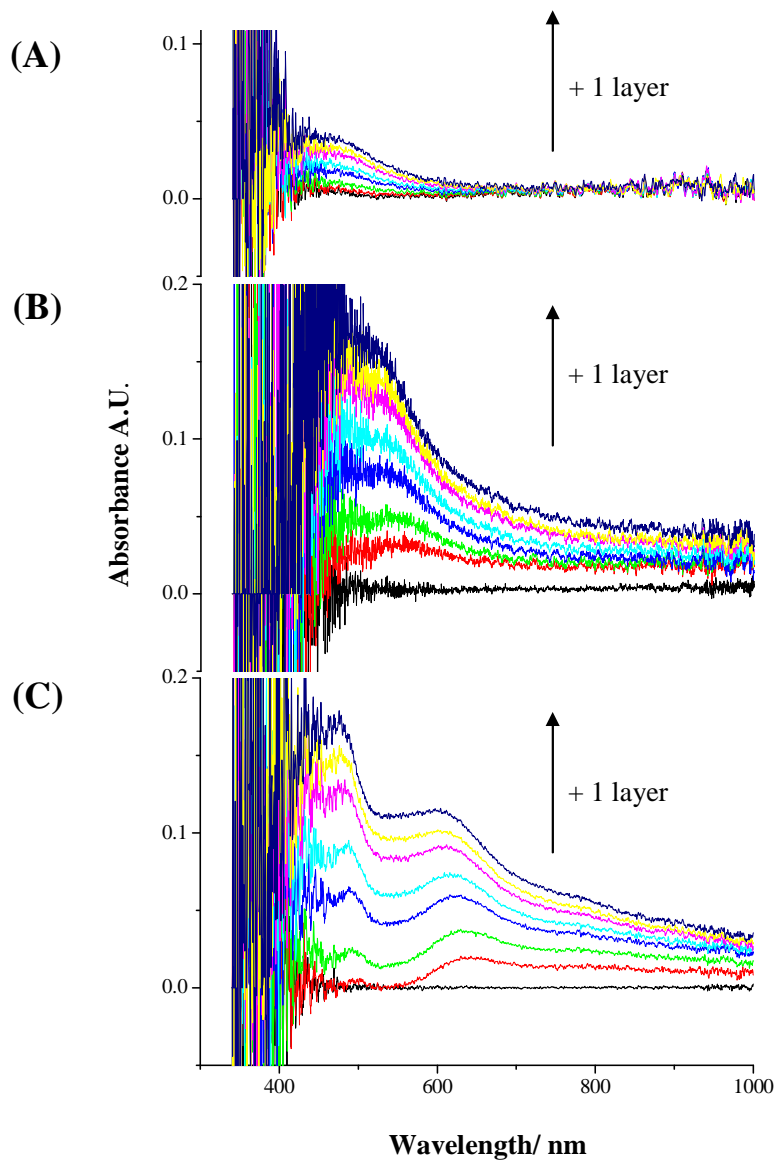


**Figure 4.6.19:** Evolution of the relative reflection absorbance spectra of different samples after 3.5 protein double layer depositing process: (A) flat/dense gold film (EG evaporated gold), (B) 5 min and (C) 24 hours dealloyed NPG membrane. The gold (evaporated or nanoporous) film was first functionalized by a biotinylated self assembled monolayer containing  $\sim 10\%$  functional biotin groups. Then, an avidin layer was formed followed by a biotinylated antiavidin antibody layer. Subsequently 7 layers were deposited, alternately avidin and antibody.

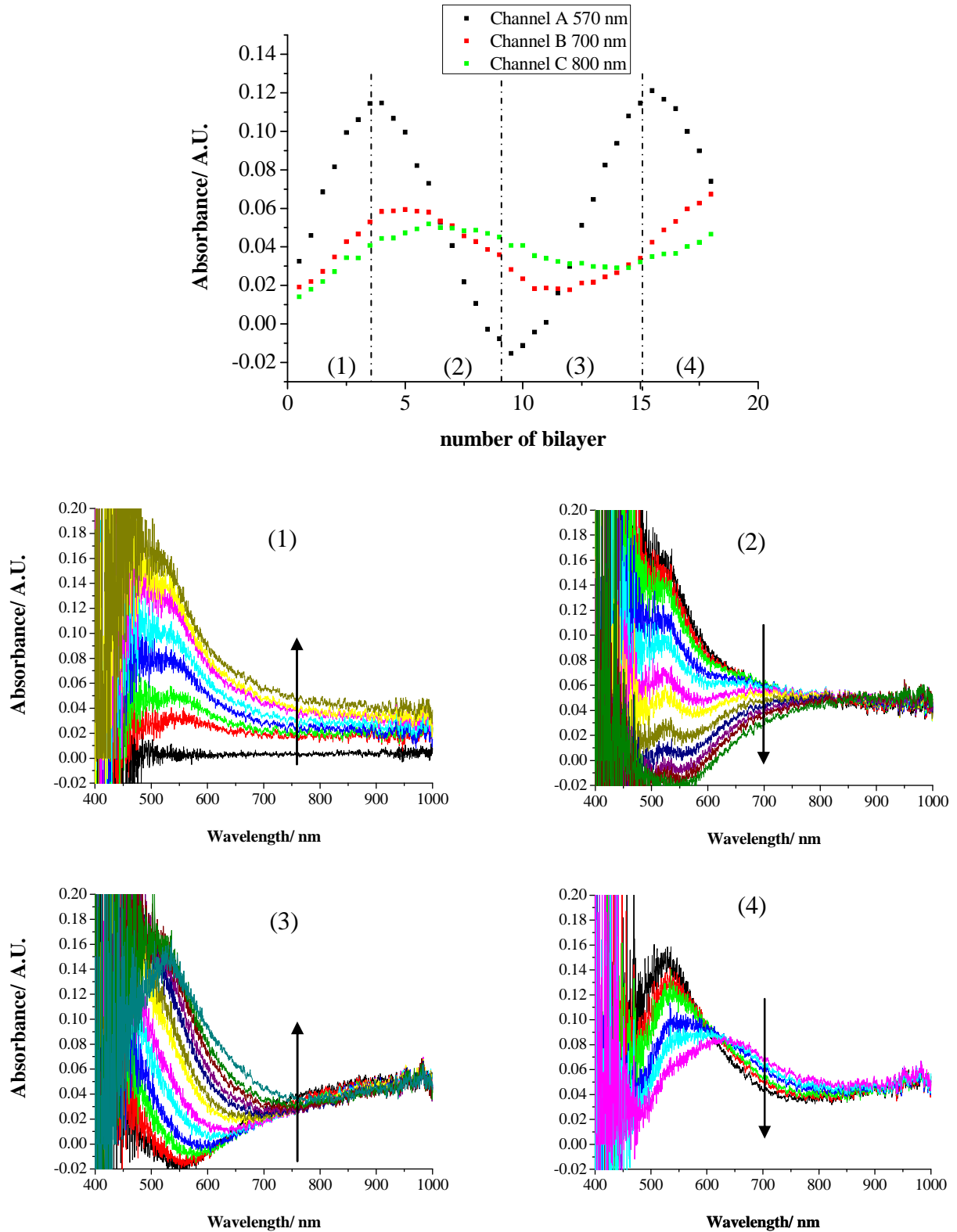


**Figure 4.6.20: Evolution of the relative reflection absorbance spectra of 5 min etched NPG sample after 18 protein double layer depositing process. The NPG was first functionalized by a biotinylated self assembled monolayer containing ~10 % functional biotin groups. Then, an avidin layer was formed followed by a biotinylated antiavidin antibody layer. Subsequently 36 layers were deposited, alternately avidin and antibody. In the kinetic measurement, the change in absorbance was recorded for three selected wavelength (570 nm, 700 nm and 800nm). For clarity, the complete double layer depositing process is shown separately in four graphs for all the measured layer wavelength: (1) first 3.5 double layer (2) next 5.5 double layer (3) following 6 double layer (4) 3 double layer deposition.**

The interference pattern observed for the 5 min etched NPG might be described as the interference of the light waves that were reflected off the protein covered surface and the gold surface, respectively (Figure 4.6.21):

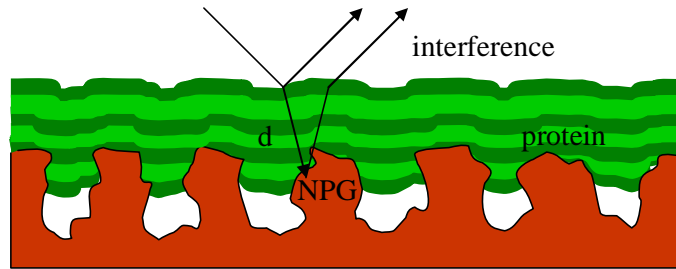


**Figure 4.6.21: Scheme of the interference of light due to the protein layers.**

The difference in the optical route of the light can be calculated as:

$$\Delta x = 2 \cdot d \cdot n \quad \text{--- 4.11}$$

while the optical interference was expressed in:

$$I = I_0 + I_1 \sin\left(\frac{2\pi\Delta x}{\lambda_0} + \varphi_0\right) \quad \text{--- 4.12}$$

An assumption was made,

$$\Delta d = d_B m \quad \text{--- 4.13}$$

where  $m$  was the number of bilayers and  $d_B$  was the thickness of a single bilayer. The refractive index of  $n = 1.45$  for the proteins is based on an assumption as well. Finally, equation 4.14 resulted:

$$I = I_0 + I_1 \sin\left(\frac{2\pi}{\lambda_0} \cdot 2 \cdot n \cdot d_B m + \varphi_0\right) \quad \text{--- 4.14}$$

The periodical oscillation in the measured reflectivity was fitted by using the following sine function:

$$f(x) = a + b \cdot m + c \cdot \sin(\zeta \cdot m - e) \quad \text{--- 4.15}$$

Some variables were chosen, so that the sine function was able to follow the slight drift of the measurement and a proper fit result was achieved. Variable  $a$  represents the vertical offset; variable  $b$  stands for variations in the gradient; variable  $c$  is altering the amplitude and variable  $e$  corresponds to the phase shift. Again  $m$  is the number of bilayers. The fit provided a result for the term  $\zeta = \frac{4\pi n}{\lambda_0} d_B$  for each wavelength. Figure 4.6.22 shows the fit results.

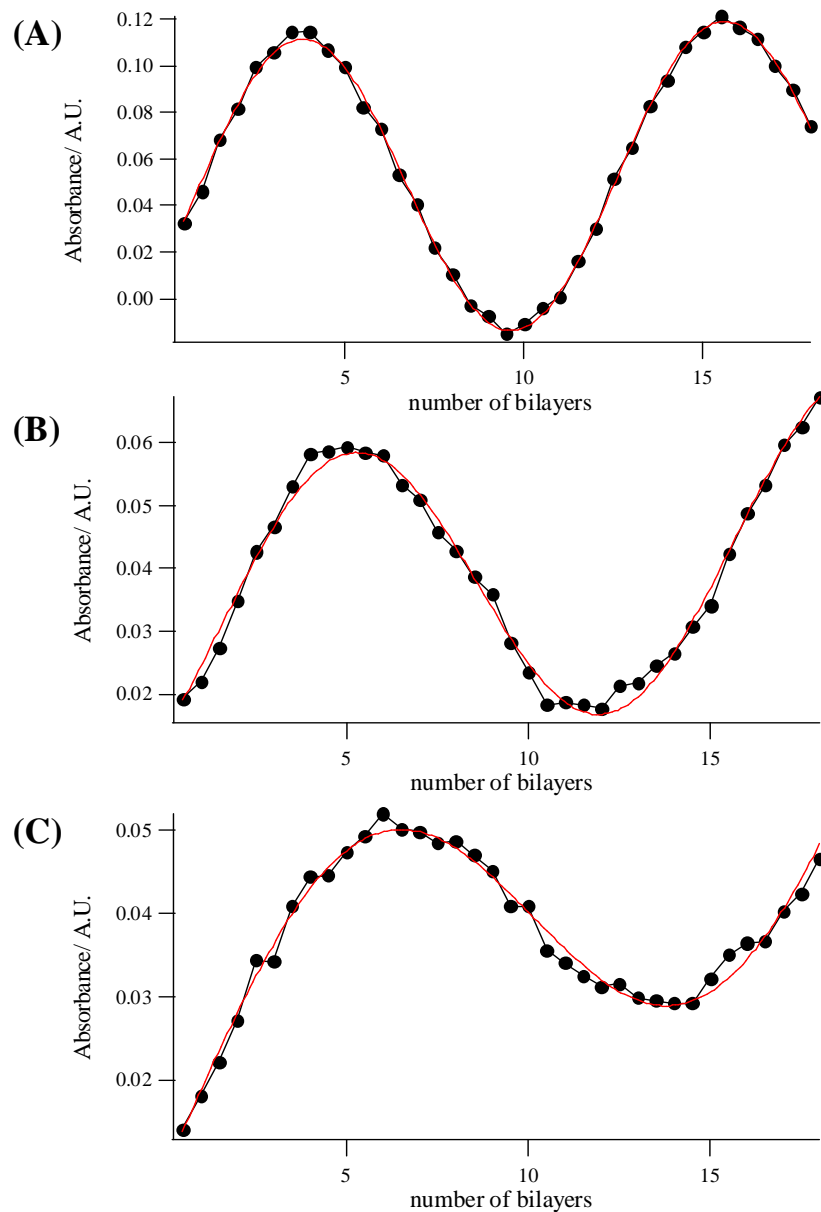


**Figure 4.6.22:** A sine function was employed to fit the periodical oscillations in the measured reflectivity curves after the protein layer deposition on the 5 min etched NPG (confer Figure 4.6.20). The fits were generated by using the software Igor Pro (version 5.02). Reflectivity curves of (A) 570 nm, (B) 700 nm and (C) 800 nm were fitted.

The correlation of the obtained thicknesses for a protein bilayer and the corresponding excitation wavelengths is shown in plot 4.6.23. A linear fit through zero was conducted with the software Origin (version 7.5).

The error ( $\Delta f$ ) of the ratio  $\frac{\lambda_0}{d_B}$  in the plot was calculated as follows:

$$\Delta f = 4\pi n \cdot \frac{1}{\zeta^2} \cdot \Delta \zeta \quad \text{--- 4.16}$$

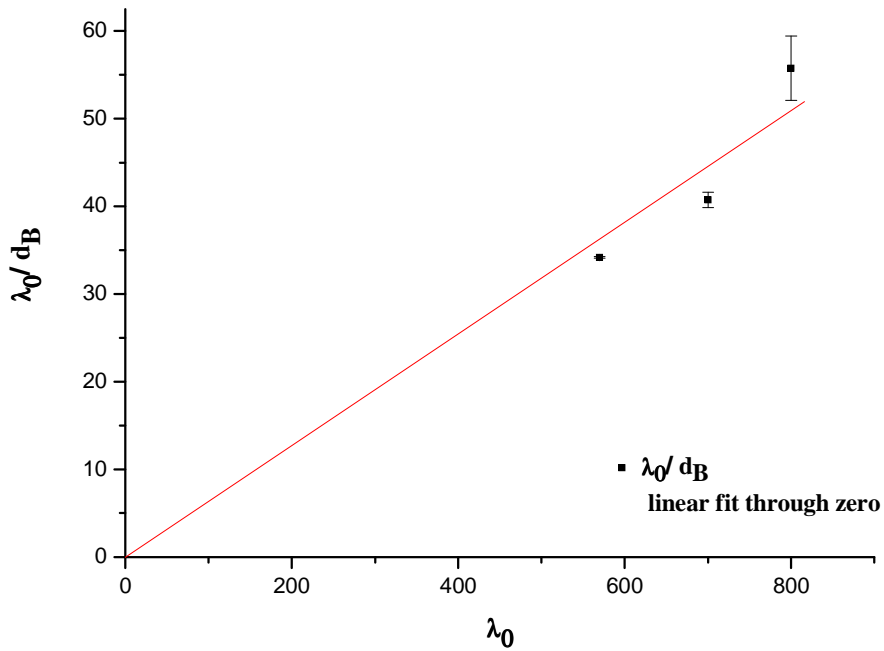


**Figure 4.6.23:** Correlation of the calculated thicknesses versus the three excitation wavelengths. The refractive index of the proteins was assumed to be  $n = 1.45$ .

The calculated values for the thicknesses of a bilayer ( $d_B$ ) are summarized in Table 4.6.4 as well. The error in the thickness of a protein bilayer ( $\Delta d_B$ ) was computed with the following equation:

$$\Delta d_B = \frac{\lambda_0}{4\pi n} \Delta \zeta \quad \text{--- 4.17}$$

**Table 4.6.4:** The thickness of the bilayer ( $d_B$ ) was calculated for all three excitation wavelengths.

$\lambda$	$d_B$
570 nm	$16.7 \pm 0.1$ nm
700 nm	$17.2 \pm 0.4$ nm
800 nm	$14.4 \pm 0.9$ nm

It was possible to determine the thickness of the protein bilayer ( $d_B$ ) composed of avidin and biotinylated antiavidin antibody (IgG) by the analysis of the interference pattern. But the resulting thicknesses of 14.4 - 16.7 nm (Table 4.6.4) are much higher than the expected 9.3 nm, that were found for a flat dense substrate measured by Jing Liu<sup>58</sup>. The size of avidin is  $5.6 \times 5.0 \times 4.0$  nm<sup>60</sup> and the size of the biotinylated antiavidin antibody (IgG) is around  $15 \times 15 \times 3$  nm<sup>61</sup>, so that the maximum thickness of a densely packed bilayer could be  $\sim 20$  nm (Figure 4.6.24). The biotinylated antiavidin antibody (IgG) is able to bind several avidins, so that on the rough NPG surface seemingly more material was immobilized than on an evaporated gold film.

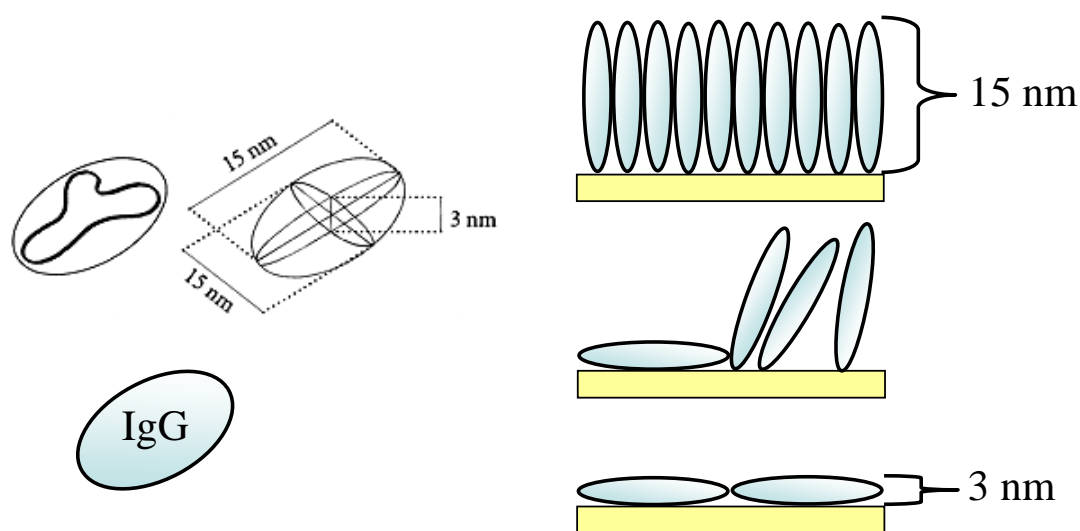


**Figure 4.6.24:** The Y-shaped IgG antibody will approximately seize the volume of a lens-shaped spheroid with a diameter of 15 nm and a thickness of 3 nm<sup>61</sup>. On the right side: Profiles of the IgG packings on a surface illustrating the density ratio of 5 to 1 between molecules densest packed in upright position (above) and in lying position (below). A packing density, that is experimentally achieved, is presumably in between the two extremes.

## **4.7 Application of NPG**

### **The Protein-Tethered Lipid Bilayer established on a Nanoporous Gold Substrate**

No living cell can exist without a membrane. The membrane consists of a lipid bilayer with proteins incorporated. Membrane proteins play an important role in the metabolism of each cell. The study of membrane proteins has long been a challenge because of the lack of experimentally addressable biomimetic systems for the incorporation of membrane proteins.

Various model systems of the biological membrane have been investigated, e.g., black lipid membranes (BLMs). They provide easy access to both sides of the membrane but lack mechanical stability<sup>62</sup>. To solve the problem of instability, solid-supported lipid membranes were developed<sup>63</sup>. Different types of supported membranes were introduced with the inner leaflet of the bilayer either covalently or electrostatically bound to a solid substrate. To provide a biologically relevant model system of the lipid bilayer, it was separated from the substrate by ultrathin water layers ( $\sim 10 \text{ \AA}$ ) or a soft hydrated polymer film (polymer cushion)<sup>64</sup>. The so called tethered lipid bilayer (tBLM) strategy developed during the last decade was an important step towards mimicking the natural plasma membrane. This strategy offers a flexible and stable lipid bilayer. Tethering molecules of various structures can be applied. A novel concept developed recently<sup>65-67</sup> used the membrane protein itself to act as a tethering molecule.

The submembrane space provided by these model systems is relatively small, e.g. the tBLM system presented reservoirs of 20 - 60  $\text{\AA}$  length<sup>68</sup>, dependent on the hydrophilic part of the tethering molecules. Attempts have been made to increase the submembrane space and consequently the ionic reservoir to offer enough space to allow for the incorporation of membrane proteins with larger hydrophilic domains. This can be achieved by a different design of spacer molecules (branched thiol, longer chains<sup>69</sup>) or by the use of a porous solid support<sup>70-72</sup>.

Here, the concept of the protein tethered lipid bilayer membrane (ptBLM) for the oriented immobilization of cytochrome c oxidase on a solid support was transferred to a nanoporous support. The aim was to use the volume inside the pores of the nanoporous gold (NPG) and the submembrane space together to mimic the inside (cytosol) of a living cell. The arrangement on the NPG allows for the simultaneous application of surface plasmon resonance (SPR) and electrochemical impedance spectroscopy (EIS) measurements. The SPR and EIS measurements obtained from a five minute dealloyed NPG substrate were directly compared to the data taken from an ultraflat template stripped gold (TSG) surface<sup>73</sup>.

The membrane work was conducted with the NPG substrate featuring the smallest pore size reached by chemically dealloying method (NPG 5 min etched). By scanning electron microscopy (SEM) and autocorrelation function (ACF) a pore size distribution around 12 nm was found for the five minute etched NPG [cf. Chapter 4.3 and 4.4]. This pore size is still too large compared to the size of the protein ( $6 \times 9$  nm cross section). NPG with the smallest pores ( $\sim 7 - 8$  nm) were obtained by electrochemically dealloying at 2 volts, followed by 1.2 volt NPG ( $\sim 9$  nm) [cf. Chapter 4.3, 4.4]. But these samples were too brittle to be used for SPR or EIS measurements in solution.

Figure 4.7.1 illustrates the modification of the 5 min etched nanoporous gold substrate. To modify the NPG substrate, it is first provided with a self assembled monolayer of dithiodipropionic acid (DTP) (A) and dithiobis (*N*-succinimidyl propionate) (DTSP) (B) (mole fraction 0.6; viz 60 % DTSP). DTP was chosen to dilute the DTSP molecules. The disulfides DTP and DTSP anchored to the gold via thiolate linkages to form thiopropionic acid and thio (*N*-succinimidyl propionate) (TP and TSP). TSP was thereafter coupled with compound (C), an amino–nitrilo-triacetic acid (ANTA), forming a NTA functionalized surface (E).  $\text{Ni}^{2+}$  addition enabled chelating of NTA with two histidines of the histidine-tag of the protein (F). In that way, recombinantly expressed his-tagged cytochrome c oxidase (from *Rhodobacter sphaeroides* with the His-tag fused to the C-terminus of subunit I) was anchored on the nitrilo-triacetic acid (NTA) modified NPG surface (Figure 4.7.2). For further experimental details<sup>65</sup> see Chapter 3.8, Materials.

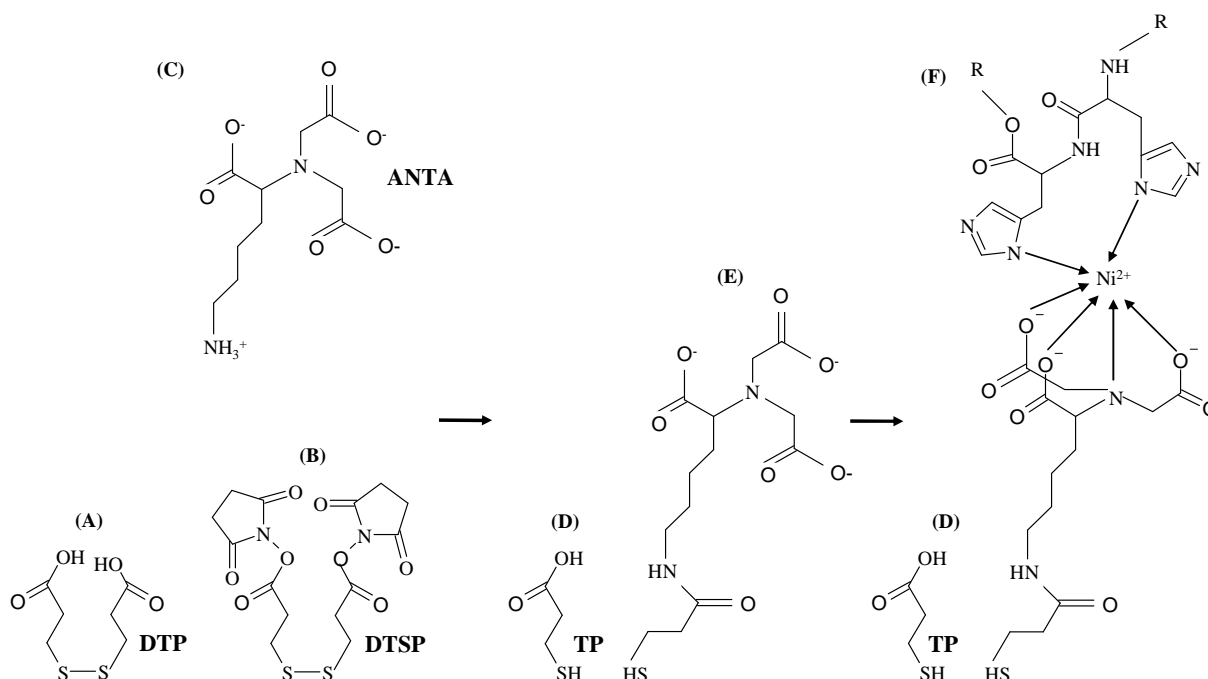
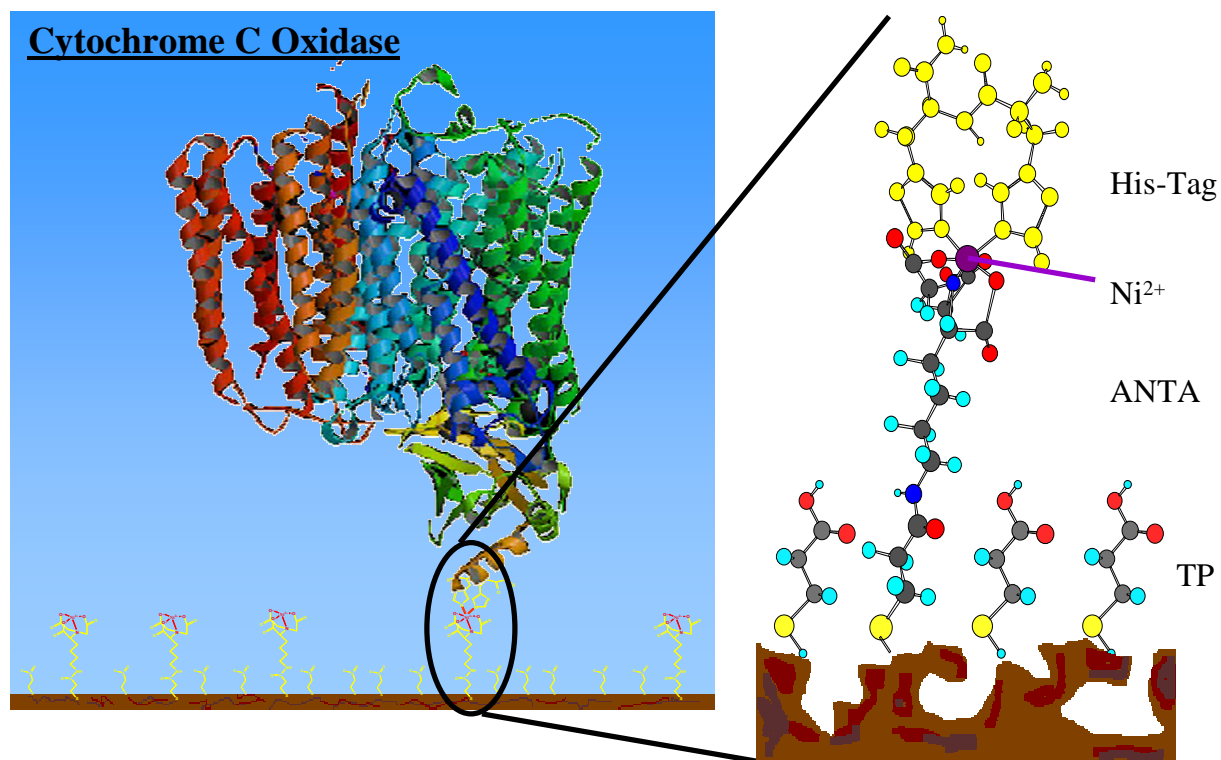
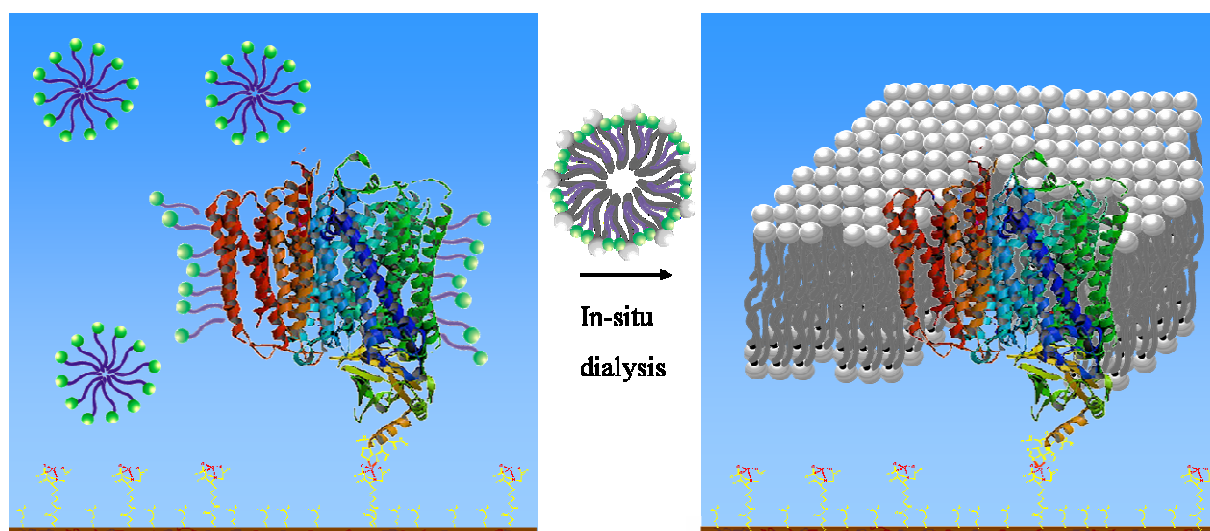


Figure 4.7.1: Illustration of the coupling reaction leading to the chelating surface architecture<sup>65, 66</sup>



**Figure 4.7.2:** Schematic representation of the surface-bound cytochrome c oxidase via the affinity of the His-tag to the Ni-NTA modified nanoporous gold surface.

In order to preserve the conformation of the cytochrome c oxidase, a 1 % solution of detergent *n*-Dodecyl- $\beta$ -D-maltoside (DDM) was used for the immobilization. Finally, the substitution of the detergent by a lipid (1,2-diphytanoyl-*sn*-glycero-3-phosphocholine (DiPhyPC)) formed a membrane around the protein (Figure 4.7.3).



**Figure 4.7.3:** Schematic illustration of the in-situ dialysis: substitution of the detergent by the lipid.

### 4.7.1 Characterization of the layer formation by SPR and EIS

Surface plasmon resonance spectroscopy scans were recorded in PBS/DDM buffer before and after cytochrome c oxidase binding; and after exchange of the detergent DDM by the lipid. Therefore, a p-polarized IR laser ( $\lambda = 1152$  nm) was used to excite a plasmon on NPG dealloyed for 5 minutes.

The binding of the His-tagged cytochrome c oxidase in its detergent solubilized form to the NTA modified NPG surface resulted in a significant shift of the minimum of the SPR curve ( $\sim 0.35^\circ$ ) (Figure 4.7.4). Assuming a refractive index of  $\sim 1.45$  ( $\epsilon' \sim 2.1$ ) for the cytochrome c oxidase, the shift in the minimum correlated to a thickness of  $\sim 6$  nm (winspall simulation, version 2.20). The reconstitution of the lipid bilayer (1,2-diphytanoyl-*sn*-glycero-3-phosphocholine (DiPhyPC)) resulted in a slight minimum shift ( $\sim 0.047^\circ$ ) corresponding to a thickness of  $\sim 0.5$  nm ( $\epsilon' \sim 2.1$ ).

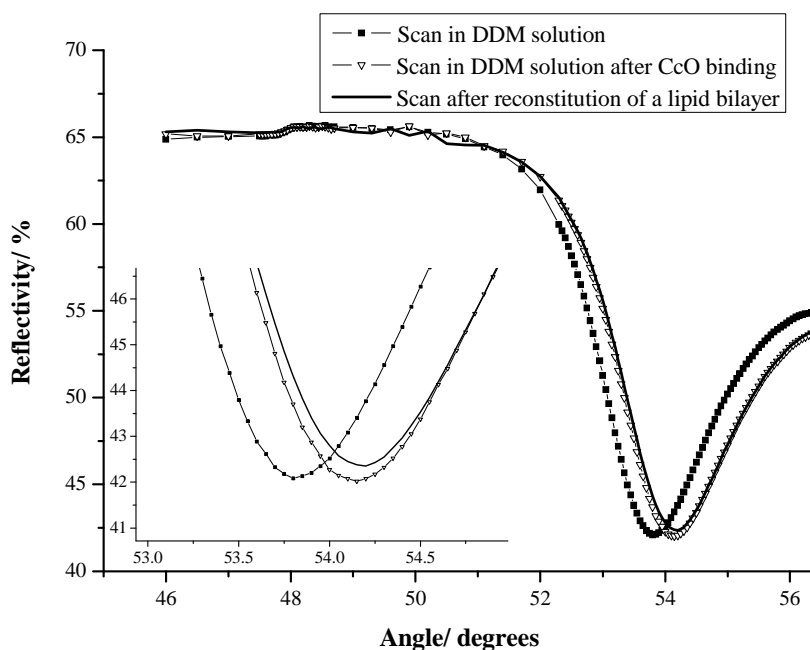


**Figure 4.7.4:** Surface plasmon resonance spectroscopy scans on NPG (dealloyed for 5 minutes). The inset zooms in the minimum angles.

Electrochemical impedance spectroscopy was measured simultaneously with surface plasmon spectroscopy. Data were fitted to the equivalent circuit  $R_s(R_m C_m)CPE$ , where  $R_s$  was the solution resistance;  $R_m$  the resistance of the lipid membrane;  $C_m$  the capacitance of the lipid membrane. A constant phase element (CPE) was chosen to model the complexity of the submembrane space (Figure 4.7.5).

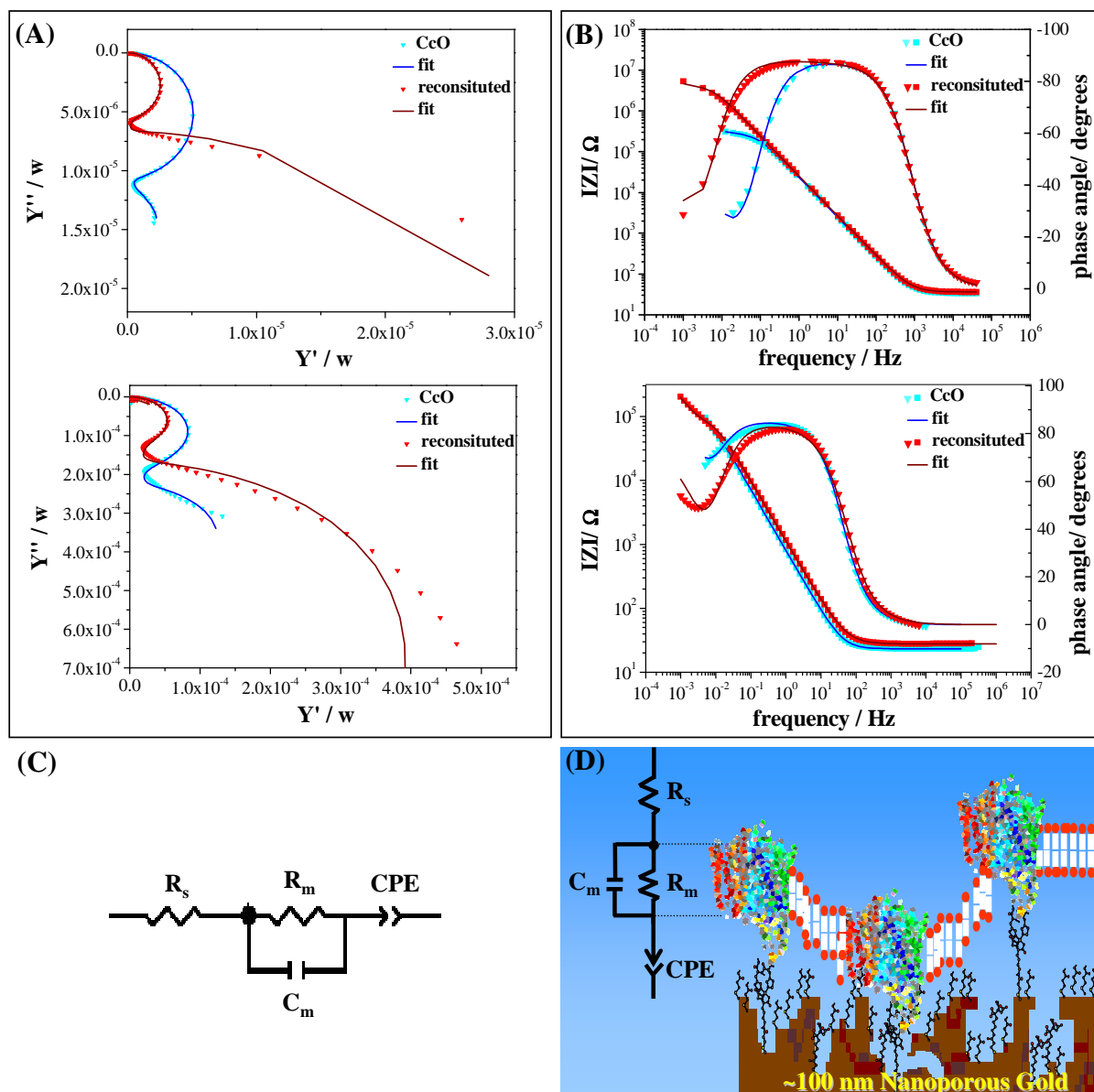


**Figure 4.7.5:** Illustration of the electrochemical impedance spectroscopy measurements observing the lipid bilayer reconstitution. (A) Nyquist admittance plots and (B) Bode impedance diagrams of the TSG (upper) and the NPG (lower) samples measured after CcO binding and after membrane reconstitution, respectively. (C) Equivalent circuit to model the system. (D) Illustration of the system. Table 4.7.1 summarizes the fitting results using the described electrical circuit.

**Table 4.7.1:** Summary of the fit results obtained for TSG and NPG, respectively.

Sample	Capacitance CcO [ $\mu\text{F}/\text{cm}^2$ ]	Capacitance reconstituted [ $\mu\text{F}/\text{cm}^2$ ]	Resistance CcO [ $\text{M}\Omega \cdot \text{cm}^2$ ]	Resistance reconstituted [ $\text{M}\Omega \cdot \text{cm}^2$ ]
Template stripped Au ~ 50 nm (TSG)	$13.1 \pm 3.9$	$7.3 \pm 0.5$	$0.3 \pm 0.08$	$12 \pm 7$
5 min etched NPG	$792 \pm 82$	$335 \pm 9$	$0.021 \pm 0.005$	$0.042 \pm 0.0015$

Substitution of the detergent by the lipid led to an effective decrease of the capacitance ( $C_m$ ) and an increase of the resistance ( $R_m$ ). Parameter obtained of the fit procedure are given in Table 4.7.1 for both substrates, 5 min etched NPG and TSG, respectively.

The capacitance of the protein layer was very large for the NPG  $792 \pm 82$  [ $\mu\text{F}/\text{cm}^2$ ] compared to the TSG  $13.1 \pm 3.9$  [ $\mu\text{F}/\text{cm}^2$ ], which is, however, not only accounted for by the high surface area. The capacitance of a homogeneous dielectric layer can be calculated using the equation for the parallel plate condenser:

$$C = \varepsilon \cdot \varepsilon_0 \cdot \frac{A}{d} \quad \text{--- 4.18}$$

where

- C is the capacitance,
- $\varepsilon$  is the permittivity of the insulator used (or  $\varepsilon_0$  for vacuum),
- A is the surface area of the electrode,
- d is the thickness of a homogeneous layer.

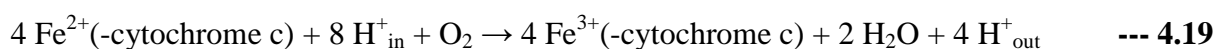
Accordingly, a 5 nm thick protein<sup>74</sup> layer of  $\varepsilon_{\text{protein}} = 30$  formed on TSG is expected to yield  $C = 6 \mu\text{F}/\text{cm}^2$ . The higher value of  $C = 13 \mu\text{F}/\text{cm}^2$  found experimentally is explained in terms of water<sup>75</sup> ( $\varepsilon_{\text{water}} = 81$ ) and detergent molecules interspersed between the proteins. If they are replaced by lipids ( $\varepsilon_{\text{lipid}} = 2$ ) the capacitance decreased approximately approaching the theoretical value of the homogeneous protein layer  $C = 6 \mu\text{F}/\text{cm}^2$ . Other effects are expected from the surface-confinement geometry of the NPG-CcO structure. The pores are large as compared to the protein molecules. Hence the cytochrome c oxidase will bind not only to the outer surface of the NPG but also to surfaces inside the pores (Fig. 4.7.5 D). Consequently a closed layer of CcO molecules cannot be formed on the NPG, contrary to TSG where the roughness is small (Root mean square  $\leq 1\text{nm}$ )<sup>73</sup> compared to the size of the CcO.

For this extremely heterogeneous CcO layer on NPG, a larger amount of water molecules and detergent should be present between the proteins. Water<sup>75</sup> with an  $\varepsilon_{\text{water}} = 81$  increased the capacitance according to equation 4.18. Even if some of the detergent and water molecules were replaced by lipids during dialysis, as evidenced by the decrease of capacitance, the reconstitution will never result in a closed bilayer spanning the pores, due to the marked inhomogeneity of the protein layer. A correlation of the electrical properties between nanoporous gold and template stripped gold is therefore hard to achieve.

However, first indications of a membrane can be seen from the decrease of the capacitance and the slight increase of resistance of  $0.042 \pm 0.0015$  [ $\text{M}\Omega \cdot \text{cm}^2$ ] which is small compared to the TSG  $12 \pm 7$  [ $\text{M}\Omega \cdot \text{cm}^2$ ].

### 4.7.2 Activation of the Cytochrome C Oxidase

In order to probe the functionality of the cytochrome c oxidase, cytochrome c was injected after the reconstitution of the membrane. By adding reduced cytochrome c (Cyt c; from bovine heart; Sigma) as the substrate of the cytochrome c oxidase a decrease in the resistance ( $R_m$ ) was monitored due to the turnover of the enzyme. With increasing Cyt c concentration the resistance ( $R_m$ ) decreased continuously until saturation was reached (Figure 4.7.6). The mechanism of Cyt c oxidation<sup>76</sup> by cytochrome c oxidase is well studied<sup>77</sup>. The overall reaction is (cf. Figure 4.7.6):



The effect of Cyt c addition seemed to be reversible, because after rinsing with pure buffer the initially high resistance was regained (data not shown).

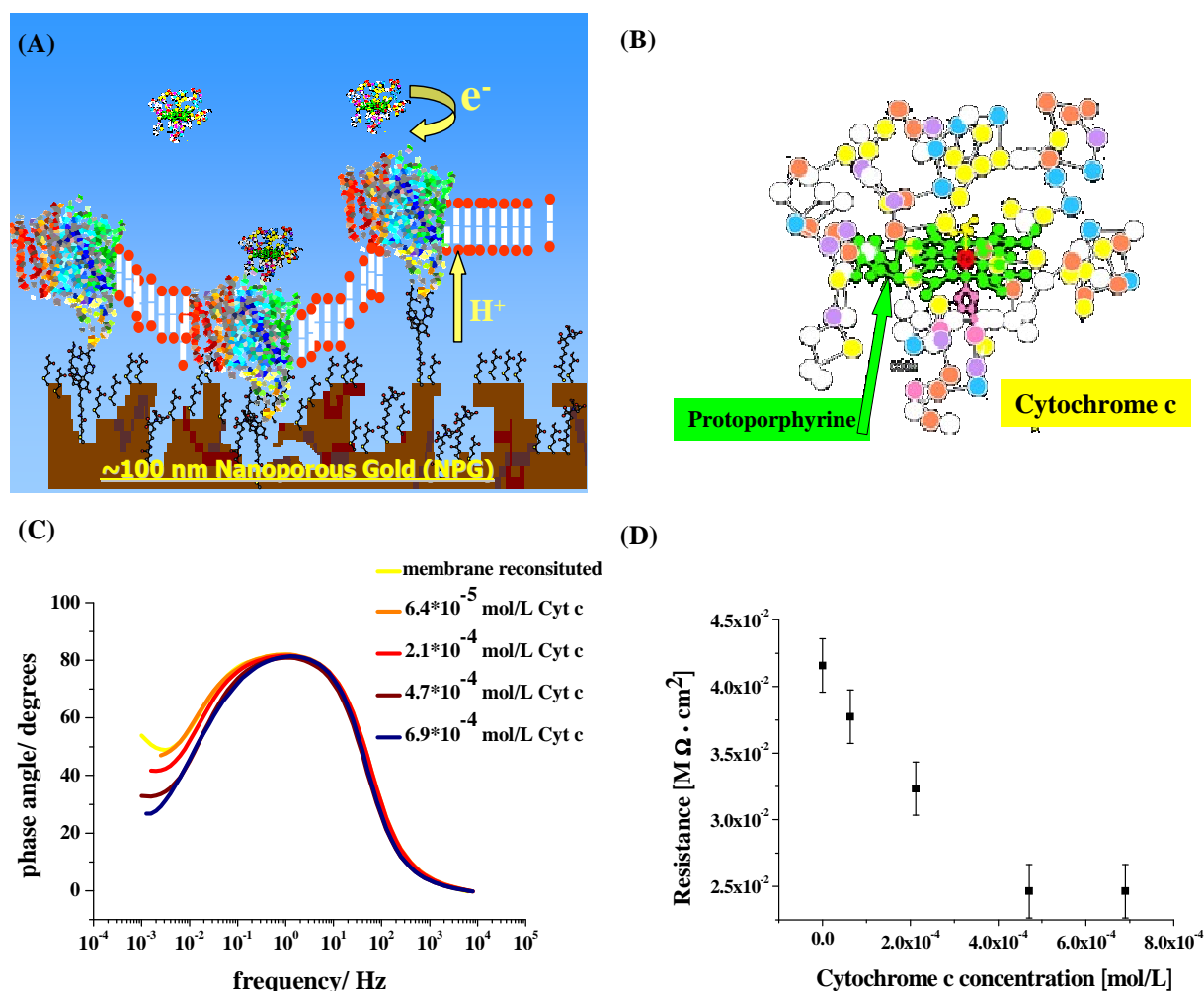


Figure 4.7.6: Illustration of the cytochrome c effect: (A) sketch of the surface architecture; (B) structure of the cytochrome c<sup>78</sup>; (C) EIS spectra (Bode plots) were recorded after every addition of Cyt c; (D) decreasing resistance plotted versus the Cyt c concentration.

As a conclusion from the results so far, the CcO was efficiently immobilized on the NPG. The pore size was not optimal, so that the protein ( $\sim 9 \times 6 \times 9 \text{ nm}$ )<sup>79</sup> seemed to bind not only to the top layer of the NPG comprising 12 nm pore diameter, but also to some lower regions so that the membrane was not really suspended across the pores (Figure 4.7.7 (middle)). However, the effective decrease of the capacitance ( $C_m$ ) and the slight increase of the resistance ( $R_m$ ) was a strong indication that a membrane was formed around the protein.

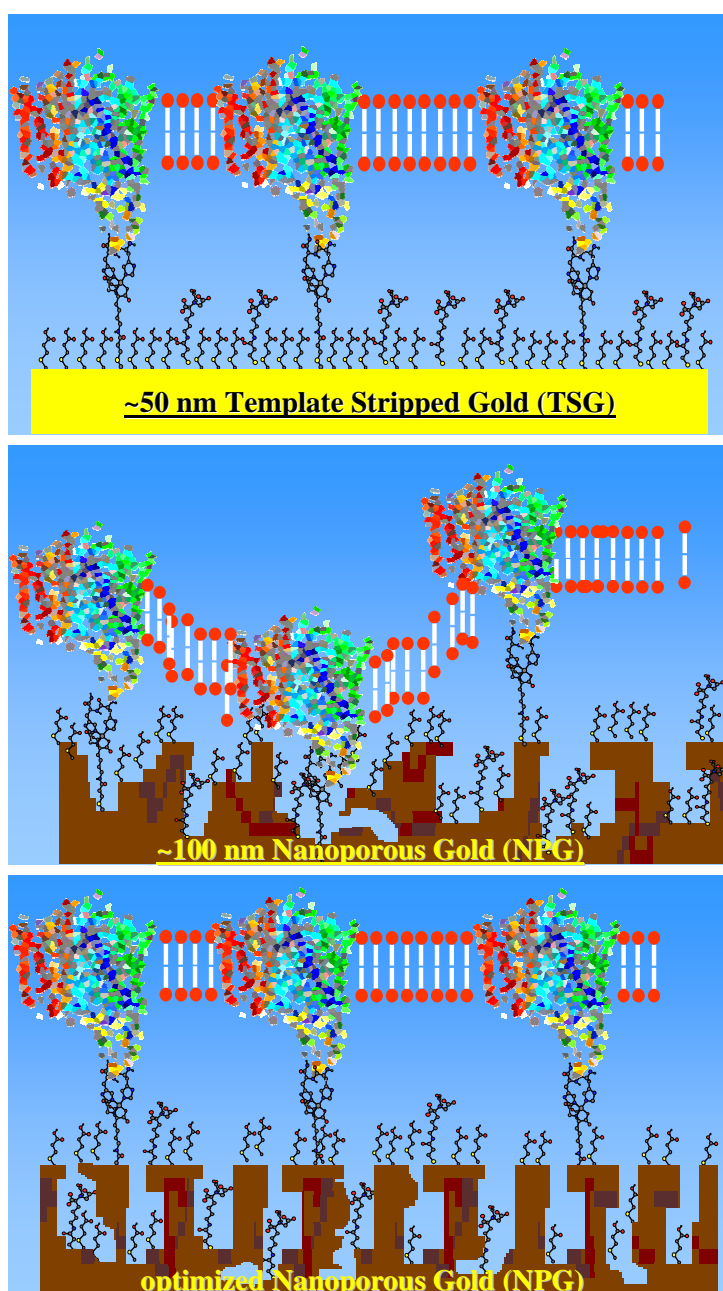


Figure 4.7.7: Demonstration of the membrane suspension on different substrates.

Porous substrates with a defined aspect ratio (ratio between depth and width of the pores) using a smaller pore width and larger depth, might be suitable (Figure 4.7.7 (lower)). Another option would be stamping of the DTSP to the top layer of the NPG via a polydimethyl siloxane (PDMS) stamp, instead of immersing the whole substrate into the thiol solution. In this case the Cyt c oxidase would be able to bind only to the exposed pinnacles of the NPG, thus a smooth membrane could be suspended across the pores.

### **4.8 Conclusion**

First of all, NPG provided a significantly enhanced surface-to-volume ratio which was shown by cyclic voltammetry and electrical impedance measurements. The electrochemical studies indicated a nearly one order-of-magnitude enhancement of the surface area of NPG compared to an evaporated gold film, which was of assistance to achieve better reaction efficiency and detection sensitivity.

Secondly, porous materials, as well as NPG, are in general particularly useful as separation media for their size-selectivity in chromatographical isolation, adsorption and catalysis, etc. The nano-sized porous structure strongly affects the sequential build-up of functional supramolecular architectures on substrates that is inherent in the sensing process itself. The diffusion of molecules to the NPG interior was hindered when pore size was comparable with the molecular dimension; this “molecular sieve” effect was used to for realizing size-selective adsorption. This means the accessible surface area of the NPG substrate changed drastically with the analyte size. Twice the amount of streptavidin/avidin binding was found on NPG compared to a flat dense gold film; and no access for molecules larger than the average pore size such as biotinylated IgG and polystyrene latex beads was seen. The charged dendrimer molecules showed similar coverage of NPG as they did on the evaporated gold. Taking into account the enhanced surface area of NPG (shown by the streptavidin binding result), this result indicates slightly smaller dendrimer coverage per layer on the NPG surface, which may suggest that electrostatically driven binding can be biased inside nanopores (Figure 4.8.1).

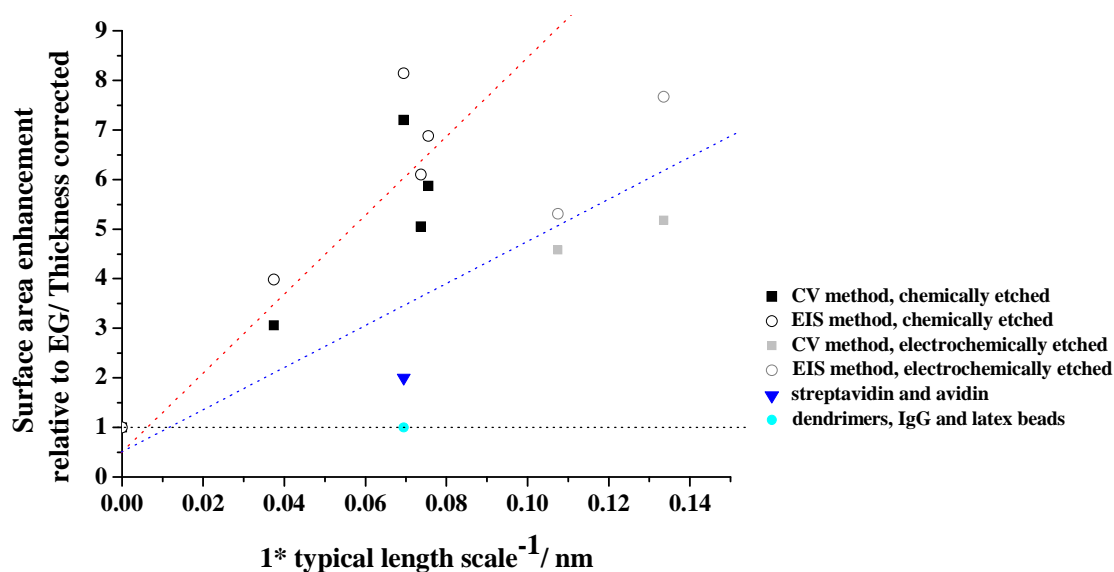


**Figure 4.8.1:** Surface area enhancement of the differently etched NPG substrates relative to an evaporated gold film. The dotted lines are guides for the eye of the beholder: the “base line” for a flat/dense gold film is shown in black; the trend for the enhancement of electrochemically etched NPG samples is marked in blue and the trend for the chemically etched NPG substrates is shown in red [confer Figure 4.5.7].

Thirdly, NPG uniquely offered propagating (p-SPR) and localized (l-SPR) surface plasmon resonance modes that could be used to probe interfacial refractive index variations on different length scales. The p-SPR possessed a 200 - 300 nm decay length (20 - 25 % of the light’s wavelength) of the evanescent field, whereas an exponential fit of the l-SPR curve for the 5 min etched NPG yielded a decay length of only  $ld = 12.3$  nm. But the field enhancement of the l-SPR was strongly dependent on the size and shape of the pores; and the excitation wavelength. Species that went *into* the pores of NPG and modified their dielectric atmosphere, were detectable by absorption measurements of l-SPR excitations, whereas species that adsorbed *onto* the geometric surface of the pores of a film of NPG were less influential to l-SPR but equally detectable by p-SPR measurements (Figure 4.8.2). The surface plasmon resonance signals were therefore directly linked to the accessibility of NPG pores which can be tuned by the dealloying condition and time. The combination of p-SPR and l-SPR monitoring provided size-selectivity in bio-recognition reactions using the NPG. The streptavidin-doped bead binding experiment demonstrated the utility of NPG for quantitative p-SPR measurement. Layer by layer studies revealed the different binding modes of large biomolecules (e.g. avidin and IgG) to NPGs possessing different pore sizes, where the hypothesis was confirmed by both l-SPR and SEM observation.

Finally, for supported membrane applications, first experiments on NPG were promising.

All these results will help to further understand the character of NPG as a novel plasmonic substrate for wider applications.

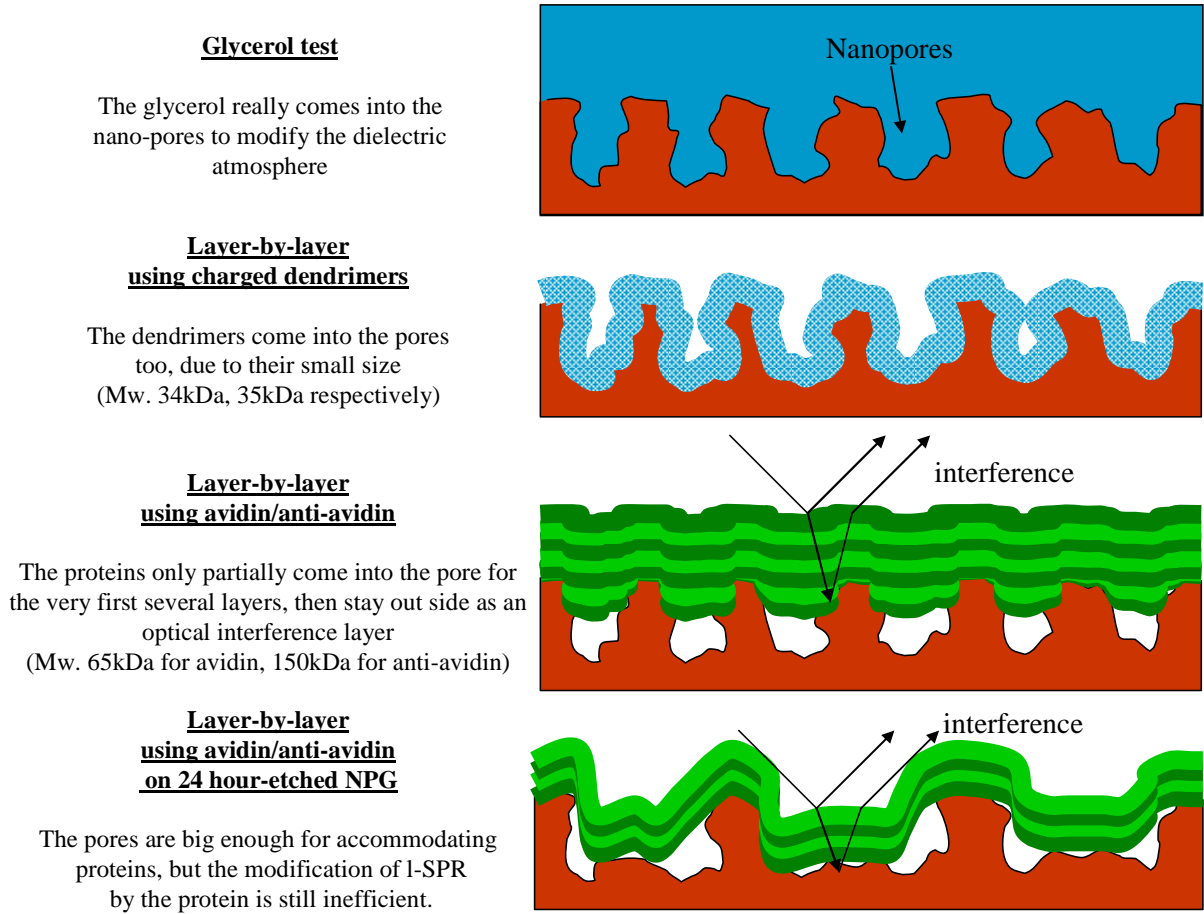


Figure 4.8.2: Summary of layer by layer experiments

## 4.9 References

1. Chan, V. Z. H.; Hoffman, J.; Lee, V. Y.; Iatrou, H.; Avgeropoulos, A.; Hadjichristidis, N.; Miller, R. D.; Thomas, E. L., Ordered bicontinuous nanoporous and nanorelief ceramic films from self assembling polymer precursors. *Science* **1999**, 286, (5445), 1716-1719.
2. Xia, Y. N.; Gates, B.; Yin, Y. D.; Lu, Y., Monodispersed colloidal spheres: Old materials with new applications. *Advanced Materials* **2000**, 12, (10), 693-713.
3. Kresge, C. T.; Leonowicz, M. E.; Roth, W. J.; Vartuli, J. C.; Beck, J. S., Ordered Mesoporous Molecular-Sieves Synthesized By A Liquid-Crystal Template Mechanism. *Nature* **1992**, 359, (6397), 710-712.
4. Seshadri, R.; Meldrum, F. C., Bioskeletons as templates for ordered, macroporous structures. *Advanced Materials* **2000**, 12, (15), 1149-+.
5. Masuda, H.; Fukuda, K., Ordered Metal Nanohole Arrays Made By A 2-Step Replication Of Honeycomb Structures Of Anodic Alumina. *Science* **1995**, 268, (5216), 1466-1468.
6. Sun, F. Q.; Cai, W. P.; Li, Y.; Cao, B. Q.; Lei, Y.; Zhang, L. D., Morphology-controlled growth of large-area two-dimensional ordered pore arrays. *Advanced Functional Materials* **2004**, 14, (3), 283-288.
7. Kulinowski, K. M.; Jiang, P.; Vaswani, H.; Colvin, V. L., Porous metals from colloidal templates. *Advanced Materials* **2000**, 12, (11), 833-838.
8. Sakintuna, B.; Yurum, Y., Templated porous carbons: A review article. *Industrial & Engineering Chemistry Research* **2005**, 44, (9), 2893-2902.
9. Tekeste, M. Y.; Yarrison-Rice, J. M., High efficiency photonic crystal based wavelength demultiplexer. *Optics Express* **2006**, 14, (17), 7931-7942.
10. Forty, A. J., Corrosion Micro-Morphology Of Noble-Metal Alloys And Depletion Gilding. *Nature* **1979**, 282, (5739), 597-598.
11. Mattei, G.; Marchi, G. D.; Maurizio, C.; Mazzoldi, P.; Sada, C.; Bello, V.; Battaglin, G., Chemical- or radiation-assisted selective dealloying in bimetallic nanoclusters. *Physical Review Letters* **2003**, 90, (8).
12. Ding, Y.; Kim, Y. J.; Erlebacher, J., Nanoporous gold leaf: "Ancient technology"/advanced material. *Advanced Materials* **2004**, 16, (21), 1897-+.
13. Kucheyev, S. O.; Hayes, J. R.; Biener, J.; Huser, T.; Talley, C. E.; Hamza, A. V., Surface-enhanced Raman scattering on nanoporous Au. *Applied Physics Letters* **2006**, 89, (5).
14. Thorp, J. C.; Sieradzki, K.; Tang, L.; Crozier, P. A.; Misra, A.; Nastasi, M.; Mitlin, D.; Picraux, S. T., Formation of nanoporous noble metal thin films by electrochemical dealloying of Pt<sub>x</sub>Si<sub>1-x</sub>. *Applied Physics Letters* **2006**, 88, (3).
15. IUPAC, *Compendium of Chemical Terminology, 2nd edition* **1997**, Vol.31.
16. IUPAC, *Compendium of Chemical Terminology, 2nd edition* **1997**, Vol.46.
17. Rouquerol, J.; Avnir, D.; Fairbridge, C. W.; Everett, D. H.; Haynes, J. H.; Pernicone, N.; Ramsay, J. D. F.; Sing, K. S. W.; Unger, K. K., Recommendations For The Characterization Of Porous Solids. *Pure And Applied Chemistry* **1994**, 66, (8), 1739-1758.
18. Yeh, F. H.; Tai, C. C.; Huang, J. F.; Sun, I. W., Formation of porous silver by electrochemical alloying/dealloying in a water-insensitive zinc chloride-1-ethyl-3-methyl imidazolium chloride ionic liquid. *Journal Of Physical Chemistry B* **2006**, 110, (11), 5215-5222.
19. Huang, J. F.; Sun, I. W., Fabrication and surface functionalization of nanoporous gold by electrochemical alloying/dealloying of Au-Zn in an ionic liquid, and the self-assembly of L-cysteine monolayers. *Advanced Functional Materials* **2005**, 15, (6), 989-994.
20. Smith, A. J.; Tran, T.; Wainwright, M. S., Kinetics and mechanism of the preparation of Raney (R) copper. *Journal Of Applied Electrochemistry* **1999**, 29, (9), 1085-1094.

21. Li, R.; Sieradzki, K., Ductile-Brittle Transition In Random Porous Au. *Physical Review Letters* **1992**, 68, (8), 1168-1171.
22. Ding, Y.; Chen, M. W.; Erlebacher, J., Metallic mesoporous nanocomposites for electrocatalysis. *Journal Of The American Chemical Society* **2004**, 126, (22), 6876-6877.
23. Huang, X. H.; Huang, H. Z.; Wu, N. Z.; Hu, R. S.; Zhu, T.; Liu, Z. F., Investigation of structure and chemical states of self-assembled - Au nanoscale particles by angle-resolved X-ray photoelectron spectroscopy. *Surface Science* **2000**, 459, (1-2), 183-190.
24. Thompson, W. R.; Pemberton, J. E., Thin Sol-Gel Silica Films On (3-Mercaptopropyl)Trimethoxysilane-Modified Ag And Au Surfaces. *Chemistry Of Materials* **1995**, 7, (1), 130-136.
25. Dona, J. M.; Gonzalezvelasco, J., Mechanism Of Surface-Diffusion Of Gold Adatoms In Contact With An Electrolytic Solution. *Journal Of Physical Chemistry* **1993**, 97, (18), 4714-4719.
26. [http://www.ruhr-uni-bochum.de/exogeol/zrem\\_web/page1/page1.html](http://www.ruhr-uni-bochum.de/exogeol/zrem_web/page1/page1.html)
27. Talukdar, M. S.; Torsaeter, O.; Ioannidis, M. A.; Howard, J. J., Stochastic reconstruction of chalk from 2D images. *Transport in Porous Media* **2002**, 48, (1), 101-123.
28. Talukdar, M. S.; Torsaeter, O.; Ioannidis, M. A., Stochastic reconstruction of particulate media from two-dimensional images. *Journal of Colloid and Interface Science* **2002**, 248, (2), 419-428.
29. Ruckelshaus, M. H., Spatial scale of genetic structure and an indirect estimate of gene flow in eelgrass, *Zostera marina*. *Evolution* **1998**, 52, (2), 330-343.
30. Pajkossy, T., Impedance Of Rough Capacitive Electrodes. *Journal Of Electroanalytical Chemistry* **1994**, 364, (1-2), 111-125.
31. Bonroy, K.; Friedt, J. M.; Frederix, F.; Laureyn, W.; Langerock, S.; Campitelli, A.; Sara, M.; Borghs, G.; Goddeeris, B.; Declerck, P., Realization and characterization of porous gold for increased protein coverage on acoustic sensors. *Analytical Chemistry* **2004**, 76, (15), 4299-4306.
32. Jurczakowski, R.; Hitz, C.; Lasia, A., Impedance of porous Au based electrodes. *Journal Of Electroanalytical Chemistry* **2004**, 572, (2), 355-366.
33. Raether, H., Surface-Plasmons on Smooth and Rough Surfaces and on Gratings. *Springer Tracts in Modern Physics* **1988**, 111, 1-133.
34. Kretschmann, E.; Raether, H., Radiative decay of nonradiative surface plasmons excited by light. *Z. Naturforsch. A* **1968**, 23, 2135-2136
  
35. Mie, G., Articles on the optical characteristics of turbid tubes, especially colloidal metal solutions. *Annalen Der Physik* **1908**, 25, (3), 377-445.
36. Zeman, E. J.; Schatz, G. C., An Accurate Electromagnetic Theory Study Of Surface Enhancement Factors For Ag, Au, Cu, Li, Na, Al, Ga, In, Zn, And Cd. *Journal Of Physical Chemistry* **1987**, 91, (3), 634-643.
37. Gresillon, S.; Aigouy, L.; Boccara, A. C.; Rivoal, J. C.; Quelin, X.; Desmarest, C.; Gadenne, P.; Shubin, V. A.; Sarychev, A. K.; Shalaev, V. M., Experimental observation of localized optical excitations in random metal-dielectric films. *Physical Review Letters* **1999**, 82, (22), 4520-4523.
38. Maarroof, A. I.; Cortie, M. B.; Smith, G. B., Optical properties of mesoporous gold films. *Journal Of Optics A-Pure And Applied Optics* **2005**, 7, (7), 303-309.
39. Haes, A. J.; Van Duyne, R. P., A nanoscale optical biosensor: Sensitivity and selectivity of an approach based on the localized surface plasmon resonance spectroscopy of triangular silver nanoparticles. *Journal Of The American Chemical Society* **2002**, 124, (35), 10596-10604.

40. Haes, A. J.; Zou, S. L.; Schatz, G. C.; Van Duyne, R. P., A nanoscale optical biosensor: The long range distance dependence of the localized surface plasmon resonance of noble metal nanoparticles. *Journal Of Physical Chemistry B* **2004**, 108, (1), 109-116.
41. Whitney, A. V.; Elam, J. W.; Zou, S. L.; Zinovev, A. V.; Stair, P. C.; Schatz, G. C.; Van Duyne, R. P., Localized surface plasmon resonance nanosensor: A high-resolution distance-dependence study using atomic layer deposition. *Journal Of Physical Chemistry B* **2005**, 109, (43), 20522-20528.
42. Dahlin, A.; Zach, M.; Rindzevicius, T.; Kall, M.; Sutherland, D. S.; Hook, F., Localized surface plasmon resonance sensing of lipid-membrane-mediated biorecognition events. *Journal Of The American Chemical Society* **2005**, 127, (14), 5043-5048.
43. Fontana, E.; Pantell, R. H., Characterization Of Multilayer Rough Surfaces By Use Of Surface-Plasmon Spectroscopy. *Physical Review B* **1988**, 37, (7), 3164-3182.
44. Lyon, L. A.; Pena, D. J.; Natan, M. J., Surface plasmon resonance of Au colloid-modified Au films: Particle size dependence. *Journal of Physical Chemistry B* **1999**, 103, (28), 5826-5831.
45. Spinke, J.; Liley, M.; Guder, H. J.; Angermaier, L.; Knoll, W., Molecular Recognition At Self-Assembled Monolayers - The Construction Of Multicomponent Multilayers. *Langmuir* **1993**, 9, (7), 1821-1825.
46. Wilchek, M.; Bayer, E. A., Avidin-Biotin Technology - Preface. *Methods In Enzymology* **1990**, 184, R17-R18.
47. Yu, F.; Ahl, S.; Caminade, A. M.; Majoral, J. P.; Knoll, W.; Erlebacher, J., Simultaneous excitation of propagating and localized surface plasmon resonance in nanoporous gold membranes. *Analytical Chemistry* **2006**, 78, (20), 7346-7350.
48. Weisser, M.; Tovar, G.; Mittler-Neher, S.; Knoll, W.; Brosinger, F.; Freimuth, H.; Lacher, M.; Ehrfeld, W., Specific bio-recognition reactions observed with an integrated Mach-Zehnder interferometer. *Biosensors & Bioelectronics* **1999**, 14, (4), 405-411.
49. Schott Glass Inc. Publications.
50. Ordal, M. A.; Long, L. L.; Bell, R. J.; Bell, S. E.; Bell, R. R.; Alexander, R. W.; Ward, C. A., Optical-Properties of the Metals Al, Co, Cu, Au, Fe, Pb, Ni, Pd, Pt, Ag, Ti, and W in the Infrared and Far Infrared. *Applied Optics* **1983**, 22, (7), 1099-1119.
51. Kohlrausch, F., *Praktische Physik*. **1968**, Vol.1 , p. 408.
52. Schiebener, P.; Straub, J.; Sengers, J.; Gallagher, J. S., Refractive-Index of Water and Steam as Function of Wavelength, Temperature and Density. *Journal of Physical and Chemical Reference Data* **1990**, 19, (3), 677-717.
53. Majoral, J. P.; Caminade, A. M., Dendrimers containing heteroatoms (Si, P, B, Ge, or Bi). *Chemical Reviews* **1999**, 99, (3), 845-880.
54. Kim, D. H.; Karan, P.; Goring, P.; Leclaire, J.; Caminade, A. M.; Majoral, J. P.; Gosele, U.; Steinhart, M.; Knoll, W., Formation of dendrimer nanotubes by layer-by-layer deposition. *Small* **2005**, 1, (1), 99-102.
55. Launay, N.; Caminade, A. M.; Lahana, R.; Majoral, J. P., A General Synthetic Strategy For Neutral Phosphorus-Containing Dendrimers. *Angewandte Chemie-International Edition In English* **1994**, 33, (15-16), 1589-1592.
56. Loup, C.; Zanta, M. A.; Caminade, A. M.; Majoral, J. P.; Meunier, B., Preparation of water-soluble cationic phosphorus-containing dendrimers as DNA transfecting agents. *Chemistry-A European Journal* **1999**, 5, (12), 3644-3650.
57. Cui, X. Q.; Pei, R. J.; Wang, X. Z.; Yang, F.; Ma, Y.; Dong, S. J.; Yang, X. R., Layer-by-layer assembly of multilayer films composed of avidin and biotin-labeled antibody for immunosensing. *Biosensors & Bioelectronics* **2003**, 18, (1), 59-67.
58. Liu, J., Systematic Studies of Protein Immobilization by Surface Plasmon Field-Enhanced Fluorescence Spectroscopy. *PhD Thesis* **2005**, University of Mainz.

59. Christensen, D., Assembly and Characterization of Protein Multi-layer Systems. *Master Thesis* **2004**.
60. Pugliese, L.; Coda, A.; Malcovati, M.; Bolognesi, M., 3-Dimensional Structure of the Tetragonal Crystal Form of Egg-White Avidin in Its Functional Complex with Biotin at 2.7-Angstrom Resolution. *Journal of Molecular Biology* **1993**, 231, (3), 698-710.
61. <http://www.nalgenunc.co.jp/data/bulletins/06.htm>
62. Winterhalter, M., Black lipid membranes. *Current Opinion In Colloid & Interface Science* **2000**, 5, (3-4), 250-255.
63. Richter, R. P.; Brisson, A. R., Following the formation of supported lipid bilayers on mica: A study combining AFM, QCM-D, and ellipsometry. *Biophysical Journal* **2005**, 88, (5), 3422-3433.
64. Sackmann, E., Supported membranes: Scientific and practical applications. *Science* **1996**, 271, (5245), 43-48.
65. Giess, F.; Friedrich, M. G.; Heberle, J.; Naumann, R. L.; Knoll, W., The protein-tethered lipid bilayer: A novel mimic of the biological membrane. *Biophysical Journal* **2004**, 87, (5), 3213-3220.
66. Friedrich, M. G.; Giess, F.; Naumann, R.; Knoll, W.; Ataka, K.; Heberle, J.; Hrabakova, J.; Murgida, D. H.; Hildebrandt, P., Active site structure and redox processes of cytochrome c oxidase immobilised in a novel biomimetic lipid membrane on an electrode. *Chemical Communications* **2004**, (21), 2376-2377.
67. Ataka, K.; Giess, F.; Knoll, W.; Naumann, R.; Haber-Pohlmeier, S.; Richter, B.; Heberle, J., Oriented attachment and membrane reconstitution of his-tagged cytochrome c oxidase to a gold electrode: In situ monitoring by surface-enhanced infrared absorption spectroscopy. *Journal of the American Chemical Society* **2004**, 126, (49), 16199-16206.
68. Raguse, B.; Braach-Maksvytis, V.; Cornell, B. A.; King, L. G.; Osman, P. D. J.; Pace, R. J.; Wiczorek, L., Tethered lipid bilayer membranes: Formation and ionic reservoir characterization. *Langmuir* **1998**, 14, (3), 648-659.
69. Baumgart, T.; Kreiter, M.; Lauer, H.; Naumann, R.; Jung, G.; Jonczyk, A.; Offenhausser, A.; Knoll, W., Fusion of small unilamellar vesicles onto laterally mixed self-assembled monolayers of thiolopeptides. *Journal of Colloid and Interface Science* **2003**, 258, (2), 298-309.
70. Doshi, D. A.; Dattelbaum, A. M.; Watkins, E. B.; Brinker, C. J.; Swanson, B. I.; Shreve, A. P.; Parikh, A. N.; Majewski, J., Neutron reflectivity study of lipid membranes assembled on ordered nanocomposite and nanoporous silica thin films. *Langmuir* **2005**, 21, (7), 2865-2870.
71. Worsfold, O.; Voelcker, N. H.; Nishiya, T., Biosensing using lipid bilayers suspended on porous silicon. *Langmuir* **2006**, 22, (16), 7078-7083.
72. Drexler, J.; Steinem, C., Pore-suspending lipid bilayers on porous alumina investigated by electrical impedance spectroscopy. *Journal of Physical Chemistry B* **2003**, 107, (40), 11245-11254.
73. Naumann, R.; Schiller, S. M.; Giess, F.; Grohe, B.; Hartman, K. B.; Karcher, I.; Koper, I.; Lubben, J.; Vasilev, K.; Knoll, W., Tethered lipid Bilayers on ultraflat gold surfaces. *Langmuir* **2003**, 19, (13), 5435-5443.
74. Smith, P. E.; Brunne, R. M.; Mark, A. E.; Vangunsteren, W. F., Dielectric-Properties of Trypsin-Inhibitor and Lysozyme Calculated from Molecular-Dynamics Simulations. *Journal of Physical Chemistry* **1993**, 97, (9), 2009-2014.
75. Stöcker, H., Taschenbuch der Physik. *Verlag Harri Deutsch* **1998**, 3., völlig überarbeitete und erweiterte Auflage, Seite 422.
76. Yoshikawa, S.; Shinzawa-Itoh, K.; Nakashima, R.; Yaono, R.; Yamashita, E.; Inoue, N.; Yao, M.; Fei, M. J.; Libeu, C. P.; Mizushima, T.; Yamaguchi, H.; Tomizaki, T.;

Tsukihara, T., Redox-coupled crystal structural changes in bovine heart cytochrome c oxidase. *Science* **1998**, 280, (5370), 1723-1729.

77. FergusonMiller, S.; Babcock, G. T., Heme/copper terminal oxidases. *Chemical Reviews* **1996**, 96, (7), 2889-2907.

78. [http://www.chups.jussieu.fr/polys/biochimie/RMbioch/RM\\_32\\_PICT.jpg](http://www.chups.jussieu.fr/polys/biochimie/RMbioch/RM_32_PICT.jpg), cytochrome c structure.

79. Svensson-Ek, M.; Abramson, J.; Larsson, G.; Tornroth, S.; Brzezinski, P.; Iwata, S., The X-ray crystal structures of wild-type and EQ(I-286) mutant cytochrome c oxidases from *Rhodobacter sphaeroides*. *Journal of Molecular Biology* **2002**, 321, (2), 329-339.

## 5. Gold/Silica Composite Inverse Opals

### **5.1 Advantage of gold/silica composite inverse opals - new plasmonic material and the aim of the study**

Nanostructured metal materials strongly attracted the interest of scientists, as mentioned above [Chapter 4, NPG], and various surface patterning methods are known, such as chemical patterning<sup>1</sup>, laser patterning<sup>2</sup>, etc. In chapter 4 random nanoporous gold substrates were investigated, whereas here, 3D macroporous, well defined gold coated structures from colloidal crystal templates were examined.

Using self-assembled colloidal crystals (synthetic opals) as templates, highly ordered interconnected macroporous films (so-called “inverse opals”)<sup>3</sup> were created. These structures exhibit special features and are of interest for catalysts, bioreactors, photonic and phononic band gap materials etc<sup>4-12</sup>.

Inverse opals from a variety of materials, such as metals, inorganic oxides, or polymers, have been created by utilizing colloidal crystal templates. With traditional patterning procedures, for instance photolithography<sup>13</sup>, soft lithography<sup>14</sup> and holographic patterning<sup>15</sup>, it is difficult, or even impossible to fabricate such kind of ordered 3D array with highly structural quality. However, colloidal crystal self-assembly is an easy, inexpensive and efficient mass production method<sup>16, 17</sup>. Recent work has been done on the preparation and characterization of binary colloidal crystals<sup>18-20</sup>. In this study, multilayered colloidal crystal substrates fabricated by vertical lifting deposition were used.

The aim of this section is to further explore established plasmonic techniques on silica inverse opals with bio- or chemical sensing applications in mind. For this special application gold nanoparticles were deposited onto the silica inverse opal wall and electroless plating was used to prepare so called gold/silica composite inverse opals [Chapter 5.2]. Gold nanoparticles alone feature interesting physical properties, such as localized surface plasmon resonances (L-SPR)<sup>21, 22</sup> giving rise to, e.g., surface enhanced Raman scattering (SERS)<sup>23</sup>. But here, inverse opals were used as a substrate to host gold nanoparticles in order to investigate the optical features that may be created as a combinatory result of both the ordered macropores and the L-SPR from the nano metallic particles.

The substantially enhanced available surface area of the three dimensional gold/silica composite inverse opals is an additional advantage towards biosensing applications.

## 5.2 Fabrication of gold/silica composite inverse opals

BK7 glass substrates were cleaned by piranha solution ( $\text{H}_2\text{O}_2 : \text{H}_2\text{SO}_4 = 30 : 70$ , v/v. Caution: piranha solution reacts violently with organic compounds) and subsequently washed with copious amounts of Milli Q water (ultrapure water, Milli-Q system from Millipore GmbH, Eschborn, Germany).

Monodisperse polystyrene latex particles ( $d = 626 \pm 16$  nm) were prepared by emulsion polymerisation<sup>24</sup> and were purified by several cycles of centrifugation and re-dispersion in Milli Q water. The particle size was measured by dynamic light scattering with a Zeta Sizer 3000 HS (Malvern Instrument Ltd.)<sup>25</sup> and confirmed by SEM [Chapter 2.4]. Silica nanoparticles ( $d = 10$  nm) were provided by EKA Chemicals.

The formation of a binary colloidal crystal multilayer film was obtained from the colloidal suspension of the mixture of polystyrene and silica particles by using the so-called vertical lifting deposition method<sup>26</sup>. A concentration of 0.01 w/v polystyrene was used in order to form a high quality crystal.

The cleaned glass slides were lifted out of the colloidal suspension by a home made dipping devise (Figure 5.2.1). The optimized lifting speed was  $0.2 \mu\text{m s}^{-1}$ . Hence, the large crystal-forming polystyrene latex particles (the sacrificial template) and the replica-forming silica nanoparticles (the matrix material filling the interstitial space) were deposited simultaneously.

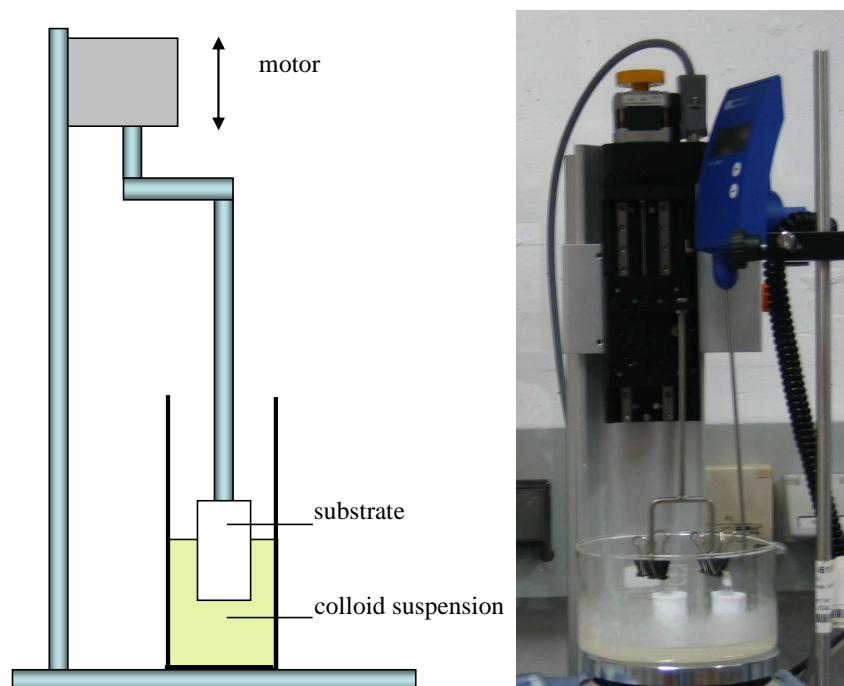
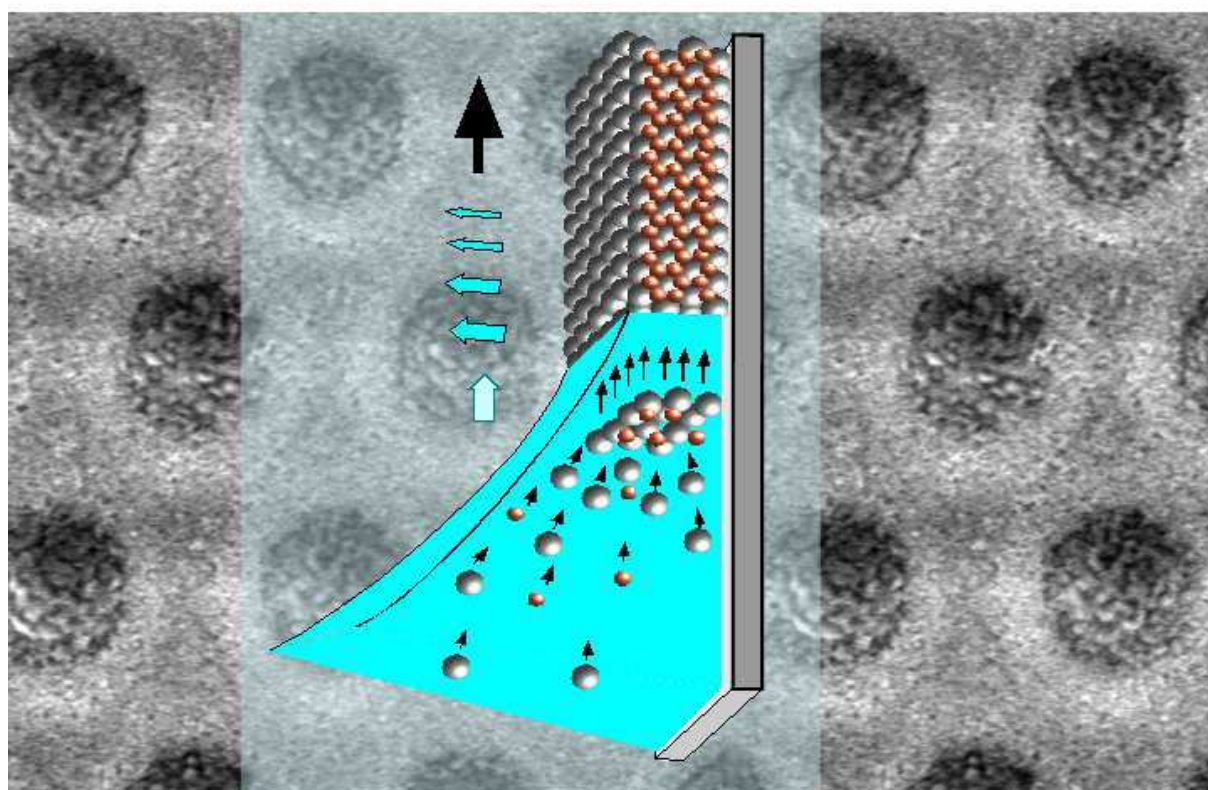


Figure 5.2.1: A) Schematic and B) photographic picture of the dip coating setup

By vertical lifting, preparation of colloidal crystal multilayers with high order and large dimensions, practically over several square centimetres, was achieved within 15 hours. This technique relies on the particle transport and deposition at the growing crystal front (confer Figure 5.2.2), which is induced by the liquid flow from the suspension bulk to the drying crystal layer (besides capillary forces at the liquid-air interface)<sup>27-29</sup>. The common lattice geometry generally formed by vertical lifting deposition is the close-packed face-centered cubic lattice (fcc) with the (111) plane parallel to the substrate interface. Large clusters of the silica nanoparticles were embedded within the interstitial space of the fcc lattice between the large polystyrene particles without disrupting the crystal order.



**Figure 5.2.2:** Schematic representation of the particle transfer and crystallization mechanism during vertical lifting deposition, which is largely driven by the liquid and particle flux from the suspension bulk to the porous crystal layer, where the liquid is evaporating. The black arrows show the lifting direction and the cyan arrows demonstrate the water evaporation. In the background an original SEM of a binary colloid crystal sample from a mixed suspension of large (626 nm) polystyrene colloids and silica nanoparticles (10 nm) is shown.

The formed composite films consisting of polystyrene microspheres and silica nanoparticles were used to fabricate inverse opals by annealing the film at 450°C in air in order to remove the polystyrene template and sinter the silica nanoparticle matrix. The top view of the resulting macroporous film is shown in Figure 5.2.3) with the void diameter of

620 ± 11 nm being comparable to the diameter of the templating PS microspheres ( $d = 626 \pm 16$  nm), which indicates a negligible shrinkage during the pyrolysis. The inset with higher magnification revealed that each air sphere is connected with its neighbours by round holes resulting from the contact points of the templating polystyrene particles. The image in Figure 5.2.3 at lower magnification together with the inset, the fast Fourier transformation (FFT) of this image, shows that the domain of the perfect crystals film with pronounced hexagonal lattice geometry between cracks can be as large as several hundred microns. Due to the sintering process at 450°C the fabricated film is mechanically robust and thermally stable, which renders it strong enough for further processing such as washing with water, blowing with nitrogen, and further wet-chemical surface modification.

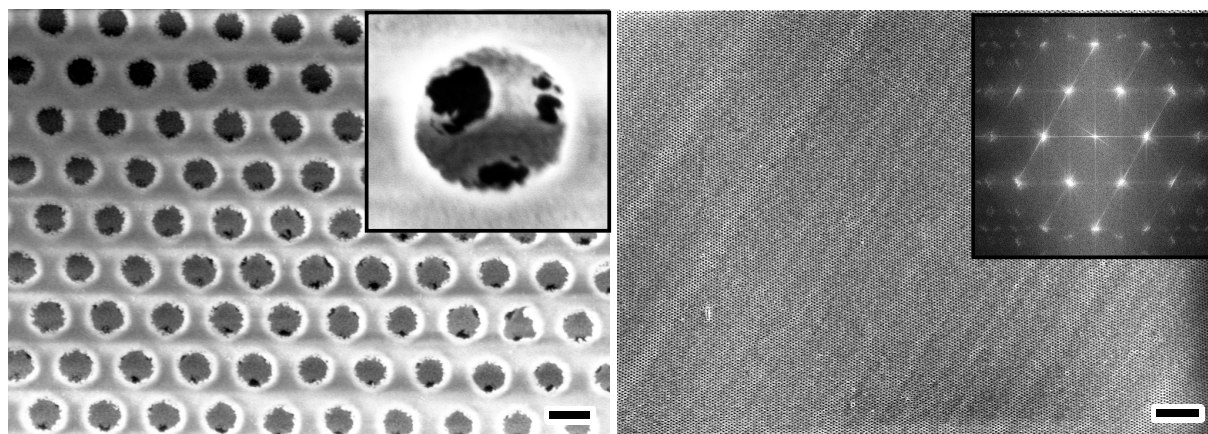


**Figure 5.2.3:** Scanning electron micrographs show the top view of inverse opals obtained by calcination of the film with optimal parameters. The scale bar of the left image is 500 nm and of the right image is 10 μm. The left inset is taken at a very high magnification. The right inset with the fast Fourier transformation (FFT) demonstrates the hexagonal lattice geometry.

Next, the silica inverse opal wall was functionalized with a positively charged silane,  $NR_4^+$  (N-trimethoxysilylpropyl- N, N, N- trimethylammonium chloride)<sup>30</sup> (Figure 5.2.4) [Chapter 3.7 silanization procedure]. In the next step, negatively charged gold nanoparticles ( $d = 20$  nm) were deposited from suspension onto the positively charged, silane modified silica inverse opal wall as shown in the SEM image, Figure 5.2.5 A, which reveals the individual gold particles adsorbed on the silica inverse opal wall through the electrostatic attraction via anchored cationic  $NR_4^+$  groups. The spacing between the gold nanoparticles is caused by interparticle Coulomb repulsions<sup>31</sup>. During the following electroless plating, adsorbed gold nanoparticles behaved as catalysts and seeds, with  $Au^{3+}$  from solution being reduced by hydroxylamine-hydrochloride<sup>32</sup> resulting in an increment in diameter of the existing gold nanoparticles. The plating time was set to 10 minutes, so that a thin granular

gold film was formed along the silica inverse opal scaffold with the openings of the composite inverse opal being preserved as shown in the SEM image, Figure 5.2.5 B.

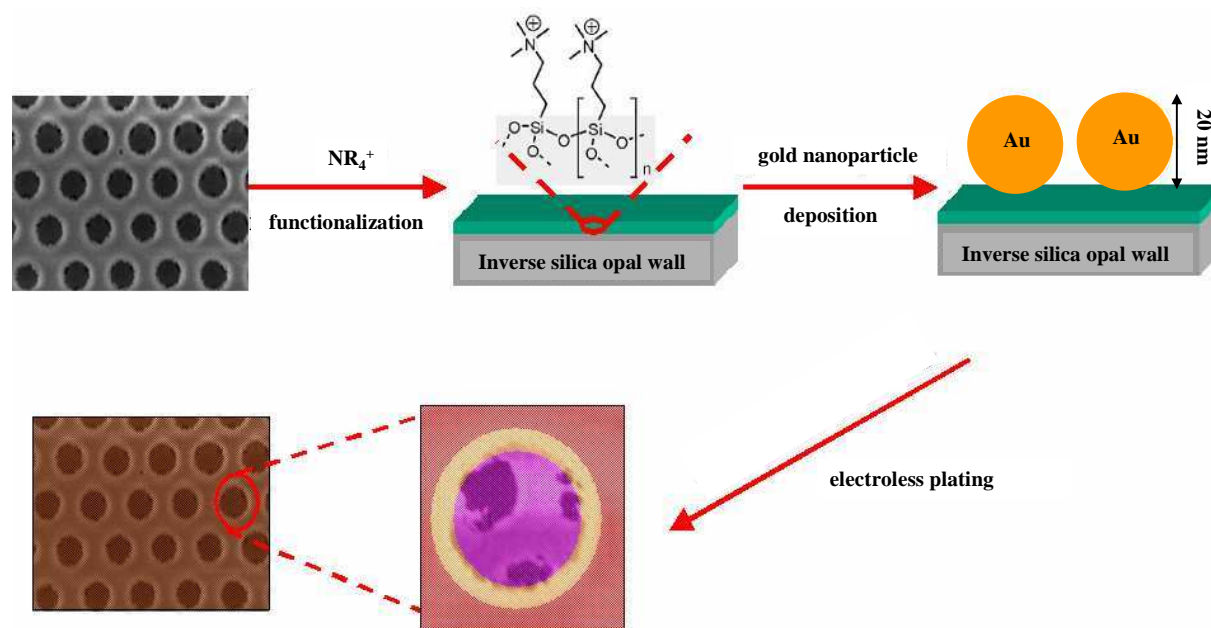


Figure 5.2.4: Scheme of the fabrication of gold/silica composite inverse opals starting from a sintered silica nanoparticle matrix.

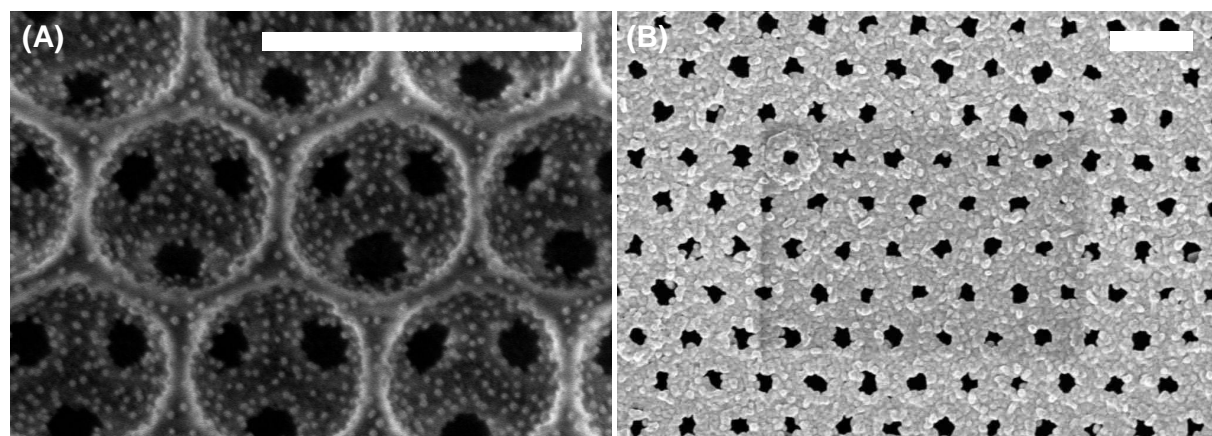


Figure 5.2.5: (A) SEM image of gold nanoparticles with a diameter of 20 nm deposited on walls of silica inverse opals. (B) Gold/silica composite inverse opal obtained after electroless plating. The scale bars are 1  $\mu\text{m}$ , respectively.

Fracture SEM images revealed that the whole three dimensional structure of the silica nanoparticle matrix was covered by gold particles, thus a complete gold coverage was achieved by subsequent electroless plating. The holes that resulted from the contact points of the templating polystyrene particles guarantee the accessibility of the greatly enhanced gold covered surface area for the bio-molecules to allow for sensing applications.

### 5.3 Surface plasmon resonance features of gold/silica composite inverse opals

In order to examine the plasmonic response of gold/silica composite inverse opals to the changes of the surrounding refractive index, visible light reflection absorption spectra were measured while tuning the refractive index (RI) of the dielectric medium within the inverse opals by immersing the composite films in water/glycerol mixture of different composition; the same procedure as described for the investigations of localized plasmons on nanoporous gold (NPG) samples [Chapter 4.6.2]. Representative reflection absorption spectra of gold/silica composite inverse opals are shown in Figure 5.3.1.

Relative changes in surface reflectivity again were recorded using the fiber-optic spectrometer [Chapter 3.1]. The reflectivity was measured perpendicular to the (111) plane of the gold/silica composite inverse opals. An ‘apparent absorbance’ was obtained by calculating  $\log(I(n)/I(n_0))$  with  $n$  and  $n_0$  being the refractive index of the surrounding medium and pure water respectively.

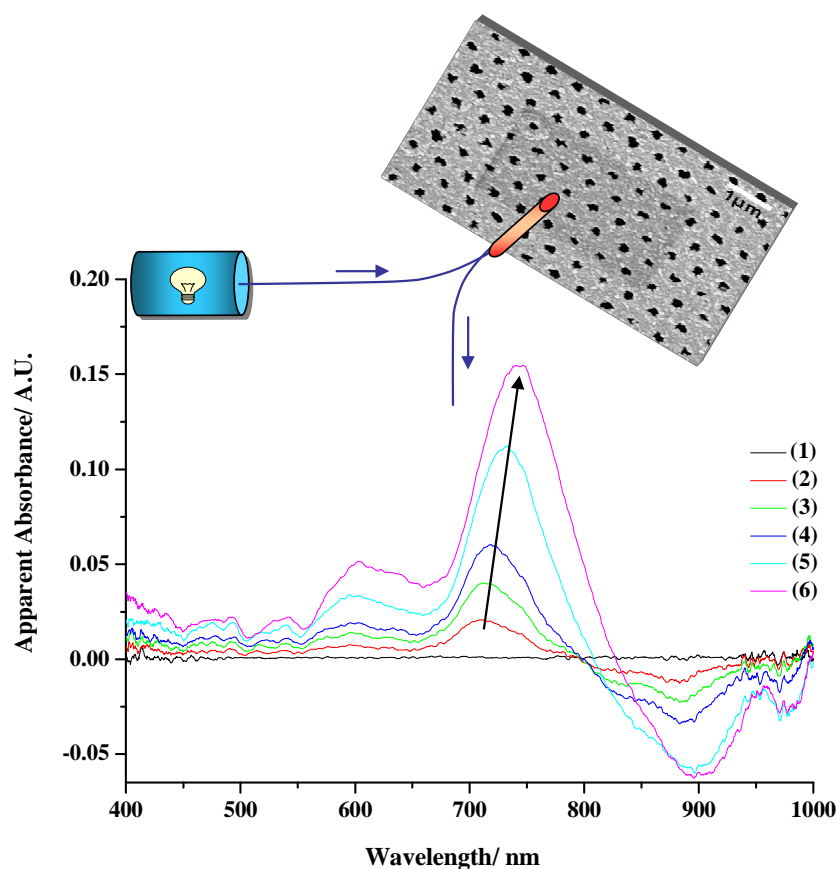


Figure 5.3.1: Evolution of the apparent absorbance spectra of a gold/silica composite inverse opal immersed in solutions of increasing glycerol concentration: (1) pure water, RI=1.333, (2) 10 % RI=1.346, (3) 20 % RI=1.359, (4) 30 % RI=1.372, (5) 60 % RI=1.410; (6) 87 % RI=1.445; the RI of the glycerol solutions are calculated by the mass fraction of glycerol in water.

As a prominent feature in Figure 5.3.1, an increase in the apparent absorbance was seen around  $\lambda = 730$  nm and a corresponding decrease around  $\lambda = 890$  nm. This represents a clear signal due to refractive index changes which is measured by standard laboratory equipment in a straightforward fashion. This spectral feature is due to an extinction peak around  $\lambda = 790$  nm which is shifting to longer wavelength with increasing  $n$ .

The increase of the peak intensity was explained [Chapter 4.6.2] in the context of the nanoporous gold substrates and holds for the gold/silica composite inverse opals as well. But in the case of the gold/silica composite inverse opals, a much sharper peak of the apparent absorbance and a much more distinct shift in the peak position was observed due to the regularity of the sample. The corresponding decrease of the apparent absorbance, that was predicted from the calculations [Chapter 4.6.2], and was not seen in the absorbance spectra of the NPG substrates due to the broadened peak that resulted from the randomly distributed pores. Here it was confirmed by the optic measurements on the gold/silica composite inverse opals. The peak intensity of the gold/silica composite inverse opals was higher compared to the intensities obtained for the NPG samples.

All these observations are consistent and thus were explainable by the properties of the substrates, random structured NPG and highly ordered gold/silica composite inverse opals, respectively.

### **5.4 Conclusion and Outlook**

In conclusion, binary colloidal crystals with a thickness of several ten layers were directly co-crystallized across a uniform area of several square centimeters within 15 hours by vertical lifting deposition from suspension of binary colloidal mixture. The lattice type of the formed crystals was the close-packed face-centered cubic lattice (fcc) with the (111) plane parallel to the substrate interface. Typical structural defects, like point defects (e.g. vacancies), line defects (e.g. dislocations), planar defects (e.g. stacking faults), and cracks, usually present in colloidal crystals formed by vertical deposition<sup>33, 34</sup> were also found in this material. But in this study, the defect density was significantly reduced at the appropriate preparation conditions. This might be due to variations of the evaporation kinetics and capillary condensation effects in the mesoporous structure formed by the hydrophilic silica nanoparticles between the polystyrene colloids in contrast to other colloidal materials.

By calcination of the high quality inverse opals, following silanization, gold deposition and electroless plating an optically interesting sample substrate was fabricated.

This hierarchical composite porous material showed a distinct response to the changes of refractive index of the surrounding medium, which may offer a significant potential for a bio-/chemo-sensing platform.

Compared to the nanoporous gold (NPG) substrates discussed in the previous chapter [Chapter 4], the gold/silica composite inverse opals showed a much sharper peak of the apparent absorbance and a much more distinct shift in the peak position due to the regularity of the sample. Actually, a much higher optical signal was obtained than in the case of the NPG that promised sensitive detection.

Both substrates possess an enhanced surface area compared to a flat, dense gold film. But the accessibility for biomolecules is expected to be quite different. The NPG substrates have limitations due to the average pore size of around 7 - 28 nm, while the gold/silica composite inverse opals offer sufficient large pores up to ~ 100 nm to allow for unhindered protein diffusion. In future, this material may be used to probe bio-recognition reactions.

Some future work may include further sample development, such as tuning of the pore size and entire sample thickness by variation of the polystyrene or silica particle size as well.

## 5.5 References

1. Shukla, N.; Svedberg, E. B.; Ell, J., FePt nanoparticle adsorption on a chemically patterned silicon-gold substrate. *Surface & Coatings Technology* 2006, 201, (3-4), 1256-1261.
2. Hoche, T.; Bohme, R.; Gerlach, J. W.; Rauschenbach, B.; Syrowatka, F., Nanoscale laser patterning of thin gold films. *Philosophical Magazine Letters* 2006, 86, (10), 661-667.
3. Tian, S. J.; Wang, J. J.; Jonas, U.; Knoll, W., Inverse opals of polyaniline and its copolymers prepared by electrochemical techniques. *Chemistry of Materials* 2005, 17, (23), 5726-5730.
4. Wijnhoven, J.; Vos, W. L., Preparation of photonic crystals made of air spheres in titania. *Science* 1998, 281, (5378), 802-804.
5. Braun, P. V.; Wiltzius, P., Microporous materials - Electrochemically grown photonic crystals. *Nature* 1999, 402, (6762), 603-604.
6. Tetreault, N.; Miguez, H.; Ozin, G. A., Silicon inverse opal - A platform for photonic bandgap research. *Advanced Materials* 2004, 16, (16), 1471-1476.
7. Lodahl, P.; van Driel, A. F.; Nikolaev, I. S.; Irman, A.; Overgaag, K.; Vanmaekelbergh, D. L.; Vos, W. L., Controlling the dynamics of spontaneous emission from quantum dots by photonic crystals. *Nature* 2004, 430, (7000), 654-657.
8. Jiang, P., Surface-templated nanostructured films with two-dimensional ordered arrays of voids. *Angewandte Chemie-International Edition* 2004, 43, (42), 5625-5628.
9. Cassagneau, T.; Caruso, F., Conjugated polymer inverse opals for potentiometric Biosensing. *Advanced Materials* 2002, 14, (24), 1837-1841.
10. Cassagneau, T.; Caruso, F., Inverse opals for optical affinity biosensing. *Advanced Materials* 2002, 14, (22), 1629-1633.
11. Wang, Y. J.; Caruso, F., Macroporous zeolitic membrane bioreactors. *Advanced Functional Materials* 2004, 14, (10), 1012-1018.
12. Wang, Y. J.; Caruso, F., Enzyme encapsulation in nanoporous silica spherest. *Chemical Communications* 2004, (13), 1528-1529.
13. General reviews on photolithography: *Optical Lithography* 1997, a special issue of *IBM J. Res. Dev.*, (1-2,3).
14. Xia, Y. N.; Whitesides, G. M., Soft lithography. *Annual Review of Materials Science* 1998, 28, 153-184.
15. Hariharan, P., *Optical Holography: Principles, Techniques, and Applications* 1996, 2nd ed.; Cambridge University Press: New York.
16. Glotzer, S. C.; Solomon, M. J.; Kotov, N. A., Self-assembly: From nanoscale to microscale colloids. *Aiche Journal* 2004, 50, (12), 2978-2985.
17. Norris, D. J.; Arlinghaus, E. G.; Meng, L. L.; Heiny, R.; Scriven, L. E., Opaline photonic crystals: How does self-assembly work? *Advanced Materials* 2004, 16, (16), 1393-1399.
18. Bartlett, P.; Ottewill, R. H.; Pusey, P. N., Superlattice Formation in Binary-Mixtures of Hard-Sphere Colloids. *Physical Review Letters* 1992, 68, (25), 3801-3804.
19. Velikov, K. P.; Christova, C. G.; Dullens, R. P. A.; van Blaaderen, A., Layer-by-layer growth of binary colloidal crystals. *Science* 2002, 296, (5565), 106-109.
20. Leunissen, M. E.; Christova, C. G.; Hynninen, A. P.; Royall, C. P.; Campbell, A. I.; Imhof, A.; Dijkstra, M.; van Roij, R.; van Blaaderen, A., Ionic colloidal crystals of oppositely charged particles. *Nature* 2005, 437, (7056), 235-240.
21. Link, S.; El-Sayed, M. A., Spectral properties and relaxation dynamics of surface plasmon electronic oscillations in gold and silver nanodots and nanorods. *Journal of Physical Chemistry B* 1999, 103, (40), 8410-8426.

22. Coyle, S.; Netti, M. C.; Baumberg, J. J.; Ghanem, M. A.; Birkin, P. R.; Bartlett, P. N.; Whittaker, D. M., Confined plasmons in metallic nanocavities. *Physical Review Letters* 2001, 8717, (17).
23. Lim, J. K.; Joo, S. W.; Shin, K. S., Concentration dependent Raman study of 1,4-diethynylbenzene on gold nanoparticle surfaces. *Vibrational Spectroscopy* 2007, 43, (2), 330-334.
24. Wang, J., Colloidal Crystals: Preparation, Characterization, and Applications. *PhD Thesis* 2006, University of Mainz (Chapter 2).
25. Wang, J., Colloidal Crystals: Preparation, Characterization, and Applications. *PhD Thesis* 2006, University of Mainz (Chapter 2), pages 25 and 26
26. Wang, J., Colloidal Crystals: Preparation, Characterization, and Applications. *PhD Thesis* 2006, University of Mainz (Chapter 3).
27. Fan, F. Q.; Stebe, K. J., Assembly of colloidal particles by evaporation on surfaces with patterned hydrophobicity. *Langmuir* 2004, 20, (8), 3062-3067.
28. Fan, F. Q.; Stebe, K. J., Size-selective deposition and sorting of lyophilic colloidal particles on surfaces of patterned wettability. *Langmuir* 2005, 21, (4), 1149-1152.
29. Fustin, C. A.; Glasser, G.; Spiess, H. W.; Jonas, U., Parameters influencing the templated growth of colloidal crystals on chemically patterned surfaces. *Langmuir* 2004, 20, (21), 9114-9123.
30. Jonas, U.; Krüger, C., The Effect of Polar, Nonpolar, and Electrostatic Interactions and Wetting Behavior on the Particle Assembly at Patterned Surfaces. *J. Supramol. Chem.* 2002, 2 (1-3), 255-270.
31. Liang, Z. J.; Susha, A.; Caruso, F., Gold nanoparticle-based core-shell and hollow spheres and ordered assemblies thereof. *Chemistry of Materials* 2003, 15, (16), 3176-3183.
32. Brown, K. R.; Natan, M. J., Hydroxylamine seeding of colloidal Au nanoparticles in solution and on surfaces. *Langmuir* 1998, 14, (4), 726-728.
33. Jiang, P.; Bertone, J. F.; Hwang, K. S.; Colvin, V. L., Single-crystal colloidal multilayers of controlled thickness. *Chemistry of Materials* 1999, 11, (8), 2132-2140.
34. Gu, Z. Z.; Fujishima, A.; Sato, O., Fabrication of high-quality opal films with controllable thickness. *Chemistry of Materials* 2002, 14, (2), 760-765.

## 6. Epitope mapping to identify the centrin sequence interacting to transducin

### 6.1 Processes of optical signaling

The third part of this thesis focuses on the protein/protein interaction of the calcium binding protein centrin [Chapter 6.3] with the heterotrimeric G-protein transducin [Chapter 6.2]. While the centrin is ubiquitously expressed in eukaryotic cells, the expression of the transducin alpha subunit ( $G_t\alpha$ ) is restricted to photoreceptor cells. In the context of the photoreceptor cell, the anatomy of the human eye and the visual signal transduction cascade are described briefly.

An eye is a specialized organ of vision that detects photons. Light enters through the pupil, and is focused by the cornea and the lens onto the retina (Figure 6.1.1). The ciliary muscle allows for exact focusing by changing the shape (thickness and curvature) of the lens. The suspensory ligaments support the lens and connect it to the ciliary muscle. The sclera (“white of the eye”), a tough and fibrous outer layer, covers and protects the whole eye except for the cornea. The cornea is protected by the conjunctiva, a membrane that is kept moist by the tear glands.



**Figure 6.1.1:** A photograph of a human eye (left). Schematic presentation of a human eye<sup>1</sup> (right).

The retina and the optic nerve originate as outgrowths of the developing brain<sup>2-4</sup>. The retina<sup>5</sup> is a network of nerve cells containing two types of photosensitive cells, rods and cones that are important for vision. Rod cells are highly sensitive to dim light and black/white detection. In contrast, cones need higher light intensities to respond and detect color. Directly behind the lens is the localization of the fovea (human) that consists of mostly densely-packed cone cells. The pigmented iris decides the color of the eye (Figure 6.1.1 (left)) and protects the photoreceptors in the retina from being damaged by too high light intensities.

Furthermore, light shines through all layers of neuronal retinal cells before hitting the light sensitive photoreceptor cells. Hence, the vertebrate eye is also called inverse eye.

The structure of a rodent's retina is comparable to the structure of a human retina. In contrast to the human retina, the retina of rodents is adjusted to the nocturnal behavior of the animal. Therefore, the mouse retina possesses no fovea and consists of ~97,2 % rods and only ~2,8 % cones that are distributed homogeneously all over the retina<sup>6,7</sup>.

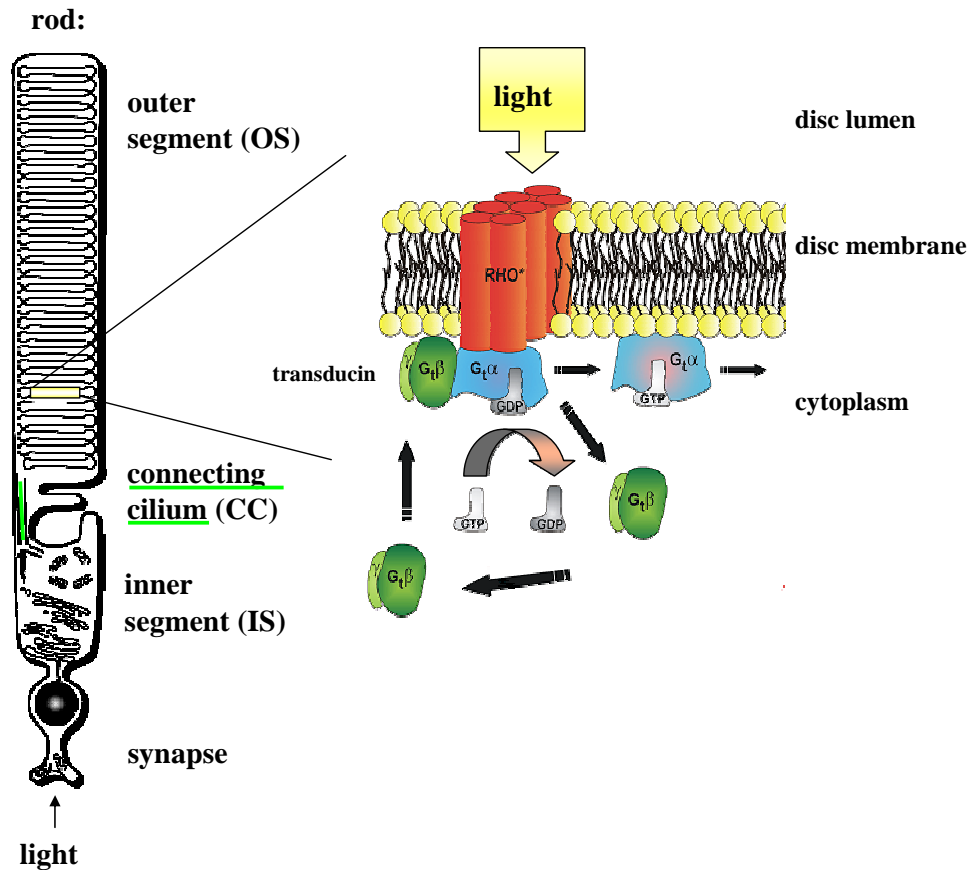
Vertebrate photoreceptor cells (PRC) offer morphological and functional structuring in several compartments (Figure 6.1.2). The nucleus is arranged next to the basal end with the synaptic connection. Energy producing and protein synthesizing components are located in the inner segment (IS), while the light absorbing machinery is concentrated in the outer segment (OS). All proteins synthesized in the inner segment but required for the outer segment have to pass through a narrow non-motile connecting cilium (CC) as an intracellular linkage between inner and outer segment.

#### 6.1.1. The vertebrate visual signal transduction cascade

The visual signal transduction pathway in rods is the mechanism by which the energy of an incoming photon results in an electrical hyperpolarization of the photoreceptor cell (PRC). This hyperpolarization leads to the transmittance of a neuronal signal that reaches the brain via the optic nerve.

An incoming photon reaches the disc membranes in the outer segment of the photoreceptor cell and is absorbed by the 7-transmembrane-receptor rhodopsin (RHO; a G-protein-coupled-receptor). Rhodopsin consists of opsin, a protein that is reversibly covalently bound to the chromophore 11-cis-retinal<sup>8</sup>, a derivative of vitamin A. The absorption of the photon causes an isomerization of the 11-cis-retinal to the more energetic trans-form. The resulting change in conformation of the rhodopsin<sup>8</sup> leads to the binding of the G-protein transducin (Figure 6.1.2). Each photo activated rhodopsin (RHO\*) triggers activation of about 100 transducins<sup>9,10</sup>. That is the first amplification step.

Opsin is phosphorylated by rhodopsin kinase (GRK1)<sup>11</sup>. Then arrestin<sup>12</sup>, that binds specifically to phosphorylated active G-protein coupled receptors, arrests or reduces signaling by inhibiting transducin binding to rhodopsin in a fast protecting manner.



modified from Giebl, A.; PhD Thesis 2004

**Figure 6.1.2:** Schematic drawing of a rod photoreceptor cell. Due to the inverse eye geometry, the light shines through multi neuronal layers before illuminating the outer segment (OS) of the photoreceptor cells (PRC). The PRC consists of a light sensitive outer segment (OS) that is linked via non-motile connecting cilium (CC) to the inner segment (IS). The signal transduction is taking place in the membrane discs of the outer segment (zoomed in). After the absorption of light and the activation of rhodopsin (RHO\*) the inactive heterotrimeric G-protein transducin ( $G_t\alpha + \text{GDP}$  and  $G_t\beta\gamma$  [Chapter 6.2; Figure 6.2.1]) can be bound. The  $G_t\beta\gamma$  dissociates from the  $G_t\alpha$  subunit and the activated  $G_t\alpha + \text{GTP}$  affects second messenger molecules in the following steps<sup>13, 14</sup>.

Otherwise, the activation of transducin causes the exchange of guanosine diphosphate (GDP) to guanosine triphosphate (GTP) that is bound to the alpha subunit ( $G_t\alpha$ ), respectively, and results in an activated alpha subunit ( $G_t\alpha$ ) dissociating from beta-gamma subunit ( $G_t\beta\gamma$ ) [Chapter 6.2]. Each alpha subunit ( $G_t\alpha$ ) then activates the enzyme cyclic guanosine monophosphate (cGMP)-specific phosphodiesterase (PDE). Phosphodiesterase then catalyzes the hydrolysis of about 1000 cGMP (cyclic guanosine-3'5'-monophosphate) molecules to 5'GMP. That is the second amplification step.

If the intracellular concentration of cGMP is reduced, cGMP dependent  $\text{Na}^+/\text{Ca}^{2+}$  ion channels in the photoreceptor membrane close<sup>15, 16</sup>. As a result,  $\text{Na}^+$  and  $\text{Ca}^{2+}$  ions can no longer enter the cell, and the photoreceptor cell hyperpolarizes<sup>17</sup>. The hyperpolarization of the

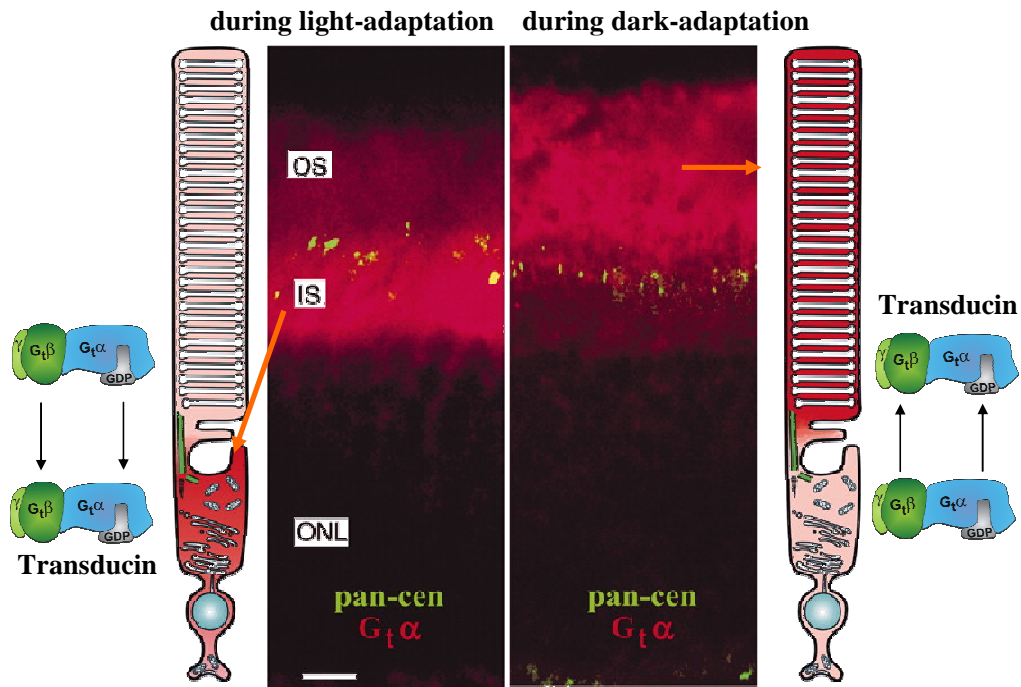
photoreceptor cell slows the release of the neurotransmitter glutamate at its postsynaptic terminal to the bipolar cells<sup>17</sup>. The glutamate affects the bipolar cells (ON- and OFF-bipolar cells) differently, depending upon the type of receptor imbedded in that cell's membrane<sup>18-20</sup>. One population of bipolar cells is excited by light and the other population is inhibited by it. The optic nerve is composed of retinal ganglion cell axons and support cells and passes the signals to the visual cortex.

### 6.1.2. Light and dark adaptation

Light and dark adaptation in human vision describe the remarkable ability of the visual system to automatically adjust its sensitivity to the amount of incoming photons. During dim light conditions, vertebrates need rod photoreceptors for vision. The phenomenon of dark adaptation in the rod cell is complex<sup>8</sup> and still not fully understood. Here, the light and dark adaptation at the subcellular level will be discussed.

Products of light absorption from the photoreceptor outer segment have to be removed, the released retinoid to be recycled to its original isomeric form as 11-cis retinal, the visual pigment rhodopsin to be regenerated<sup>21</sup>, etc. Light induced exchanges of signal cascade components between the outer and inner segment were observed about one decade ago<sup>22-24</sup> and are currently of interest<sup>25, 26</sup>.

The localization of transducin in the vertebrate photoreceptor cell is regulated by light (Figure 6.1.3). In the dark, transducin is concentrated in the outer segments of rod photoreceptor cells, while light adapted rod cells show a high concentration of the translocated transducin in the inner segment<sup>22-24, 27-33</sup>. About 80 % of transducin ( $G_t\alpha$  and  $G_t\beta\gamma$ ) move in minutes from the outer to the inner segment and the cell body of rod photoreceptor cell<sup>29</sup>.  $G_t\alpha$  was more mobile than  $G_t\beta$ , with a half-time of translocation that is ~ 3-fold shorter (5 min for  $G_t\alpha$  versus 12.5 min for  $G_t\beta$ )<sup>29</sup>. A time course of hours was found for the repopulation of  $G_t$  subunits in the outer segment<sup>29</sup>.



modified from Giebl, A.; PhD Thesis 2004

**Figure 6.1.3: Immunolocalization of transducin ( $G_t\alpha$ ) and all centrin isoforms in mouse retinas (pan-cen monoclonal antibody (clone 20H5) detects all four isoforms)<sup>34, 35</sup>. Indirect anti-transducin (red) and anti-centrin (green) immunofluorescence in light adapted mouse retina (left) and dark adapted mouse retina (right). Significant translocation of the  $G_t$  between the inner and outer segment (IS/OS) through the narrow connecting cilium (CC) contributes to the light-dark adaptation of photoreceptor cells. ONL is the outer nuclear layer. Bar, 10  $\mu$ m. Schematic representations of the adapted rod photoreceptor cells are beside the real immunofluorescence pictures. Red color indicates the transducin contribution and green color the centrin localization. For clarity, the directions of transducin movement are also illustrated (outside margin).**

The light dependent translocation of proteins is also known in the case of arrestin that is involved in the signal transduction cascade as well. But the translocation of arrestin happens in the opposite direction to transducin<sup>22, 24, 32</sup>. Light induced translocation processes of proteins have to occur through or along the connecting cilium (CC) that is the only intracellular linkage between the inner and outer segment and allows for bidirectional exchange<sup>36</sup>. Different mechanism for the translocation of diverse proteins via elements of the cytoskeleton, such as actin filaments and microtubules, are discussed<sup>37-39</sup>.

The two proteins, rhodopsin kinase<sup>40</sup> and arrestin<sup>41</sup>, inactivate metarhodopsin, the active state of rhodopsin, in a fast manner to protect against to high light intensities (see above). The phenomenon of translocation of transducin is a much slower process, but reduces the sensitivity to light without changing the kinetic answer<sup>42</sup>. Therefore, the translocation-function of transducin and arrestin may be described as “molecular sunglasses”<sup>42, 43</sup>.

During translocation process centrins are potential interaction partners of transducin<sup>43</sup>. Centrin 1, 2, 3 and 4 [Chapter 6.3] are components of the cytoskeleton of the connecting cilium<sup>44, 45</sup>. Double immunofluorescence analyses with antibodies detecting transducin and centrin showed clearly colocalization of the two proteins in the connecting cilium. Actually, electro microscopic immunolocalization of the proteins and quantification of the labeled areas revealed that centrin and transducin are indeed colocalized at the inner surface of the microtubule ring<sup>34, 35</sup> in the same subcellular compartment of the connecting cilium (Figure 6.1.3).

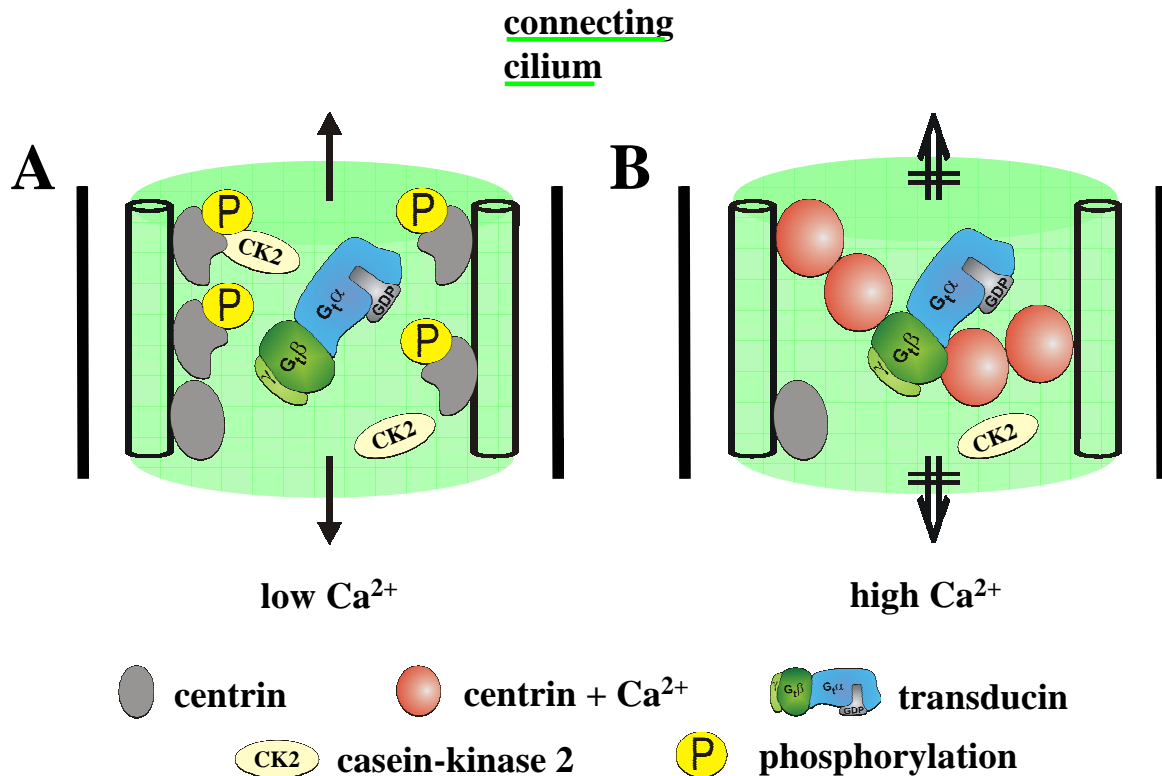
Light modulated changes of the free calcium ions in the outer segment (OS) of the photoreceptor cells are known as well<sup>35, 46-49</sup>. If these changes in the  $\text{Ca}^{2+}$  concentration are transmitted into the connecting cilium,  $\text{Ca}^{2+}$  dependent assembly of centrin-transducin complexes can take place.

### 6.1.3. Barrier hypothesis - relevance of centrin-G-protein complex

Since any intracellular exchange between the outer segment (OS) and the inner segment (IS) should occur through the connecting cilium (CC)<sup>36</sup>, this represents an appropriate domain for regulation processes<sup>45</sup>.

The high affinities of centrin 1 and 2 to the beta-gamma subunit of transducin and the localization in the connecting cilium suggest that the centrins are relevant candidates for this  $\text{Ca}^{2+}$  dependent protein-protein interaction<sup>35</sup>. Centrins may regulate transducin movement through the connecting cilium in a  $\text{Ca}^{2+}$  dependent manner<sup>28, 30, 34, 50</sup> (Figure 6.1.4).

An increase of the intracellular  $\text{Ca}^{2+}$  concentration in the photoreceptor cell should activate the centrins due to the binding of calcium ions. This activation is thought to induce a binding of centrin molecules or centrin oligomers to transducin that is transported through the connecting cilium. It is shown for centrin 1 that only two  $\text{Ca}^{2+}$  ions are needed to form a complex together with transducin<sup>30</sup>. Due to the  $\text{Ca}^{2+}$  dependent interaction, the passage of transducin should be decelerated or rather stopped for high  $\text{Ca}^{2+}$  concentrations (Figure 6.1.4).



modified from Gießl, A.; PhD Thesis 2004

**Figure 6.1.4:** Schematic illustration of the barrier hypothesis.  $\text{Ca}^{2+}$  triggered assembly of centrin-transducin complexes in the connecting cilium of vertebrate photoreceptor cells is thought to regulate transducin movements<sup>26, 34, 35</sup>. (A) Under low  $\text{Ca}^{2+}$  concentrations centrin is phosphorylated and not activated, so that transducin can float through the connecting cilium. Casein kinase 2 (CK2) phosphorylates centrin. (B) High  $\text{Ca}^{2+}$  concentrations cause the centrins to be dephosphorylated and activated by  $\text{Ca}^{2+}$ , which induces also the centrin-transducin complex assembly. The centrin-transducin complexes can be composed of either  $\text{G}_i\text{holo}$  or  $\text{G}_i\beta\gamma$  subunits.

It is not yet fully understood, if the heterotrimeric transducin is transported through the connecting cilium or the subunits of transducin move separately through the connecting cilium. Serial tangential sections through the retina show that the translocation of  $\text{G}_i\alpha$  is three times faster than the translocation of  $\text{G}_i\beta\gamma$  from the outer to the inner segment<sup>29</sup> [Chapter 6.1.2]. This result indicates a separate transport<sup>29</sup>. However, a knockout  $\text{G}_i\alpha$  mouse did not show redistribution to the inner segment of  $\text{G}_i\beta\gamma$  alone, which is a hint for the heterotrimeric transducin movement<sup>51, 52</sup>. If this is true, only completed not yet activated  $\text{G}_i\alpha\beta\gamma$  is transported back to the inner segment or the heterotrimeric  $\text{G}_i\alpha\beta\gamma$  has to be formed before passing the connecting cilium<sup>43</sup>.

The accumulation of  $G_t\alpha\beta\gamma$  in the connecting cilium of light adapted retinas suggests a light-induced assembly of centrin-G-protein complexes. It can be concluded that the interaction between centrins and transducin in the connecting cilium is responsible for light dependent translocation of transducin. Changes in the  $Ca^{2+}$  concentration of the rod photoreceptor cells that are needed for interaction have been well characterized<sup>46</sup>. Usually, after light activation of the visual transduction cascade a dramatic decrease in calcium ion concentration in the outer segment is observed. But under light saturated conditions indeed a calcium ion increase in the outer segment is found<sup>47</sup> that can be the  $Ca^{2+}$  source for assembly of centrin-G-protein complexes. To ensure translocation of transducin a low  $Ca^{2+}$  concentration in the connecting cilium is required. No details about the fluctuation of  $Ca^{2+}$  concentration in the connecting cilium are known so far. The assembly of centrin and transducin could build a  $Ca^{2+}$  induced barrier for transducin movements<sup>30</sup>.

The centrin-G-protein complex is expected to dissociate if the  $Ca^{2+}$  concentration drops, so that transducin can float through the connecting cilium<sup>22, 24, 27-30, 32, 33, 38</sup>.

To understand related diseases on the molecular level, it is important to locate and annotate the processes involved in the light perception in the retina.

## 6.2 Characteristics of Transducin

Transducin ( $G_t$ ) is a heterotrimeric guanine nucleotide binding protein (G-protein). The alpha subunit of transducin is naturally only expressed in vertebrate retina photoreceptor cells. In each cell type, rods and cones, a different transducin gene is expressed.

In general, G-proteins are a family of proteins involved in various second messenger cascades. Their signaling mechanism is based on the exchange of guanosine diphosphate (GDP) for guanosine triphosphate (GTP)<sup>53, 54</sup>. Basically, two different classes of G proteins are known, the *small* and the *large* G-proteins. The *small* G-proteins are monomeric. The *large* G-proteins are membrane-associated and made up of alpha ( $\alpha$ ), beta ( $\beta$ ) and gamma ( $\gamma$ ) subunits. These G-proteins are activated by G-protein coupled receptors, that are integral membrane proteins<sup>55</sup>. G-protein coupled receptors represent the largest class of receptors in the mammalian genome. These receptors are involved in the sensations of light, smell, and taste and other regulatory processes.

Transducin consists of a catalytic alpha subunit  $G_t\alpha$  and an inhibitory  $G_t\beta\gamma$  – dimer that play a role in the signal amplification in the visual cascade<sup>53, 54</sup> (Figure 6.2.1). Transducin is a mediator between the light sensitive seven transmembrane receptor rhodopsin and phosphodiesterase<sup>53, 56</sup>. The GTP-activated alpha subunit of transducin hydrolyses cyclic GMP to 5'GMP resulting in a closure of the ion-channels in the plasma membrane<sup>53, 54</sup>. Closing of these ion-channels leads to a hyperpolarization of the photoreceptor cell membrane.

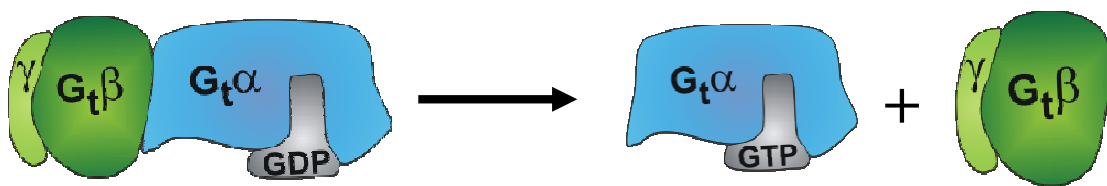


**Figure 6.2.1:** The heterotrimeric transducin (alpha-beta-gamma subunits) is activated by a conformational change in rhodopsin due to the adsorption of a photon [cf. Chapter 6.1.1]. This activation causes the exchange of GDP to GTP that is bound to the alpha subunit, respectively, and results in activated alpha subunit dissociating from beta-gamma subunit.

Generally, the alpha subunits contain two domains, the GTPase domain and the alpha-helical domain. Roughly 20 different types of alpha subunits are discovered. For instance  $G_s$  activates adenylate cyclase,  $G_i$  inhibits adenylate cyclase;  $G_{olf}$  couples to olfactory receptors. A

recently discovered family of G proteins,  $G_q$ , stimulates phospholipase C. Transducin ( $G_t$ ) however couples to rhodopsin.

The  $\beta$  and  $\gamma$  subunits are tightly bound together and are referred as the *beta-gamma complex*. The  $G\beta\gamma$  complex is released from the  $G\alpha$  subunit after the exchange of guanosine diphosphate (GDP) for guanosine triphosphate (GTP)<sup>53</sup>. Free  $G\beta\gamma$  complexes can activate other second messengers or gate ion channels. Table 6.2.1 summarizes the characteristics of the three subunits of transducin extracted from the bovine retina.

**Table 6.2.1: Characteristics of the three subunits of transducin extracted from the bovine retina (bos taurus). Omega software was used to calculate the values for the different protein subunits (Omega: Programmes „Omega 2.0“; company: Oxford Molekular Ltd.)**

Protein	Molecular weight, MW	Length	Isoelectric point, pI	Charge at pH 7.0
Alpha subunit $G_t\alpha$	39.965 kDa	350 aa	5.331	-9.643
Beta subunit $G_t\beta$	37.377 kDa	340 aa	5.490	-7.127
Gamma subunit $G_t\gamma$	8.544 kDa	74 aa	4.508	-5.172

In search of centrin 1 interaction partners located in the vertebrate retina, a  $Ca^{2+}$  dependent interaction with the  $G_t\beta$  subunit was found in a testing system so called overlay-assay. Coimmunoprecipitation experiments confirmed that also the heterotrimeric G-protein is an interaction partner of centrins. In the following surface plasmon resonance studies only the  $G_t\beta\gamma$  complex was immobilized on the surface to probe centrin interactions [Chapter 6.6]. Figure 6.2.2 shows the  $G_t\beta\gamma$  subunits in three different perspectives.

The extracted and purified transducin  $G_t\beta\gamma$  subunits from the bovine retina were kindly provided by Alexander Pulvermüller; lab of Klaus Peter Hofmann, Institut für Medizinische Physik und Biophysik, Charité – Universitätsmedizin Berlin, Ziegelstr. 5-9, D-10098 Berlin, Germany.

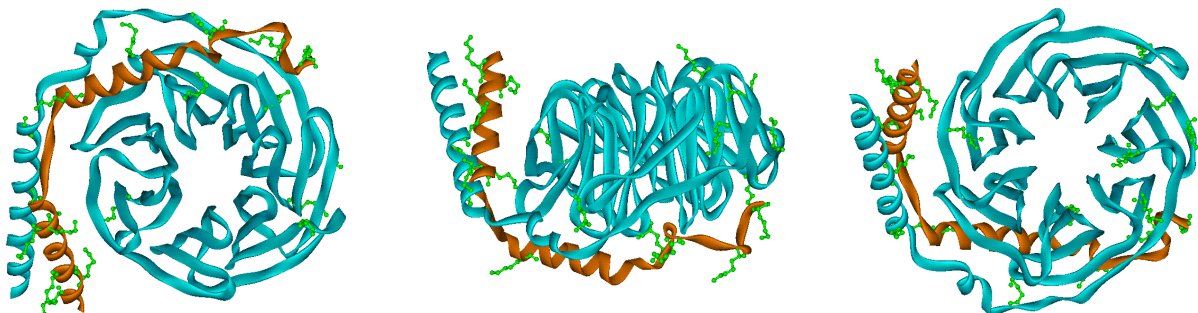


**Figure 6.2.2: The beta and gamma subunits of the G-protein transducin are shown in three different perspectives (determined by x-ray crystal structure). The larger beta subunit is pictured in blue, the gamma subunit in brown. The seventeen accessible lysine moieties are presented in green.**

### 6.3 Centrins in the vertebrate cells

The centrins are relatively small acidic proteins with a molecular weight of about 20 kDa (~ 170 aa). Centrins are phospho proteins and belong to the parvalbumin superfamily of the calcium binding proteins<sup>57, 58</sup>. Centrins contain like the second messenger calmodulin<sup>57, 58</sup> four EF-hand motifs, that are Ca<sup>2+</sup> binding helix-loop-helix structural motifs. The term EF-hand stems actually from the two flanking  $\alpha$ -helices E and F, that are positioned roughly perpendicular to one another. They look like a hand with helix E as the thumb and helix F as the index finger. The predicted 3D structure<sup>59</sup> of human centrin 1 is shown in Figure 6.3.1.

During evolution some EF motifs apparently lost their ability of Ca<sup>2+</sup> binding. Human centrins 1 and 2 bind two moles of calcium per mole of protein (EF1 or EF3 and EF4)<sup>59</sup>, whereas centrin isoforms 3 and 4 bind only one mole of calcium per mole of protein (EF4)<sup>50, 59</sup>. Ca<sup>2+</sup> activated centrins are more compact in structure and can form dimers, oligomers or even polymers<sup>34, 60-62</sup>, The binding of Ca<sup>2+</sup> enhances the affinity of the centrins to their interaction partners as well<sup>60, 61, 63</sup>.

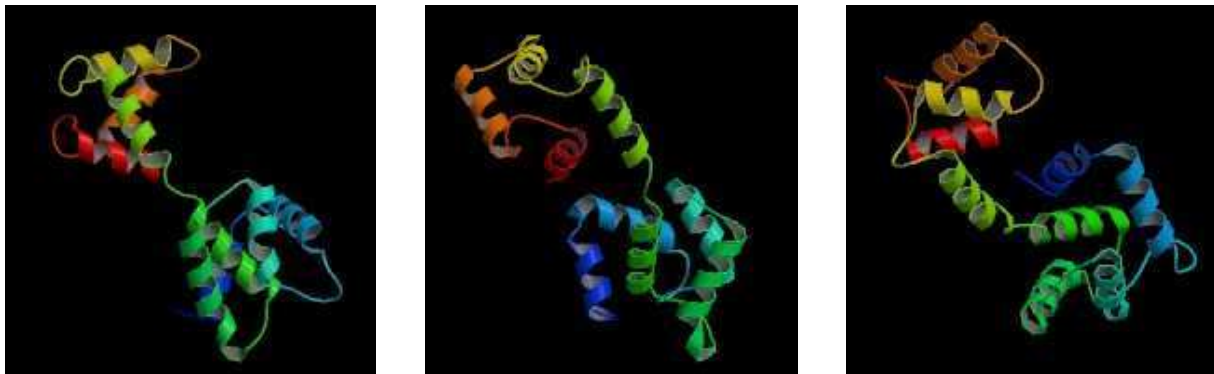


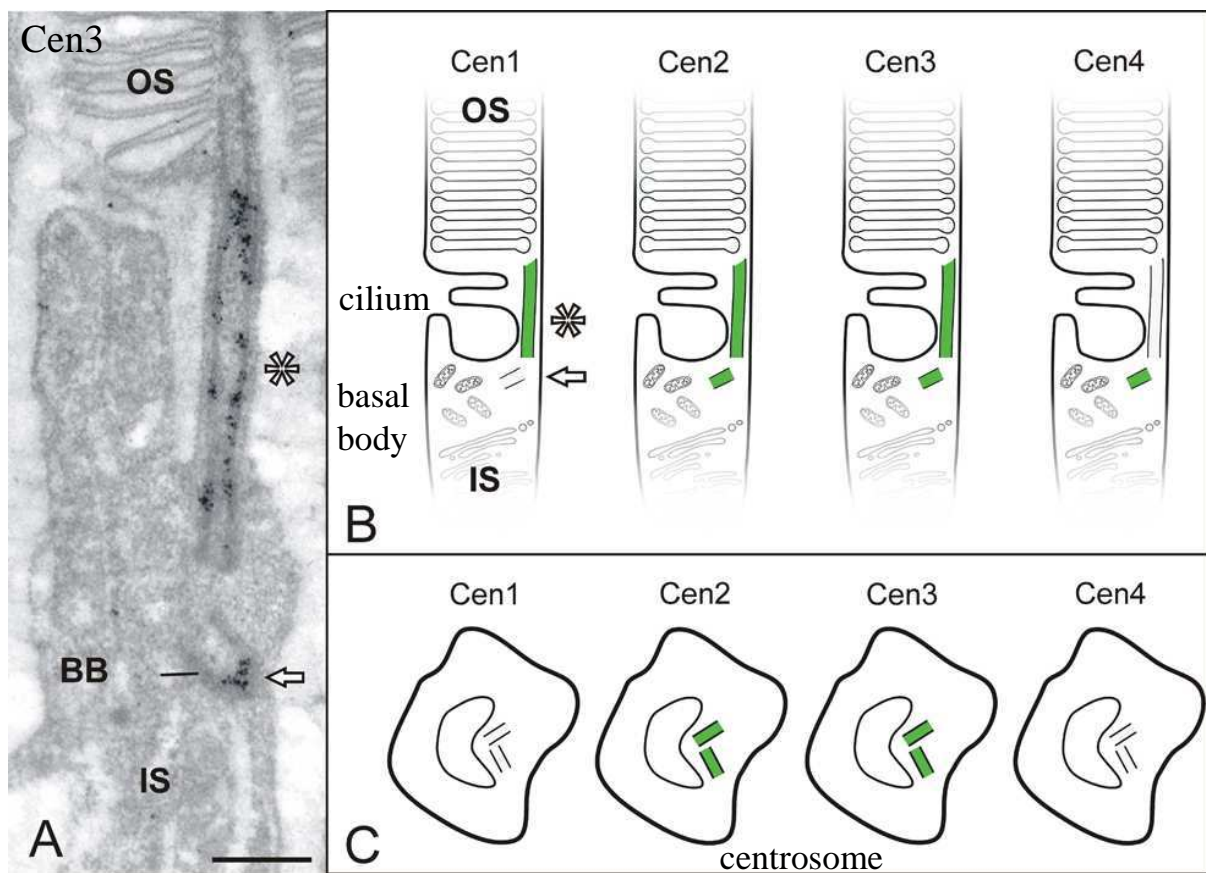
**Figure 6.3.1:** ModBase<sup>64</sup> predicted 3D structure of human centrin 1 (caltractin isoform 2) containing 4 EF-hand domains<sup>59</sup>. Three different perspectives are shown (front view, side view, top view- rightwards, from the left to the right). ModBase is a database of 3D protein models calculated by comparative modeling<sup>64</sup>. The models are derived by ModPipe that relies on the two programs PSI-BLAST and MODELLER. The theoretically calculated models include fold assignments and alignments, but may contain errors.

Other Ca<sup>2+</sup> binding proteins are for example the signaling protein calmodulin and a muscle protein troponin C. The centrins are ~ 50 % similar to calmodulin, one of the best known proteins of the Ca<sup>2+</sup> binding family.

Centrins were first described in unicellular green algae *Tetraselmis striata*<sup>65</sup> and *Chlamydomonas reinhardtii*<sup>57, 58, 66</sup>. Over the last decade, centrins have been found in various species from all kingdoms of eucaryotic organism, protists, fungi, plants and animals<sup>66-77</sup>. Centrins from diverse species have relatively high sequence homologies (55 – 85 %) <sup>66, 78</sup>. The

high level of conservation in the amino acid sequence of the centrins suggest that centrins play a fundamental role for the cells<sup>66</sup>.

In green algae centrins are the major compounds of flagellar rootlets, where they form filamentous contractile structures that contract ATP-independent in a response to an increase of calcium ions<sup>57, 58, 79</sup>. These nano filaments feature a length of 2 - 6 nm. In green algae and yeast only two centrin isoforms are expressed. In rodent cells four different centrin isoforms (centrin 1 - 4) were discovered<sup>66, 70, 72-77</sup>. Centrins are commonly associated with centrosome-related structures<sup>80-82</sup>. They are found for example in centrioles of centrosomes, basal bodies, spindle poles and the transition zone of cilia<sup>57, 58</sup>. They are involved in the biological processes of cell division and mitotic centrosome separation.



modified from Giebl *et al.*, 2004

**Figure 6.3.2:** (A) Immunoelectron microscopy to localize centrin 3 in a mouse photoreceptor cell [OS-outer segment; IS-inner segment; BB-basal body; Bar, 0.5  $\mu$ m]. (B) Schematic illustration of the differential localization of the four centrin isoforms in vertebrate photoreceptor cells. (C) Schematic illustration of the differential localization of the four centrin isoforms in non-specialized cells<sup>34</sup>.

In vertebrates centrin 2 and centrin 3 are expressed ubiquitously. In contrast, centrin 1 and centrin 4 expression is constrained to ciliated cells. The four known centrin isoforms are all expressed in the ciliated photoreceptor cells of the rodents<sup>34</sup>. These isoforms are differentially localized in the subcellular compartments<sup>34</sup> (Figure 6.3.2). In

immunofluorescence analysis, preadsorbed antibodies were utilized to show different localizations of the centrin isoforms in the retina<sup>34</sup>. Centrin 1 is selectively associated with the connecting cilium<sup>34</sup> [Chapter 6.1.3]. Centrin 2 and 3 were localized in the connecting cilium as well as in the basal body of photoreceptor cells and at the centrosomes of non-photoreceptor cells<sup>34</sup>. But the antibody of centrin 4 shows staining only with the basal body of photoreceptor cells<sup>34</sup>.

The colocalization of centrin 1 – centrin 3 in the photoreceptor connecting cilium suggests centrin-transducin-complexes have been formed, whereas the centriolar localization of centrin 2 - 4 indicates a second function of the centrins<sup>34</sup>. Soluble cytoplasmatic centrins may regulate enzymatic reactions in a calcium dependent manner similar to calmodulin. So far little is known about centrin function in mammalian cells.

Sequence analysis of the centrins revealed the largest differences in the N terminus. Thus, the N terminal region is thought to be responsible for variable functions of the centrins in the different species as well as between the different isoforms of the same species<sup>57, 60, 83</sup>. The N terminus is also responsible for the Ca<sup>2+</sup> induced polymerization of the centrins<sup>60, 62</sup>. Therefore several centrin 1 constructs that are shortened from the N terminus will be examined in the following studies to further approve this theory (Figure 6.3.3). This centrin fragments and isoforms originate all from the genome of *Mus musculus*.

Table 6.3.1 refers to the absolute values of the centrin 1 constructs used in my studies as interaction partners of the beta-gamma subunit of the G-protein transducin (G<sub>t</sub>βγ) [Chapter 6.4 - 6.9].

**Table 6.3.1: Properties of the different centrin 1 constructs that I used in my studies. The complete sequence of centrin 1 protein is abbreviated as Cen1p *holo*; the missing N-terminal sequence of centrin 1 plus 6 amino acids is abbreviated as Cen1pΔS1Nterm; the absent N-terminal sequence of centrin 1- Cen1pΔNterm; missing EF-hand 1 centrin 1 is called Cen1pΔEF1. Isoform centrin 3 was studied as well. All centrins originate from the genome of *Mus musculus*. Omega software was used to calculate the values for the different protein fragments (Omega: Programmes „Omega 2.0“; company: Oxford Molekular Ltd.).**

Constructs	Molecular weight, MW	Length	Isoelectric point, pI	Charge at pH 7.0
Cen1p <i>holo</i>	19.696 kDa	172 aa	4.538	-9.965
Cen1pΔS1Nterm	17.044 kDa	148 aa	4.235	-14.961
Cen1pΔNterm	16.329 kDa	142 aa	4.251	-13.967
Cen1pΔEF1	12.420 kDa	107 aa	4.265	-10.980
Cen3p <i>holo</i>	19.519 kDa	167 aa	4.369	-14.782

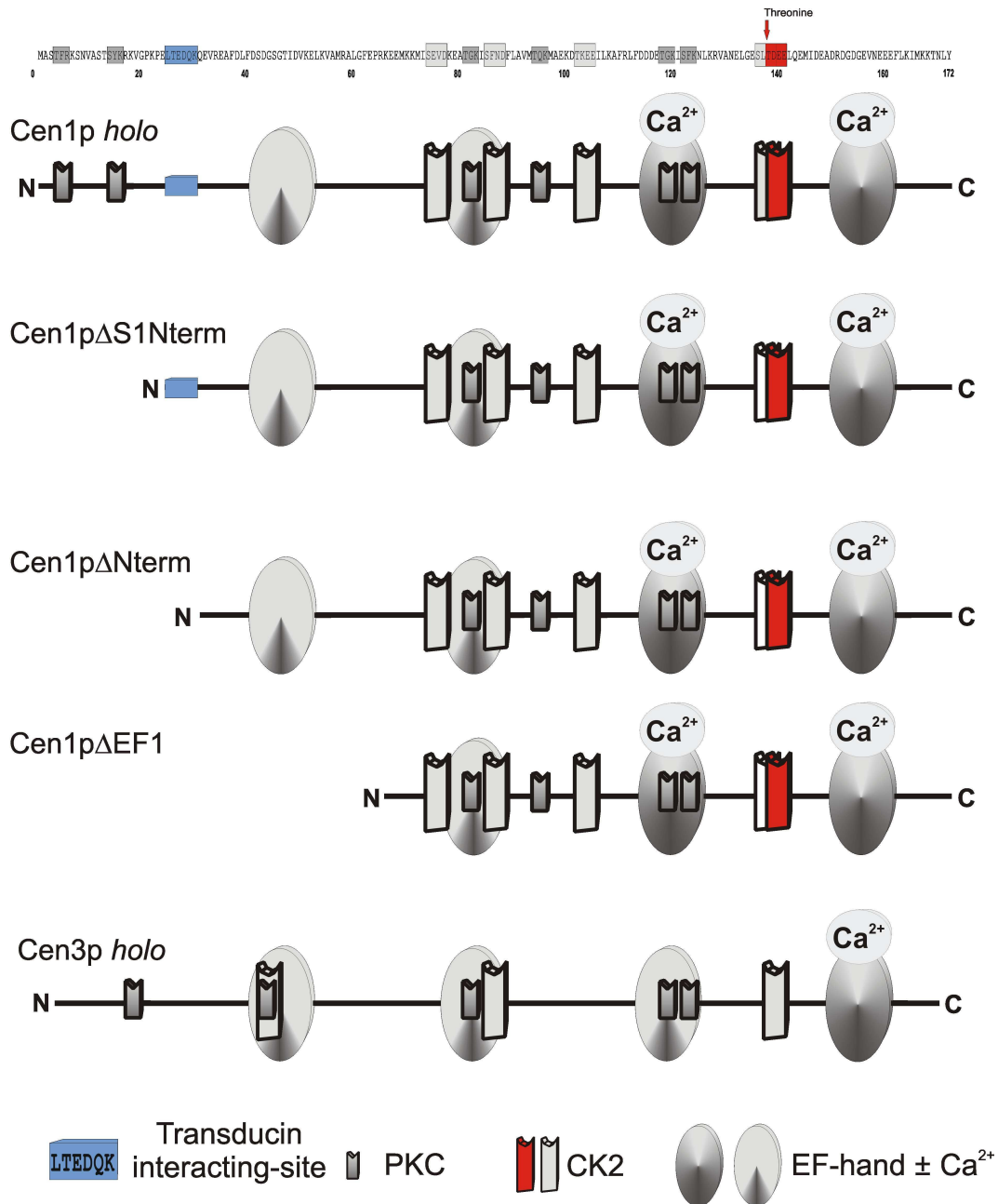


**Figure 6.3.3:** Schematic illustration of generated centrin 1 fragments for identification of functional protein domains (MmCen1p -Mus musculus, centrin 1 protein)<sup>43</sup>. Isoform centrin 3 was also used in the study and is depicted below the centrin 1 fragments. The EF-hand motifs are pictured in a round shape. Ca<sup>2+</sup> binding is indicated, if the EF-hand is not degenerated. Additionally, domains for phosphorylation by protein kinase C (PKC- small, black rectangle) and by casein kinase 2 (CK2- big, red rectangle) are shown. The nomenclature of the fragments refers to missing domains, e.g. Cen1pΔNterm misses the N terminus. The notation S1 in Cen1pΔS1Nterm stands for additional 6 amino acids in comparison to the Cen1pΔNterm construct (cf. Table 6.3.1).

The different centrin 1 fragments and centrin isoforms were bacterially expressed and kindly provided by Andreas Gießl; lab of Prof. U. Wolfrum, Institute of Zoology, Dept. of cell & Matrix Biology; Johannes Gutenberg University, Mainz, Germany.

In the first step, the complete centrin isoforms were amplified using reverse transcription polymerase chain reaction. During this reaction the m-RNA is transcribed in a c-DNA strand that is amplified with specially designed primers for the centrin amplification. In the next step, the centrin clones were cloned in Bluescript vectors (Amersham) suitable for the storage. Then, the clones were used for recombinant expression with another expression vector pGex4T3 inserted. The GST expression vectors code for the glutathione S-transferase as well. GST fused to the N-terminus of the centrin allows for various applications.

Firstly, GST-fusion proteins can be easily purified by a glutathione-sepharose column. Addition of free glutathione that binds to the GST-centrin releases the GST-protein after purification from the column. Secondly, GST-fused centrin possesses a mass of ~ 46 kDa compared to the mass of ~ 20 kDa for the centrin protein alone. By using surface plasmon resonance spectroscopy as a mass sensitive detection method, it is a quite obvious advantage to double the mass of the centrin. Thirdly, the GST is cleaved from the GST-fusion protein.

#### **6.4 Motivation**

During the last decade, four different isoforms of the  $\text{Ca}^{2+}$  binding protein centrin have been identified in rodents [Chapter 6.3]. Although centrin is ubiquitously expressed, only little is known about their biological functions. This thesis focuses on the function of the centrin in rod photoreceptor cells of the vertebrate retina. The different localizations of the isoforms suggest that the centrin may conduct special functions. In search of interaction partners, previous studies revealed binding of centrin to the  $\beta\gamma$ -subunits of the visual G-protein transducin in a calcium dependent manner [Chapter 6.2]. While the centrin is expressed universally, the expression of the transducin alpha subunit ( $G_t\alpha$ ) is limited to the vertebrate retina photoreceptor cells. The connecting cilium of the photoreceptor cell is predestinated for the binding event of centrin and transducin [Chapter 6.1].

The aim of this study is to identify the interacting-sites of centrin 1 (Cen1) to the  $\beta\gamma$ -subunits of transducin by epitope mapping. Demanding interest exists in a method that allows not only for the identification of the interacting-site but also for differentiating between the centrin isoforms. Basic monitors, such as light scattering, absorption and fluorescence, investigate the proteins in their natural environment. These methods exploit the endogenous properties of proteins, e.g. the intrinsic fluorescence of tryptophan, Trp-207 in transducin that is localized near the active center of the G-protein, is utilized for detection. Light scattering uses the activation dependent solubility of transducin. The scattering signal is interpreted as a

gain of protein mass that is bound to the disc membranes of photoreceptor cells<sup>9, 84</sup>. Another completely different technique is size-exclusion chromatography that detects a weight shift for protein complexes in contrast to the single protein molecule.

Kinetic light scattering and size-exclusion chromatography experiments provided first data for possible centrin transducin interaction. Here, surface plasmon resonance spectroscopy as a method to monitor specific interactions at surfaces is used to further investigate the protein-protein interaction. The significant advantage of the SPR technique is its capability of label-free detection to monitor real-time interactions without changing the natural kinetic characteristics of the proteins. SPR is thought to give a detailed kinetic interpretation of the centrin-transducin interaction. It is expected to confirm the data derived from light scattering and to determine the affinity constants ( $k_{on}$ ,  $k_{off}$ ).

Several GST-Cen1 and Cen1 fragments, respectively, are expressed to give a detailed answer, which sequence of the centrin 1 is essential for the binding to transducin ( $G_t\beta\gamma$ ) [Chapter 6.3].

Centrin 3 isoform was expressed as well and compared to the binding behaviour of centrin 1. The regulation mechanism of the protein binding is under investigation as well. It is analyzed, whether there is an *in vitro* regeneration of the protein complexes possible or not. This thesis contributes to further understanding of centrin function in sensory systems.

## **6.5 Development of the sensor architecture**

### **6.5.1. Commercial CM5 sensor chip (Biacore)**

The commercial CM5 Chip from Biacore as an established surface matrix was chosen for the molecular interaction of centrin to transducin. As we learned from previous chapter [Chapter 4; NPG] that surface enhancement increases the signal of detection, the three dimensional dextran matrix was also expected to exhibit a better signal than a two dimensional matrix. The carboxy-methyl-dextran (CMD) matrix bound to gold films for surface plasmon resonance spectroscopy purposes was firstly described by Stefan Löfås and Bo Johnsson in 1990<sup>85</sup>.

In my studies, CM5 chips without the housing (Biacore; Uppsala, Sweden) were used to excite surface plasmon resonances in the homebuilt setup [Chapter 3.1]. The chips consist of a D263 glass ( $n = 1.523$  at  $\lambda = 588$  nm) with a thickness of  $\sim 0.5$  mm that is coated with  $\sim 50$  nm of gold. The refractive index mismatch between the D263 glass and the LaSFN9 prism ( $n = 1.85$  at  $\lambda = 633$  nm) was negligible for angles smaller than  $\sim 62 - 63$  degrees<sup>86</sup>. The plasmon reflectivity dip appeared at the same position as in the case of a LaSFN9 glass substrate coupled to a LaSFN9 prism<sup>86</sup>.

The CM5 chip (Figure 6.5.1) is a specially modified substrate. On the gold surface, a self assembled monolayer (SAM) of a long chain 1, $\omega$ -hydroxyalkyl thiol (typically, 16-mercaptohexadecan-1-ol) is formed<sup>87</sup> to prevent unspecific binding of ligands. Then, this hydroxy terminated layer is activated by epichlorohydrin under basic condition to generate epoxy groups. In the next step, dextran, a linear polymer of 1,6- linked glucose units, is covalently bound to the epoxides. The dextran provides a highly stable, flexible, non-crosslinked brush-like matrix that extends  $\sim 100$  nm from the gold coated surface if incubated with physiological buffer. Further functionalization of the dextran was done by reaction with bromoacetic acid to form carboxylic groups. The detailed preparation steps are described by Löfås<sup>85</sup>. The main advantages of the CM5 chip are the minimization of non-specific binding, due to the SAM and the dextran brush, and the greatly enhanced surface for sensing.

The carboxylated dextran chains of the CM5 chip provide a negatively charged hydrogel-covered surface ( $-\text{COO}^-$ ) that can be utilized for covalent coupling of various ligands. Biacore developed an activation-coupling-deactivation protocol to immobilize proteins. A fraction of carboxy groups ( $\sim 25 - 30$  %) was activated by using a mixture of

freshly prepared 0.2 M N-ethyl-N'-(3-dimethylaminopropyl) carbodiimide hydrochloride (EDC) and 0.05 M N-hydroxy-succinimide (NHS) in Milli Q water (Figures 6.5.2 and 6.5.3). After 10 minutes of activation, 1  $\mu$ M transducin in Gabi buffer [Chapter 3, Materials] was injected directly to bind to the reactive N-hydroxysuccinimide esters. Actually, the key of protein immobilization to a negatively charged dextran matrix is to use electrostatic attraction to preconcentrate a positively charged protein (protein  $-\text{NH}_3^+$ ) in the matrix (dextran  $-\text{COO}^-$ ). Therefore, a solution with a pH smaller than the isoelectric point of the protein and low ionic strength is preferred.

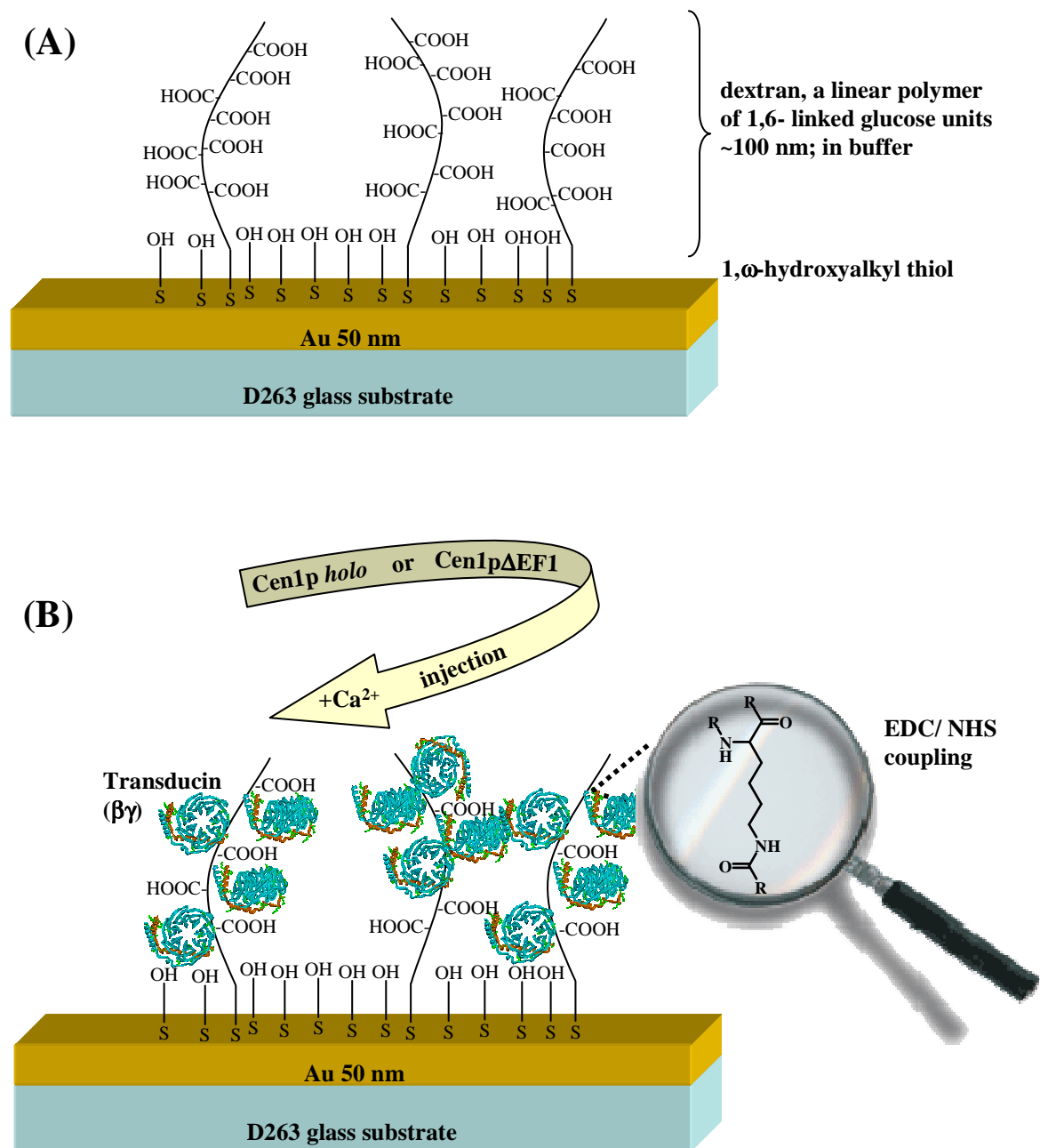
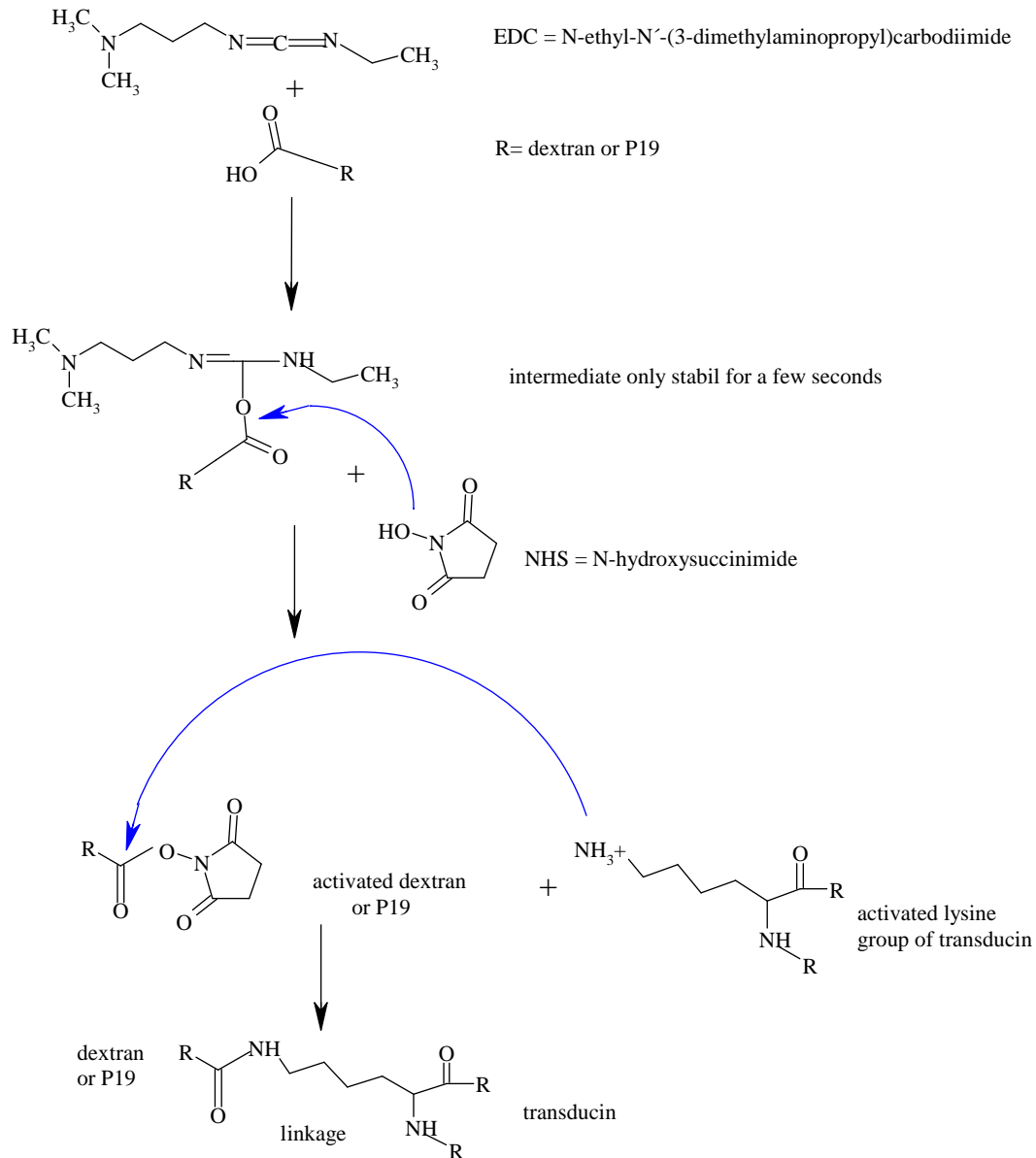


Figure 6.5.1: Schematic presentation of a CM5 sensor chip. A) Unloaded 3D carboxy-methyl-dextran matrix, commercially available. B) Dextran matrix loaded with transducin for further interaction experiments with the centrin 1 *holo* and centrin delta EF1 construct.



**Figure 6.5.2: Chemical reaction of EDC/NHS activation.** Here, the first step in the binding reaction is an N-ethyl-N'-(3-dimethylaminopropyl) carbodiimide (EDC) activation of the carboxy group of either the dextran matrix or the P19 matrix (Chapter 6.5.2) to form O-acylisourea intermediates. These intermediates are only stable for a few seconds. If no amine is coupled, the intermediates will hydrolyze and result in the carboxyl group. In the presence of NHS reagent the O-acylisourea intermediates can be converted to amine-reactive NHS-esters.

N-hydroxy-succinimide esters yield stable products upon reaction with primary amines. Accessible  $\alpha$ -amine groups exist on the N-termini of proteins and  $\epsilon$ -amines on lysine residues of proteins react with NHS-esters to form amide bonds. Relatively efficient coupling can be achieved under physiological buffer conditions.

Both beta and gamma subunits of transducin ( $G_t\beta\gamma$ ) are negatively charged in Gabi buffer at pH = 7.1 [Table 6.2.1]. Due to the unsuitable binding condition only poor binding of transducin was obtained. Furthermore, transducin ( $G_t\beta\gamma$ ) offers ~ 17 lysine residues and thus was bound in sterically random way, so that some centrin binding sites may not be accessible in the protein-protein interaction assay. After the immobilization of the transducin ( $G_t\beta\gamma$ ) and

the following rinsing step, excess NHS-esters were then deactivated using 1 Mol ethanolamine hydrochloride adjusted to pH 8.5 with sodium hydroxide. Ethanolamine solution also desalted loosely bound transducin, which was seen in the kinetic measurement as a decrease in reflectivity (Figure 6.5.3). When 10  $\mu$ M Cen1p $\Delta$ EF1 in buffer F [Chapter 3, Materials] was injected, a slight increase in reflectivity was detected. But after the rinsing step no centrin fragment remained bound to the beta and gamma subunits of transducin ( $G_t\beta\gamma$ ). 10  $\mu$ M Cen1p *holo* in buffer F showed similar behaviour, even though centrin 1 *holo* was the positive control. The centrins diluted in buffer F with a pH of  $\sim$  8.0 were negatively charged since the centrins feature isoelectric points of  $\sim$  4.2 - 4.5 (Table 6.3.1).

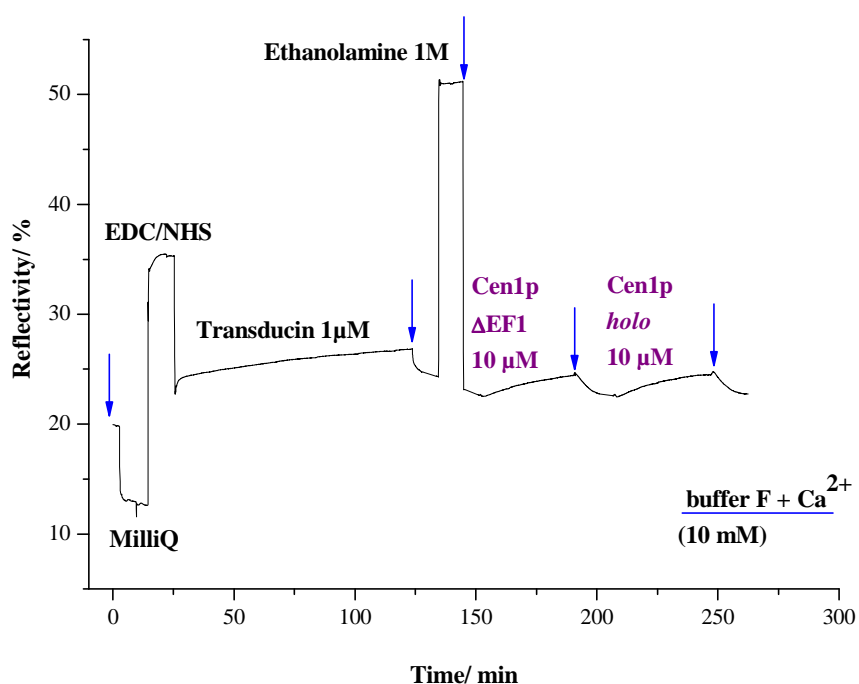


**Figure 6.5.3: Centrin-transducin interaction on a Biacore CM5 Chip. SPR kinetic measurement monitors the different steps: EDC-NHS activation of the carboxy groups; binding of transducin to the NHS-esters; binding of ethanolamine to excess NHS-esters and desalting of loosely bound transducin; interaction of the centrin fragment Cen1p $\Delta$ EF1 and the holo protein Cen1p *holo*. The blue arrows indicate injection of buffer F with Ca<sup>2+</sup> (10 mM) as rinsing steps.**

It can be concluded from surface plasmon resonance measurements on Biacore CM5 Chip, that the negatively charged carboxylated dextran matrix indeed was not suitable to probe transducin centrin interaction due to the low isoelectric points of the proteins. Around 70 - 75 % of the carboxy groups remained inactivated as  $-\text{COO}^-$ , so that the negatively charged proteins of interest were repulsed from the dextran matrix.

### 6.5.2. Peptide P19 matrix

Since the three dimensional dextran matrix was not appropriate to probe transducin-centrin interaction, a two dimensional surface architecture was considered in a second approach. The 19-mer peptides CSRARKQAASIKVAVSADR (CYS-SER-ARG-ALA-ARG-LYS-GLN-ALA-ALA-SER-ILE-LYS-VAL-ALA-VAL-SER-ALA-ASP-ARG) abbreviated as P19 were used as hydrophilic spacer molecules to immobilize the transducin at the evaporated gold surfaces [Chapter 3.4]. P19 (Sigma) is a fragment of laminin derived from the alpha subunit of the heterotrimeric protein<sup>88</sup>. Laminins<sup>89</sup> are a family of large extracellular glycoproteins that are involved in cell growth and differentiation.

The self assembly of the peptide P19 layer was allowed by the gold-sulfur interaction of the N-terminal cysteine (C; CYS) residues<sup>90</sup>. The C-terminus of the peptide P19 was activated by EDC/NHS coupling reagent (cf. Figure 6.5.2). The helical structure of the peptide P19 is self-spacing and thus enables unhindered binding of the beta and gamma subunits of transducin ( $G_t\beta\gamma$ ) to the activated NHS-esters.

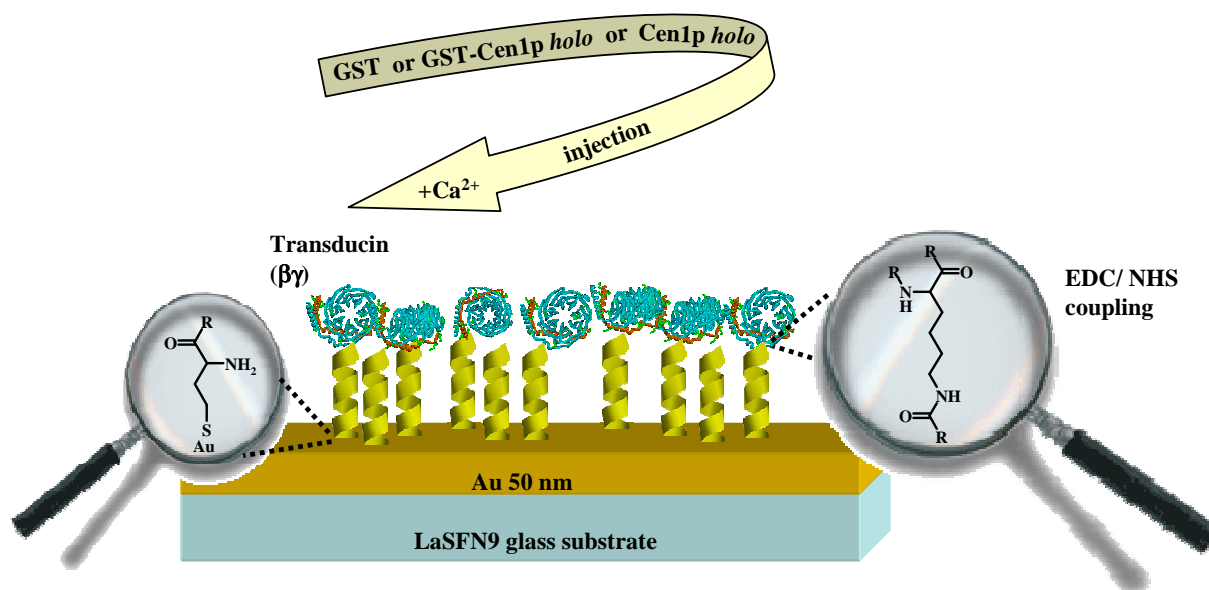


**Figure 6.5.4:** Two dimensional surface architecture based on peptide P19 matrix to probe centrin-transducin interaction.

After the built up of the surface architecture (Figure 6.5.5) centrin-transducin interaction was probed. In order to gain enhancement of the surface plasmon resonance signal on a 2D matrix, glutathione S-transferase (GST-Cen1p) fusion proteins were chosen. GST-fused centrin possess a mass of  $\sim 46$  kDa compared to the mass of  $\sim 20$  kDa for the centrin

protein alone [Chapter 6.4]. Firstly, glutathione S-transferase (GST) as a negatively control was investigated. Subsequent to a short rinsing interval with  $\text{Ca}^{2+}$  containing buffer F (10 mM), the positive control of GST-Cen1p *holo* was probed. The proteins both in a concentration of 10  $\mu\text{M}$  showed different binding behaviour. For GST a low binding signal was observed, while GST-Cen1p *holo* high binding signal during the same time interval.

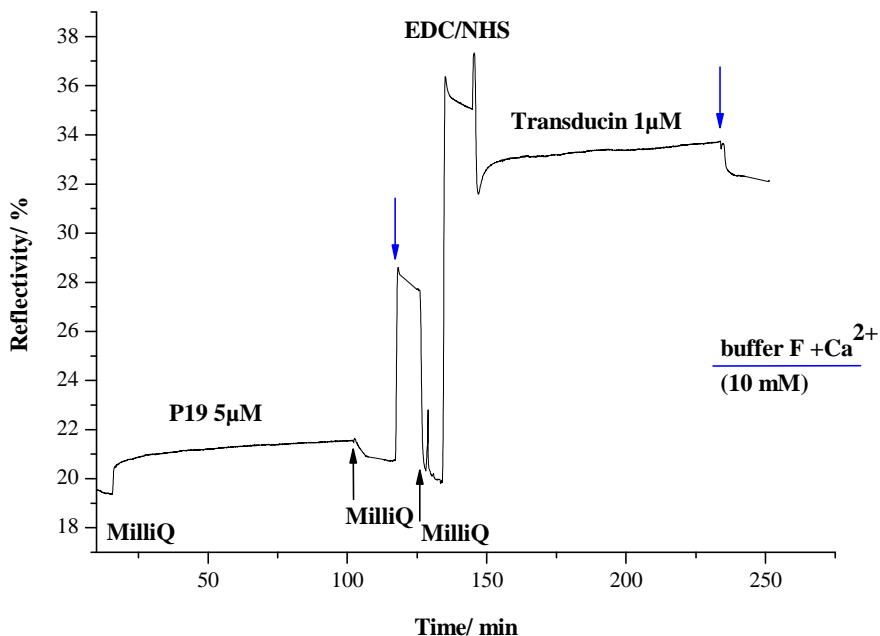


Figure 6.5.5: Built up of the two dimensional surface architecture based on peptide P19. SPR kinetic measurement monitors the different steps: self-assembly of P19 in Milli Q; EDC-NHS activation of the carboxy groups; binding of transducin ( $\text{G}_i\beta\gamma$ ) to the NHS-esters. The black arrows show injection of Milli Q water and the blue arrows indicate injection of buffer F with  $\text{Ca}^{2+}$  (10 mM) as rinsing steps.

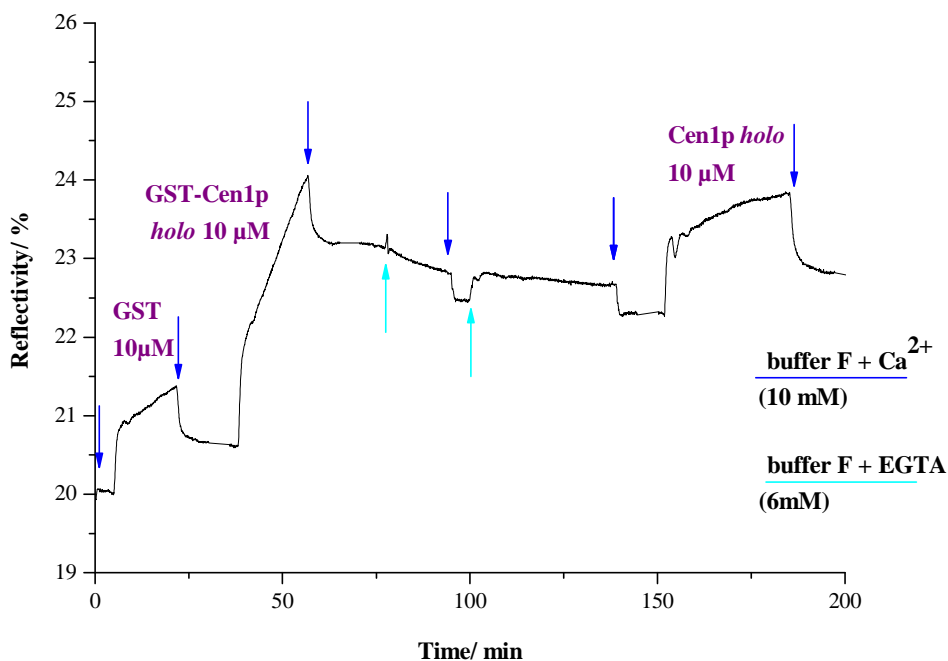


Figure 6.5.6: Centrin-transducin interaction on the two dimensional peptide P19 matrix. GST was utilized as a negative control. GST-fusion protein (GST-Cen1p *holo*) was used for an enhancement of the SPR signal compared to the centrin (Cen1p *holo*). The blue arrows show injection of buffer F containing  $\text{Ca}^{2+}$  and the cyan arrows indicate injection of buffer F with EGTA.

During rinsing with buffer F containing  $\text{Ca}^{2+}$  (10 mM) not much of the proteins was dissociated. For regeneration purposes, buffer F with 6 mM ethylene glycol tetracetic acid (EGTA) was chosen, because the binding of centrin to transducin is thought to be  $\text{Ca}^{2+}$  dependent. Buffer F with 6 mM EGTA was applied for two times, but was not able to regenerate the surface completely. After changing back to buffer F containing  $\text{Ca}^{2+}$  centrin 1 *holo* (10  $\mu\text{M}$ ) was probed.

As results from the use of the two dimensional P19 matrix can be concluded, that the peptide P19 formed a reproducible and stable mono layer and transducin was coupled to the P19 via active ester chemistry. As well as on the Biacore chip the binding of transducin was undirected. But this time at least a poor centrin binding was detected afterwards.

GST attached to the N-terminus of the centrin apparently did not strongly influence the interaction between transducin and centrin, because centrin 1 *holo* resulted in less binding than the GST-centrin 1 *holo* fusion protein with the double mass of ~ 46 kDa.

Centrin binding to transducin is thought to be  $\text{Ca}^{2+}$  dependent [Chapter 6.1.2/6.1.3]. However, the centrin interaction with transducin was not completely reversible by just adding ethylene diamine tetracetic acid (EDTA; data not shown) nor ethylene glycol tetracetic acid (EGTA), a highly specific  $\text{Ca}^{2+}$  chelating agent, to the buffer.

The negative control, GST alone, resulted in binding to the P19 sensor surface. This indicates the need of additional improvements to the P19 matrix.

## 6.5.3. Combined mPEG thiol matrix

In order to minimize non-specific protein absorption of the peptide P19 matrix the sensor had to be further developed. Poly (ethylene glycol) monomethylether (mPEG) as one of the most promising materials that prevent non-specific binding of proteins to glass<sup>91</sup> and metal coated surfaces<sup>92</sup>, was chosen to cover the intermolecular space of the helical P19 molecules.

Subsequent to the self-assembly of the peptide P19 (5  $\mu$ M P19 (Sigma) in Milli Q; ~ 80 min) mPEG thiol (1  $\mu$ M mPEG (Polypure) in Milli Q; ~ 20 min) was assembled on the evaporated gold film. The structure of the used mPEG thiol and conformation of the improved sensor architecture is depicted in Figure 6.5.7.

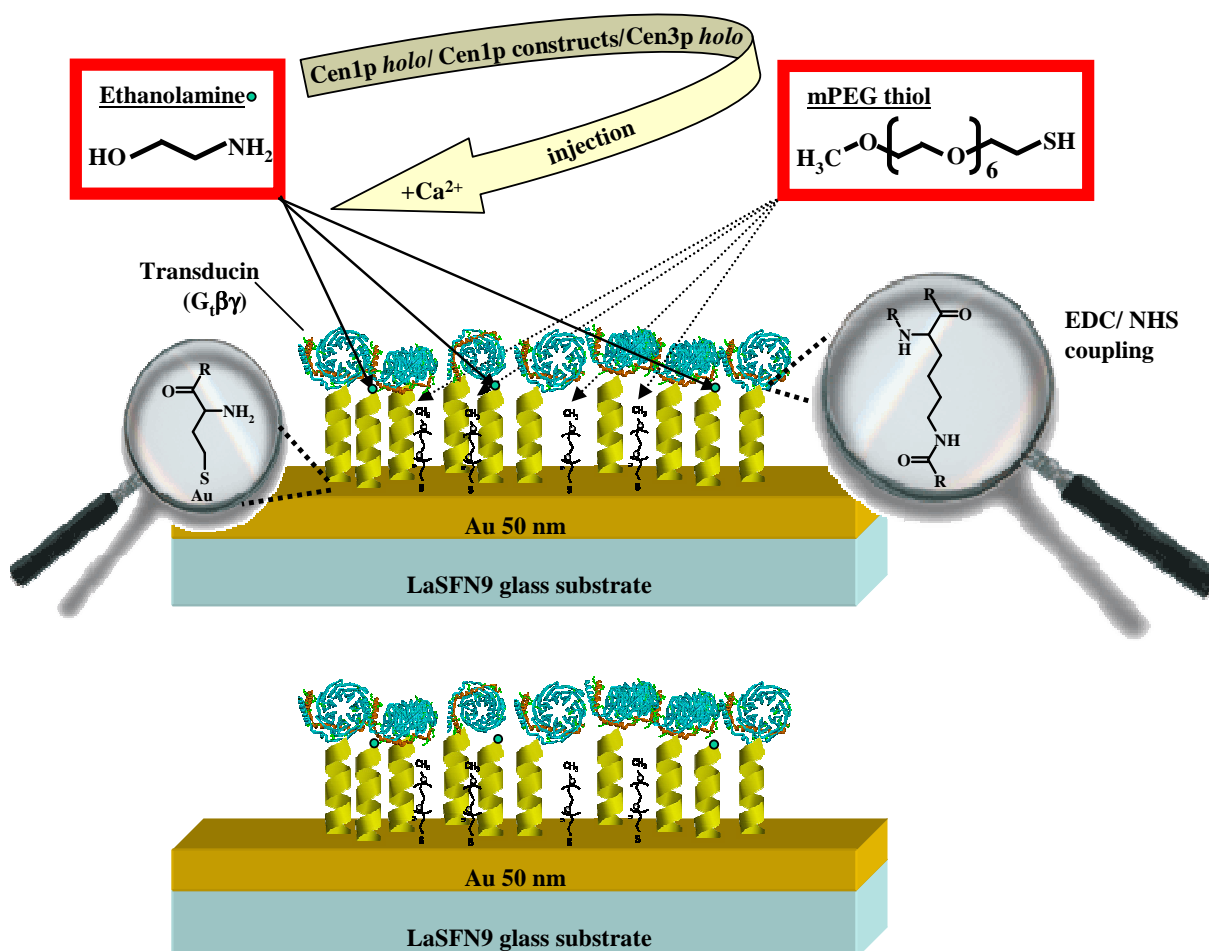
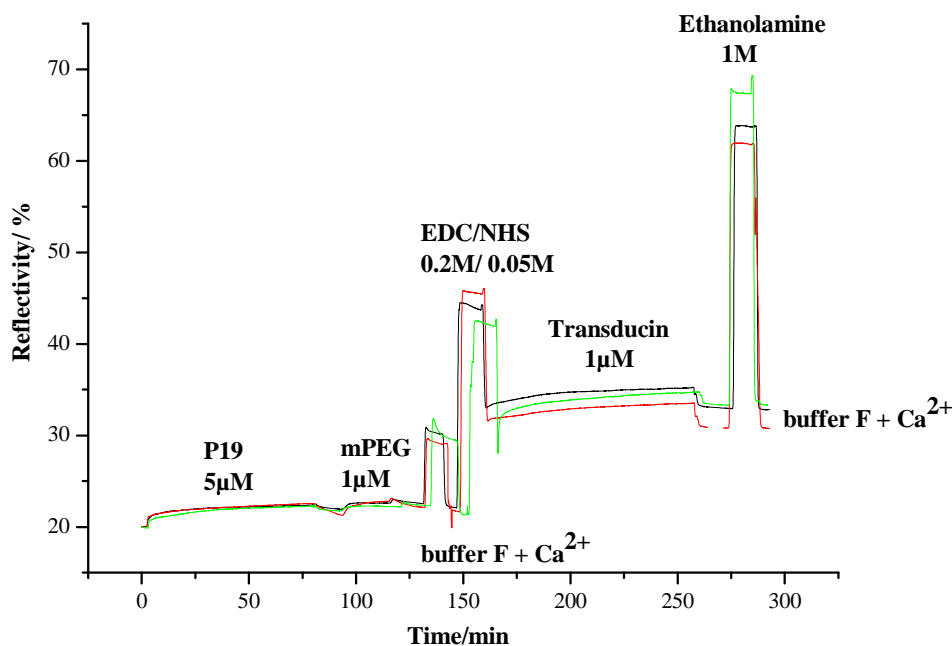


Figure 6.5.7: Combined mPEG thiol matrix. Two improvements were made compared to the peptide P19 matrix. Firstly, passivation of the accessible gold sensor surface was completed with mPEG thiol. Secondly, deactivation of the excess NHS-esters was achieved by using ethanolamine. All of the centrin fragments, centrin 1 *holo* and centrin 3 *holo* isoform were probed on this sensor surface.

Additional to the passivation of the gold surface with the mPEG thiol, excess NHS-esters were deactivated this time by ethanolamine as it was done for the Biacore CM5 Chip [Chapter 6.5.1]. After the passivation, no proteins, neither transducin nor centrin, were bound non-specifically to the gold film. And after the deactivation of the NHS-ester groups, no further protein could be covalently bound to the peptide P19 matrix.



**Figure 6.5.8: Built up of the improved two dimensional surface architecture based on P19. SPR kinetic measurement monitors the different steps: self-assembly of peptide P19 in Milli Q; self-assembly of mPEG thiol; injection of buffer F + Ca<sup>2+</sup> as a reference; EDC-NHS activation of the carboxy groups of the c-terminus of P19; binding of transducin (G<sub>i</sub>βγ) to the NHS-esters; binding of ethanolamine to remaining NHS-esters; floating the cell with buffer F +Ca<sup>2+</sup> as the last step. Three different kinetic curves (black, red and green line) resultant of three different gold films are shown.**

Henceforth, only the combined mPEG thiol matrix was used to investigate centrin-transducin interactions. All of the centrin fragments, centrin 1 *holo* and centrin 3 *holo* isoform were probed on this sensor surface in the following chapter.

### **6.6. Regeneration of the sensor surface**

Fundamental to an optimal sensor is the ability to perform multiple cycles of an assay on the same sensor surface. Not only to minimize the expenditure of the measurement time, but also to have reproducible conditions. Since slight sample to sample variations can cause some undesired error. Surface regeneration should guarantee an efficient removal of the bound material from the sensor surface whilst maintaining the activity of the immobilized compound.

In this study, transducin ( $G_t\beta\gamma$ ) was covalently bound to the peptide P19 matrix. The interaction partner centrin was expected to be removed to allow for probing of the differently expressed centrin constructs. The binding of centrin to the beta and gamma subunit of transducin is thought to be  $Ca^{2+}$  dependent. Therefore, in the very first approach buffer F with ethylene glycol tetracetic acid (EGTA) was chosen to regenerate the sensor. EGTA is a chelating agent that is similar to the well-known ethylene diamine tetracetic acid (EDTA) reagent, but with a higher affinity for calcium than for magnesium ions. From other binding assays it is known that quite high concentrations of the chelating agent are needed to release the interaction partner out of a complex<sup>93, 94</sup>. Therefore, in the binding study of centrin-transducin, EGTA concentrations of 6 mM up to 250 mM were applied to the system. But the centrin was dissociated only to some extent. Even in use of high concentrated chelating agent, a full regeneration of the P19 sensor surface was not achieved.

Regeneration protocols often exploit a pH jump or optional low or high ionic strength solutions. But the beta and gamma subunits of the transducin started to unfold at pH values lower than pH 6. Variations in ionic strength also did not regenerate the peptide P19 surface. Another conventional regeneration method that causes dissociation of protein complexes uses sodium dodecyl sulfate (SDS). A short pulse of SDS disrupts non-covalent bounds in the proteins, thereby partially denatures the proteins and causes a change in conformation. In this study SDS concentrations of 1 % up to 10 % were injected to dissociate the centrin-transducin complexes without success.

Due to the failure of the conventional regeneration methods, a more complex regulation than only the presence or absence of  $Ca^{2+}$  in centrin-transducin complexes had to be considered. *In vivo* the centrin-transducin complexes may be dissociated after phosphorylation by the casein kinase 2 (confer Figure 6.1.4). In one test experiment casein kinase 2 and adenosine 5'-triphosphate (ATP) containing buffer was applied to the centrin-transducin complexes anchored to the peptide P19 matrix. But no change in the surface plasmon

resonance signal was observed. No effect of the casein kinase 2 under these buffer conditions does not mean that no interaction between the casein kinase 2 and the protein complex is possible in general.

### **6.7 Further experimental optimization**

Since the flow cell volume of  $\sim 11 \mu\text{L}$  was really small, the flow rate had to be optimized for the peptide P19 system first. The P19 matrix was very sensitive to turbulences that caused bubbles. But when the peristaltic pump was switched off completely, mass transport limitations of centrin binding were observed. So the lowest flow of  $\sim 35 \mu\text{L}/\text{min}$  that could be obtained from the peristaltic pump was chosen to probe centrin-transducin interactions.

Centrin-transducin binding was also dependent on the concentrations of both interaction partners. A densely packed layer of transducin molecules resulted from a  $10 \mu\text{M}$  solution and did not show a satisfying centrin signal, while a  $1 \mu\text{M}$  solution of transducin yielded a good signal. The centrin was always used in a concentration of  $10 \mu\text{M}$ .

The contact time for the interaction had to be optimized as well. Due to really slow binding of centrin to transducin a binding interval over  $\sim 1000$  minutes with the flow of  $\sim 35 \mu\text{L}/\text{min}$  was selected. During this time interval a saturation of the surface plasmon resonance signal was reached mostly.

*In vivo* the centrin-transducin reaction should happen within minutes. The much longer time period that is needed for the interaction might be due to the fact that transducin is immobilized on the surface. Also the accessibility of the transducins is limited, because the transducins are linked to the matrix in an undirected way. In principle, a His-tag strategy for the immobilization of transducin is practical. But in this study, the His-tag strategy was purposely not chosen to interfere as less as possible with the natural kinetic characteristics of the protein.

### **6.8 SPR results of centrin-transducin interactions**

The following surface plasmon resonance measurements were conducted under all these optimized conditions. Firstly, the interactions of centrin 1 protein constructs and centrin 1 *holo* protein were probed. Secondly, centrin 3 *holo* isoform was compared to the centrin 1 *holo*. Since no complete regeneration of the sensor surface was possible, for each interaction experiment a new sample was used. The centrin constructs or centrin 3 isoform

were measured first and centrin 1 *holo* as the positive control was monitored afterwards. For all interaction experiments buffer F containing  $\text{Ca}^{2+}$  (10 mM) pH 8 was used.

### 6.8.1. Centrin 1 (Cen1p) constructs

First of all the Cen1p $\Delta$ EF1 construct was analysed, because it was the shortest protein fragment (Figure 6.3.3). The N-terminus and the first EF-hand were missing. If a difference existed between centrin 1 *holo* and the constructs, it was expected to be clearly seen for the Cen1p $\Delta$ EF1 construct. Indeed, the surface plasmon measurements proved the expectation (Figure 6.8.1). In the kinetic measurement a small signal ( $\sim 1\%$  change in reflectivity) was observed for the binding of Cen1p $\Delta$ EF1 to the beta and gamma subunits of transducin ( $G_t\beta\gamma$ ). After 1000 min of binding reaction, the sample was rinsed with buffer F +  $\text{Ca}^{2+}$  for  $\sim 400$  min. Almost no Cen1p $\Delta$ EF1 construct remained at the peptide P19 matrix after the rinsing step.

At the same sensor surface the centrin 1 *holo* protein showed a huge binding to the subunits of transducin ( $G_t\beta\gamma$ ). This binding was not reversible by rinsing with buffer F +  $\text{Ca}^{2+}$  for  $\sim 400$  min.

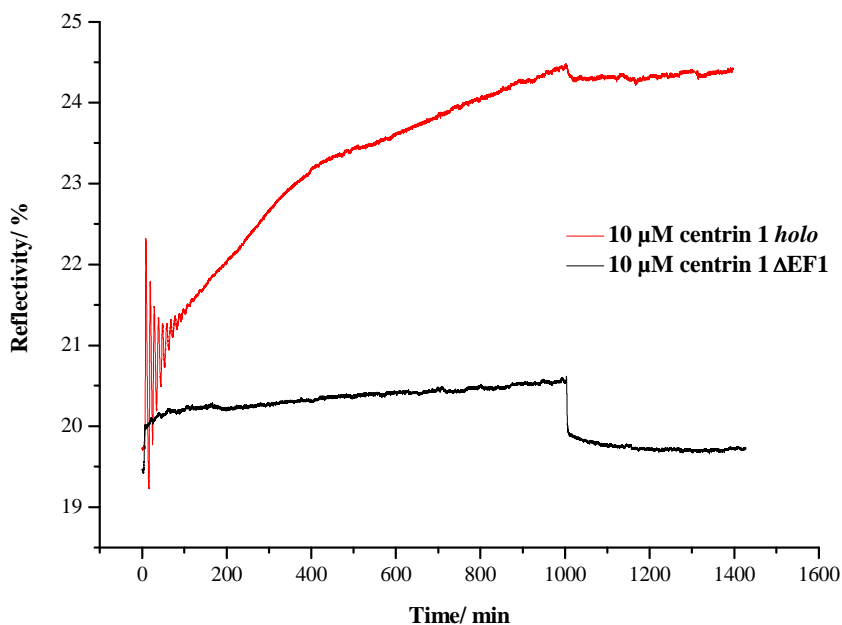


**Figure 6.8.1:** Surface plasmon resonance kinetic measurement of Cen1p $\Delta$ EF1 versus Cen1p *holo*. The measurement was conducted on the combined mPEG thiol/P19 matrix, where the beta and gamma subunits of transducin were immobilized [the oscillations at the beginning of the kinetic measurement of the centrin 1 *holo* are artefacts due to liquid handling problems].

In a second experiment the affinity of Cen1p $\Delta$ Nterm construct to transducin ( $G_t\beta\gamma$ ) was investigated. This centrin 1 fragment was missing only the N-terminus (Figure 6.3.2). Thus, the length of the Cen1p $\Delta$ Nterm construct (142 aa) was not much different to the length of the centrin 1 *holo* protein (172 aa); ~ 83 % of the length of centrin 1 *holo*. But still showed a similar binding behaviour to the transducin ( $G_t\beta\gamma$ ) than the Cen1p $\Delta$ EF1 construct (107 aa).

After 1000 min of binding reaction, ~ 1.5 % change in reflectivity was derived in the case of the Cen1p $\Delta$ Nterm fragment (Figure 6.8.2). Subsequent rinsing with buffer F +  $Ca^{2+}$  for ~ 400 min dissociated around two third of the protein. The following centrin 1 *holo* binding yielded a very high signal, which was not reversible by rinsing the sensor surface.

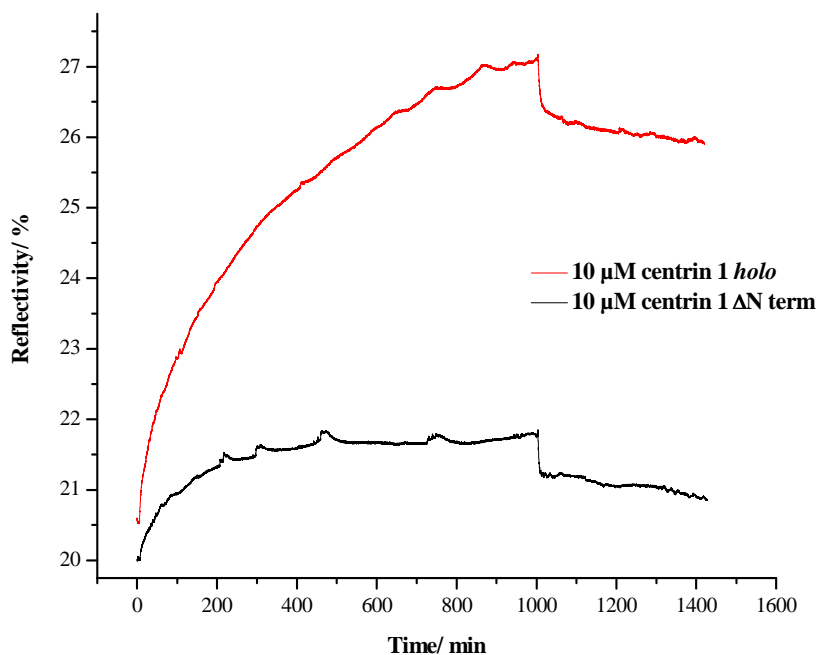


**Figure 6.8.2: Surface plasmon resonance kinetic measurement of Cen1p $\Delta$ Nterm versus Cen1p *holo*. The measurement was conducted on the combined mPEG thiol/P19 matrix, where the beta and gamma subunits of transducin were immobilized.**

A third experiment was conducted with Cen1p $\Delta$ S1Nterm, a centrin 1 construct that was only 6 amino acids longer than the previously analyzed Cen1p $\Delta$ Nterm (Figure 6.8.3). This time a huge binding signal was observed. The change in reflectivity was comparable to the signal of centrin 1 *holo* protein. Subsequently rinsing did not much influence the binding signal.

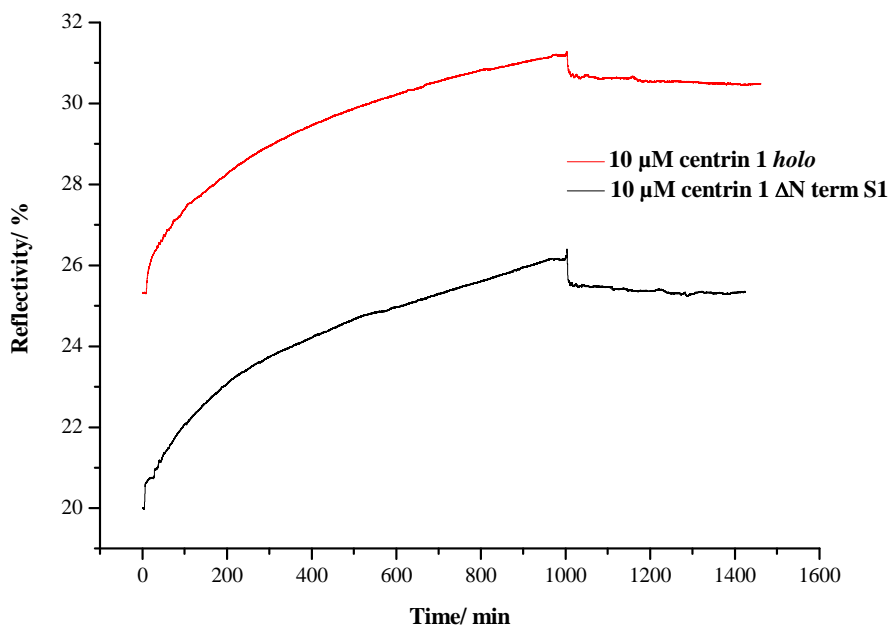


**Figure 6.8.3:** Surface plasmon resonance kinetic measurement of Cen1p $\Delta$ S1Nterm versus Cen1p *holo*. The measurement was conducted on the combined mPEG thiol/P19 matrix, where the beta and gamma subunits of transducin were immobilized.

### 6.8.2. Centrin 3 (Cen3p) isoform

In this experiment, centrin 3 *holo* isoform was compared to the centrin 1 *holo* protein (Figure 6.8.4). Again the optimized combined mPEG thiol/P19 matrix was used. Centrin 3 *holo* (167 aa) showed a slightly higher surface plasmon resonance signal than Cen1p $\Delta$ EF1 construct (107 aa) and Cen1p $\Delta$ Nterm construct (142 aa), that might be due to the larger size of centrin 3 *holo*.

But after rinsing for  $\sim 400$  min, almost no centrin 3 *holo* protein remained at the sensor surface. The positive control of centrin 1 *holo* protein showed a high surface plasmon signal as in the experiments before.

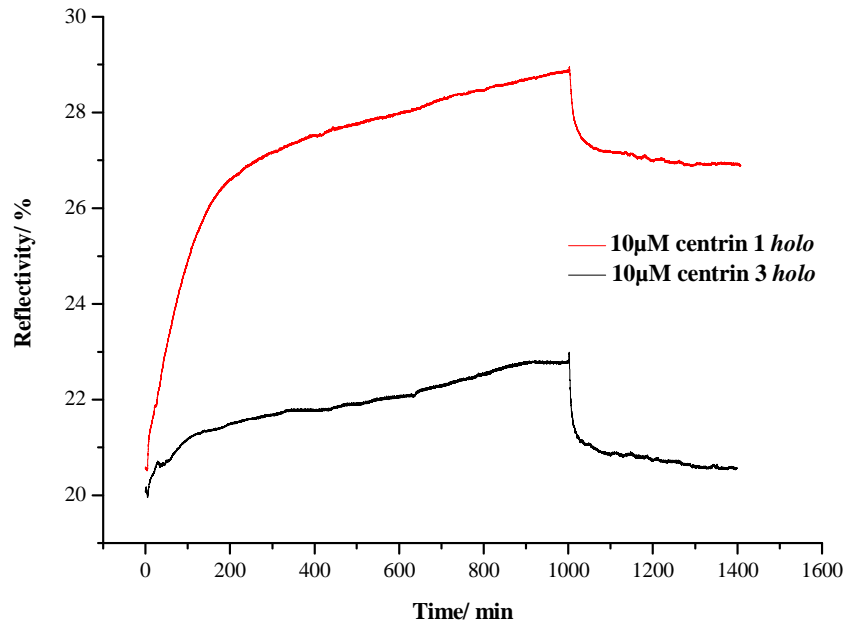


**Figure 6.8.4:** Surface plasmon resonance kinetic measurement of Cen3p *holo* versus Cen1p *holo*. The measurement was conducted on the combined mPEG thiol/P19 matrix, where the beta and gamma subunits of transducin were immobilized.

## **6.9 Conclusion and Outlook**

A surface plasmon resonance sensor platform for centrin-transducin interaction measurements was successfully developed. The so-called combined mPEG thiol/P19 matrix was stable, reproducible and non-fouling.

The surface plasmon resonance measurements suggest the evidence that centrin 1 (Cen1p *holo*) and transducin indeed interact with high affinity<sup>28</sup>. *In vitro* assays, such as co-immunoprecipitation, overlay and co-sedimentation as well as size exclusion chromatography and kinetic light scattering experiments, all of these methods, previously demonstrated that Cen1p *holo* binds with high affinity to transducin. Therefore, Cen1p *holo* was capable to serve as the positive control in the interaction experiments.

This study showed additionally the variations in binding affinity that exist for the differently expressed centrin 1 constructs. Although the constructs possessed very different masses, a clear differentiation in binding to the transducin was investigated in comparison to the centrin 1 *holo* protein. The Cen1p $\Delta$ EF1 and Cen1p $\Delta$ Nterm constructs exhibited nearly no binding affinity to the beta and gamma subunit of transducin. But the Cen1p $\Delta$ S1Nterm fragment, that is only six amino acids longer than the Cen1p $\Delta$ Nterm protein constructs, resulted in a similar binding behavior than the Cen1p *holo* protein. For that reason, these six amino acids, LTEDQK, are thought to be responsible for the binding to transducin ( $G_i\beta\gamma$ ) (Figure 6.9.1).

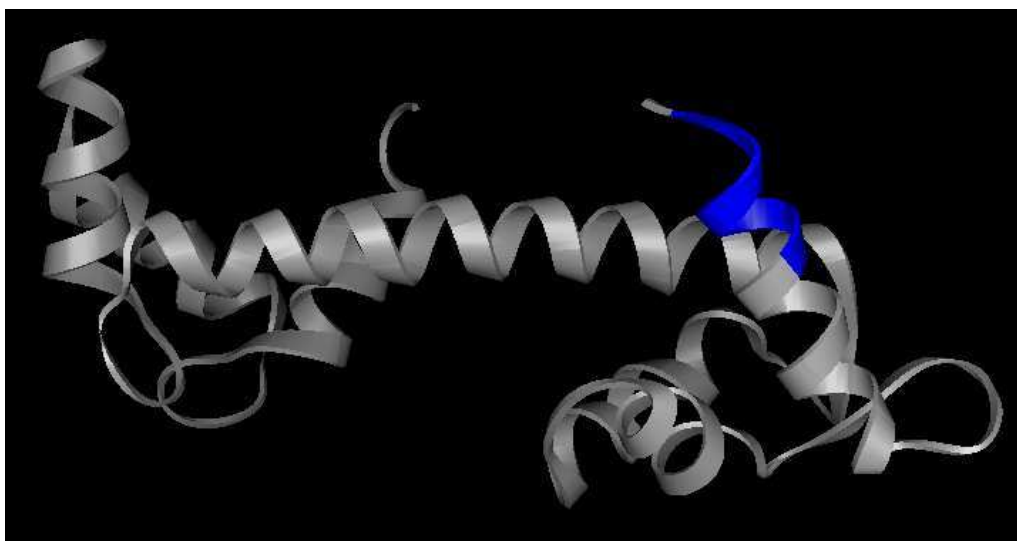


**Figure 6.9.1:** Simulation of the centrin 1 *holo* protein. The six amino acids, that were found to be responsible for the binding to the beta and gamma subunits of transducin, are marked in blue. The simulation was generated with software Vector-NTI-Suite (3D-viewer of Vector-NTI) using the 3D-coordinates of the Brookhaven Protein Database (PDB).

Cen3p *holo*, an isoform of centrin 1, was investigated in the surface plasmon resonance studies as well. In comparison to Cen1p *holo* the centrin 3 isoform resulted in very limited binding to the beta and gamma subunits of transducin. In Table 6.9.1 the SPR results of the binding study were summarized.

**Table 6.9.1: Summary of the SPR binding study to probe centrin-transducin interactions.**

<b>Limited binding to transducin (<math>G_t\beta\gamma</math>)</b>	<b>high affinity to transducin (<math>G_t\beta\gamma</math>)</b>
Cen1p $\Delta$ EF1	Cen1p <i>holo</i>
Cen1p $\Delta$ Nterm	Cen1p $\Delta$ S1Nterm
Cen3p <i>holo</i>	

The affinity constants  $k_{on}$  and  $k_{off}$  could not be determined in this study for several reasons. The main difficulty to verify the binding affinity of centrin to transducin was that no 1 : 1 ratio for the interaction was found. SPR measurements for longer periods of time, over some days, showed a binding curve of centrin 1 *holo* that became linear and constantly increased. Therefore, dimerization and oligomerization of centrin 1 could be possible. Item *in vivo*, centrin 1 *holo* protein was thought to form dimers and oligomers to build nanofilaments. A second problem to determine the affinity constants was that the centrin-transducin interaction was irreversible under the applied buffer conditions. Hence no dissociation process with buffer F (+  $Ca^{2+}$ ) was monitored and no  $k_{off}$  was determinable. Even the usual regeneration methods for sensors failed to separate centrin and transducin. *In vivo*, the centrin-transducin dissociation might be regulated by an enzyme. Casein kinase 2 in an ATP containing buffer was applied in this study as possible candidate for regulation, but did not show any effect under the testing conditions.

Thirdly, every interaction experiment was conducted on a different substrate due to the irreversibility of the centrin-transducin interaction. As the beta and gamma subunits of transducin that expose 17 lysin residues were linked to the matrix in an undirected way, the response and the affinity constants could vary from sample to sample slightly.

There still remain unresolved issues in the centrin-transducin interaction mechanism. Especially the sensor regeneration needs a lot of further work. The binding behaviour of the two other centrin isoforms, centrin 2 and centrin 4, can be investigated on the combined mPEG thiol/P19 matrix as well. Different buffer conditions for the interaction can be studied.

Another approach to get an idea about the affinity constants,  $k_{on}$  and  $k_{off}$ , could be realized on a Biacore surface plasmon resonance device under completely controlled conditions. Constant temperature and flow in a Biacore machine, injection by robot-controlled

pipettes, smaller reaction volumes etc., all these factors could improve the measurements. For example, Biacore 2000 and 3000 instruments use a sensor chip technology, where the thin gold film (~ 50 nm) on the glass substrate is divided into four channels or flow cells. Both devices can record from all four flow cells at the same time, allowing real-time reference subtraction and measurement of analyte binding, so that three different analytes can be probed simultaneously. A Biacore device could not only fasten the SPR kinetic measurements, but also increase the reproducibility. The centrin fragments could be traced and compared to the centrin 1 *holo* in real time, each on a newly built sensor matrix. For the experiments on Biacore instruments the combined mPEG thiol/P19 matrix could be used as well.

## 6.10 References

1. <http://www.bbc.co.uk/schools/gcsebitesize/img/biyestructure.gif>.
2. Mann, I. C., The Development of the human eye. *British Medical Association, London 1964*.
3. Leonhardt, H., Taschenlehrbuch der gesamten Anatomie III. Histologie, Zytologie und Mikroanatomie des Menschen. *Georg Thieme Verlag, Stuttgart 1990*.
4. Wehner, G.; Gehring, W., Zoologie. *Georg Thieme Verlag, Stuttgart 1995*.
5. Kolb, H., How the retina works - Much of the construction of an image takes place in the retina itself through the use of specialized neural circuits. *American Scientist 2003, 91, (1), 28-35*.
6. Carterdawson, L. D.; Lavail, M. M., Rods and Cones in the Mouse Retina .1. Structural-Analysis Using Light and Electron-Microscopy. *Journal of Comparative Neurology 1979, 188, (2), 245-262*.
7. Carterdawson, L. D.; Lavail, M. M., Rods and Cones in the Mouse Retina .2. Autoradiographic Analysis of Cell Generation Using Tritiated-Thymidine. *Journal of Comparative Neurology 1979, 188, (2), 263-272*.
8. Fain, G. L.; Matthews, H. R.; Cornwall, M. C.; Koutalos, Y., Adaptation in vertebrate photoreceptors. *Physiological Reviews 2001, 81, (1), 117-151*.
9. Heck, M.; Hofmann, K. P., Maximal rate and nucleotide dependence of rhodopsin-catalyzed transducin activation - Initial rate analysis based on a double displacement mechanism. *Journal of Biological Chemistry 2001, 276, (13), 10000-10009*.
10. Burns, M. E.; Baylor, D. A., Activation, deactivation, and adaptation in vertebrate, photoreceptor cells. *Annual Review of Neuroscience 2001, 24, 779-805*.
11. Liu, P.; Osawa, S.; Weiss, E. R., M opsin phosphorylation in intact mammalian retinas. *Journal of Neurochemistry 2005, 93, (1), 135-144*.
12. Gurevich, E.; Gurevich, V., Arrestins: ubiquitous regulators of cellular signaling pathways. *Genome Biology 2006, 7, (9), 236*.
13. Jan, L. Y.; Jan, Y. N., Receptor-regulated ion channels. *Current Opinion in Cell Biology 1997, 9, (2), 155-160*.
14. Offermanns, S., G-proteins as transducers in transmembrane signalling. *Progress in Biophysics & Molecular Biology 2003, 83, (2), 101-130*.
15. Arshavsky, V. Y.; Lamb, T. D.; Pugh, E. N., G proteins and phototransduction. *Annual Review of Physiology 2002, 64, 153-187*.
16. Ridge, K. D.; Abdulaev, N. G.; Sousa, M.; Palczewski, K., Phototransduction: crystal clear. *Trends in Biochemical Sciences 2003, 28, (9), 479-487*.
17. Hofmann, K. P.; Ernst, O. P., [To see from light--biophysics of visual signal transduction]. *Z Med Phys 2001, 11, (4), 217-225*.
18. Brandstatter, J. H.; Koulen, P.; Wassle, H., Diversity of glutamate receptors in the mammalian retina. *Vision Research 1998, 38, (10), 1385-1397*.
19. Boycott, B.; Wassle, H., Parallel processing in the mammalian retina - The Proctor Lecture. *Investigative Ophthalmology & Visual Science 1999, 40, (7), 1313-1327*.
20. Brandstatter, J. H.; Hack, I., Localization of glutamate receptors at a complex synapse - The mammalian photoreceptor synapse. *Cell and Tissue Research 2001, 303, (1), 1-14*.
21. Lamb, T. D.; Pugh, E. N., Dark adaptation and the retinoid cycle of vision. *Progress in Retinal and Eye Research 2004, 23, (3), 307-380*.
22. Philp, N. J.; Chang, W.; Long, K., Light-Stimulated Protein Movement in Rod Photoreceptor Cells of the Rat Retina. *Febs Letters 1987, 225, (1-2), 127-132*.

23. Brann, M. R.; Cohen, L. V., Diurnal Expression of Transducin Messenger-Rna and Translocation of Transducin in Rods of Rat Retina. *Science* 1987, 235, (4788), 585-587.
24. Whelan, J. P.; McGinnis, J. F., Light-Dependent Subcellular Movement of Photoreceptor Proteins. *Journal of Neuroscience Research* 1988, 20, (2), 263-270.
25. Hardie, R., Adaptation through translocation. *Neuron* 2002, 34, (1), 3-5.
26. Wolfrum, U.; Gießl, A.; Pulvermüller, A.; Trojan, P.; Hofmann, K. P., Centrins as potential regulators of light-induced transducin translocation. *Investigative Ophthalmology & Visual Science* 2004, 45, U184-U184.
27. Organisciak, D. T.; Xie, A.; Wang, H. M.; Jiang, Y. L.; Darrow, R. M.; Donoso, L. A., Adaptive-Changes in Visual Cell Transduction Protein-Levels - Effect of Light. *Experimental Eye Research* 1991, 53, (6), 773-779.
28. Pulvermüller, A.; Gießl, A.; Heck, M.; Wottrich, R.; Schmitt, A.; Ernst, O. P.; Choe, H. W.; Hofmann, K. P.; Wolfrum, U., Calcium-dependent assembly of centrin-G-protein complex in photoreceptor cells. *Molecular And Cellular Biology* 2002, 22, (7), 2194-2203.
29. Sokolov, M.; Lyubarsky, A. L.; Strissel, K. J.; Savchenko, A. B.; Govardovskii, V. I.; Pugh, E. N.; Arshavsky, V. Y., Massive light-driven translocation of transducin between the two major compartments of rod cells: A novel mechanism of light adaptation. *Neuron* 2002, 34, (1), 95-106.
30. Wolfrum, U.; Gießl, A.; Pulvermüller, A., Centrins, a novel group of Ca<sup>2+</sup>-binding proteins in vertebrate photoreceptor cells. In *Photoreceptors and Calcium*, 2002; Vol. 514, pp 155-178.
31. Arshavsky, V. Y., Rhodopsin phosphorylation: from terminating single photon responses to photoreceptor dark adaptation. *Trends in Neurosciences* 2002, 25, (3), 124-126.
32. Mendez, A.; Lem, J.; Simon, M.; Chen, J., Light-dependent translocation of arrestin in the absence of rhodopsin phosphorylation and transducin signaling. *Journal of Neuroscience* 2003, 23, (8), 3124-3129.
33. Sokolov, M.; Strissel, K. J.; Leskov, I. B.; Michaud, N. A.; Govardovskii, V. I.; Arshavsky, V. Y., Phosducin facilitates light-driven transducin translocation in rod photoreceptors - Evidence from the phosducin knockout mouse. *Journal of Biological Chemistry* 2004, 279, (18), 19149-19156.
34. Gießl, A.; Pulvermüller, A.; Trojan, P.; Park, J. H.; Choe, H. W.; Ernst, O. P.; Hofmann, K. P.; Wolfrum, U., Differential expression and interaction with the visual G-protein transducin of centrin isoforms in mammalian photoreceptor cells. *Journal Of Biological Chemistry* 2004, 279, (49), 51472-51481.
35. Gießl, A.; Trojan, P.; Rausch, S.; Pulvermüller, A.; Wolfrum, U., Centrins, gatekeepers for the light-dependent translocation of transducin through the photoreceptor cell connecting cilium. *Science Direct* 2006, 46, 4502-4509.
36. Besharse, J. C.; Horst, C. J., Ciliary and Flagellar Membranes. *Plenum Press, New York* 1990, (Bloodgood, R.A., ed), pp. 389-417.
37. Marszalek, J. R.; Liu, X. R.; Roberts, E. A.; Chui, D.; Marth, J. D.; Williams, D. S.; Goldstein, L. S. B., Genetic evidence for selective transport of opsin and arrestin by kinesin-II in mammalian photoreceptors. *Cell* 2000, 102, (2), 175-187.
38. Zhang, H.; Huang, W.; Zhang, H.; Zhu, X.; Craft, C.; Baehr, W.; Chen, C., Light-dependent redistribution of visual arrestins and transducin subunits in mice with defective phototransduction. *Mol Vis* 2003, 9, 231-237.
39. Elias, R. V.; Sezate, S. S.; Cao, W.; McGinnis, J. F., Temporal kinetics of the light/dark translocation and compartmentation of arrestin and alpha-transducin in mouse photoreceptor cells. *Mol Vis* 2004, 10, 672-681.

40. Kuhn, H.; Dreyer, W. J., Light Dependent Phosphorylation of Rhodopsin by Atp. *Febs Letters* 1972, 20, (1), 1-&.
41. Dolph, P. J.; Ranganathan, R.; Colley, N. J.; Hardy, R. W.; Socolich, M.; Zuker, C. S., Arrestin Function in Inactivation of G-Protein Coupled Receptor Rhodopsin In vivo. *Science* 1993, 260, (5116), 1910-1916.
42. Arshavsky, V. Y., Protein Translocation in Photoreceptor Light Adaptation: A Common Theme in Vertebrate and Invertebrate Vision. *Sci. STKE* 2003, Vol. 2003, (204), p. pe43.
43. Gießl, A., Molekulare Charakterisierung der Centrin-Isoformen in der Retina von Säugetieren. *PhD Thesis* 2004.
44. Wolfrum, U.; Salisbury, J. L., Centrin - New Ca<sup>2+</sup>-Binding Protein for the Retina and a Novel Component of the Connecting Cilium of Photoreceptors in Mammals and Man. *Investigative Ophthalmology & Visual Science* 1995, 36, (4), S513-S513.
45. Wolfrum, U.; Salisbury, J. L., Expression of centrin isoforms in the mammalian retina. *Experimental Cell Research* 1998, 242, (1), 10-17.
46. Molday, R. S.; Kaupp, U. B., Ion channels of vertebrate photoreceptors. In D.G. Stavenga, W.J.DeGrip, & E.N.Pugh Jr (Eds.), *Molecular mechanism in visual transduction* 2000, (pp.143-182), Amsterdam: Elsevier Science Publishers B.V.
47. Matthews, H. R.; Fain, G. L., A light-dependent increase in free Ca<sup>2+</sup> concentration in the salamander rod outer segment. *Journal of Physiology-London* 2001, 532, (2), 305-321.
48. Matthews, H. R.; Fain, G. L., Time course and magnitude of the calcium release induced by bright light in salamander rods. *Journal of Physiology-London* 2002, 542, (3), 829-841.
49. Woodruff, M. L.; Lem, J.; Fain, G. L., Early receptor current of wild-type and transducin knockout mice: photosensitivity and light-induced Ca<sup>2+</sup> release. *Journal of Physiology-London* 2004, 557, (3), 821-828.
50. Gießl, A.; Trojan, P.; Pulvermüller, A.; Wolfrum, U., Centrins, potential regulators of transducin translokation in photoreceptor cells. *Williams DS (ed) Cell biology and related disease of the outer retina World Scientific Publishing Company Pte. Ltd., Singapore* 2004, 122-195.
51. Zhang, H. B.; Huang, W.; Zhang, H. K.; Zhu, X. M.; Craft, C.; Baehr, W.; Chen, C. K., Light-dependent redistribution of visual arrestins and transducin subunits in mice with defective phototransduction. *Molecular Vision* 2003, 9, (33-34), 231-237.
52. Cronin, M. A.; Diao, F.; Tsunoda, S., Light-dependent subcellular translocation of Gq{alpha} in Drosophila photoreceptors is facilitated by the photoreceptor-specific myosin III NINAC. *J Cell Sci* 2004, 117, (20), 4797-4806.
53. Fung, B. K. K., Characterization of Transducin from Bovine Retinal Rod Outer Segments .1. Separation and Reconstitution of the Subunits. *Journal of Biological Chemistry* 1983, 258, (17), 495-502.
54. Fung, B. K. K.; Nash, C. R., Characterization of Transducin from Bovine Retinal Rod Outer Segments .2. Evidence for Distinct Binding-Sites and Conformational-Changes Revealed by Limited Proteolysis with Trypsin. *Journal of Biological Chemistry* 1983, 258, (17), 503-510.
55. Denker, B. M.; Neer, E. J.; Schmidt, C. J., Mutagenesis of the Amino Terminus of the Alpha-Subunit of the G-Protein G<sub>0</sub> - In vitro Characterization of Alpha-0-Beta-Gamma-Interactions. *Journal of Biological Chemistry* 1992, 267, (9), 6272-6277.
56. Hurley, J. B., Isolation and Recombination of Bovine Rod Outer Segment Cgmp Phosphodiesterase and Its Regulators. *Biochemical and Biophysical Research Communications* 1980, 92, (2), 505-510.

57. Salisbury, J. L., Centrin, Centrosomes, and Mitotic Spindle Poles. *Current Opinion in Cell Biology* 1995, 7, (1), 39-45.
58. Schiebel, E.; Bornens, M., In Search of a Function for Centrins. *Trends in Cell Biology* 1995, 5, (5), 197-201.
59. UCSC Genome Bioinformatics, Human Gene CETN1 Description, Human Gene CETN3 Description. <http://genome.ucsc.edu>, Known Gene ID: NM\_004066, NM\_004365.
60. Wiech, H.; Geier, B. M.; Paschke, T.; Spang, A.; Grein, K.; Steinkotter, J.; Melkonian, M.; Schiebel, E., Characterization of green alga, yeast, and human centrins - Specific subdomain features determine functional diversity. *Journal of Biological Chemistry* 1996, 271, (37), 22453-22461.
61. Durussel, I.; Blouquit, Y.; Middendorp, S.; Craescu, C. T.; Cox, J. A., Cation- and peptide-binding properties of human centrin 2. *Febs Letters* 2000, 472, (2-3), 208-212.
62. Tourbez, M.; Firanescu, C.; Yang, A.; Unipan, L.; Duchambon, P.; Blouquit, Y.; Craescu, C. T., Calcium-dependent self-assembly of human centrin 2. *Journal of Biological Chemistry* 2004, 279, (46), 47672-47680.
63. Geier, B. M.; Wiech, H.; Schiebel, E., Binding of centrins and yeast calmodulin to synthetic peptides corresponding to binding sites in the spindle pole body components Kar1p and Spc110p. *Journal of Biological Chemistry* 1996, 271, (45), 28366-28374.
64. Pieper, U.; Eswar, N.; Braberg, H.; Madhusudhan, M. S.; Davis, F. P.; Stuart, A. C.; Mirkovic, N.; Rossi, A.; Marti-Renom, M. A.; Fiser, A.; Webb, B.; Greenblatt, D.; Huang, C. C.; Ferrin, T. E.; Sali, A., MODBASE, a database of annotated comparative protein structure models, and associated resources. *Nucleic Acids Research* 2004, 32, D217-D222.
65. Salisbury, J. L.; Floyd, G. L., Calcium-Induced Contraction of Rhizoplast of a Quadriflagellate Green-Alga. *Science* 1978, 202, (4371), 975-977.
66. Lee, V. D.; Huang, B., Molecular-Cloning and Centrosomal Localization of Human Caltractin. *Proceedings of the National Academy of Sciences of the United States of America* 1993, 90, (23), 11039-11043.
67. Baum, P.; Furlong, C.; Byers, B., Yeast Gene Required for Spindle Pole Body Duplication - Homology of Its Product with Ca<sup>2+</sup>-Binding Proteins. *Proceedings of the National Academy of Sciences of the United States of America* 1986, 83, (15), 5512-5516.
68. Baum, P.; Yip, C.; Goetsch, L.; Byers, B., A Yeast Gene Essential for Regulation of Spindle Pole Duplication. *Molecular and Cellular Biology* 1988, 8, (12), 5386-5397.
69. Huang, B.; Mengersen, A.; Lee, V. D., Molecular-Cloning of Cdna for Caltractin, a Basal Body Associated Ca<sup>2+</sup>-Binding Protein - Homology in Its Protein-Sequence with Calmodulin and the Yeast Cdc31 Gene-Product. *Journal of Cell Biology* 1988, 107, (1), 133-140.
70. Errabolu, R.; Sanders, M. A.; Salisbury, J. L., Cloning of a Cdna-Encoding Human Centrin, an Ef-Hand Protein of Centrosomes and Mitotic Spindle Poles. *Journal of Cell Science* 1994, 107, 9-16.
71. Zhu, J. A.; Bloom, S. E.; Lazarides, E.; Woods, C., Identification of a Novel Ca<sup>2+</sup>-Regulated Protein That Is Associated with the Marginal Band and Centrosomes of Chicken Erythrocytes. *Journal of Cell Science* 1995, 108, 685-698.
72. Levy, Y. Y.; Lai, E. Y.; Remillard, S. P.; Heintzelman, M. B.; Fulton, C., Centrin is a conserved protein that forms diverse associations with centrioles and MTOCs in Naegleria and other organisms. *Cell Motility and the Cytoskeleton* 1996, 33, (4), 298-323.
73. Madeddu, L.; Klotz, C.; LeCaer, J. P.; Beisson, J., Characterization of centrin genes in Paramecium. *European Journal of Biochemistry* 1996, 238, (1), 121-128.
74. Meng, T. C.; Aley, S. B.; Svard, S. G.; Smith, M. W.; Huang, B.; Kim, J.; Gillin, F. D., Immunolocalization and sequence of caltractin/centrin from the early branching

- eukaryote *Giardia lamblia*. *Molecular and Biochemical Parasitology* 1996, 79, (1), 103-108.
75. Middendorp, S.; Kuntziger, T.; Abraham, Y.; Holmes, S.; Bordes, N.; Paintrand, M.; Paoletti, A.; Bornens, M., A role for centrin 3 in centrosome reproduction. *Journal of Cell Biology* 2000, 148, (3), 405-415.
76. Wottrich, R., Klonierung und computergestützte Strukturanalyse von Centrinisofomen der Ratte (*Rattus norvegicus*). *Diploma thesis* 1998, University of Karlsruhe, Germany.
77. Gavet, O.; Alvarez, C.; Gaspar, P.; Bornens, M., Centrin4p, a novel mammalian centrin specifically expressed in ciliated cells. *Molecular Biology of the Cell* 2003, 14, (5), 1818-1834.
78. Park, J. H.; Pulvermüller, A.; Scheerer, P.; Rausch, S.; Giebl, A.; Hohne, W.; Wolfrum, U.; Hofmann, K. P.; Ernst, O. P.; Choe, H. W.; Krauss, N., Insights into functional aspects of centrins from the structure of N-terminally extended mouse centrin 1. *Vision Research* 2006, 46, (27), 4568-4574.
79. Salisbury, J. L.; Baron, A.; Surek, B.; Melkonian, M., Striated Flagellar Roots - Isolation and Partial Characterization of a Calcium-Modulated Contractile Organelle. *Journal of Cell Biology* 1984, 99, (3), 962-970.
80. Salisbury, J. L.; Baron, A. T.; Sanders, M. A., The Centrin-Based Cytoskeleton of *Chlamydomonas-Reinhardtii* - Distribution in Interphase and Mitotic Cells. *Journal of Cell Biology* 1988, 107, (2), 635-641.
81. Baron, A. T.; Greenwood, T. M.; Salisbury, J. L., Localization of the Centrin-Related 165,000-Mr Protein of Ptk2 Cells During the Cell-Cycle. *Cell Motility and the Cytoskeleton* 1991, 18, (1), 1-14.
82. Baron, A. T.; Greenwood, T. M.; Bazinet, C. W.; Salisbury, J. L., Centrin Is a Component of the Pericentriolar Lattice. *Biology of the Cell* 1992, 76, (3), 383-388.
83. Bhattacharya, D.; Steinkotter, J.; Melkonian, M., Molecular-Cloning and Evolutionary Analysis of the Calcium-Modulated Contractile Protein, Centrin, in Green-Algae and Land Plants. *Plant Molecular Biology* 1993, 23, (6), 1243-1254.
84. Heck, M.; Pulvermüller, A.; Hofmann, K. P., Light scattering methods to monitor interactions between rhodopsin-containing membranes and soluble proteins. In *Vertebrate Phototransduction and the Visual Cycle, Part A*, 2000; Vol. 315, pp 329-347.
85. Löfås, S.; Johnsson, B., A Novel Hydrogel Matrix on Gold Surfaces in Surface-Plasmon Resonance Sensors for Fast and Efficient Covalent Immobilization of Ligands. *Journal of the Chemical Society-Chemical Communications* 1990, (21), 1526-1528.
86. Yu, F., Surface Plasmon Fluorescence Spectroscopy and Surface Plasmon Diffraction in Biomolecular Interaction Studies. *PhD Thesis* 2004, University of Mainz
87. Nuzzo, R. G.; Allara, D. L., Adsorption of Bifunctional Organic Disulfides on Gold Surfaces. *Journal of the American Chemical Society* 1983, 105, (13), 4481-4483.
88. Colognato, H.; Yurchenco, P. D., Form and function: The laminin family of heterotrimers. *Developmental Dynamics* 2000, 218, (2), 213-234.
89. Malinda, K. M.; Kleinman, H. K., The laminins. *The International Journal of Biochemistry & Cell Biology* 1996, 28, (9), 957-959.
90. Fujita, K.; Yokoyama, R.; T., T., Molecular orientation in the peptide self-assembled monolayers. Growth, Evolution and Properties of Surfaces, Thin Films and Self-Organized Structures. *Mater.Res.Soc.Symposium Proceedings*, 648, *Mater.Res.Soc.*, 6241 Warrendale, PA, USA 2001.
91. Wazawa, T.; Ishizuka-Katsura, Y.; Nishikawa, S.; Iwane, A. H.; Aoyama, S., Grafting of poly(ethylene glycol) onto poly(acrylic acid)-coated glass for a protein-resistant surface. *Analytical Chemistry* 2006, 78, (8), 2549-2556.

92. Chen, R. J.; Choi, H. C.; Bangsaruntip, S.; Yenilmez, E.; Tang, X. W.; Wang, Q.; Chang, Y. L.; Dai, H. J., An investigation of the mechanisms of electronic sensing of protein adsorption on carbon nanotube devices. *Journal of the American Chemical Society* 2004, 126, (5), 1563-1568.
93. Sinner, E. K.; Reuning, U.; Kok, F. N.; Sacca, B.; Moroder, L.; Knoll, W.; Oesterhelt, D., Incorporation of integrins into artificial planar lipid membranes: characterization by plasmon-enhanced fluorescence spectroscopy. *Analytical Biochemistry* 2004, 333, (2), 216-224.
94. Lössner, D.; Kessler, H.; Thumshirn, G.; Dahmen, C.; Wiltshi, B.; Tanaka, M.; Knoll, W.; Sinner, E. K.; Reuning, U., Binding of small mono- and oligomeric integrin ligands to membrane-embedded integrins monitored by surface plasmon-enhanced fluorescence spectroscopy. *Analytical Chemistry* 2006, 78, (13), 4524-4533.

## 7. Summary

In this study, surface plasmon phenomena, i.e. propagating and localized surface plasmon resonances (p-/l-SPR), were used for detailed investigations of molecular interactions on different substrate surfaces. Other surface characterization methods such as cyclic voltammetry, impedance spectroscopy, and scanning electron microscopy were used to obtain complementary information.

In the first part of this study, nanoporous gold (NPG) substrates were examined. It emerged that the use of NPG substrates was not a simple reiteration of “another metal” for plasmonic sensing. The NPG substrates displayed unique properties due to their porosity. They were uniquely suited to the examination of surface plasmons because the material simultaneously showed features of both planar metal films exhibiting p-SPR excitations and nanoparticles exhibiting l-SPR excitations. The streptavidin-doped bead binding experiment proved the utility of NPG for quantitative p-SPR measurements. Taken together, the experimental results led to an hypothesis regarding optical sensing of size-selective adsorption on nanoporous metal membranes: that species that were able to diffuse *into* the pores of NPG and modify their dielectric atmosphere were detectable by changes in the l-SPR excitations, whereas species that adsorbed only *onto* the geometric surface of the pores of a film of NPG were less influential to l-SPR but equally detectable by p-SPR measurements. More generally, the results of this research provide insights into the fundamental optical properties of mesoporous materials and the design of new high surface area materials for dynamic optical sensing of adsorbates.

The second part of this study was based on the investigations of macroporous gold/silica composite inverse opals. The substrates were prepared through silane surface modification, followed by gold nanoparticle deposition and electroless plating on the silica inverse opal templates. These samples combined the advantages of a larger available gold surface area with a regular and highly ordered grating structure. A plasmonic response of the gold/silica composite inverse opals was observed, which showed a pronounced spectral change upon the variation of the surrounding dielectrics. This observation demonstrated the capability of this novel material to be used for sensing applications.

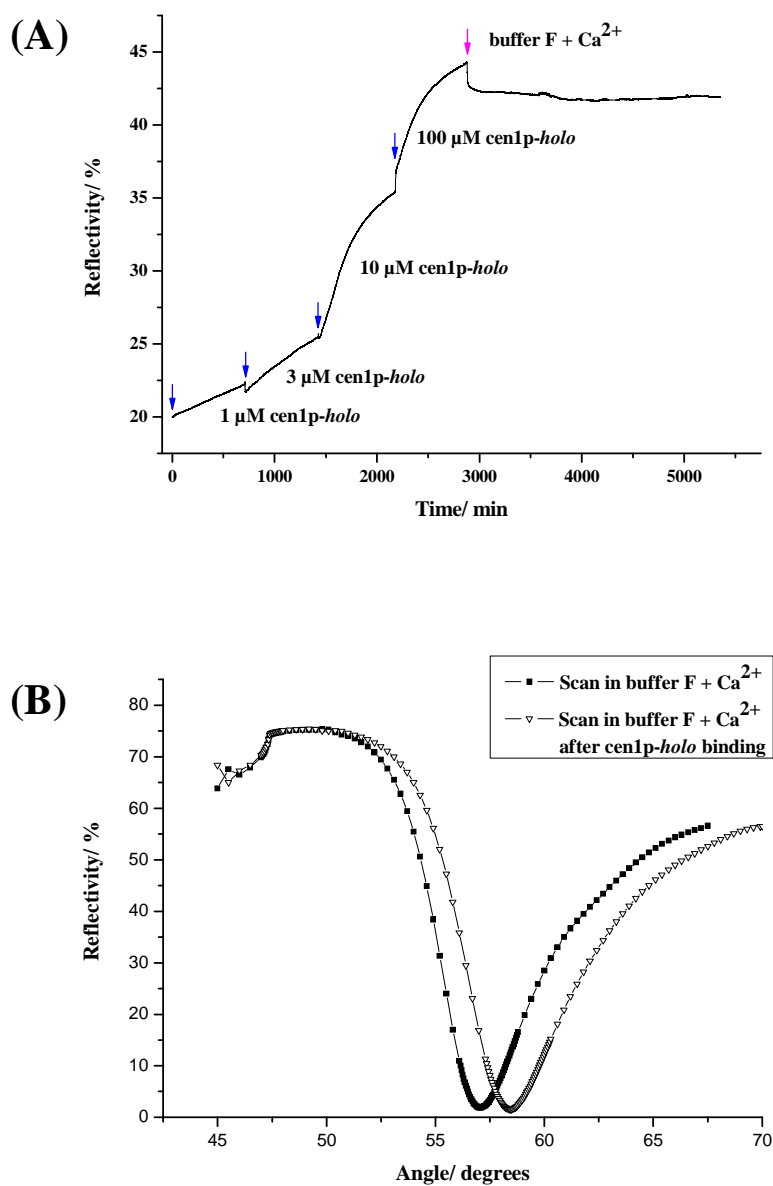
In the final part of this thesis, surface plasmon resonance spectroscopy was utilized to monitor interfacial protein/protein interactions of the calcium binding protein centrin with the heterotrimeric G-protein transducin on an evaporated flat/dense gold film in order to understand the molecular concept of vision better. A sensor platform for centrin-transducin

interaction measurements was successfully developed. The interacting-site of centrin 1 was identified by probing differently expressed centrin 1 fragments. Six amino acids, LTEDQK, were shown to be responsible for the binding to transducin ( $G_t\beta\gamma$ ). Kinetic measurements showed that centrin-transducin binding does not occur in a 1:1 ratio. Furthermore, dimerization and oligomerization of centrin 1 was indicated. Consequently, centrin 1 can bind the transducin passing the ciliary lumen and may contribute to a  $Ca^{2+}$  dependent barrier for transducin in the connecting cilium.

## 8. Appendix

### 8.1 Summary of advantages and disadvantages of NPG at a glance

Advantage of NPG	Disadvantage of NPG
Inexpensive material and production (low-cost) > affordable (hammering)	Inhomogeneities in film thickness
Compatible with well-studied SAMs of thiols > biocompatible	NPG roughness causes forward scattering and directional backward scattering of nonradiative SPs, no sharp signals (both in plasmon and in absorbance peak)
Free corrosion of Ag-Au alloy in 70 % HNO <sub>3</sub> at room temperature	Production of toxic NO <sub>2</sub> during fabrication
Pore size tuneable with time of exposure in acid bath	No major differences in pore size for samples 5 min to 2 h etched
High surface area due to 3D pore structure > sponge like morphology	Fractal structure leads to size limitations – pores are not accessible for larger molecules - > penetrable only by molecules of certain shapes and sizes.
Stable NPG substrate with only a few defects such as cracks – sponge like morphology stays stable for at least 6 month (in water and dried state)	Critical step in NPG fabrication is the silanization of the glass slide, where 3D self-assembly of the 3 MPT molecules can happen preventing the NPG from being fully glued to the glass substrate i.e. the NPG could come off during the experiment
Continuous gold can exhibit p-SPR	A sharp resonance can be derived only by an invisible IR laser. This laser should be parallel aligned, for example to a red laser, for visualizing the measuring spot.
Nanostructures can exhibit l-SPR	Small signals, such as DNA-DNA hybridization are smeared out / in the noise range due to large pore size distribution
p-SPR and l-SPR modes can be excited simultaneously	
NPG is compatible with typical electrochemical impedance spectroscopy EIS measurements	
NPG membranes are translucent > transmission to determine the thickness	
Floats on water	
NPG morphology can function as ionic fluid reservoir	

**8.2 Supporting material for chapter 6**

**Figure 8.2.1: (A) Centrin-1-holo protein – titration experiment: centrin-1-holo protein as a positive control was injected in different concentrations to probe the interaction between transducin and centrin. The surface architecture was the combined mPEG thiol matrix described in chapter 6 (6.5.3); (B) Scans were recorded before and after the deposition of centrin-1-holo protein. A fit of the scan curves revealed a thickness of 10.6 nm for the centrin coverage assuming an homogeneous centrin layer with a refractive index of 1.45; Winspall (version 2.20) was used for the fitting.**

**8.3 Table of standard amino acid abbreviations**

Symbols of the 20 standard amino acids are listed in the following table according to IUPAC (International Union of Pure and Applied Chemistry) and IUB (International Union of Biochemistry) nomenclature recommendations (UPAC-IUB Commission on Biochemical Nomenclature (CBN). Abbreviations and symbols for nucleic acids, polynucleotides and their constituents. Recommendations 1970). The following abbreviations were used in this thesis.

<b>Amino Acid</b>	<b>3-Letter</b>	<b>1-Letter</b>
Alanine	Ala	A
Arginine	Arg	R
Asparagine	Asn	N
Aspartic acid	Asp	D
Cysteine	Cys	C
Glutamic acid	Glu	E
Glutamine	Gln	Q
Glycine	Gly	G
Histidine	His	H
Isoleucine	Ile	I
Leucine	Leu	L
Lysine	Lys	K
Methionine	Met	M
Phenylalanine	Phe	F
Proline	Pro	P
Serine	Ser	S
Threonine	Thr	T
Tryptophan	Trp	W
Tyrosine	Tyr	Y
Valine	Val	V

**8.4 List of Abbreviations**

This is a list of abbreviations that are used in the text.

aa	amino acid (protein length)
AC	alternating current
ACF	autocorrelation function
AFM	atomic force microscopy
ANTA	amino-nitrilotriacetic acid
ATP	adenosine triphosphate (universal energy currency of organisms)
BK7	Borkron glass (Fisher Scientific)
BLMs	black lipid membranes
CC	connecting cilium
CcO	cytochrome c oxidase
C <sub>dl</sub>	capacitance of the double layer
cen (cen1-cen4)	centrin (centrin 1- centrin 4)
cf.	confer
cGMP	cyclic guanosine monophosphate
CK2	casein kinase 2
CPE	constant phase element
CV	cyclic voltammetry
Cyt c	cytochrome c
1D	one dimensional
2D	two dimensional
3D	three dimensional
DC	direct current
DDM	<i>n</i> -Dodecyl- $\beta$ -D-maltoside
DiPhyPC	1,2-diphytanoyl- <i>sn</i> -glycero-3-phosphocholine
DMSO	dimethyl sulfoxide (CH <sub>3</sub> ) <sub>2</sub> SO
DNA	deoxyribonucleic acid
DTSP	dithiobis ( <i>N</i> -succinimidyl propionate)
DTP	dithiodipropionic acid
E	potential
EDTA	ethylenediaminetetraacetic acid (chelating agent)
EG	evaporated gold (film)
e.g.	for example ( <i>abbr. of Latin exempli gratia</i> )
EIS	electrochemical impedance spectroscopy
EtOH	ethanol
FEG	field emission gun
Fig.	figure
FRA	frequency response analyzer
FT-IR	Fourier Transform Infrared
FWHM	full width at half maximum
G-protein	guanine nucleotide binding protein
GDP	guanosine diphosphate
GRK1	rhodopsin kinase
G <sub>4</sub>	generation 4 (dendrimer)
G <sub>i</sub>	G-protein (alpha subunit) that inhibits adenylat cyclase
G <sub>olf</sub>	olfactory-type G protein (alpha subunit)

G <sub>q</sub>	G-protein (alpha subunit) that stimulates phospholipase C
G <sub>s</sub>	G-protein (alpha subunit) that activates adenylate cyclase
G <sub>t</sub>	transducin (guanine nucleotide binding protein)
G <sub>t</sub> α	alpha subunit of transducin
G <sub>t</sub> βγ	beta-gamma subunit of transducin
G <sub>t</sub> αβγ	heterotrimeric transducin (alpha-beta-gamma subunit)
GST	glutathione S-transferase
GTP	guanosine triphosphate
GTase	enzyme that can bind and hydrolyze GTP
h	hour
HeNe (laser)	helium-neon (laser)
i	current response
IgG	immunoglobulin G
IHP	inner Helmholtz plane
IR	infrared
IS	inner segment
kDa	kilodalton being equal to 1000 daltons
LaSFN9	Lanthanschwerflint glass (Schott)
LbL	layer-by-layer
min	minute
Mm	<i>Mus musculus</i>
Mm	millimeter, 10 <sup>-3</sup> m
mHz/ MHz	millihertz, 10 <sup>-3</sup> Hz/ megahertz, 10 <sup>6</sup> Hz
MPA	mercaptopropionic acid
MPT	(3-mercaptopropyl) trimethoxy-silane
MW	molecular weight
mV	milli, 10 <sup>-3</sup> Volt
nm	nanometer, 10 <sup>-9</sup> m
NP	nanoparticle
NPG	nanoporous gold
OHP	outer Helmholtz plane
OS	outer segment
PBS	phosphate buffer saline
pI	isoelectric point
PDE	phosphodiesterase
PDMS	polydimethyl siloxane
PKC	protein kinase C
PRC	photoreceptor cell
QCM	quartz crystal microbalance
R	resistance
R <sub>s</sub>	series resistance
R <sub>F</sub>	Faradaic resistance
RI	refractive index
RHO	rhodopsin
SA	streptavidin
SA-LX	polystyrene latex bead doped with streptavidin
SAM	self assembled monolayer
SE	secondary electrons
SEM	Scanning Electron Microscopy
SP	surface plasmon
SPR	surface plasmon resonance

l-SPR	localized surface plasmon resonance
p-SPR	propagating surface plasmon resonance
tBLM	tethered lipid bilayer
TSG	template stripped gold (ultra flat sample)
XPS	X-ray photoelectron spectroscopy
Y	admittance
Z	impedance

## **8.5 List of Figures**

**Figure 1.1.1:** Principle of a biosensor

**Figure 2.1.1:** Dispersion relation

**Figure 2.1.2:** Prism coupling in the Kretschmann/Raether configuration

**Figure 2.1.3:** Simulated surface plasmon resonance signal

**Figure 2.1.4:** Simulated SPR signal, influenced by the excitation wavelength

**Figure 2.1.5: (A)** Prism coupling to probe adsorption of layers

**Figure 2.1.5: (B)** Dispersion relation, here  $\omega$  versus  $k_{SP}$

**Figure 2.1.5: (C)** The angular reflectivity curves; shifted due to adsorption of layers

**Figure 2.1.6:** Absorption spectra of a porous film before and after immobilization of hIgG

**Figure 2.2.1:** Cyclic voltammogram for a reversible electron transfer reaction

**Figure 2.2.2: (A)** Model of the electrical double layer of Helmholtz (1853)

**Figure 2.2.2: (B)** Model of the electrical double layer of Bockris, Devanathan and Müller

**Figure 2.3.1:** Drawing of an AC voltage over time (the sine wave) and a resulting current

**Figure 2.3.2:** Equivalent circuit for a single electrochemical cell

**Figure 2.3.3:** Equivalent circuit for a complex system

**Figure 2.3.4:** Simulated Bode plot for a simple equivalent circuit model

**Figure 2.3.5:** Simulated admittance plot for a simple equivalent circuit model

**Figure 2.4.1:** LEO (Zeiss) 1530 Gemini

**Figure 2.5.1:** Exploitation of the 1D correlation function

**Figure 3.1.1:** Setup for simultaneous measurements of propagating and localized SPR

**Figure 3.1.2:** Photograph of the setup

**Figure 3.1.3:** Details of the sample configuration

**Figure 3.1.4:** Photograph of the sample holder

**Figure 3.3.1:** Sketch of the electrochemical flow cell

**Figure 3.4.1:** Harrick Scientific Plasma Cleaner (expanded model)

**Figure 3.4.2:** Computerized Surface Profiler: KLA-Tencor P-10

**Figure 3.4.3:** Perkin Elmer Lambda 900 UV/VIS/NIR spectrometer

**Figure 3.7.1:** Schematic representation of the silanization reaction mechanism

**Figure 4.1.1:** A photograph of a nanoporous gold membrane

- Figure 4.2.1:** Gold island nucleation by the surface dis- and reordering mechanism
- Figure 4.2.2:** Fabrication of the NPG substrates
- Figure 4.2.3:** Experimental setup for electrochemical dealloying method
- Figure 4.3.1:** Scanning electron micrographs of the chemically dealloyed NPG substrates
- Figure 4.3.2:** SEM images of the electrochemically dealloyed NPG substrates
- Figure 4.4.1:** SEM image of the two volt electrochemically dealloyed NPG substrate
- Figure 4.4.2:** 3D image plot that represents the autocorrelation function ACF ( $\Delta x$ ,  $\Delta y$ )
- Figure 4.4.3:** 2D diagram of the data points resulting from the ACF
- Figure 4.4.4:** Schematic presentation to find typical length scales with ACF method
- Figure 4.4.5:** Typical length scales of the NPG substrates resulting from the ACF
- Figure 4.5.1:** Cyclic voltammogram for a 15 minutes etched NPG sample
- Figure 4.5.2:** Cyclic voltammograms of 5 min, 15 min, 1 hour dealloyed NPG and EG film
- Figure 4.5.3:** CV and EIS measurements for the chemically dealloyed NPG samples
- Figure 4.5.4:** CV and EIS results of electrochemically etched NPG (1.2 volt and 2 volt)
- Figure 4.5.5:** UV/ VIS spectra of the differently etched NPG substrates
- Figure 4.5.6:** The formation of bigger gold structures during the dealloying procedure
- Figure 4.5.7:** Coherency between surface area enhancement and typical length scale<sup>-1</sup>
- Figure 4.6.1:** Demonstration of the different evanescent decay length of l- and p-SPR field
- Figure 4.6.2: (A)** Excitation of p-SPR on NPG (100 nm) using lasers of different wavelengths
- Figure 4.6.2: (B)** P-SPR curves of 100 nm NPG, p and s-polarized; 200 nm NPG, p-polarized
- Figure 4.6.3:** Winspall simulations for surface plasmon excitation of 47 nm and 100 nm EG
- Figure 4.6.4:** SPR excitation on 100 nm thick NPG substrates of different pore sizes
- Figure 4.6.5: (I)** P-SPR of streptavidin/ biotinylated IgG bindings on NPG and EG
- Figure 4.6.5: (II)** Multi-layer formation on NPG – a model system
- Figure 4.6.6:** P-SPR of streptavidin/bio-IgG/latex bead bindings on NPG and EG in buffer
- Figure 4.6.7:** P-SPR of streptavidin/bio-IgG/latex bead bindings on NPG and EG in air
- Figure 4.6.8: (A)** Sketch of the polystyrene latex beads deposited on the NPG substrate
- Figure 4.6.8: (B)** SEM images show the surface coverage of the latex beads on NPG (15 min)
- Figure 4.6.9:** Evolution of absorbance spectrum of NPG (15 min) in different glycerol conc.
- Figure 4.6.10:** Mathematic explanation of the absorbance results using Gaussian curves
- Figure 4.6.11:** Exposure of different gold substrates to increasing glycerol concentrations
- Figure 4.6.12:** Absorbance spectra of different samples exposed to a 60 % glycerol solution
- Figure 4.6.13:** Molecular structures of dendrimers:  $G_4(\text{CH-COO}^- \text{Na}^+)_{96}$  and  $G_4(\text{NH}^+ \text{Et}_2 \text{Cl})_{96}$
- Figure 4.6.14:** Dendrimer molecule  $G_4(\text{NH}^+ \text{Et}_2 \text{Cl})_{96}$  showing all 96 functional groups

**Figure 4.6.15: (A)** P-SPR on NPG (15 min) during the formation of dendrimer multilayers

**Figure 4.6.15: (B)** Absorbance spectra taken at the same time as the SPR scans

**Figure 4.6.15: (C)** Kinetic measurement recorded at  $\lambda = 570$  nm and  $\lambda = 700$  nm

**Figure 4.6.15: (D)** Signals of p-SPR and l-SPR on NPG as the dendrimer layers grow

**Figure 4.6.16:** SEM images of NPG (15 min) - before and after LbL deposition of dendrimers

**Figure 4.6.17:** LbL assembly of avidin and biotinylated antiavidin antibody on NPG

**Figure 4.6.18:** SEM of NPG (5 min and 24 h) after LbL of avidin/ biotinylated anti-avidin

**Figure 4.6.19:** Absorbance spectra of EG, 5 min and 24 h NPG for 3.5 protein double layer

**Figure 4.6.20:** Absorbance spectra of 5 min etched NPG after 18 protein double layer

**Figure 4.6.21:** Scheme of the interference of light due to the protein layers

**Figure 4.6.22:** A sine function was employed to fit the periodical oscillations (5 min NPG)

**Figure 4.6.23:** Correlation of the calculated thicknesses versus the 3 excitation wavelengths

**Figure 4.6.24:** The volume of the Y-shaped IgG antibody and IgG packings on a surface

**Figure 4.7.1:** Illustration of the coupling reaction leading to the chelating surface architecture

**Figure 4.7.2:** Schematic representation of the surface-adsorbed cytochrome c oxidase

**Figure 4.7.3:** Schematic illustration of the in-situ dialysis

**Figure 4.7.4:** P-SPR scans before and after cyt c oxidase binding; and after lipid assembly

**Figure 4.7.5:** Illustration of the electrochemical impedance spectroscopy measurements

**Figure 4.7.6:** Illustration of the cytochrome c effect

**Figure 4.7.7:** Demonstration of the membrane suspension on different substrates

**Figure 4.8.1:** Surface area enhancement of the different NPG substrates relative to EG

**Figure 4.8.2:** Summary of layer by layer experiments

**Figure 5.2.1: (A)** Schematic and **(B)** photographic picture of the dip coating setup

**Figure 5.2.2:** Particle transfer and crystallization mechanism during vertical lifting deposition

**Figure 5.2.3:** Scanning electron micrographs show the top view of inverse opals

**Figure 5.2.4:** Scheme of the fabrication of gold/silica composite inverse opals

**Figure 5.2.5: (A)** SEM image of gold nanoparticles deposited on walls of silica inverse opals

**Figure 5.2.5: (B)** Gold/silica composite inverse opal obtained after electroless plating

**Figure 5.3.1:** Apparent absorbance of a gold/silica composite inverse opal (glycerol conc.)

**Figure 6.1.1:** Schematic presentation and photograph of a human eye

**Figure 6.1.2:** Rod photoreceptor cell, where signal transduction is taking place

**Figure 6.1.3:** Light/dark adapted photoreceptor cells that show translocation of transducin

- Figure 6.1.4:** Schematic illustration of the barrier hypothesis
- Figure 6.2.1:** Activation of the heterotrimeric transducin (alpha-beta-gamma subunits)
- Figure 6.2.2:** Beta/gamma subunits of the G-protein transducin in three perspectives
- Figure 6.3.1:** ModBase predicted 3D structure of human centrin 1 in three perspectives
- Figure 6.3.2: (A)** Immunoelectron microscopy of centrin 3 in a mouse photoreceptor cell
- Figure 6.3.2: (B)** Differential localization of the four centrin isoforms in photoreceptor cells
- Figure 6.3.2: (C)** Differential localization of the four centrin isoforms in non-specialized cells
- Figure 6.3.3:** Schematic illustration of generated centrin 1 fragments and centrin 3 isoform
- Figure 6.5.1: (A)** Unloaded 3D carboxy-methyl-dextran matrix of a CM5 sensor chip
- Figure 6.5.1: (B)** Dextran matrix loaded with transducin for further interaction experiments
- Figure 6.5.2:** Chemical reaction of EDC/NHS activation
- Figure 6.5.3:** Centrin-transducin interaction on a Biacore CM5 Chip
- Figure 6.5.4:** Two dimensional surface architecture based on P19 matrix
- Figure 6.5.5:** Built up of a 2D surface architecture based on P19 (SPR kinetic measurement)
- Figure 6.5.6:** Centrin-transducin interaction on the two dimensional P19 matrix
- Figure 6.5.7:** Combined mPEG thiol matrix; 2 improvements: mPEG thiol and ethanolamine
- Figure 6.5.8:** Built up of the improved two dimensional surface architecture based on P19
- Figure 6.8.1:** SPR kinetic measurement of Cen1p $\Delta$ EF1 fragment versus Cen1p *holo* protein
- Figure 6.8.2:** SPR kinetic measurement of Cen1p $\Delta$ Nterm fragment versus Cen1p *holo*
- Figure 6.8.3:** SPR kinetic measurement of Cen1p $\Delta$ S1Nterm fragment versus Cen1p *holo*
- Figure 6.8.4:** SPR kinetic measurement of Cen3p *holo* protein versus Cen1p *holo* protein
- Figure 6.9.1:** Simulation of the centrin-1-*holo* protein (6 crucial amino acids marked in blue)

## **8.6 List of Tables**

- Table 4.1.1:** IUPAC nomenclature for porous materials
- Table 4.6.1:** Parameters for Winspall (version 2.20) simulations of dense gold surface
- Table 4.6.2:** Refractive indices at  $\lambda = 1152$  nm (IR laser) and temperature of 25,00°C
- Table 4.6.3:** P-SPR on NPG and flat gold, multilayer assembling system with latex beads
- Table 4.6.4:** The thickness of the bilayer ( $d_B$ ) was calculated for all 3 excitation wavelengths
- Table 4.7.1:** Summary of EIS fit results obtained for membrane reconstitution on TSG/NPG
- Table 6.2.1:** Characteristics of the 3 subunits of transducin extracted from the bovine retina
- Table 6.3.1:** Properties of the centrin 1 constructs and isoform centrin 3 (from *Mus musculus*)

**Table 6.9.1:** Summary of the SPR binding study to probe centrin-transducin interactions

## **Acknowledgements:**

First of all, I want to deeply thank my Ph.D. supervisor, Prof. Wolfgang Knoll. Without his care and inspiration my thesis would never have been completed. His fascination for surface science and travelling jumped over. Thank you for leading me the right direction and supporting me all the way along!

My thanks go to Dr. Eva-Kathrin Sinner, my bio-project leader. Her advice helped me to achieve my results in the centrin project. Thank you for encouraging me!

Thanks to Prof. Uwe Wolfrum for supporting me in the centrin project and allowing me to work in the labs of AG Wolfrum.

I thank Prof. Jonah Erlebacher for teaching me the method of chemically and electrochemically dealloying during my stay in Baltimore, Maryland at the Department of Materials Science and Engineering, Johns-Hopkins University; April 2006. The cherry blossom was beautiful.

My thanks also go to Dr. Fang Yu. He taught me how to generate propagating and localized plasmons. And his wife Dr. Danfeng Yao, who taught me how to cook chinese seaweed salad.

I acknowledge Dr. Jianjun Wang and Gunnar Glasser for numerous scanning electron microscope examinations of the NPG samples. Dr. Jianjun Wang also prepared the gold/ silica inverse opals and shared his knowledge about the colloid crystals with me.

Special thanks go to Dr. Petra Cameron for being such a nice lab mate and friend, always supporting me in the electrochemical studies as well.

I would like to thank Prof. J.-P. Majoral and Dr. Dongha Kim for sharing the dendrimer samples and their experience in the field of dendrimers with me.

I want to thank Adriana Rueda for her patience to measure the NPG substrates in the multi-wavelength setup, even over the weekend. Every 10 nm a scan was taken, that was really taking its time.

I am very grateful to the group of Dr. Renate Naumann, the protein tethered membrane-subgroup of AK-Knoll, for introducing this special membrane system to me. I was able to compare my NPG results directly to the well studied TSG substrates measured by Vinzenz Kirste.

I would also like to thank all the other members of AK-Knoll and cooperation partners who monitored my work and took effort in reading and providing me with valuable comments

on earlier versions of this thesis, especially Dr. Max Kreiter, Dr. Petra Cameron, Dr. Rudolf Robelek and Dr. Andreas Gießl. I thank you all!

Thanks to AG Wolfrum, our cooperation partners from the Institute of Zoology, Johannes Gutenberg-University of Mainz for the highly interesting definition of the centrin-transducin project and the constant supply of protein materials. Special thanks go to Dr. Andreas Gießl, who introduced me to the protein expression and purification steps. Since I started my Phd at the Max-Planck-Institute for polymer research, my life became international. I would like to thank all my friends from all over the world for the support and the friendship. I really hope that we will be able to stay in touch despite the large distances between us.

Many thanks to Andreas Scheller for the really great PC-support in the office as well as in the lab. His patience to solve any kind of problem.

I would like to thank my uncle Manfred Ahl, who helped me with the design of title page. Finally, I want to thank my whole family, who always believed in me.

**Curriculum Vitae****CONTACT INFORMATION**

Name Stefanie Ahl  
 Address Am Schlossgarten 9  
 67259 Kleinniedesheim  
 Telephone +49 6131 379269 (Office)  
 +49 1624312583 (Mobile)  
 Email ahl@mpip-mainz.mpg.de

**PERSONAL INFORMATION**

Date of Birth 07/January 1980  
 Place of Birth Ludwigshafen  
 Citizenship German  
 Sex Female  
 Marital Status Unmarried

**EDUCATION**

1990-1999 Rudi-Stephan-Gymnasium (Worms/Germany); final secondary-school examinations: 21.06.1999  
 1999-2004 Johannes-Gutenberg-University (Mainz/Germany); state examination in pharmacy: 29.11.2004  
 Since 2004 Max Planck Institute for Polymer Research (Mainz/Germany); PhD studies

**RESEARCH**

2004-present Max Planck Institute for Polymer Research, Ackermannweg 10, D-55128 Mainz

- organic supramolecular architectures at interfaces including membrane-mimetic approaches;
- nanoporous gold used as biosensors;
- epitope mapping to identify the centrin sequence binding to the G-protein transducin

**PUBLICATIONS**

1. Balushev, S.; Yu, F.; Miteva, T.; Ahl, S.; Yasuda, A.; Nelles, G.; Knoll, W.; Wegner, G., Metal-enhanced up-conversion fluorescence: Effective triplet-triplet annihilation near silver surface. *Nano Letters* 2005, 5, (12), 2482-2484.
2. Yu, F.; Ahl, S.; Caminade, A.-M.; Majoral, J.-P.; Knoll, W.; Erlebacher, J., Simultaneous Excitation of Propagating and Localized Surface Plasmon Resonance in Nanoporous Gold Membranes. *Analytical Chemistry* 2006, 78, (20), 7346-7350.

**COMPETENCIES & INTERESTS**

- Certificate of competence as group leader and commissioner for biological safety (§ 15 and § 17 GenTSV); 07.-08.12.2006
- Personal Interests: Dancing, Fitness training